Fundamental Physics through Gravitational Waves: From No-Hair Theorem to Quantum Structures of Black Holes

Thesis by
Song Ming Du

In Partial Fulfillment of the Requirements for the
Degree of
Doctor of Philosophy

CALIFORNIA INSTITUTE OF TECHNOLOGY
Pasadena, California

2019
Defended December 20, 2018

Song Ming Du
ORCID: 0000-0003-0083-7014

ACKNOWLEDGEMENTS

I am deeply grateful to my advisor, Prof. Yanbei Chen, for his support, supervision and encouragement throughout my research during the past four and half years, without which this research would not have been completed. Yanbei not only led me into the field of general relativity, gravitational waves and black holes, but also influenced my view and taste of science in general.

I would also like to thank my colleagues at TAPIR, especially Atsushi Nishizawa, Zachary Mark and Aaron Zimmerman. The discussions with them have provided me valuable inspirations. I am also indebted to JoAnn Boyd, for helping me with administrative matters.

I am also thankful to Prof. Alan Weinstein, Prof. Saul Teulkolsky and Prof. Frank Porter for serving my PhD thesis committee. Their comments and suggestions have significantly improved my thesis.

Finally, I would like to thank my family, for their long-lasting support and understanding.

ABSTRACT

In general relativity, black hole is the simplest macroscopic object in the universe: any black hole can be completely described by its mass, charge and angular momentum. However, such a simple picture might be changed if the gravitational field equations are modified or quantum effects are taken into consideration. These additional hairs of black hole, if exist, may provide valuable information to reveal the deepest mystery of the universe: quantum theory of gravity.

In this thesis, we try to relate the hypothetical extra hairs of black hole with the observational evidence as gravitational waves – another prediction of general relativity and are recently detected. In Chapter I, we provide a pedagogical introduction to the black hole hairs introduced by modified gravity and quantum mechanics, and lay out a mathematical framework to describe the gravitational wave emission with the existence of near-horizon quantum hair. In Chapter II we show that in scalar-tensor theory of gravity, the formation process of a black hole from gravitational collapse is accompanied with the emission of scalar hair. This mechanism gives rise to a scalar type memory effect of gravitational wave, which does not exist in general relativity. This phenomenon can further be used to study the parameter space of the scalar-tensor theory. In Chapter III, we find the scalar gravitational memory effect from stellar collapses provide the strongest sources for the stochastic gravitational wave background with scalar polarization in Brans-Dicke theory. The energy density spectrum for this background is provided and its model dependencies are studied. In Chapter IV, we provide a Green's function method to study the echoes, which are the gravitational waves reflected by the quantum hair near the event horizon of a black hole. In Chapter V, we build phenomenological models to describe the near-horizon quantum hair and predict its implication to the binary black hole stochastic gravitational wave background. Our study indicates that the existence of the quantum hair will significantly increases such a background and pins down the most relevant model parameter to be the area under the effective potential. Further, we also demonstrate that the result is rather robust against the uncertainties about the nature of the near-horizon quantum hair. In the end, a field theory based treatment to the gravitational waves in general relativity is provided as the appendix.

PUBLISHED CONTENT AND CONTRIBUTIONS

Song Ming Du, Yanbei Chen. (2018).
"Searching for near-horizon quantum structures in the binary black-hole stochastic gravitational-wave background".
Physical Review Letters 121, 051105.
DOI: 10.1103/PhysRevLett.121.051105.
S.M.D developed the idea, did all the calculation and analysis, and wrote the manuscript.

Song Ming Du (2018).
"Scalar Stochastic Gravitational-Wave Background in Brans-Dicke Theory of Gravity".
Under review by *Physical Review D*.
S.M.D developed the idea, did all the calculation and analysis, and wrote the manuscript.

Zachary Mark, Aaron Zimmerman, Song Ming Du, Yanbei Chen. (2017).
"A recipe for echoes from exotic compact objects".
Physical Review D 96, 084002.
DOI: 10.1103/PhysRevD.96.084002.
S.M.D involved in developing the idea, did partial calculation and analysis, and provided comments to the manuscript.

Song Ming Du, Atsushi Nishizawa. (2016).
"Gravitational wave memory: A new approach to study modified gravity".
Physical Review D 94, 104063.
DOI: 10.1103/PhysRevD.94.104063.
S.M.D developed the idea, did all the calculation and analysis, and wrote the manuscript.

TABLE OF CONTENTS

LIST OF ILLUSTRATIONS

LIST OF TABLES

Chapter 1

INTRODUCTION

Four fundamental interactions exist in the universe: the electromagnetic interaction, which governs everything about electricity, magnetism and light; the weak interaction, which is related to the conversion of a neutron into a proton through beta decay; the strong interaction, without which the atomic nuclei cannot be tied together; and gravitational interaction, which governs the falling of an apple on the earth as well as the motion of stars in the sky.

Among the four interactions, only electromagnetic and gravitational interactions can propagate on a cosmological scale. Until very recently, almost everything we know about the universe is from the information conveyed by the electromagnetic wave.

In the year of 1610, Galileo Galilei pointed his self-made telescope to Jupiter and discovered four moons of this planet. 400 years later, Galileo's simple telescope has evolved into giant telescopes, observatories and satellites, receiving signals across the whole spectrum, from radio to gamma ray. From these signals, we have established modern cosmology and astronomy. In the meantime, we should be aware that all of this information is emitted from electromagnetic interaction. What is our next step?

On February 11, 2016 the LIGO and Virgo collaboration announced the first direct detection of gravitational-wave from the merger of binary black hole, which marks the beginning of gravitational-wave astronomy and opens up a new window to the Universe. Since then, more GW events both from the merger of binary black hole and binary neutron star are detected by the Advanced LIGO/Virgo network (Table 1.1). Besides these resolvable individual GW sources we have discovered, a stochastic gravitational-wave background, which arises from the population of unresolved GW events at large distance, is anticipated to be detected in the upcoming years. These gravitational-wave events observed so far and will be detected in the future, not only prove the great success of Einstein's general theory of relativity, but also provide us a test field for other topics of fundamental physics, such as modified gravity theories as well as quantum properties of black holes.

In general relativity, the gravitational effect is described by the curve of spacetime

GW event	Source	Distance	Chirp Mass	Energy Radiated
GW150914	BH-BH	440 Mpc	28.2 $M_\odot$	3.0 $M_\odot$
LVT151012	BH-BH	1000 Mpc	15.1 $M_\odot$	1.5 $M_\odot$
GW151226	BH-BH	440 Mpc	8.9 $M_\odot$	1.0 $M_\odot$
GW170104	BH-BH	880 Mpc	21.1 $M_\odot$	2.0 $M_\odot$
GW170608	BH-BH	340 Mpc	7.9 $M_\odot$	0.85 $M_\odot$
GW170817	NS-NS	40 Mpc	1.12 $M_\odot$	0.03 $M_\odot$

Table 1.1: Observed gravitational-wave events

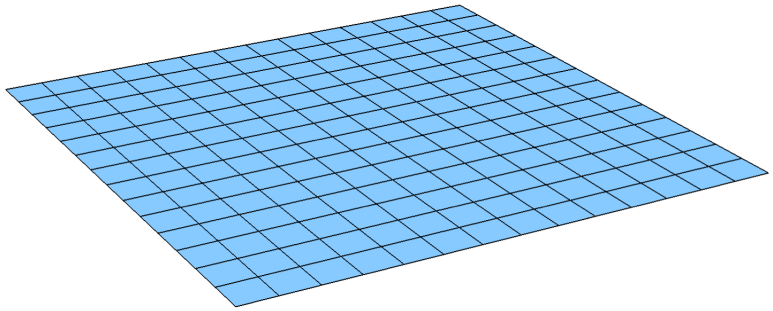

Figure 1.1: Geometry of Minkovski spacetime

geometry, which is characterized by the infinitesimal line element:

$$ds^2 = g_{\mu\nu} dx^\mu dx^\nu. \tag{1.1}$$

The metric tensor $g_{\mu\nu}$ is related to the distribution of matter via Einstein field equation:

$$R_{\mu\nu} - \frac{1}{2} g_{\mu\nu} R = 8\pi G \, T_{\mu\nu} \,, \tag{1.2}$$

where $R_{\mu\nu}$ is the Ricci tensor associated with the metric $g_{\mu\nu}$ and $T_{\mu\nu}$ is the stress-energy tensor of matter. The physical essence of Einstein field equation is summarized as "Spacetime tells matter how to move, while matter tells spacetime how to curve." [J.A.Wheeler]. In the vacuum where there is no matter to curve the spacetime, one solution to the Einstein field equation is the Minkovski spacetime (Fig. 1.1):

$$g_{\mu\nu} dx^\mu dx^\nu = -dt^2 + dx^2 + dy^2 + dz^2 \tag{1.3}$$

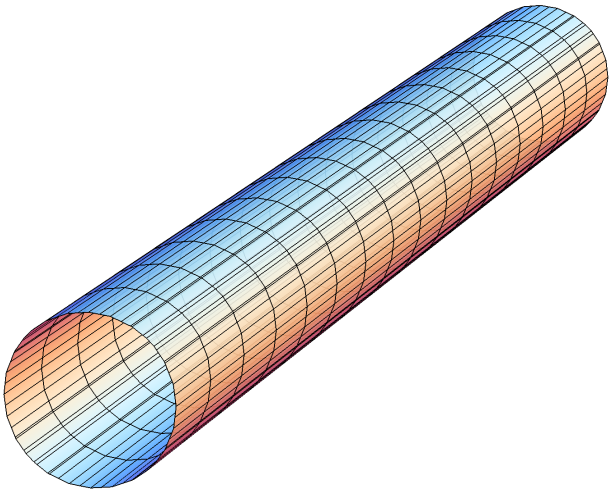

$h_{+,\times} = 0$

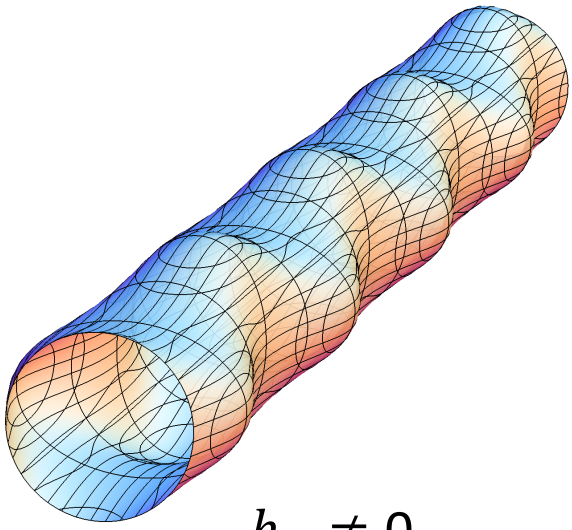

$h_{+} \neq 0$

Figure 1.2: Upper: The geometry of spacetime with no gravitational-wave. Lower: The geometry of spacetime when gravitational-wave is passing by with the + polarization mode.

This flat spacetime is the platform for special relativity.

Under the weak field approximation (and after properly choosing the gauge), the Einstein's field equation has the form of a wave equation for the perturbation of the metric. It suggests that the change of gravity caused by the motion of matter will propagate as a wave in the speed of light, as opposed to the picture of Newton's gravity in which the impact to the distant observer is instantaneous. Such a ripple of spacetime is called gravitational wave, whose existence was first predicted by Einstein in 1916. Imagine a gravitational wave propagating along the z-axis, the spacetime geometry is described by

$$g_{\mu\nu}dx^\mu dx^\nu = -dt^2 + (1+h_+)\,dx^2 + (1+h_\times)\,dy^2 + dz^2\ . \tag{1.4}$$

When a gravitational wave passes by, it stretch and squeeze the spacetime in the plane perpendicular to the wave propagating direction, as sketched in Fig. 1.2. In the equation above, the two wave functions correspond to the two polarization modes:

$$\begin{cases} h_+ = h_+(t-z) & : \quad + \text{ mode} \\ h_\times = h_\times(t-z) & : \quad \times \text{ mode} \end{cases} \tag{1.5}$$

For the plus mode, if a wave is propagating along z axis it stretches and squeezes the spacetime along x and y axis alternatively. The other mode (cross mode) is a 45 degree rotation of the plus mode. The vibrations of these two modes are shown in Fig. 1.3. Any tensor polarizations can be expanded as an overlap of these two modes.

Next consider the gravitational field caused by an object with spherical symmetry. It can be proved that such a spacetime is described by the Schwarzschild geometry (Fig. 1.4):

$$ds^2 = -\left(1-\frac{2M}{r}\right)dt^2 + \frac{1}{1-\frac{2M}{r}}dr^2 + r^2 d\theta^2 + r^2\sin^2\theta d\phi^2 \tag{1.6}$$

Suppose an observer and a source of light located at $r = r_o$ and $r = r_e$ respectively, the time (as measured from null infinity) between a photon is emitted from the source and detected by the observer is

$$\Delta t = \int_{r_e}^{r_o} \frac{1}{1-\frac{2M}{r}}\,dr = r_o - r_e + \ln\left(\frac{r_o-2M}{r_e-2M}\right)\ . \tag{1.7}$$

We find $\Delta t \to \infty$, as $r_e \to 2M$. This result indicates that the signal emitted at the surface $r = 2M$ will never reach to the outside observer. Such a surface separate

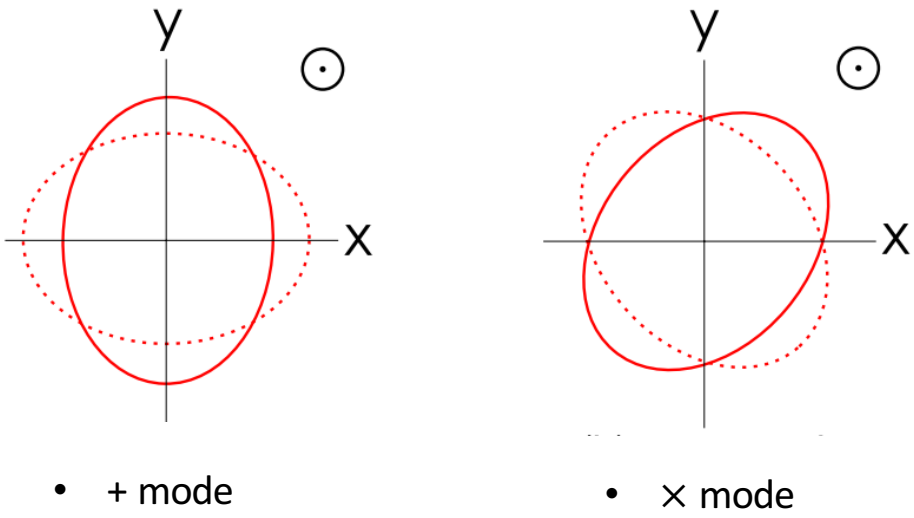

Figure 1.3: The two polarization modes of the gravitational wave which propagates along the z-axis.

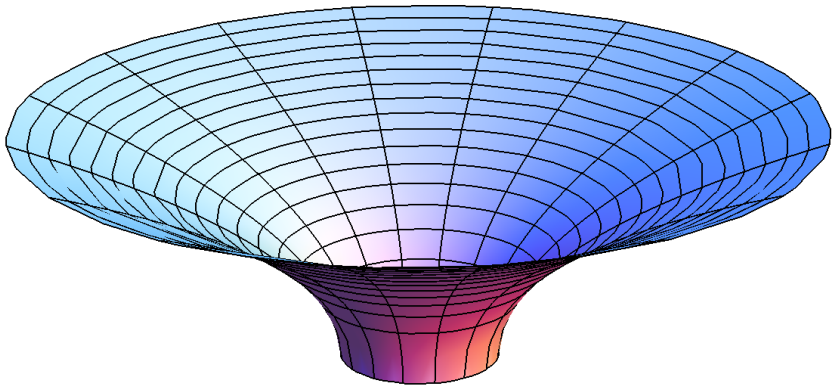

Figure 1.4: Geometry of Schwarzschild spacetime

the interior spacetime with the outside universe, as no information can escape from it. Such a spacetime region is called a Black Hole and its boundary is called Event Horizon.

In general relativity, these black holes are the simplest macroscopic objects in the universe. From the no-hair theorem, any black hole can be described by three observables: mass M, angular momentum J and charge Q. All types of black holes

are summarized in Table 1.2.

BH Observables	Solution to the Einstein equation
$M \neq 0$	Schwarzschild solution
$M,\ Q \neq 0$	Reissner-Nordstrom solution
$M,\ J \neq 0$	Kerr solution
$M,\ J,\ Q \neq 0$	Kerr-Newman solution

Table 1.2: Zoology of black holes

Two assumptions of the no-hair theorem are I. Gravity is governed by the Einstein equation, and II. Both the spacetime and the matter are treated classically. What if one of these two assumptions does not hold? Will it bring forth new observables of black hole? Will it cause other theoretical problems? These questions are partially answered in the following sections.

1.1 Black Hole's Hair in Modified Gravity

In the year of 1961, Brans and Dicke put forward a new set of equations to describe gravity which reconciles both the relativity principle as well as the Mach's principle. In this equation, the gravitation is not only described by the metric tensor $g_{\mu\nu}$, but also by a univeral scalar field ϕ. The Brans-Dicke field equation reads:

$$\begin{cases} \phi\left(R_{\mu\nu} - \frac{1}{2}g_{\mu\nu}R\right) - \left(\phi_{;\mu\nu} - g_{\mu\nu}\phi_{;}{}^{\rho}_{\rho}\right) = 8\pi T_{\mu\nu} + \frac{\omega}{\phi}\left(\phi_{,\mu}\phi_{,\nu} - \frac{1}{2}g_{\mu\nu}\phi_{,\rho}\phi_{,}{}^{\rho}\right) \\ (3+2\omega)\phi_{;}{}^{\mu}_{\mu} = 8\pi T_{\mu}{}^{\mu} - \omega_{,\phi}\phi_{,\mu}\phi_{,}{}^{\mu} \end{cases} \tag{1.8}$$

Now consider a spherical and homogeneous Newtonian star ($p \ll \rho$) with mass M and radius R. The source term in the second Brans-Dicke field equation is

$$T_{\mu}{}^{\mu} = -\frac{3M}{4\pi R^3} \tag{1.9}$$

In the Brans-Dicke limit ($\omega = \omega_{\rm BD} = Const.$). Under the boundary conditions

$$\begin{aligned} &\phi(r \to \infty) = \phi_0, \qquad &&\phi(r \to 0) < \infty \\ &\phi(R^+) = \phi(R^-), \qquad &&\phi'(R^+) = \phi'(R^-) \end{aligned} \tag{1.10}$$

where ϕ_0 is the asymptotic value of the universal scalar field at null infinity, the external solution for the scalar field is

$$\phi(r > R) = \frac{2}{2\omega + 3}\frac{M}{r}\ . \tag{1.11}$$

This result indicates that every star in the universe is a source to the universal scalar field. A simple estimation shows on large scale

$$\phi(r \to \infty) \simeq \frac{c}{\omega} \frac{\int_0^{r_H} 4\pi r^2 \rho dr}{r_H} \simeq \frac{c'}{\omega} \frac{1}{G} , \tag{1.12}$$

where $\rho = \rho_c = H_0^2/(8\pi G)$ is the critical density of the universe, $r_H = 1/H_0$ is the Hubble distance. This equation relates the Gravitational constant with the asymptotic value of the scalar field at the cosmological scale, which is determined by the total mass distribution in the universe. This is a reemergence of Mach's principle.

Apparently such a result does not apply to black holes, whose stress-energy tensor is zero outside the event horizon. Then what is the contribution to the universal scalar field from black holes? If it is non-zero, does it indicate besides M, J, and Q black holes also have a scalar hair?

A negative answer to this question is found in 1971 by S. Hawking, by proving the *no scalar hair theorem*:

The stationary black holes in Brans-Dicke theory is exactly described by the solution to Einstein's field equation. In other words, black hole is not a source to the scalar field.

A proof of this theorem is as follows. First consider a conformal transformation of the Brans-Dicke field equation by introducing

$$g^*_{\mu\nu} = G_0 \phi \, g_{\mu\nu} , \tag{1.13}$$

where G_0 is a constant to balance the dimension. In this conformal frame, the Brans-Dicke field equation without source converts to

$$\begin{cases} R^*_{\mu\nu} - \frac{1}{2} g^*_{\mu\nu} R^* = \frac{2\omega+3}{16\pi G_0 \phi^2} \left(\nabla^*_\mu \phi \nabla^*_\nu \phi - \frac{1}{2} g^*_{\mu\nu} \nabla^*_\rho \phi \nabla^\rho_* \phi \right) \\ \nabla^*_\mu \nabla^\mu_* \ln \phi = 0 \end{cases} , \tag{1.14}$$

where $R^*_{\mu\nu}$ and ∇^*_μ are correspondent to $g^*_{\mu\nu}$. The spacetime outside a axially symmetric stationary black hole contains two Killing vectors: ξ^μ, corresponding to time translation; and ζ^μ, corresponding to rotation. Due to symmetry, the scalar field ϕ must be constant along the two Killing vectors, which gives

$$\xi^\mu \nabla^*_\mu \ln(\phi/\phi_0) = 0 , \qquad \zeta^\mu \nabla^*_\mu \ln(\phi/\phi_0) = 0 . \tag{1.15}$$

The first equation further indicates that the vector $\nabla^*_\mu \ln(\phi/\phi_0)$ is space-like and hence

$$\nabla^*_\mu \ln(\phi/\phi_0)\, \nabla^\mu_* \ln(\phi/\phi_0) \geq 0\,. \tag{1.16}$$

As shown in Fig. 1.5, volume V is the spacetime region bounded by two Cauchy hypersurfaces, a portion of black hole event horizon and a time-like 3-surface at infinity. Consider an integral over V:

$$\begin{aligned}&\int_V d^4x\, \sqrt{-g_*}\, \left[\nabla^*_\mu \ln(\phi/\phi_0)\, \nabla^\mu_* \ln(\phi/\phi_0)\right] \\ =&\int_{\partial V} d^3x\, \sqrt{\gamma_*}\, \left[\ln(\phi/\phi_0)\, \nabla^*_\mu \ln(\phi/\phi_0)\right] n^\mu - \int_V d^4x\, \sqrt{-g_*}\, \left[\nabla^*_\mu \nabla^\mu_* \ln(\phi/\phi_0)\right]\,.\end{aligned} \tag{1.17}$$

Here we used the Stokes's theorem. The second term vanishes as a result of the Brans-Dicke field equation in conformal frame. Now let us consider the integral on the boundary:

$$\begin{aligned}&\int_{\partial V} d^3x\, \sqrt{\gamma_*}\, \left[\ln(\phi/\phi_0)\, \nabla^*_\mu \ln(\phi/\phi_0)\right] n^\mu \\ =&\int_{S_1} d^3x\, \sqrt{\gamma_*}\, \left[\ln(\phi/\phi_0)\, \nabla^*_\mu \ln(\phi/\phi_0)\right] n^\mu_1 + \int_{S_2} d^3x\, \sqrt{\gamma_*}\, \left[\ln(\phi/\phi_0)\, \nabla^*_\mu \ln(\phi/\phi_0)\right] n^\mu_2 \\ +&\int_I d^3x\, \sqrt{\gamma_*}\, \left[\ln(\phi/\phi_0)\, \nabla^*_\mu \ln(\phi/\phi_0)\right] n^\mu + \int_H d^3x\, \sqrt{\gamma_*}\, \left[\ln(\phi/\phi_0)\, \nabla^*_\mu \ln(\phi/\phi_0)\right] n^\mu\end{aligned} \tag{1.18}$$

The first two integrals are canceled out since $n^\mu_1 = -n^\mu_2$. The third integral vanishes because at infinity $\phi = \phi_0$. Since the normal vector for the event horizon is a combination of Killing vectors ξ^μ and ζ^μ, from Eq. (1.15) the last integral is also zero.

Now all the surface integrals vanish, the volume integral in Eq. (1.17) is zero. Together with the non-negative condition Eq. (1.16) and at infinity $\phi = \phi_0$, we have

$$\partial_\mu \ln(\phi/\phi_0) = 0 \quad \Rightarrow \quad \phi = \phi_0\,, \qquad \forall x \in V\,. \tag{1.19}$$

When the scalar field is a constant, the Brans-Dicke field equation recovers to the Einstein field equation. Consequently, the black hole solutions to Einstein field equation also describe the black holes in Brans-Dicke theory.

This no scalar hair property of black holes raises a question: according to the field equation the energy contained in the scalar field is conserved in the universe,

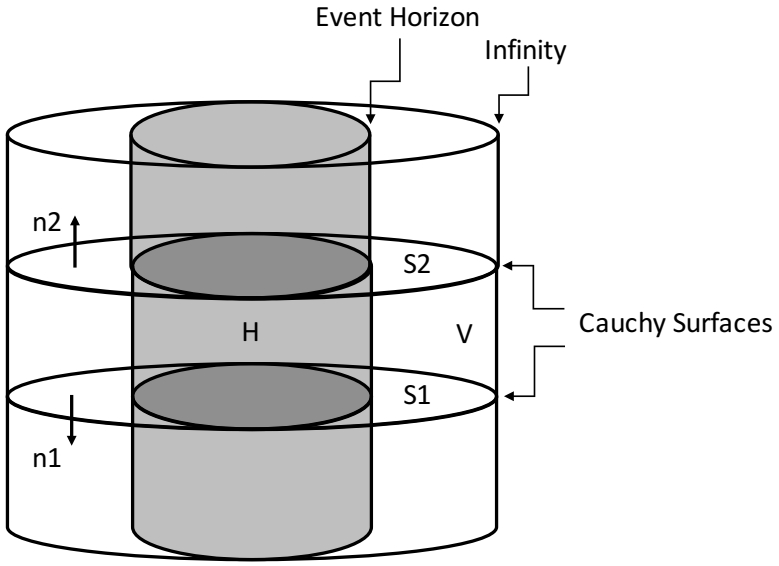

Figure 1.5: Spacetime of an axially symmetric stationary black hole.

but such energy is lost when a black hole forms. The only possibility is that the scalar energy is radiated away during the black hole formation from gravitational collapse. Is such a phenomenon observable? What is the mechanism of scalar wave emission? Can we use it to study modified gravity theory or to test the no scalar hair theorem? How can it relate to the stochastic gravitational wave background with scalar polarization? Does the scalar GW background produced by the same source as the tensor background? The answers to these questions are the main topic of Chapter II and Chapter III.

1.2 Black Hole's Hair in Quantum Mechanics

Imagine an observer located on a particle entering a black hole from free fall, is there anything different when it passes through the event horizon? The answer is no in classical general relativity, as required by the equivalence principle.

Will such a picture be changed after quantum mechanics is taken into consideration? To answer this question, a quantum theory of gravity is required. Although until today we are still looking for a complete theory of quantum gravity, some phenomena have been discovered by considering the quantum field in curved spacetime. In this framework, the matter is quantized while the spacetime is described classically. Just like fields have no absolute identification in special relativity (for example, electric field and magnetic field are transforming into each other as observed from different

reference frames), there is no unique definition of vacuum in curved spacetime.

This result changes the view from the falling observer, who now will see something different: particles are created near the event horizon, even if he is in the vacuum as observed from an inertial frame. Such a phenomenon was first discovered by S.Hawking in 1975 and is later called the *Hawking Radiation*:

As a quantum effect near the event horizon, black holes are creating and emitting particles as a hot body with a temperature proportional to the inverse of the surface gravity.

A simple derivation of this phenomenon is as follows. Consider a black hole formed from gravitational collapse. For a spherical collapse, the exterior spacetime is always described by the Schwarzschild solution as a proposition of Birkhoff's theorem. In Schwarzschild spacetime, the future and past null geodesics are described by $u = Const.$ and $v = Const.$ respectively, with

$$\begin{cases} u = t - r_* \\ v = t + r_* \end{cases} ,$$

where the tortoise coordinate is used:

$$r_* = t + 2M \ln\left(\frac{r}{2M} - 1\right) . \tag{1.20}$$

As a result, an event on the hypersurface of future null infinity (I^+) or the past null infinity (I^-) is described by coordinate (u, θ, φ) or (v, θ, φ) respectively.

Next consider a mass less Klein-Gordon field in Schwarzschild spacetime:

$$\Box\, \Phi = \sqrt{-g}\partial_\mu \left[\sqrt{-g} g^{\mu\nu} \partial_\nu \Phi\right] = 0 . \tag{1.21}$$

After introducing the mode decomposition

$$\Phi(t, r, \theta, \varphi) = \frac{1}{r}\phi(t, r) Y_{lm}(\theta, \varphi), \tag{1.22}$$

where Y_{lm} are the spherical harmonics. Then the radial function is governed by the equation

$$\frac{\partial^2 \phi}{\partial t^2} - \frac{\partial^2 \phi}{\partial r_*^2} + V_l(r)\phi = 0 , \tag{1.23}$$

with the effective potential

$$V_l(r) = \left(1 - \frac{2M}{r}\right)\left[\frac{l(l+1)}{r^2} + \frac{2M}{r^3}\right] , \tag{1.24}$$

notice at infinity $V_l = 0$.

The field ϕ can be described by the information on the Cauchy surfaces I^- *or* $I^+ \cup H$ (event horizon). Hence it can be quantized as

$$\begin{aligned}\phi &= \sum_i (f_i\ a_i + f_i^*\ a_i^\dagger) \\ &= \sum_i (p_i\ b_i + p_i^*\ b_i^\dagger + q_i\ c_i + q_i^*\ c_i^\dagger)\,,\end{aligned} \tag{1.25}$$

where f_i, p_i and q_i are wave functions satisfying the wave equation Eq. (1.23), and $(a_i,\ a_i^\dagger)$, $(b_i,\ b_i^\dagger)$, $(c_i,\ c_i^\dagger)$ are the creation annihilation operators for a particle with momentum $\vec{k}_i$ on I^-, I^+ and H respectively. The wave functions and operators on the past and future null infinity are related via Bogoliubov transform:

$$\begin{cases} p_i = \sum_j [\alpha_{ij} f_j + \beta_{ij} f_j^*] \\ b_i = \sum_j [\alpha_{ij}^* a_j - \beta_{ij}^* a_j^\dagger] \end{cases} \tag{1.26}$$

The completeness relation for the coefficients α_{ij} and β_{ij} resulted from the commutation relation of b_i and $b_i^\dagger$ will no longer hold in this case. This is because for wave with finite energy, only a portion can penetrate through the effective potential caused by the Schwarzschild spacetime. Now the complete relation changes to

$$\sum_j \left[|\alpha_{ij}|^2 - |\beta_{ij}|^2\right] = |\mathcal{T}_{\omega_i}|^2\ . \tag{1.27}$$

Here $\mathcal{T}$ is the transmissivity of Schwarzschild potential, which will be further studied in the following chapters.

Applying the particle number operator of vacuum I^+ onto the vacuum state of I^-, from the Bogoliubov transform we have

$$\langle 0_{I^-}|b_i^\dagger b_i|0_{I^-}\rangle = \sum_j |\beta_{ij}|^2\ . \tag{1.28}$$

This result indicates that the initial vacuum state will be filled with particles as observed from I^+. To find the Bogoliubov coefficients we start from the in-going and out-going wave functions at the past and future infinities:

$$f_\omega(v) \sim e^{i\omega v}\,, \quad u \to -\infty \quad \text{and} \quad p_\omega(u) \sim e^{i\omega u}\,, \quad v \to +\infty\ . \tag{1.29}$$

As we know f_ω is complete on I^-, to compare the two wave functions in the same spacetime region we need to push p_ω back to I^-. Consider a null geodesics starting

from v at I^- and ending with $u(v)$ at I^+. In Kruskal coordinates:

$$\begin{cases} V = \sqrt{\frac{r}{2M} - 1} e^{\frac{r+t}{4M}} \\ U = -\sqrt{\frac{r}{2M} - 1} e^{\frac{r-t}{4M}} \end{cases}, \tag{1.30}$$

let $V_0 = v_0$ be the critical coordinate at I^- that the geodesics marginally enters the event horizon, which relates to the coordinate $U_0 = 0$ at the future infinity. Apparently all geodesics with $v \geq v_0$ will be captured by the event horizon. On the other hand the geodesics with $V_1 = v < v_0$ will escape to the future null geodesics, and the corresponding Kruskal coordinate on I^+ is $U_1 = -Ce^{(r-t)/4M} = -Ce^{u/4M}$. Since the separation between two null geodesics in Kruskal coordinate remains a constant, as a result

$$U_1 - U_0 = V_1 - V_0 \quad \Rightarrow \quad u = \begin{cases} -\frac{1}{\kappa} \ln\left(\frac{v_0 - v}{C}\right) & \text{for } v < v_0 \\ 0 & \text{for } v \geq v_0 \end{cases}. \tag{1.31}$$

Here, $\kappa = 1/4M$ is the surface gravity of Schwarzschild black hole. Applying this result to the wave functions leads to

$$\begin{cases} f_\omega(v) = e^{i\omega v} \\ p_\omega(v) = Ke^{-i\frac{\omega}{\kappa} \ln \frac{v_0 - v}{C}} \Theta(v_0 - v) \end{cases}, \tag{1.32}$$

on the past null infinity I^+. Notice the constant is chosen so that f_ω satisfies the normal relation $\int f_\omega f'_\omega \, dv = \delta_{\omega\omega'}$. Accordingly, the Bogoliubov coefficients

$$\begin{aligned} \alpha_{ij} &= \int_{-\infty}^{+\infty} dv \; p_i f_j^* = \int_{-\infty}^{v_0} dv \; Ke^{-i\frac{\omega_i}{\kappa} \ln \frac{v_0 - v}{C} - i\omega_j v} \\ &= Ke^{-i\omega_j v_0} \int_0^\infty dz \; e^{-i\frac{\omega_i}{\kappa} \ln \frac{z}{C} + i\omega_j z} \\ \beta_{ij} &= \int_{-\infty}^{+\infty} dv \; p_i f_j = \int_{-\infty}^{v_0} dv \; Ke^{-i\frac{\omega_i}{\kappa} \ln \frac{v_0 - v}{C} + i\omega_j v} \\ &= Ke^{+i\omega_j v_0} \int_0^\infty dz \; e^{-i\frac{\omega_i}{\kappa} \ln \frac{z}{C} - i\omega_j z} \end{aligned} \tag{1.33}$$

To compute the integral we consider the integration contour in Fig. 1.6, from the analyticity inside the contour we have

$$\oint_C dz \; e^{-i\frac{\omega_i}{\kappa} \ln \frac{z}{C} + i\omega_j z} = 0 \tag{1.34}$$

Since on the arc of the contour the integrand is zero for $\mathrm{Im}(z) \to \infty$, we have

$$\begin{aligned} &\int_0^{+\infty} dz \; e^{-i\frac{\omega_i}{\kappa} \ln \frac{z}{C} + i\omega_j z} \\ &= -\int_{-\infty}^0 dz \; e^{-i\frac{\omega_i}{\kappa} \ln\left(\frac{z}{C} + i\epsilon\right) + i\omega_j z} = -\int_0^{+\infty} dz \; e^{-i\frac{\omega_i}{\kappa} \ln\left(-\frac{z}{C} + i\epsilon\right) - i\omega_j z}. \end{aligned} \tag{1.35}$$

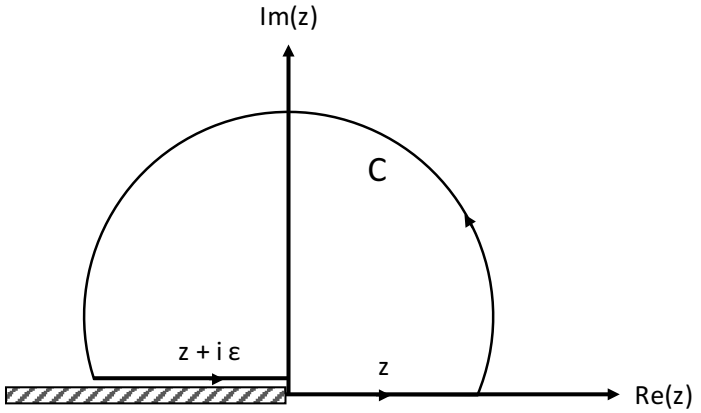

Figure 1.6: The integration contour C in complex z plane.

Notice that $\ln(-z/C + i\epsilon) = \ln(z/C) + i\pi$, then the coefficients can be calculated as

$$\alpha_{ij} = K\, C^{i\frac{\omega_i}{\kappa}} e^{-i\omega_j v_0} (-i\omega_j)^{i\frac{\omega_i}{\kappa}-1} \Gamma\left(1 - i\frac{\omega_i}{\kappa}\right) , \tag{1.36}$$

$$\beta_{ij} = -e^{2i\omega_j v_0} e^{-\pi\frac{\omega_i}{\kappa}} \alpha_{ij} . \tag{1.37}$$

Combining Eq. (1.27), (1.28) and (1.37), the expected number of particle with energy ω_i is

$$n_i = \sum_j |\beta_{ij}|^2 = \frac{|\mathcal{T}_{\omega_i}|^2}{e^{\frac{2\pi\omega_i}{\kappa}} - 1} \tag{1.38}$$

This is the Hawking's formula, which describes the distribution of particles created by black holes as a hot body with a temperature :

$$T = \frac{\kappa}{2\pi} . \tag{1.39}$$

One direct implication of this result is that such temperature reveals the entropy of a black hole. Start from the formula of the surface area of event horizon:

$$A = \int d\theta d\phi \, \sqrt{\gamma} = 4\pi r_s^2 , \tag{1.40}$$

where γ_{ij} is the induced metric on the event horizon: $ds^2 = r_s^2 d\theta^2 + r_s^2 \sin^2\theta d\phi^2$. If we take derivatives for both sides of equation $A = 16\pi M^2$, we find

$$dM = \frac{\kappa}{2\pi} d(A/4) . \tag{1.41}$$

Relating it with the first law of thermodynamics: $dE = TdS$ gives us the Bekenstein-Hawking entropy:

$$S = \frac{1}{4}A \tag{1.42}$$

In classical GR, the surface area of a black hole will never decrease: $\Delta A \geq 0$. This coincides with the second law of thermodynamics: $\Delta S \geq 0$. However, quantum mechanics can decrease the mass of a black hole due to Hawking radiation. From the Stefan-Boltzmann law, the emitted power is given by

$$P = A \cdot J = A \cdot \sigma T^4 \quad \Rightarrow \quad \frac{dM}{dt} = -P = -\frac{\sigma}{1024\pi^3} M^{-2}\,, \tag{1.43}$$

where σ is the Stefan-Boltzmann constant. This equation indicates the black hole mass is changing with time as

$$M(t) = M_0 \left[1 - \frac{3\sigma t}{1024\pi^3 M_0^3}\right]^{\frac{1}{3}}\,, \tag{1.44}$$

where M_0 is the initial mass of the black hole. Apparently, all the mass will be evaporated away within a finite time $t = 1024\pi^3 M_0^3/3\sigma$.

Does the evaporation send out additional information besides the macroscopic quantities such as M, J, Q? The answer is negative, from the fact that the only information contained in the black-body radiation spectrum is the temperature. However, the temperature is determined by the surface gravity, which is solely dependent on the three hairs of black hole. This result presents a quantum version of no-hair theorem.

However, such an argument will lead to paradox if one considers the information loss during the black hole formation from gravitational collapse. To elucidate this, let's consider the Hilbert space at the past null infinity I^-, the future null infinity I^+, the horizon H and there related bases states:

$$|A\rangle \in \mathcal{H}_{I^+}\,, \quad |B\rangle \in \mathcal{H}_H, \quad |C\rangle \in \mathcal{H}_{I^-}\,. \tag{1.45}$$

The initial and final state are expanded into wave functions:

$$|\Psi^{I^-}\rangle = \sum_C \xi_C |C\rangle\,, \quad \langle\Phi^{I^+\cup H}| = \sum_A \sum_B \chi_A \zeta_B \langle A|\langle B|\,. \tag{1.46}$$

Suppose the state is evolved with an S matrix: $|\Psi^{I^+\cup H}\rangle = \hat{S}\,|\Psi^{I^-}\rangle$. The scattering amplitude is then given by

$$\mathcal{A} = \langle\Phi^{I^+\cup H}|\Psi^{I^+\cup H}\rangle = \sum_A \sum_B \sum_C \chi_A \zeta_B \xi_C S_{ABC}\,. \tag{1.47}$$

However, as we will see such a scattering amplitude is not observable since the horizon H acts as a hidden surface. The initial and final system can be described by a density operators:

$$\hat{\rho}^{I^-} = |\Psi^{I^-}\rangle\langle\Psi^{I^-}|, \qquad \hat{\rho}^{I^+\cup H} = |\Psi^{I^+\cup H}\rangle\langle\Psi^{I^+\cup H}| \,. \tag{1.48}$$

However, we can only make observation on $\mathcal{H}_{I^-}$ and $\mathcal{H}_{I^+}$ but not on $\mathcal{H}_H$, which means the final density operator is given by the partial trace:

$$\hat{\rho}^{I^+} = \mathrm{tr}_H \hat{\rho}^{I^+\cup H} = \sum_B \langle B|\Psi^{I^+\cup H}\rangle\langle\Psi^{I^+\cup H}|B\rangle \,, \tag{1.49}$$

with the density matrix element given by

$$\rho^{I^+}_{AA'} = \sum_B \langle A|\langle B|\Psi^{I^+\cup H}\rangle\langle\Psi^{I^+\cup H}|B\rangle|A'\rangle = \sum_B \sum_C \sum_{C'} S_{ABC}\bar{S}_{A'BC'}\xi_C\bar{\xi}_{C'} \,. \tag{1.50}$$

This is the density matrix for a mixed state. Given the initial system is described by pure state, it indicates that a portion of information is lost to the hidden surface.

Where does this part of information go? Since Hawking radiation does not take away additional information, one may conjecture that the information is stored inside the black hole, especially at the singularity. However, a direct contradiction to this hypothesis is from the proposition discussed above: the black hole will evaporate completely in a finite time, nothing will be left behind including the singularity. Now that the information is stored neither inside nor outside the black hole, this leads 't Hooft conjecture that the holography principle: the information about the microscopic states is completely written on the boundary, i.e. the event horizon of a black hole [G.'t Hooft 1993]. This hypothesis also aligns with the fact that the entropy of a black hole is proportional to its surface area instead of the volume. Now consider the Bekenstein-Hawking entropy and relate it with the Boltzmann's entropy formula: $S = k \log W$, (with W representing the total number of microscopic states of the system) which gives

$$W = e^{\frac{c^3 A}{4G\hbar}} = 2^{\frac{A}{A_0}} \,. \tag{1.51}$$

This equation suggests that each unit area A_0 contains one bit of information, with

$$A_0 = 4 \log 2 \, l_p^2 \simeq 2.773 \, l_p^2 \,, \tag{1.52}$$

where l_p^2 represents the Planck area.

How the information is stored on the boundary is still an open question. However, this picture leads one to question the equivalence principle at the event horizon: when

an observer crosses enters a black hole from free fall, he may observe something nontrivial at the boundary. As a result, it is speculated that quantum gravity effects may give rise to spacetime structures at Planck scale near the event horizon of a black hole.

How is the quantum structure, if it exists, related to observational evidence? Can it reflect gravitational waves which propagate towards the event horizon to the null infinity? Can we build a mathematical model to describe this phenomenon? What is its implication to other observables such as stochastic gravitational wave background? The answers to these questions are the main topics of Chapter IV and Chapter V. Next section will provide a framework for these topics.

1.3 Quantum Hair Near the Event Horizon and Gravitational Wave Echoes in the Black Hole Perturbation Theory

Black Hole Perturbation Theory provides a framework to study the gravitational-wave emitted from a test particle plunging into a black hole along a certain trajectory. This approach can also be applied to binary systems from the Effective One-Body (EOB) formalism.

The master equation for the perturbations of the Schwarzschild geometry is given by the generalized Regge-Wheeler (Aka. Sasaki-Nakamura) equation [Sasaki and Nakamura 1981]:

$$\left[\partial_{r_*}^2 + \omega^2 - V_l(r)\right] X_{lm}(\omega, r_*) = S_{lm}(\omega, r) \,. \tag{1.53}$$

In this equation, r_* is the tortoise radius, which is related to the Schwarzschild radius via $dr/dr_* = 1 - 2M/r$, with M denoting the mass of the Schwarzschild black hole. The effective potential V_l is caused by the Schwarzschild geometry near the black hole and is expressed as

$$V_l(r) = \left(1 - \frac{2M}{r}\right)\left(\frac{l(l+1)}{r^2} - \frac{6M}{r^3}\right) \,. \tag{1.54}$$

The source term S_{lm} is determined by the trajectory of the plunging particle. If the particle is moving in the $\theta = \pi/2$ plane, the trajectory is described by its coordinates as functions of the radius: $t = T(r)$, $r = R(r)$, $\theta = \pi/2$, $\varphi = \Phi(r)$. The source term is related to a new function W_{lm} via

$$S_{lm}(\omega, r) = e^{-i\omega r_*} \frac{r^2 - r}{r^5} W_{lm}(\omega, r) \,, \tag{1.55}$$

and the function $W_{lm} = W_1 + W_2 + W_3$ is given by differential equations and the corresponding asymptotic boundary conditions:

$$\begin{cases} W_1(r) = e^{i\omega V(r)} h_1(r) \\ \dfrac{d}{dr} W_2(r) = e^{i\omega V(r)} h_2(r) \\ \dfrac{d^2}{dr^2} W_3(r) = e^{i\omega V(r)} h_3(r) \end{cases} , \qquad \begin{cases} W_2(r \to \infty) = -\dfrac{e^{i\omega V(r)}}{i\omega V'(r)} h_2(r) \\ W_3(r \to \infty) = \dfrac{e^{i\omega V(r)}}{(\omega V'(r))^2} h_3(r) \\ W_3'(r \to \infty) = -\dfrac{e^{i\omega V(r)}}{i\omega V'(r)} h_3(r) \end{cases} . \tag{1.56}$$

Here, $V(r) = T(r) + r_*(r)$ and the h functions are given by

$$\begin{cases} h_1(r) = \dfrac{\sqrt{\lambda(\lambda+2)}}{2(i\omega)^2} \, {}_0f(r) + \dfrac{\sqrt{\lambda}}{i\omega} r^2 \, {}_{-1}f(r) + \dfrac{r^4}{2} \, {}_{-2}f(r) \\ h_2(r) = \dfrac{\sqrt{\lambda(\lambda+2)}}{2(i\omega)^2} \, {}_0f'(r) + \dfrac{\sqrt{\lambda}}{i\omega} \left[r^2 \, {}_{-1}f(r) \right]' + r^3 \, {}_{-2}f(r) \\ h_3(r) = \dfrac{\sqrt{\lambda(\lambda+2)}}{2(i\omega)^2} \left[\, {}_0f'(r) V'(r) \right]' + r^2 \, {}_{-2}f(r) \end{cases} , \tag{1.57}$$

where $\lambda = (l-1)(l+2)$ and the ${}_sf$ functions are related to the spin-weighted spherical harmonics ${}_sY_{lm}$ via

$$\begin{cases} {}_0f(r) = -\dot{R}(r) \, {}_0\bar{Y}_{lm} \left[\frac{\pi}{2}, \Phi(r) \right] \\ {}_{-1}f(r) = -i \, \dot{\Phi}(r) \, {}_{-1}\bar{Y}_{lm} \left[\frac{\pi}{2}, \Phi(r) \right] \\ {}_{-2}f(r) = -\left[\dot{R}(r) \right]^{-1} \left[-i \, \dot{\Phi}(r) \right]^2 \, {}_{-2}\bar{Y}_{lm} \left[\frac{\pi}{2}, \Phi(r) \right] \end{cases} , \tag{1.58}$$

with $\dot{x}$ denoting $dx/d\tau$.

In the limit $r \to \infty$, the radial function X_{lm} is related to the observables such as the waveform and the energy spectrum via

$$h_+ + h_\times = \sum_{lm} \frac{8}{r} \, {}_{-2}Y_{lm} X_{lm}(t) \, , \tag{1.59}$$

$$\frac{dE}{d\omega} = \sum_{lm} 16\pi\omega^2 |X_{lm}(\omega)|^2 \, , \tag{1.60}$$

where the Fourier transform is given by

$$X_{lm}(t) = \int_{-\infty}^{+\infty} d\omega \; e^{-i\omega t} X_{lm}(\omega) \, . \tag{1.61}$$

When the source term is available, the master equation can be easily solved by the Green's function method:

$$X_{lm}(\omega, r_*) = \int_{-\infty}^{+\infty} dr'_* \; G^{(0)}(\omega, r_*, r'_*) S_{lm}(\omega, r'_*) \tag{1.62}$$

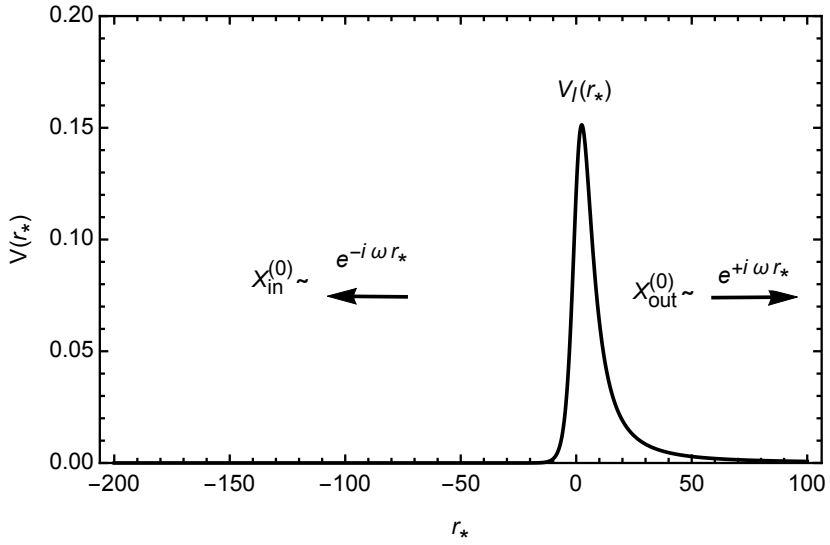

Figure 1.7: The two homogeneous solutions $X_{\rm in}^{(0)}$ and $X_{\rm out}^{(0)}$.

where $G^{(0)}$ is the Green's function:

$$\left[\partial_{r_*}^2 + \omega^2 - V_l(r)\right] G^{(0)}(\omega, r_*, r_*') = \delta(r_* - r_*') \,. \tag{1.63}$$

The Green's function can be constructed from two homogeneous functions with boundary conditions:

$$X_{\rm in}^{(0)} \sim e^{-i\omega r_*} \,, \qquad r_* \to -\infty \tag{1.64}$$

$$X_{\rm out}^{(0)} \sim e^{+i\omega r_*} \,, \qquad r_* \to +\infty \tag{1.65}$$

These two homogeneous solutions are shown in Fig. 1.7. As can be easily proved, the Green's function can be constructed as

$$G^{(0)}(\omega, r_*, r'_*) = \frac{X^{(0)}_{\rm out}(r_*)X^{(0)}_{\rm in}(r'_*)\,\Theta(r_* - r'_*) + X^{(0)}_{\rm out}(r'_*)X^{(0)}_{\rm in}(r_*)\,\Theta(r'_* - r_*)}{W[X^{(0)}_{\rm in}, X^{(0)}_{\rm out}]} \,. \quad (1.66)$$

Here $\Theta(\cdot)$ is the step function and the Wronskian

$$W[X^{(0)}_{\rm in}, X^{(0)}_{\rm out}] = X^{(0)}_{\rm in}\partial_{r_*}X^{(0)}_{\rm out} - X^{(0)}_{\rm out}\partial_{r_*}X^{(0)}_{\rm in} \quad (1.67)$$

is a constant due to the homogeneous master equation. With the help of the Green's function, the radial function approaching the null infinity (X^0) and the event horizon (X^H) are then given by

$$\begin{cases} X^0_{lm}(\omega, r_* \to +\infty) = Z^0_{lm}(\omega)\, e^{+i\omega r_*} \\ X^H_{lm}(\omega, r_* \to -\infty) = Z^H_{lm}(\omega)\, e^{-i\omega r_*} \end{cases} , \quad (1.68)$$

where Z^0 and Z^H are the corresponding amplitudes at the null infinity and the event horizon respectively, with

$$\begin{cases} Z^0_{lm}(\omega) = \frac{1}{W^{(0)}} \int_{-\infty}^{+\infty} dr'_*\; X^{(0)}_{\rm in}(\omega, r'_*) S_{lm}(\omega, r'_*) \\ Z^H_{lm}(\omega) = \frac{1}{W^{(0)}} \int_{-\infty}^{+\infty} dr'_*\; X^{(0)}_{\rm out}(\omega, r'_*) S_{lm}(\omega, r'_*) \end{cases} . \quad (1.69)$$

Now let's apply this method to an example: consider a particle with mass μ is radially plunging into a Schwarzschild black hole with mass M. The trajectory ($E = 1$) is given by

$$\frac{T(r)}{M} = -\frac{4}{3}\left(\frac{r}{2M}\right)^{\frac{3}{2}} - 4\left(\frac{r}{2M}\right)^{\frac{1}{2}} + 2\ln\left(\left[\left(\frac{r}{2M}\right)^{\frac{1}{2}} + 1\right]\left[\left(\frac{r}{2M}\right)^{\frac{1}{2}} + 1\right]^{-1}\right) . \quad (1.70)$$

This trajectory is plotted in Fig. 1.8. Inserting the trajectory to Eq. 1.55 - 1.58 gives the source term, then the radial function can be calculated from direct integration from Eq. 1.68 - 1.69. The resulting waveform and energy spectrum for the 22 mode are shown in Fig. 1.9 and Fig. 1.10. The energy spectrum is peaked at the leading quasinormal mode of Schwarzschild spacetime: $\mathrm{Re}(\omega_{\rm QNM}) = 0.37M^{-1}$.

The two amplitudes at event horizon and null infinity are compared in Fig. 1.11. One can see that the horizon wave is several order of magnitudes larger than the infinity wave at both low and high frequencies.

Now suppose a quantum structure exists near the event horizon. It can be modeled as an additional effective potential (Planck potential) centered at $r_p = r_s + \epsilon$, with $\epsilon \sim l_p$. As shown in Fig. 1.12, the existence of the Planck potential renders the in-going homogeneous solution now following a reflective boundary condition:

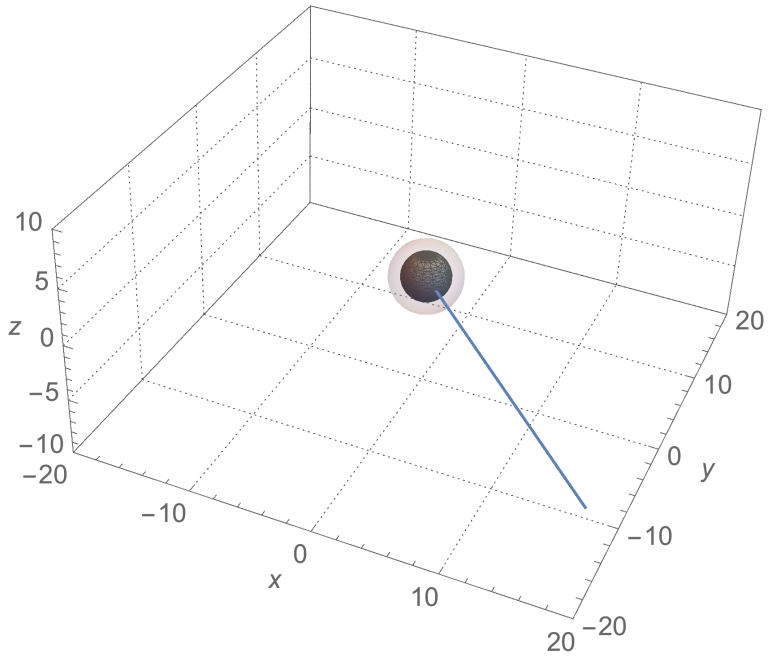

Figure 1.8: The trajectory of a particle radially plunges into a Schwarzschild black hole. The inner black sphere with radius $2M$ represents the horizon of the black hole. The outer translucent sphere with radius $3M$ represents the photon sphere, which is the location of the peak of Regge-Wheeler potential.

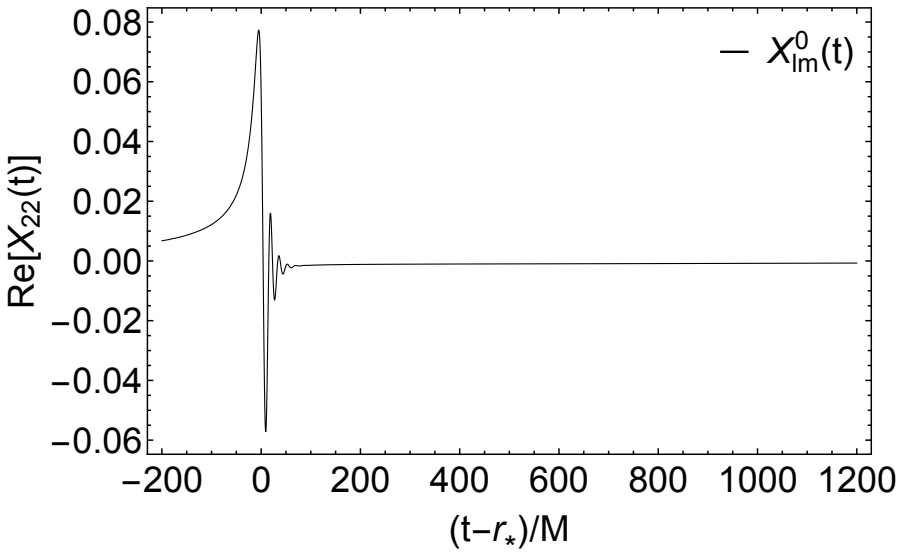

Figure 1.9: The $l, m = 2, 2$ waveform from a test particle radial plunging into a Schwarzschild black hole.

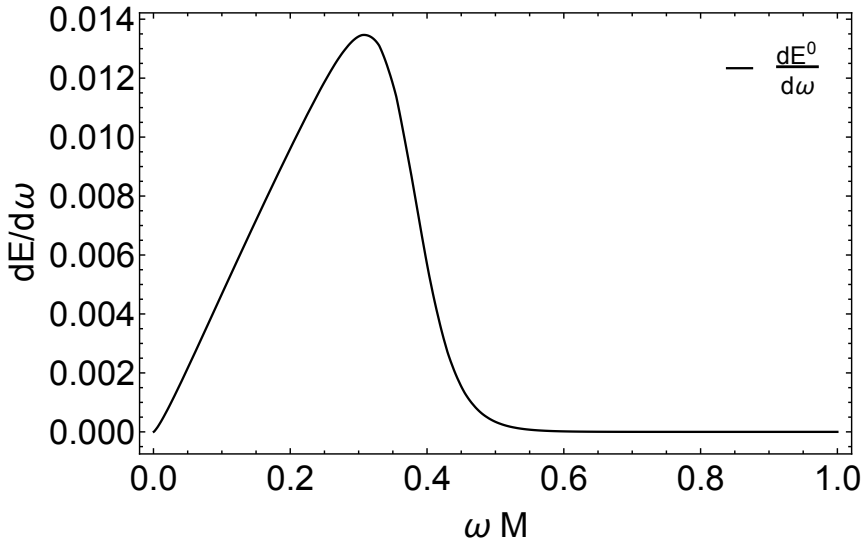

Figure 1.10: The $l, m = 2, 2$ energy spectrum from a test particle radial plunging into a Schwarzschild black hole.

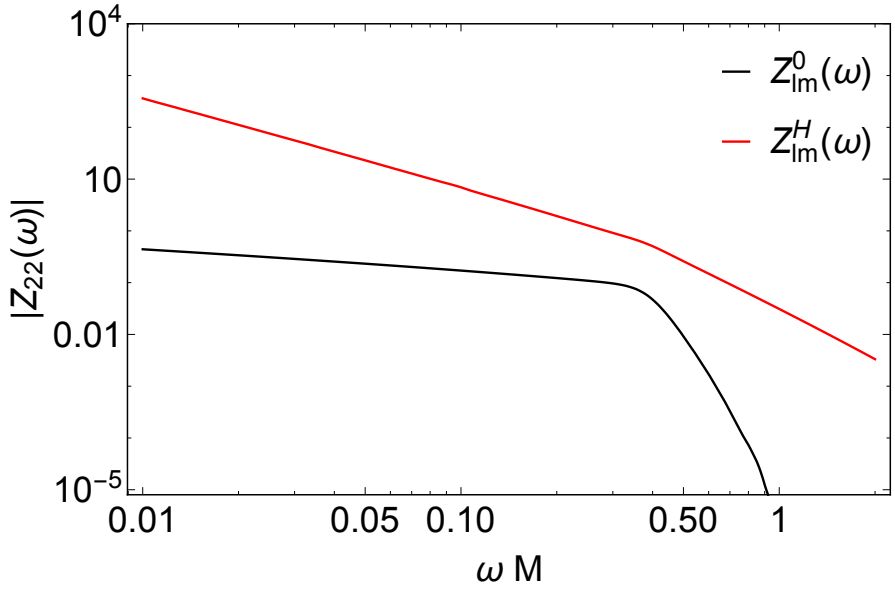

Figure 1.11: The $l, m = 2, 2$ amplitudes at null infinity and event horizon from a test particle radial plunging into a Schwarzschild black hole.

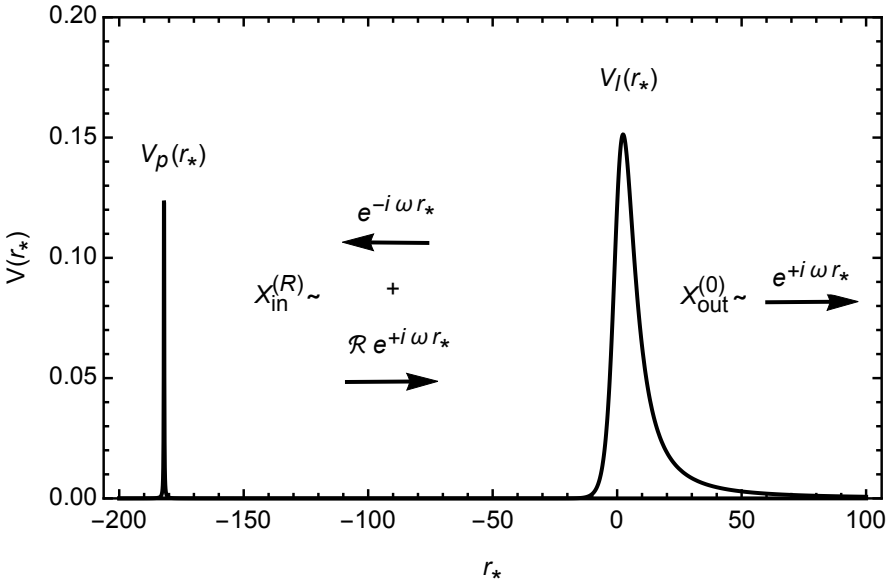

Figure 1.12: The two homogeneous solutions $X_{\text{in}}^{(R)}$ and $X_{\text{out}}^{(R)}$ with the Planck potential centered at r_p^*.

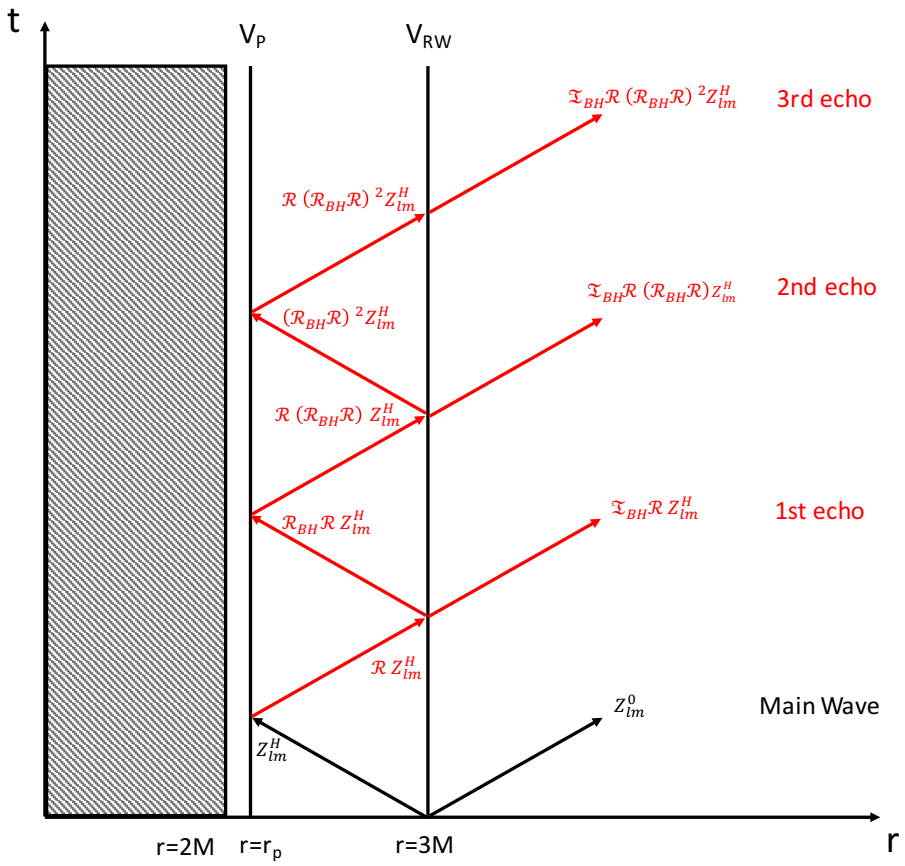

Figure 1.13: The spacetime plot for the main wave and echoes of gravitational-wave.

$$X_{\text{in}}^{(R)} \sim e^{-i\omega r_*} + \mathcal{R} e^{+i\omega r_*}\,, \qquad r_* \to r_*^p \tag{1.71}$$

$$X_{\text{out}}^{(0)} \sim e^{+i\omega r_*}\,, \qquad r_* \to +\infty\,. \tag{1.72}$$

Here $\mathcal{R}$ is the reflectivity of the Planck potential. Formally, the reflectivity and transmissivity of the Planck potential as well as the Regge-Wheeler potential can be defined by:

$$\begin{cases} \mathcal{R}_{\text{BH}} = \frac{B_-(\omega)}{B_+(\omega)} \\ \mathcal{T}_{\text{BH}} = \frac{1}{B_+(\omega)} \end{cases} \qquad\qquad \begin{cases} \mathcal{R}_{\text{BH}} = \frac{A_+(\omega)}{A_-(\omega)} \\ \mathcal{T}_{\text{BH}} = \frac{1}{A_-(\omega)} \end{cases} \tag{1.73}$$

where the coefficients are from the homogeneous radial functions satisfying the boundary conditions:

$$X_{\text{RW}} \sim \begin{cases} e^{+i\omega r_*}\,, & r_* \to +\infty \\ B_-(\omega) e^{-i\omega r_*} + B_+(\omega) e^{+i\omega r_*}\,, & r_* \to -\infty \end{cases} \tag{1.74}$$

$$X_{\text{BH}} \sim \begin{cases} e^{-i\omega r_*}\,, & r_* \to -\infty \\ A_-(\omega) e^{-i\omega r_*} + A_+(\omega) e^{+i\omega r_*}\,, & r_* \to +\infty \end{cases} \tag{1.75}$$

We have no prior knowledge about the properties of the Planck potential, except that it must be localized at $r_* = r_*^p$. For example, one simple model would be the Dirac δ-potential:

$$V_p = \mathcal{A}\, \delta[(r_* - r_*^p)/M]\,, \tag{1.76}$$

where the parameter $\mathcal{A}$ is defined as the area under potential. The corresponding reflectivity is then given by

$$\mathcal{R} = \frac{\mathcal{A} e^{-2i\omega r_*^p}}{2i\omega - \mathcal{A}}\,. \tag{1.77}$$

Now with the help of the transmissivity and reflectivity, we can relate the reflective Green's function with the original one:

$$G^{(R)}(\omega, r_*, r_*') = G^{(0)}(\omega, r_*, r_*') + \frac{\mathcal{T}_{\text{BH}}\mathcal{R}}{1 - \mathcal{R}_{\text{BH}}\mathcal{R}} \frac{X_{\text{out}}^{(0)}(r_*) X_{\text{out}}^{(0)}(r_*')}{W^{(0)}}\,. \tag{1.78}$$

This result can be obtained from the relation between $X^{(R)}$ and $X^{(0)}$:

$$X_{\text{in}}^{(R)} = (1 - \mathcal{R}_{\text{BH}}\mathcal{R}) X_{\text{in}}^{(0)} + \mathcal{T}_{\text{BH}}\mathcal{R} X_{\text{out}}^{(0)}\,, \qquad X_{\text{out}}^{(R)} = X_{\text{out}}^{(0)}\,. \tag{1.79}$$

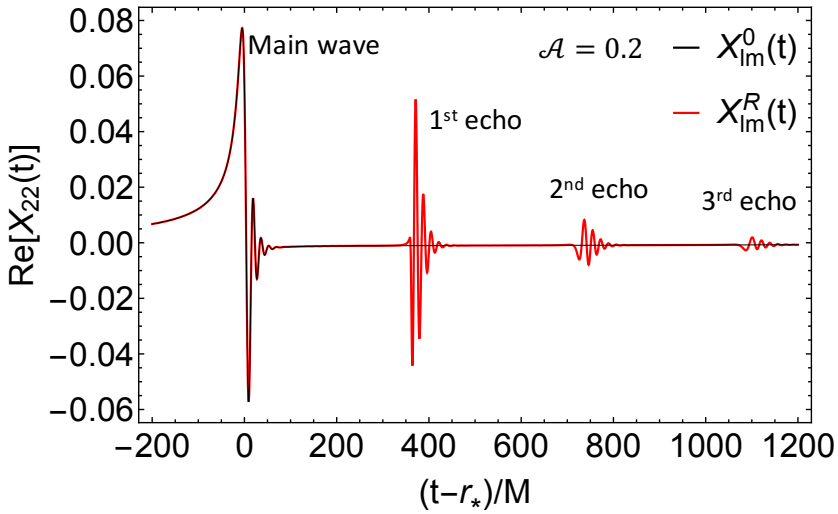

Figure 1.14: The $l, m = 2, 2$ waveform from a test particle radial plunging into a Schwarzschild black hole with quantum structure.

Integrating the reflective Green's function with the source term, the inhomogeneous solution with reflectivity is expressed by

$$X^R_{lm} = Z^0_{lm}\, e^{+i\omega r_*} + \frac{\mathcal{T}_{\rm BH}\mathcal{R}}{1-\mathcal{R}_{\rm BH}\mathcal{R}} Z^H_{lm}\, e^{+i\omega r_*} \tag{1.80}$$

The physical implication of this formula is clearer if one expands the second term in terms of *echoes*:

$$\frac{\mathcal{T}_{\rm BH}\mathcal{R}}{1-\mathcal{R}_{\rm BH}\mathcal{R}} Z^H_{lm} = \sum_{n=1}^{\infty} Z^n_{lm}\,, \qquad \text{with} \quad Z^n_{lm} = \mathcal{T}_{\rm BH}\mathcal{R}\,(\mathcal{R}_{\rm BH}\mathcal{R})^{n-1}\, Z^H_{lm}\,, \tag{1.81}$$

where Z^n represents the amplitude of the n-th echo of gravitational-wave. As shown in Fig. 1.13, the echoes are generated by the horizon wave reflecting between the two potential barriers.

Using this approach, the waveform and energy spectrum with the existence of Planck potential are shown in Fig. 1.80 and 1.15, where $\mathcal{A} = 0.2$. The resonant peaks in the energy spectrum with separation $\Delta\omega = \pi/r^p_*$ are translated to the echoes in the time domain, with separation $\Delta t = 2r^p_*$.

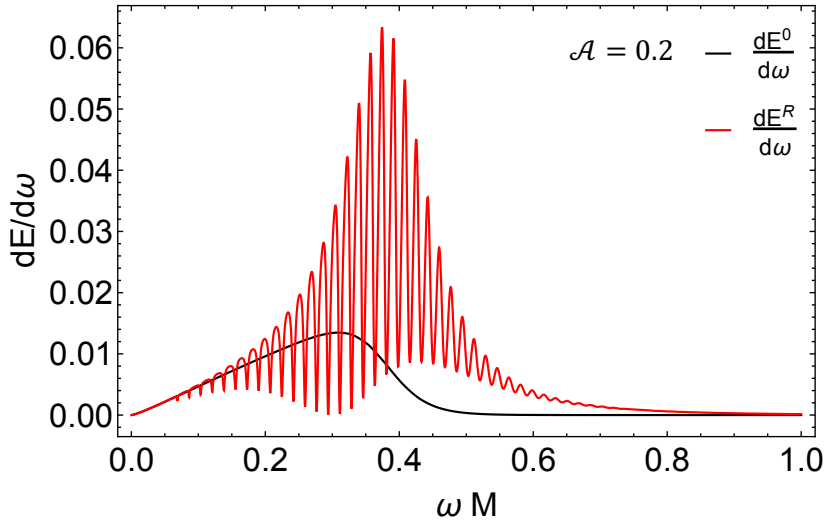

Figure 1.15: The $l, m = 2, 2$ energy spectrum from a test particle radial plunging into a Schwarzschild black hole with quantum structure.

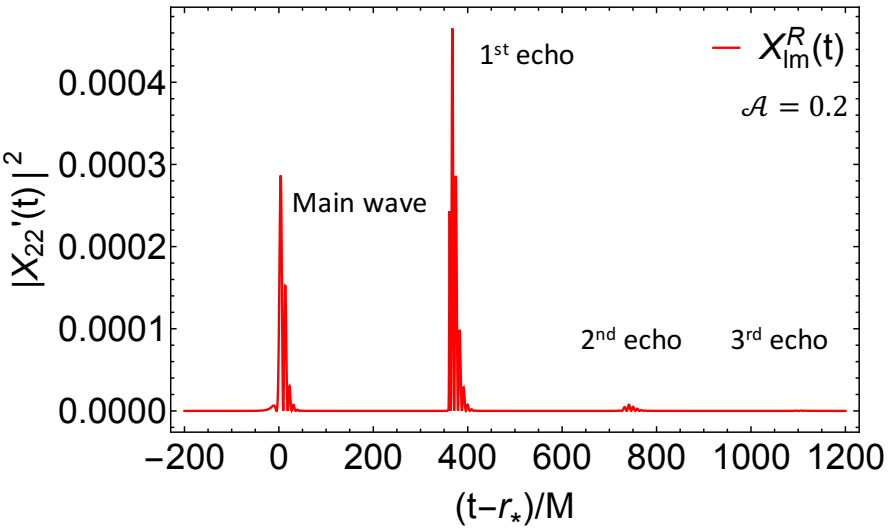

Figure 1.16: The squared changing rate of the $l, m = 2, 2$ waveform from a test particle radial plunging into a Schwarzschild black hole with quantum structure.

Simple calculation shows that the energy contained in the echoes is even larger than that contained in the main wave:

$$E^R_{\rm tot}/E^0_{\rm tot} = 2.473\,, \qquad \text{with} \quad E_{\rm tot} = \int_0^{+\infty} d\omega\, \frac{dE}{d\omega} \tag{1.82}$$

This result can be explained by Fig. 1.11: since the energy goes into the horizon is several times larger than that goes to the infinity, even if only a small fraction of the horizon wave is reflected it may render greater energy in the echoes. An apparent paradox appears in Fig. 1.80: the amplitude of the echo which contains more energy than the main wave is even smaller. The explanation lies in the fact that the energy of radiation is dependent on the changing rate instead of the amplitude of the wave. As shown in Fig. 1.16, the changing rate of the 1st echo $|\dot{X}^1_{lm}(t)|^2$ is indeed greater than the main wave $|\dot{X}^0_{lm}(t)|^2$.

This result suggests potential observable evidence for the existence of near-horizon quantum structures of black holes. However, to find a reliable observable one needs to consider the gravitational-wave emitted from the inspiral-merger-ringdown stages of binary black holes, instead of an over simplified model as radial plunge which describes the head-on collision of two black holes. A more detailed study along this direction is presented in Chapter V.

Chapter 2

GRAVITATIONAL WAVE MEMORY: A NEW APPROACH TO STUDY MODIFIED GRAVITY

It is well known that two types of gravitational wave memory exist in general relativity (GR): the linear memory and the non-linear, or Christodoulou memory. These effects, especially the latter, depend on the specific form of Einstein equation. It can then be speculated that in modified theories of gravity, the memory can differ from the GR prediction, and provides novel phenomena to study these theories. We support this speculation by considering scalar-tensor theories, for which we find two new types of memory: the T memory and the S memory, which contribute to the tensor and scalar components of gravitational wave, respectively. In particular, the former is caused by the burst of energy carried away by scalar radiation, while the latter is intimately related to the no scalar hair property of black holes in scalar-tensor gravity. We estimate the size of these two types of memory in gravitational collapses, and formulate a detection strategy for the S memory, which can be singled out from tensor gravitational waves. We show that (i) the S memory exists even in spherical symmetry, and is observable under current model constraints, and (ii) while the T memory is usually much weaker than the S memory, it can become comparable in the case of spontaneous scalarization.

2.1 Introduction

The discovery of GW150914 [8] by advanced LIGO marks the beginning of a new era in gravitational physics, and brings forth new opportunities to study properties of black holes and to test theories of gravity. In this letter, we will show that both objectives can be met using gravitational wave memory.

The gravitational wave memory is a permanent change in spacetime geometry, which in general relativity (GR) is a jump in the transverse-traceless part of the spacetime metric $\Delta h_{ij}^{\rm TT}$ before and after a burst event [45]. Gravitational-wave memory was first predicted in the 1970s as originating from an overall change in the source term of the linearized Einstein equation [43, 44, 94, 133, 151]. This is now referred to as the "linear memory". Decades later, Christodoulou found that nonlinearities of the Einstein's equation lead to another memory [64], which is now referred to as the *nonlinear* or *Christodoulou memory*. Shortly after, the nonlinear memory was

interpreted as sourced by bursts of gravitational radiation [138, 147].

Since both memories depend on the specific form of the field equation, one can speculate that other types of memory may arise in modified theories of gravity. Modifications to GR seems inevitable if one considers general relativity as a low-energy effective theory to a quantum theory of gravity, which adds new terms to the Einstein-Hilbert action, such as higher-order curvature terms, or extra scalar degree of freedom coupled to the tensor degrees of freedom [40, 65]. In this letter, we carry out a proof-of-principle discussion for new memory effects in scalar-tensor theories of gravity. Using a perturbative treatment, we will first show that a T memory arises in the tensor components of gravitational wave due to energy carried away by scalar radiation. We will then point out that the no scalar hair property of black holes in scalar-tensor theories will give rise to the S memory, a scalar component of gravitational wave. We will go on to estimate the size of both memories using the simplest progenitor model. Finally, we will formulate a detection strategy that targets the S memory, and consider detectability using the current and next generations of ground-based gravitational wave detectors.

2.2 T memory and S memory in scalar-tensor gravity

Scalar-tensor theories are a simple but attractive class of modified theory, e.g., they can be viewed as arising from dimensional compactification of higher dimensional theories [81]. Let us consider a single scalar field ϕ and a ϕ-dependent coupling constant $\omega(\phi)$, with an action of

$$S = \int d^4x \, \left\{ \sqrt{-g} \, \left(\phi R - \frac{\omega(\phi)}{\phi} \partial^\mu \phi \partial_\mu \phi \right) + 16\pi \mathcal{L}_{\rm M} \right\},$$

where R is the Ricci scalar associated with the spacetime metric $g_{\mu\nu}$, $\mathcal{L}_{\rm M}$ is the matter-sector Lagrangian which depends on $g_{\mu\nu}$ and matter fields. We start by expanding the metric and the scalar field as

$$\begin{cases} g_{\mu\nu} = \eta_{\mu\nu} + h_{\mu\nu} \\ \phi = \phi_0 + \delta\phi, \end{cases} \tag{2.1}$$

where $\eta_{\mu\nu} = \mathrm{diag}(-1, 1, 1, 1)$ and ϕ_0 is the value of the scalar field at null infinity, which is related to Newton's constant via

$$G\phi_0 = (2\omega(\phi_0) + 4)/(2\omega(\phi_0) + 3). \tag{2.2}$$

The action is then expanded as:

$$S = \int d^4x \, \left\{ \mathcal{L}^0_{\rm ST} + \mathcal{L}^1_{\rm ST} + 16\pi \mathcal{L}^0_{\rm M} + 16\pi \mathcal{L}^1_{\rm M} + ... \right\}.$$

Here $\mathcal{L}^0_{\rm M}$ is the matter Lagranian in flat spacetime and

$$\mathcal{L}^0_{\rm ST} = \frac{\phi_0}{2} H^{\mu\nu}\mathcal{V}_{\mu\nu\rho\sigma}H^{\rho\sigma} - \frac{\alpha_0^{-2}}{2\phi_0}\partial^\mu\delta\phi\partial_\mu\delta\phi\,, \tag{2.3}$$

$$\mathcal{L}^1_{\rm M} = \frac{1}{2}H^{\mu\nu}T_{\mu\nu} - \frac{1}{2}\frac{\delta\phi}{\phi_0}T\,, \tag{2.4}$$

$$\begin{aligned}\mathcal{L}^1_{\rm ST} = &\frac{\alpha_0^{-2}}{2\phi_0}\left(H^{\mu\nu} - \frac{1}{2}\eta^{\mu\nu}H\right)\partial_\mu\delta\phi\partial_\nu\delta\phi \\ &- \frac{\alpha_0^{-4}\beta_0}{2\phi_0^2}\delta\phi\,\partial^\mu\delta\phi\partial_\mu\delta\phi\,,\end{aligned} \tag{2.5}$$

where $\mathcal{L}^0_{\rm ST}$ and $\mathcal{L}^1_{\rm M}$ are kinetic and source terms of $h_{\mu\nu}$ and $\delta\phi$ respectively, while we kept the leading coupling term between them and the leading self-interactive term of $\delta\phi$ in $\mathcal{L}^1_{\rm ST}$. Here all indices are raised and lowered by $\eta_{\mu\nu}$, and $T_{\mu\nu}$ is the stress-energy tensor of matter. In order to eliminate the kinetic term crossing between $h_{\mu\nu}$ and $\delta\phi$ in the original expansion, we redefined the physical degrees of freedom as

$$H_{\mu\nu} = h_{\mu\nu} + \eta_{\mu\nu}\phi_0^{-1}\delta\phi. \tag{2.6}$$

The operator $\mathcal{V}_{\mu\nu\rho\sigma}$ is given by

$$\begin{aligned}2\mathcal{V}_{\mu\nu\rho\sigma} =&(\eta_{\mu\rho}\eta_{\nu\sigma} - \eta_{\mu\nu}\eta_{\rho\sigma})\partial^2 + \eta_{\mu\nu}\partial_\rho\partial_\sigma + \eta_{\rho\sigma}\partial_\mu\partial_\nu \\ &- \eta_{\mu\rho}\partial_\nu\partial_\sigma - \eta_{\nu\sigma}\partial_\mu\partial_\rho.\end{aligned} \tag{2.7}$$

Up to leading order, we expand $\omega(\phi)$ as $\omega(\phi_0) + \omega'(\phi_0)\delta\phi$ and adopt the often used parameters:

$$\begin{cases}\alpha_0 = (2\omega(\phi_0) + 3)^{-\frac{1}{2}} \\ \beta_0 = 2\phi_0\omega'(\phi_0)/(2\omega(\phi_0) + 3)^2.\end{cases} \tag{2.8}$$

Note that all terms in Eqs. (2.34)–(2.37) are invariant under infinitesimal diffeomorphisms:

$$\begin{cases}H'_{\mu\nu} = H_{\mu\nu} - \partial_\mu\xi_\nu - \partial_\nu\xi_\mu \\ \delta\phi' = \delta\phi.\end{cases} \tag{2.9}$$

The first term of Eq. (2.34) gives the vacuum field equation for $H_{\mu\nu}$:

$$\mathcal{V}_{\mu\nu\rho\sigma}H^{\rho\sigma} = 0\,, \tag{2.10}$$

the same as in GR. We can then similarly take the Lorenz gauge

$$\partial^\mu H_{\mu\nu} - \partial_\nu H/2 = 0 \tag{2.11}$$

and use infinitesimal diffeomorphisms to gauge away redundant degrees of freedom. In this way, only two physical degrees of freedom are left for $H_{\mu\nu}$. However, gravitational-wave detectors are sensitive to $h_{\mu\nu}$, which depends on both $H_{\mu\nu}$ and $\delta\phi$. We can further gauge away remaining non-physical degrees of freedom which leaves $h_{ij} = h^{\rm T}_{ij} + h^{\rm S}_{ij}$, where

$$h^{\rm T}_{ij} = h_+ e^+_{ij} + h_\times e^\times_{ij}, \qquad h^{\rm S}_{ij} = h_\circ e^\circ_{ij}. \tag{2.12}$$

Here the polarization tensors are defined by

$$\begin{cases} e^+_{ij} = \hat{m}_i \hat{m}_j - \hat{n}_i \hat{n}_j \\ e^\times_{ij} = \hat{m}_i \hat{n}_j + \hat{n}_i \hat{m}_j \\ e^\circ_{ij} = \hat{m}_i \hat{m}_j + \hat{n}_i \hat{n}_j \,, \end{cases} \tag{2.13}$$

where $\hat{m}$, $\hat{n}$ are spatial unit vectors orthogonal to the wave propagation direction $\hat{\Omega}$. The amplitudes are related to the tensor $H_{\mu\nu}$ and the scalar $\delta\phi$ via

$$\begin{cases} h_+ = e^{ij}_+ H^{\rm TT}_{ij}/2 \\ h_\times = e^{ij}_\times H^{\rm TT}_{ij}/2 \\ h_\circ = -\phi_0^{-1} \delta\phi, \end{cases} \tag{2.14}$$

where $H^{\rm TT}_{ij}$ denotes the transverse-traceless part of H_{ij} [109]. We shall refer to the $+, \times$ modes as tensor (T) modes, and the $\circ$ mode as the scalar (S) mode.

The first term of Eq. (2.35) indicates that $H_{\mu\nu}$ is sourced by the stress-energy tensor $T_{\mu\nu}$. In addition, coupling between $H_{\mu\nu}$ and the quadratic terms of $\delta\phi$ in Eq. (2.37) provides another source for $H_{\mu\nu}$. In fact, we can define

$$8\pi \mathcal{T}_{\mu\nu} = \frac{\partial \mathcal{L}^1_{\rm ST}}{\partial H^{\mu\nu}} = \frac{\omega(\phi_0)}{\phi_0} \left(\partial_\mu \delta\phi \partial_\nu \delta\phi - \frac{\eta_{\mu\nu}}{2} \partial^\rho \delta\phi \partial_\rho \delta\phi \right) \tag{2.15}$$

as the effective stress-energy tensor of the scalar radiation. Just as the Christodoulou memory is caused by the burst of *gravitational* radiation, we expect the burst of *scalar* radiation would generate a new gravitational wave memory, which we call the T memory in scalar-tensor gravity since it contributes to the tensor components

of gravitational wave. Following a similar argument as [147], the T memory can be expressed as

$$\Delta h^{\rm T}_{ij} = \frac{4}{\phi_0 r}\int d\hat{\Omega}' \int dt\; r^2 \mathcal{T}^{0k}\hat{\Omega}'^k \left(\frac{\hat{\Omega}'^i\hat{\Omega}'^j}{1-\hat{\Omega}'\cdot\hat{\Omega}}\right)^{\rm TT}. \tag{2.16}$$

Here the spatial vector $\hat{\Omega}$ is the wave-propagation direction, $\hat{\Omega}'$ is a unit vector integrated over all sky directions, and $\mathcal{T}^{0k}$ is the effective energy flux of scalar radiation. Note that the T memory vanishes in spherical symmetry.

Let us turn now to the scalar degree of freedom. From the second term in Eq.(2.35), the scalar field $\delta\phi$ is sourced by the trace of stress-energy tensor of matter. This means any cold matter ($p \ll \rho$) can change the scalar field from its value at null infinity ϕ_0. We shall refer to the resulting $\phi_{\rm H}$ inside and outside a star as its scalar field profile. However, in 1972 Hawking discovered that black holes in Brans-Dicke theory are the same as in GR: they have no scalar hair and $\phi_{\rm H} = \phi_0$ everywhere [87]. This was also shown to be true for general scalar tensor theories [135]. The no scalar hair theorem has the following consequence: in any gravitational collapses resulting in black holes, the scalar field outside the collapsing star changes from $\phi_{\rm H}$ to ϕ_0, and (2.12) and (2.39) this causes a permanent change in the scalar component h^S_{ij}:

$$\Delta h^{\rm S}_{ij} = \phi_0^{-1}(\phi_{\rm H}-\phi_0)\, e^{\circ}_{ij}. \tag{2.17}$$

We shall call this the *S memory* . Differently from other memories, the S memory: (i) exists even in spherical symmetry, and (ii) has a reverse temporal feature — it begins with a non-zero initial value, and drops down to zero.

2.3 Analytic results of a simplified model

To estimate the size of the S and T memories, let us analyze a spherically symmetric and homogeneous Newtonian star ($p \ll \rho$), by solving the linearized field equation for $\delta\phi$ obtained from Eqs. (2.34)–(2.37), which reads:

$$\partial^2\delta\phi = 8\pi(\alpha_0^2 - \phi_0^{-1}\beta_0\delta\phi)T. \tag{2.18}$$

Here the trace of stress-energy tensor T is $-3M/4\pi R^3$ inside the star and 0 outside the star, where M and R are the mass and radius of the star respectively. In this equation we dropped the non-linear terms which are lowered by a factor of $M(\phi_0 R)^{-1}$. By

[0]Recently the extra memory effect due to the radiation of scalar energy is discussed in the circumstance of compact binary systems in [96], which is equivalent to our T memory.

taking the continuity condition for the scalar field profile and its first-order derivative at the boundary ($r = R$), the asymptotic condition $\phi_{\rm H}(\infty) = \phi_0$ at the null infinity and requiring that there is no singularity inside the star, the stationary interior scalar field profile $\delta\phi_{\rm H}(r) = \phi_{\rm H}(r) - \phi_0$ is given by

$$\delta\phi_{\rm H}(r < R) = \frac{\phi_0\alpha_0^2}{|\beta_0|} \times \begin{cases} 1 - \frac{\sinh\kappa r}{\kappa r\cosh\kappa R} & \beta_0 > 0 \\ \frac{\sin\kappa r}{\kappa r\cos\kappa R} - 1 & \beta_0 < 0 \end{cases} \tag{2.19}$$

while the stationary external scalar field profile is

$$\delta\phi_{\rm H}(r > R) = \frac{\phi_0\alpha_0^2}{|\beta_0|}\frac{R}{r} \times \begin{cases} 1 - \frac{\tanh\kappa R}{\kappa R} & \beta_0 > 0 \\ \frac{\tan\kappa R}{\kappa R} - 1 & \beta_0 < 0 \end{cases} \tag{2.20}$$

where we defined

$$\kappa \equiv (6M|\beta_0|\phi_0^{-1}R^{-3})^{1/2}\ . \tag{2.21}$$

Next we consider a progenitor with $M = 10M_\odot$ and $R = 100M_\odot$ as in [86]. We plot the scalar field profile in Fig. 3.1 for different values of β_0 while saturate α_0 to the Cassini bound [40]. As we can see from the figure, the scalar field profile is amplified for negative values of β_0 and is depressed for positive β_0. This feature agrees with the results from numerical simulations [82, 86, 116].

From Eqs. (2.17) and (2.20), the S memory is given by

$$\Delta h_{ij}^{\rm S} = \mathcal{N}(\beta_0,\mu)[2\alpha_0^2 M/(\phi_0 r)]e_{ij}^{\circ}. \tag{2.22}$$

Here $\mu \equiv M/\phi_0 R$ and the β_0-scale factor $\mathcal{N}(\beta_0,\mu)$ is defined as:

$$\mathcal{N}(\beta_0,\mu) = \frac{1}{2|\beta_0|\mu} \cdot \begin{cases} 1 - \frac{\tanh\sqrt{6\mu|\beta_0|}}{\sqrt{6\mu|\beta_0|}} & \beta_0 > 0 \\ \frac{\tan\sqrt{6\mu|\beta_0|}}{\sqrt{6\mu|\beta_0|}} - 1 & \beta_0 < 0 \end{cases}\ .$$

For the Brans-Dicke [46] limit $\beta_0 = 0$, $\mathcal{N}(0,\mu) = 1$. We also find that $\mathcal{N}(\beta_0,\mu)$ is singular at

$$\beta_0^{\rm crit} = -\frac{\pi^2}{24\mu}\,, \tag{2.23}$$

which is -4.11 for the Newtonian star in Fig. 3.1. For $\beta_0 < \beta_0^{\rm crit}$, solving Eq. (2.18) for a time dependent scalar field profile $\delta\phi_{\rm H}(t,r) = f(r)e^{-i\omega t}$ will give a quasinormal mode ω_1 with a negative imaginary part, which means the solution is not stable

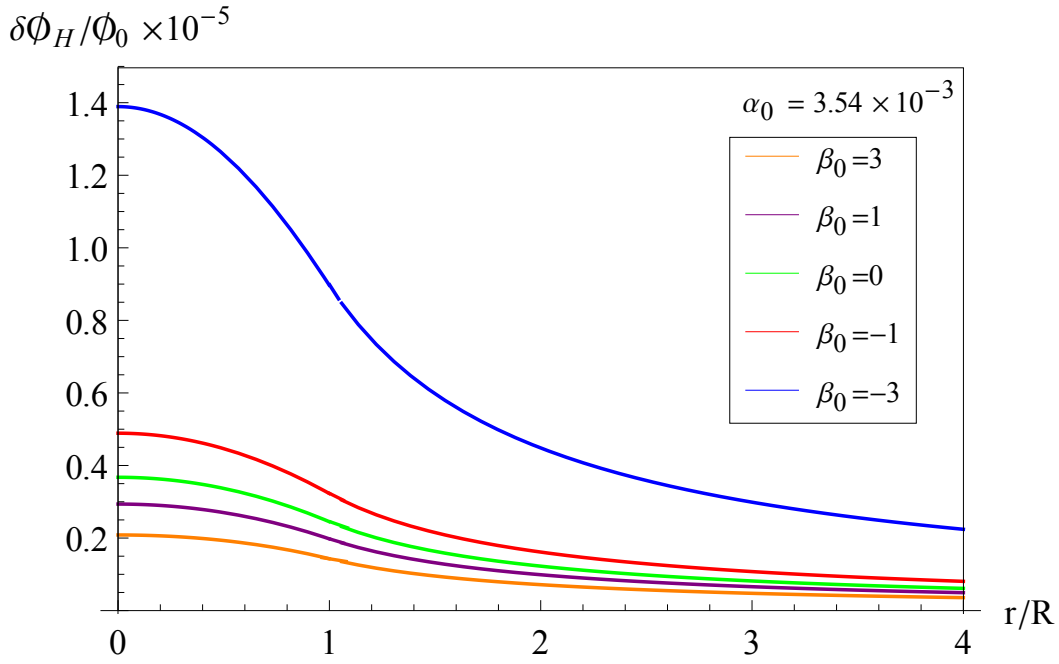

Figure 2.1: The stationary interior and exterior scalar field profile of an $M = 10M_\odot$ and $R = 100M_\odot$ Newtonian star for different values of β_0.

under small perturbations. Some negative values of β_0 are also inconsistent with the cosmological evolution of the scalar field and Solar System experiments, as explained in Appendix A of [127]. Physically, this corresponds to the effect called "spontaneous scalarization", which was first discovered by Damour and Esposito-Farese [69]. For this reason, for $\beta < \beta_0^{\rm crit}$, we should use the fully nonlinear field equation instead of our leading-order approximation. Previous numerical simulations [85, 117] indicate that scalarization changes the asymptotic value of the scalar field profile from $\delta\phi_{\rm H} \sim \alpha_0^2 M/r$ to $\delta\phi_{\rm H} \sim \alpha_0 M/r$. Thus for $\alpha_0 \sim 10^{-3}$, the scalar field profile for a scalarized star is enhanced by about 3 orders of magnitude.

Another important parameter is the time τ it takes $h_{ij}^{\rm S}$ to change from $\Delta h_{ij}^{\rm S}$ to zero. In our case, τ is the time for the progenitor collapse into a black hole. The time a star collapsing into a black hole is infinite long for an exterior observer, but here we use the *effective* collapse time, which is the time a star collapsing into its light ring as observed at null infinity. The gravitational collapse process for homogeneous spherical dust is described by Oppenheimer-Snyder model [119], which gives

$$\tau \simeq \pi R[(8GM/R)(1-2GM/R)]^{-\frac{1}{2}} \,. \tag{2.24}$$

For $M = 10M_\odot$ and $R = 100M_\odot$, $\tau = 1.93$ms, the cut-off frequency of the memory [140] is $f_{\rm c} = 1/\tau \simeq 500$Hz. This means that although the exact waveforms of scalar

radiation in gravitational collapses have been studied from numerical simulations [82, 86, 116, 132], for ground based gravitational wave detectors, most of the detection band is dominated over by the memory as the “zero-frequency limit" [43, 133].

The T memory for compact binary systems has been discussed in [96], here we consider T memory in gravitational collapses and compare it with S memory. From Eq. (2.15), a burst of energy flux carried by scalar field is generated when the scalar hair is radiated away in a short duration τ, which means both S memory and T memory appear in gravitational collapses. The amplitude of T memory can be estimated from Eq. (2.16):

$$\begin{aligned}\Delta h^{\mathrm{T}} &\simeq \frac{4\epsilon}{\phi_0 r}\int_{-\infty}^{+\infty} dt\; r^2\mathcal{T}^{0k}\hat{\Omega}'^{k} = \frac{8\epsilon}{\phi_0 r}\int_{0}^{+\infty} df\; \frac{\pi f^2 r^2}{4\phi_0\alpha_0^2}|\delta\tilde{\phi}(f)|^2 \\ &= \mathcal{N}^2(\beta_0,\mu)\frac{2\epsilon\alpha_0^2 M^2}{\pi\phi_0^2 r\tau}. \end{aligned} \tag{2.25}$$

Here the energy-flux

$$\mathcal{T}^{0k} = (16\pi\alpha_0^2\phi_0)^{-1}\delta\dot{\phi}^2(t)\hat{\Omega}'^{k}\,, \tag{2.26}$$

and the Fourier transform of the scalar field in the zero-frequency limit is

$$\delta\tilde{\phi}(f) = \delta\phi_{\mathrm{H}}/(2\pi i f), \qquad \text{for} \quad |f| < f_c\,, \tag{2.27}$$

with $\delta\phi_{\mathrm{H}}$ given by Eq. (2.20). The coefficient ϵ comes from the angular part of the integral and as a result of the asymmetric distribution of the scalar field profile.

In Fig. 5.1, we plot amplitudes of the T and S memory from Eq. (2.22) and (2.25). In the Brans-Dicke limit, T memory is lower than S memory by about three orders of magnitude. However, since $\Delta h^{\mathrm{S}} \propto \mathcal{N}(\mu,\beta_0)$ while $\Delta h^{\mathrm{T}} \propto \mathcal{N}^2(\mu,\beta_0)$, T memory becomes comparable to S memory near β_{crit} where the scalar field profile is significantly magnified by the spontaneous scalarization.

2.4 Detection Strategies

Since T and S memories contribute to the tensor and scalar components of gravitational wave, respectively, and mixed in observed data, we need a mode separation method [88] to detect each component. Because the S memory is always larger than T memory in gravitational collapse processes as shown in Fig. 5.1, and the existence of non-tensor polarized gravitational wave is a strong evidence for modification to

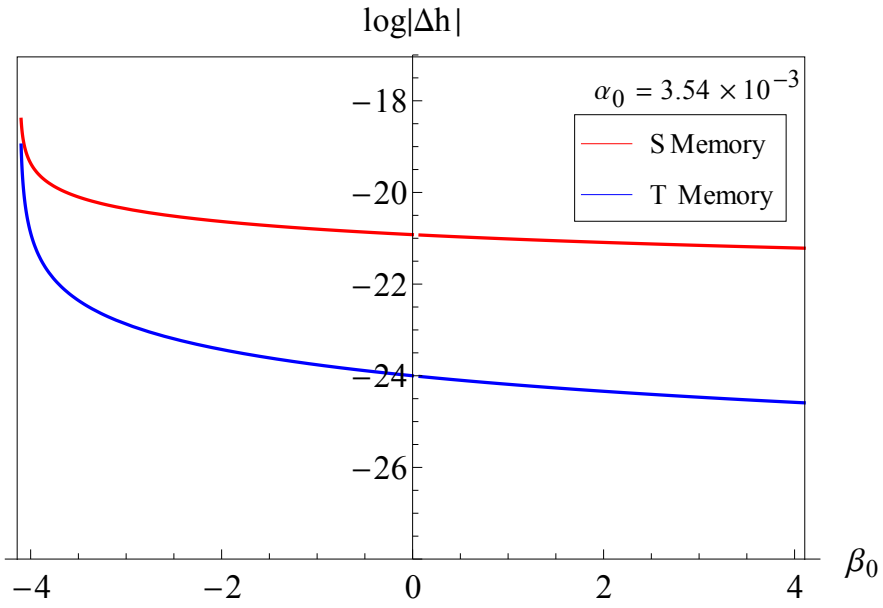

Figure 2.2: Scales of T memory and S memory from gravitational collapse of an $M = 10M_\odot$, $R = 100M_\odot$,$\epsilon = 0.1$ and $r = 10$kpc Newtonian star.

Einstein's theory [72], we focus on the S memory hereafter. Notice that different gravitational wave detectors on various locations have distinct responses to the three polarizations in Eq. (2.12), hence it is possible to find linear combinations of the outputs from three or more detectors which only respond to the scalar mode.

For a network of N detectors, the combined filtered output W_N can be written as

$$W_N = \vec{\alpha} \cdot \vec{w}\,, \tag{2.28}$$

with $\vec{\alpha} = (\alpha_1, ..., \alpha_N)$ the combination coefficients and $\vec{w} = (w_1, ..., w_N)$ the match-filtered outputs of each detector [140]. The signal-to-noise ratio (SNR) of the combined filtered output is defined as

$$\rho = \frac{\mathrm{E}(W_N)}{\mathrm{Var}(W_N)^{\frac{1}{2}}}\,. \tag{2.29}$$

In order to optimize SNR as well as to make it insensitive to + and × polarization modes, we should choose

$$\begin{aligned}\vec{\alpha} = \vec{F}_\circ &- \frac{(\vec{F}_\times \cdot \vec{F}_\times)(\vec{F}_+ \cdot \vec{F}_\circ) - (\vec{F}_+ \cdot \vec{F}_\times)(\vec{F}_\times \cdot \vec{F}_\circ)}{(\vec{F}_+ \cdot \vec{F}_+)(\vec{F}_\times \cdot \vec{F}_\times) - (\vec{F}_+ \cdot \vec{F}_\times)^2}\vec{F}_+ \\ &- \frac{(\vec{F}_+ \cdot \vec{F}_+)(\vec{F}_\times \cdot \vec{F}_\circ) - (\vec{F}_+ \cdot \vec{F}_\times)(\vec{F}_+ \cdot \vec{F}_\circ)}{(\vec{F}_+ \cdot \vec{F}_+)(\vec{F}_\times \cdot \vec{F}_\times) - (\vec{F}_+ \cdot \vec{F}_\times)^2}\vec{F}_\times,\end{aligned}$$

where $\vec{F}_P = \left(F_P^1(\hat{\Omega}), ..., F_P^N(\hat{\Omega})\right)$, and $F_P^n(\hat{\Omega})$ is the angular pattern function of detector $n = 1, ..., N$ for polarization $P = \circ, +, \times$. The explicit expressions of these functions can be found in [88]. The maximized SNR for the detection of S memory in Eq. (2.22) is then given by

$$\rho = \mathcal{F}_N^{1/2}(\hat{\Omega}) \frac{2\alpha_0^2 M \mathcal{N}(\beta_0, \mu)}{\pi \phi_0 r} \left[\int_0^{f_c} df \, \frac{1}{f^2 S_n(f)}\right]^{\frac{1}{2}}. \tag{2.30}$$

Here for simplicity we suppose the N detectors have approximately the same noise spectral density $S_n(f)$ and $f_c = 1/\tau$ is the cut-off frequency of memory as explained above. We describe the dependence of the SNR on the direction of the source by introducing the N-detector effective angular pattern function $\mathcal{F}_N(\hat{\Omega})$ and is given by

$$\mathcal{F}_N(\hat{\Omega}) = [\vec{\alpha} \cdot \vec{F}_\circ(\hat{\Omega})]^2 / \vec{\alpha}^2. \tag{2.31}$$

We should notice that $\mathcal{F}_N$ is non-zero only for $N \geq 3$. We plot $\mathcal{F}_3(\hat{\Omega})$ and $\mathcal{F}_4(\hat{\Omega})$ for network H-L-V and H-L-V-K respectively in Fig. 5.3, where H, L, V and K stand for LIGO-Hanford, LIGO-Livingston, Virgo and KAGRA, respectively. For $\mathcal{F}_3(\hat{\Omega})$, the peak value and the angularly averaged value are 0.485 and 0.087. For $\mathcal{F}_4(\hat{\Omega})$, these values are 0.511 and 0.240. It means that although the inclusion of a fourth detector does not significantly improve the maximal SNR, it does improve substantially the sky coverage of the network.

We next consider the detectability of S memory from our analytic model with $M = 10M_\odot$, $R = 100M_\odot$ and $r = 10$kpc. In Eq. (2.30), we take the threshold SNR to be 10, the effective angular pattern function to be the peak value of network H-L-V-K. We use the design noise spectrum of Advanced LIGO to compute the SNR for second generation detectors and the proposed Einstein Telescope for third generation [129]. The detectable region of model parameters are shown in Fig. 5.4, where we also present current constraints from the solar system (the Cassini mission) and from pulsar timing (PSR J1738+0333, PSR J0348+0432) [40]. From the figure, the discoverable curves with SNR = 10 surpass the current constraints. The gravitational collapse rate is commonly thought to be as low as ∼1–3 events per 100 years in $r < 10$kpc. However, we need to point out that this rate, which is deduced from the SNe rate, is underestimated since more massive stars tend to collapse into black holes directly with no supernova explosion [80]. Besides, such a phenomenon, which, once detected, will provide definitive evidence for the need to modify GR, should not be omitted by future searches in gravitational wave detector data. Hence we propose to add a new search pipeline for the S memory to the upcoming global gravitational wave detector network.

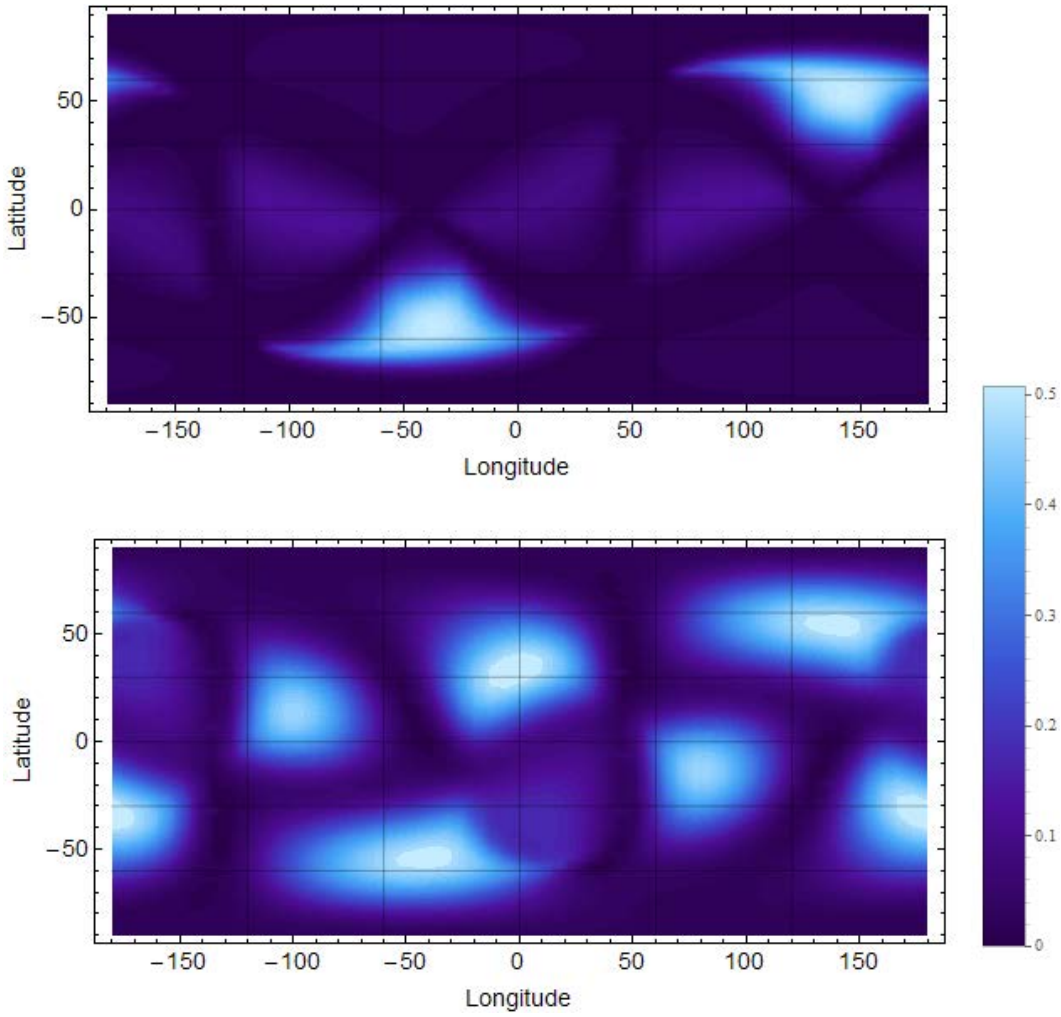

Figure 2.3: The effective angular pattern function $\mathcal{F}_3(\hat{\Omega})$ for network H-L-V (upper panel) and $\mathcal{F}_4(\hat{\Omega})$ for network H-L-V-K (lower panel) as a function of $\hat{\Omega}$, the direction of the source. The x axis is the longitude as observed on the earth and y axis the latitude.

2.5 Discussions

In this letter, we have discussed how extra terms in the actions of scalar-tensor theories of gravity and the particular property of black holes in such theories give birth to two new types of gravitational memory, and how these effects can be used as a test of modifications to GR. Another important class of modified gravity is theories with higher order curvature terms, such as Gauss-Bonet theory and Chern-Simons theory [40, 65]. We expect: (i) the $h^3_{\mu\nu}$ terms in the actions of these theories to be distinct from GR and hence lead to modifications to the Christodoulou memory, (ii) scalar radiation will continue to cause the T memory, and (iii) since black holes have hair in these theories, the S memory will differ from scalar-tensor theories. We

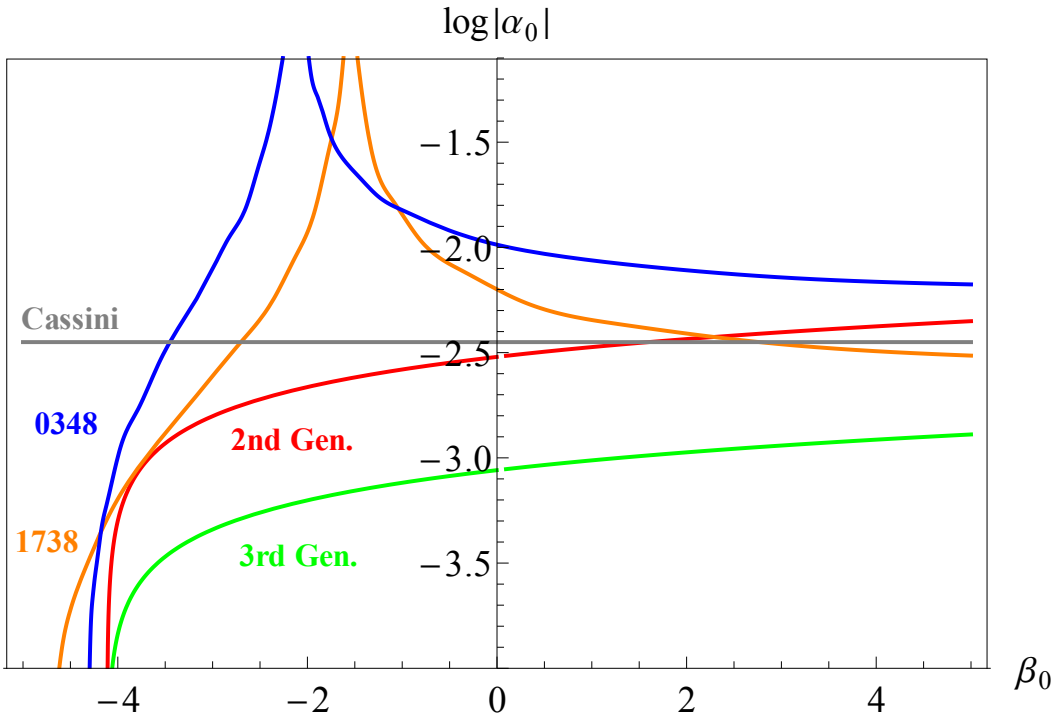

Figure 2.4: Discoverable curves of S memory from a collapsing star with $M = 10M_\odot$ $R = 100M_\odot$ and $r = 10$kpc for 2nd generation detectors (Red) and 3rd generation detectors (Green). The current constraints on the model parameters are from the Cassini Mission (Grey), PSR J1738+0333 (Orange) and PSR J0348+0432 (Blue).

leave the details for further research.

2.6 Acknowledgements

We thank Yanbei Chen for discussions and comments on the manuscript. Research of SMD and AN was supported by the National Science Foundation, Grant PHY-1404569, PHY-1055103 and the Brinson Foundation. Research of AN was also supported by the Japan Society for the Promotion of Science and the H2020-MSCA-RISE- 2015 Grant No. StronGrHEP-690904.

2.7 Appendix A: Scalar-tensor theory of gravity, scalar gravitaional wave and relation to Einstein frame

The action for scalar-tensor theory of gravity is given by

$$S_{\rm ST} = \int d^4x\sqrt{-g}\,\frac{1}{16\pi}(\phi R - \frac{\omega(\phi)}{\phi}\nabla^\mu\phi\nabla_\mu\phi) + S_{\rm M}[g_{\mu\nu},\Psi] \qquad (2.32)$$

The field equations are driven from $\delta S_{\rm ST} = 0$, which gives

$$\begin{cases} R_{\mu\nu} - \frac{1}{2} g_{\mu\nu} R = \frac{8\pi}{\phi} T_{\mu\nu} + \frac{\omega(\phi)}{\phi^2}(\nabla_\mu \phi \nabla_\nu \phi - \frac{1}{2} g_{\mu\nu} \nabla^\rho \phi \nabla_\rho \phi) + \frac{1}{\phi}(\nabla_\mu \nabla_\nu \phi - g_{\mu\nu} \nabla^2 \phi) \\ \nabla^2 \phi = \frac{8\pi}{3+2\omega(\phi)} T - \frac{\omega'(\phi)}{3+2\omega(\phi)} \nabla^\mu \phi \nabla_\mu \phi \end{cases} \tag{2.33}$$

To study the gravitational wave solution and its polarizations, we linearize the fields $g_{\mu\nu}$ and ϕ and start from the linearized field equations:

$$\begin{cases} g_{\mu\nu} = \eta_{\mu\nu} + h_{\mu\nu} \\ \phi = \phi_0 + \delta\phi \end{cases} \Rightarrow$$

$$R^{(1)}_{\mu\nu} - \frac{1}{2} \eta_{\mu\nu} \eta^{\rho\sigma} R^{(1)}_{\rho\sigma} = \frac{8\pi}{\phi_0} T_{\mu\nu} + \partial_\mu \partial_\nu \frac{\delta\phi}{\phi_0} - \eta_{\mu\nu} \partial^2 \frac{\delta\phi}{\phi_0} \tag{2.34}$$

$$\partial^2 \frac{\delta\phi}{\phi_0} = \frac{8\pi}{\phi_0} \frac{1}{3 + 2\omega_0} T \tag{2.35}$$

Introduce $\bar{h}_{\mu\nu} = h_{\mu\nu} - \frac{1}{2} \eta_{\mu\nu} h^\lambda_\lambda$, then from eq.(2.34),

$$\begin{aligned} &\partial^2 \bar{h}_{\mu\nu} - \eta_{\mu\nu} \partial^2 \frac{\delta\phi}{\phi_0} + \eta_{\mu\nu} \partial^\sigma (\partial_\rho \bar{h}^\rho_\sigma - \partial_\sigma \frac{\partial\phi}{\phi_0}) - \partial_\mu (\partial_\rho \bar{h}^\rho_\nu - \partial_\nu \frac{\delta\phi}{\phi_0}) \\ &- \partial_\nu (\partial_\rho \bar{h}^\rho_\mu - \partial_\mu \frac{\delta\phi}{\phi_0}) = -\frac{16\pi}{\phi_0} T_{\mu\nu}. \end{aligned} \tag{2.36}$$

Adding the gauge condition: $\partial_\rho \bar{h}^\rho_\mu - \partial_\mu \frac{\delta\phi}{\phi_0} = 0$, and recall eq.(2.35),

$$\partial^2 \bar{h}_{\mu\nu} = -\frac{16\pi}{\phi_0} (T_{\mu\nu} - \frac{1}{6 + 4\omega_0} \eta_{\mu\nu} T) \tag{2.37}$$

From eq.(2.35) and eq.(2.37), the wave equations in vacuum are:

$$\begin{cases} \partial^2 \bar{h}_{\mu\nu} = 0 \\ \partial^2 \Phi = 0 \end{cases} \tag{2.38}$$

where we define $\Phi = -\frac{\delta\phi}{\phi_0}$. The gauge transformation:

$$\begin{cases} \bar{h}'_{\mu\nu} = \bar{h}_{\mu\nu} - \partial_\mu \xi_\nu - \partial_\nu \xi_\mu + \eta_{\mu\nu} \partial^\lambda \xi_\lambda \\ \Phi' = \Phi \end{cases} \tag{2.39}$$

Then for the gauge condition to be held after the gauge transformation:

$$\partial^\mu \bar{h}'_{\mu\nu} + \partial_\nu \Phi' = 0 \;\Rightarrow\; \partial^\mu h_{\mu\nu} + \partial_\nu \Phi - \partial^2 \xi_\nu = 0 \;\Rightarrow\; \partial^2 \xi_\mu = 0 \tag{2.40}$$

Then $\bar{h}_{\mu\nu}(x), \Phi(x), \xi_\mu(x)$ can be expanded by plane wave solutions:

$$\bar{h}_{\mu\nu}(x) = \int \frac{d^3k}{(2\pi)^3}[\tilde{\bar{h}}_{\mu\nu}(\vec{k})e^{ik\cdot x} + \tilde{\bar{h}}^*_{\mu\nu}(\vec{k})e^{-ik\cdot x}] \tag{2.41}$$

$$\bar{\Phi}(x) = \int \frac{d^3k}{(2\pi)^3}[\tilde{\Phi}(\vec{k})e^{ik\cdot x} + \tilde{\Phi}^*(\vec{k})e^{-ik\cdot x}] \tag{2.42}$$

$$\xi_\mu(x) = \int \frac{d^3k}{(2\pi)^3}[\tilde{\xi}_\mu(\vec{k})e^{ik\cdot x} + \tilde{\xi}^*_\mu(\vec{k})e^{-ik\cdot x}] \tag{2.43}$$

Symmetric tensor $\tilde{\bar{h}}_{\mu\nu}$ has 10 DOF:

$$\tilde{\bar{h}}_{\mu\nu} = \begin{pmatrix} \tilde{\bar{h}}_{00} & \tilde{\bar{h}}_{01} & \tilde{\bar{h}}_{02} & \tilde{\bar{h}}_{03} \\ \tilde{\bar{h}}_{01} & \tilde{\bar{h}}_{11} & \tilde{\bar{h}}_{12} & \tilde{\bar{h}}_{13} \\ \tilde{\bar{h}}_{02} & \tilde{\bar{h}}_{12} & \tilde{\bar{h}}_{22} & \tilde{\bar{h}}_{23} \\ \tilde{\bar{h}}_{03} & \tilde{\bar{h}}_{13} & \tilde{\bar{h}}_{23} & \tilde{\bar{h}}_{33} \end{pmatrix} \tag{2.44}$$

Take the GW propagating direction $\vec{n}$ as the 3rd axis, estabalish a spatial orthonormal coordinate system:

$$\begin{cases} u^\mu = (0, 1, 0, 0) \\ v^\nu = (0, 0, 1, 0) \\ n^\nu = (0, 0, 0, 1) \end{cases} \tag{2.45}$$

In this coordinate system, the 4-momentum of GW becomes $k^\mu = k(1, 0, 0, 1)$. The gauge condition $k^\mu \tilde{\bar{h}}_{\mu\nu} + k_\nu \tilde{\Phi} = 0$ in this coordinate system is

$$\tilde{\bar{h}}_{00} + \tilde{\bar{h}}_{30} = \tilde{\Phi}, \quad \tilde{\bar{h}}_{01} + \tilde{\bar{h}}_{31} = 0, \quad \tilde{\bar{h}}_{02} + \tilde{\bar{h}}_{32} = 0, \quad \tilde{\bar{h}}_{03} + \tilde{\bar{h}}_{33} = -\tilde{\Phi} \tag{2.46}$$

Then only $10 - 3 = 7$ DOF left:

$$\tilde{\bar{h}}_{\mu\nu} = \begin{pmatrix} \tilde{\bar{h}}_{33} + 2\tilde{\Phi} & -\tilde{\bar{h}}_{13} & -\tilde{\bar{h}}_{23} & -\tilde{\bar{h}}_{33} - \tilde{\Phi} \\ -\tilde{\bar{h}}_{13} & \tilde{\bar{h}}_{11} & \tilde{\bar{h}}_{12} & \tilde{\bar{h}}_{13} \\ -\tilde{\bar{h}}_{23} & \tilde{\bar{h}}_{12} & \tilde{\bar{h}}_{22} & \tilde{\bar{h}}_{23} \\ -\tilde{\bar{h}}_{33} - \tilde{\Phi} & \tilde{\bar{h}}_{13} & \tilde{\bar{h}}_{23} & \tilde{\bar{h}}_{33} \end{pmatrix} \tag{2.47}$$

When a specific coordinate is choosen, it is not possible to make a global Lorentz transformation without changing the basis vectors. However, we are still free to make a coordinate-dependent translation, i.e. the gauge transformation for $\bar{h}_{\mu\nu}$ and

Φ. Recalling eq.(2.39), which give $\tilde{\bar{h}}'_{\mu\nu} = \tilde{\bar{h}}_{\mu\nu} - ik_\mu\tilde{\xi}_\nu - ik_\nu\tilde{\xi}_\mu + i\eta_{\mu\nu}k^\lambda\tilde{\xi}_\lambda$, in our coordinate system,

$$\begin{aligned}
&\tilde{\bar{h}}'_{11} = \tilde{\bar{h}}_{11} + ik(\tilde{\xi}_0 + \tilde{\xi}_3), \quad \tilde{\bar{h}}'_{13} = \tilde{\bar{h}}_{13} - ik\tilde{\xi}_1, \quad \tilde{\bar{h}}'_{12} = \tilde{\bar{h}}_{12} \\
&\tilde{\bar{h}}'_{22} = \tilde{\bar{h}}_{22} + ik(\tilde{\xi}_0 + \tilde{\xi}_3), \quad \tilde{\bar{h}}'_{23} = \tilde{\bar{h}}_{23} - ik\tilde{\xi}_2, \quad \tilde{\bar{h}}'_{33} = \tilde{\bar{h}}_{33} + ik(\tilde{\xi}_0 - \tilde{\xi}_3)
\end{aligned} \tag{2.48}$$

We can choose the following gauge transformation:

$$\begin{aligned}
&\tilde{\xi}_0 = \frac{i}{4k}(\tilde{\bar{h}}_{11} + \tilde{\bar{h}}_{22} + 2\tilde{\bar{h}}_{33} + 2\tilde{\Phi}), \quad \tilde{\xi}_1 = -\frac{i}{k}\tilde{\bar{h}}_{13}, \quad \tilde{\xi}_2 = -\frac{i}{k}\tilde{\bar{h}}_{23} \\
&\tilde{\xi}_3 = \frac{i}{4k}(\tilde{\bar{h}}_{11} + \tilde{\bar{h}}_{22} - 2\tilde{\bar{h}}_{33} - 2\tilde{\Phi}) \, .
\end{aligned}$$

Then only $7 - 4 = 3$ DOF remain, this choice of coordinates is often called the transverse tracless (TT) gauge and in the $(\vec{u}, \vec{v}, \vec{n})$ system,

$$\tilde{\bar{h}}_{\mu\nu} = \begin{pmatrix} \tilde{\Phi} & 0 & 0 & 0 \\ 0 & \tilde{h}_+ & \tilde{h}_\times & 0 \\ 0 & \tilde{h}_\times & -\tilde{h}_+ & 0 \\ 0 & 0 & 0 & -\tilde{\Phi} \end{pmatrix} \tag{2.49}$$

Where $\tilde{h}_+ = \frac{1}{2}(\tilde{\bar{h}}_{11} - \tilde{\bar{h}}_{22})$, $\tilde{h}_\times = \tilde{\bar{h}}_{12}$. They are gauge invariant. Then

$$\tilde{h}_{\mu\nu} = \tilde{\bar{h}}_{\mu\nu} - \frac{1}{2}\eta_{\mu\nu}\tilde{\bar{h}}^\lambda_\lambda = \begin{pmatrix} 0 & 0 & 0 & 0 \\ 0 & \tilde{h}_+ + \tilde{\Phi} & \tilde{h}_\times & 0 \\ 0 & \tilde{h}_\times & -\tilde{h}_+ + \tilde{\Phi} & 0 \\ 0 & 0 & 0 & 0 \end{pmatrix} \tag{2.50}$$

Under this gauge, the polarization of gravitational wave can be expressed as

$$h_{ij}(x) = h_+(x)e^+_{ij} + h_\times(x)e^\times_{ij} + \Phi(x)e^{\mathrm{S}}_{ij} \tag{2.51}$$

Where the polarization tensors can be expressed as

$$e^+_{ij} = u_iu_j - v_iv_j, \quad e^\times_{ij} = u_iv_j + u_jv_i, \quad e^S_{ij} = u_iu_j + v_iv_j \tag{2.52}$$

In order to calculate the scalar wave amplitude Φ, it is more convinient to work in the so called Einstein frame, which is obtained from a conformal transformation:

$$g_{\mu\nu} \longrightarrow g^*_{\mu\nu} = \Omega g_{\mu\nu} \tag{2.53}$$

Then under this transformation:

$$
\begin{aligned}
R &= \Omega R^* + 3\nabla_*^2\Omega - \frac{9}{2}\frac{(\nabla_*^\mu\Omega)^2}{\Omega} \\
\sqrt{-g} &= \sqrt{-g_*}\,\frac{1}{\Omega^2} \\
g^{\mu\nu} &= \Omega\, g_*^{\mu\nu}
\end{aligned}
\tag{2.54}
$$

Then the action eq.(3.1) becomes,

$$
\begin{aligned}
S_{\rm ST} &= \int d^4x\sqrt{-g_*}\frac{1}{16\pi}\{\frac{\phi}{\Omega}(R^* + \frac{3\nabla_*^2\Omega}{\Omega} - \frac{9}{2}\frac{(\nabla_*^\mu\Omega)^2}{\Omega^2}) - \omega(\phi)\frac{(\nabla_*^\mu\phi)^2}{\Omega}\} + S_{\rm M}[\frac{1}{\Omega}g^*_{\mu\nu}, \Psi_{\rm M}] \\
&= \int d^4x\sqrt{-g_*}\frac{1}{16\pi G_*}\{R^* - (\omega(\phi) + \frac{3}{2})\frac{(\nabla_*^\mu\phi)^2}{\phi^2}\} + S_{\rm M}[\frac{1}{G_*\phi}g^*_{\mu\nu}, \Psi_{\rm M}] \\
&= \int d^4x\sqrt{-g_*}\frac{1}{16\pi G_*}(R^* - \frac{1}{2}g_*^{\mu\nu}\partial_\mu\varphi\partial_\nu\varphi) + S_{\rm M}[A^2(\varphi)g^*_{\mu\nu}, \Psi_{\rm M}]
\end{aligned}
\tag{2.55}
$$

Here we define $\Omega = G_*\phi$ and $\frac{1}{G_*\phi} = A^2(\varphi)$ in the second and the third line respectively. For the third equal sign to be held, $A^(\varphi)$ should satisfies

$$
\frac{A'(\varphi)}{A(\varphi)} \equiv \alpha(\varphi) = \frac{1}{\sqrt{2\omega(\phi) + 3}}
\tag{2.56}
$$

In practice, $\alpha(\varphi)$ is often parameterized as

$$
\alpha(\varphi) = \alpha_0 + \beta_0(\varphi - \varphi_0) + \ldots
\tag{2.57}
$$

From $A(\varphi) = \frac{1}{\sqrt{G_*\phi}}$, we have the relation between $\delta\varphi = \varphi - \varphi_0$ and the scalar gravitational wave amplitude Φ:

$$
\delta\varphi = -\frac{1}{2}\left(\frac{A'(\varphi_0)}{A(\varphi_0)}\right)^{-1}\frac{\delta\phi}{\phi_0} \quad \Rightarrow \quad \delta\varphi = \frac{1}{2\alpha_0}\Phi
\tag{2.58}
$$

From eq.(2.56), we obtain the relation between α_0, β_0 with $\omega_0 \equiv \omega(\phi_0), \omega_1 \equiv \omega'(\phi_0)$:

$$
\begin{cases}
\alpha_0 = \frac{1}{\sqrt{2\omega_0+3}} \\
\beta_0 = \frac{2\omega_1\phi_0}{(2\omega_0+3)^2}
\end{cases}
\tag{2.59}
$$

From the action eq.(2.55), we can write down the field equations in Einstein frame:

$$
\begin{cases}
R^*_{\mu\nu} - \frac{1}{2}g^*_{\mu\nu}R^* = 8\pi G_*(T^*_{\mu\nu} + T^\varphi_{\mu\nu}) \\
\nabla_*^2\varphi = -4\pi G_*\alpha(\varphi)T^*
\end{cases}
\tag{2.60}
$$

Where

$$
\begin{aligned}
T^*_{\mu\nu} &= \frac{2}{\sqrt{-g_*}}\frac{\delta S_M}{g_*^{\mu\nu}} \\
T^\varphi_{\mu\nu} &= \frac{1}{4\pi G_*}(\nabla^*_\mu\varphi\nabla^*_\nu\varphi - \frac{1}{2}g^*_{\mu\nu}\nabla^{*\rho}\varphi\nabla^*_\rho\varphi)
\end{aligned}
\tag{2.61}
$$

2.8 Appendix B: Detection strategy for scalar gravitational wave memory effect by correlating 3 detectors

In scalar-tensor theory, a monochrome gravitational wave can be expanded as

$$h_{ij}(t,\vec{x}) = \int_{-\infty}^{+\infty} df\ e^{-2\pi i f(t-\hat{\Omega}\cdot\vec{x})}[\tilde{h}_+(f)e^+_{ij}(\hat{\Omega}) + \tilde{h}_\times(f)e^\times_{ij}(\hat{\Omega}) + \tilde{\Phi}(f)e^S_{ij}(\hat{\Omega})] \quad (2.62)$$

Where $\vec{x}$ is the position of the detector. $\hat{\Omega}$ is the unit vector pointing from the GW source to the detector.

The total output of one GW detector is the sum of the GW signal and detector's noise.

$$S_a(t) = s_a(t) + n_a(t) \quad (2.63)$$

Where a denotes the ath detector. The signal by definition is $s_a(t) = h_{ij}(t,\vec{x}_a)D^{ij}_a$ and its Forier transformation is

$$\tilde{s}_a(f) = e^{2\pi i f\hat{\Omega}\cdot\vec{x}_a}[\tilde{h}_+(f)F^+_a(\hat{\Omega}) + \tilde{h}_\times(f)F^\times_a(\hat{\Omega}) + \tilde{\Phi}(f)F^S_a(\hat{\Omega})] \quad (2.64)$$

Where $D^{ij}_a = \frac{1}{2}(\hat{u}^i_a\hat{u}^j_a - \hat{v}^i_a\hat{v}^j_a)$ is the detector tensor, and the angular pattern functions are defined by

$$F^+_a(\hat{\Omega}) = e^+_{ij}(\hat{\Omega})D^{ij}_a; \qquad F^\times_a(\hat{\Omega}) = e^\times_{ij}(\hat{\Omega})D^{ij}_a; \qquad F^S_a(\hat{\Omega}) = e^S_{ij}(\hat{\Omega})D^{ij}_a \quad (2.65)$$

We can combine three detectors to respond only the scalar polarization of a GW burst.

$$\begin{aligned} W^{\mathrm{S}} = \int_{-\infty}^{+\infty} df\ & [(F^+_2(\hat{\Omega})F^\times_3(\hat{\Omega}) - F^\times_2(\hat{\Omega})F^+_3(\hat{\Omega}))\tilde{S}_1(f)e^{-2\pi i f\hat{\Omega}\cdot\vec{x}_1} \\ & +(F^+_3(\hat{\Omega})F^\times_1(\hat{\Omega}) - F^\times_3(\hat{\Omega})F^+_1(\hat{\Omega}))\tilde{S}_2(f)e^{-2\pi i f\hat{\Omega}\cdot\vec{x}_2} \\ & +(F^+_1(\hat{\Omega})F^\times_2(\hat{\Omega}) - F^\times_1(\hat{\Omega})F^+_2(\hat{\Omega}))\tilde{S}_3(f)e^{-2\pi i f\hat{\Omega}\cdot\vec{x}_3}]\tilde{Q}(f) \\ = \int_{-\infty}^{+\infty} df\ & [\epsilon^{abc}F^+_a(\hat{\Omega})F^\times_b(\hat{\Omega})\tilde{S}_c(f)e^{-2\pi i f\hat{\Omega}\cdot\vec{x}_c}]\tilde{Q}(f) \qquad (a,b,c = 1,2,3) \end{aligned} \quad (2.66)$$

And its expected value and variance are

$$\begin{aligned} \mathrm{E}(W^{\mathrm{S}}) = \int_{-\infty}^{+\infty} df\ & [F^S_1(\hat{\Omega})(F^+_2(\hat{\Omega})F^\times_3(\hat{\Omega}) - F^\times_2(\hat{\Omega})F^+_3(\hat{\Omega})) \\ & +F^S_2(\hat{\Omega})(F^+_3(\hat{\Omega})F^\times_1(\hat{\Omega}) - F^\times_3(\hat{\Omega})F^+_1(\hat{\Omega})) \\ & +F^S_3(\hat{\Omega})(F^+_1(\hat{\Omega})F^\times_2(\hat{\Omega}) - F^\times_1(\hat{\Omega})F^+_2(\hat{\Omega}))]\tilde{\Phi}(f)\tilde{Q}(f) \\ = \int_{-\infty}^{+\infty} df\ & [\epsilon^{abc}F^+_a(\hat{\Omega})F^\times_b(\hat{\Omega})F^S_c(\hat{\Omega})]\tilde{\Phi}(f)\tilde{Q}(f) \end{aligned} \quad (2.67)$$

$$
\begin{aligned}
&\mathrm{Var}(W^{\mathrm{S}}) \\
&= \int_{-\infty}^{+\infty} df\, df'\, [(F_2^+(\hat{\Omega})F_3^\times(\hat{\Omega}) - F_2^\times(\hat{\Omega})F_3^+(\hat{\Omega}))^2 < \tilde{n}_1(f)\tilde{n}_1(f') > e^{-2\pi i(f-f')\hat{\Omega}\cdot\vec{x}_1} \\
&\qquad +(F_3^+(\hat{\Omega})F_1^\times(\hat{\Omega}) - F_3^\times(\hat{\Omega})F_1^+(\hat{\Omega}))^2 < \tilde{n}_2(f)\tilde{n}_2(f') > e^{-2\pi i(f-f')\hat{\Omega}\cdot\vec{x}_2} \\
&\qquad +(F_1^+(\hat{\Omega})F_2^\times(\hat{\Omega}) - F_1^\times(\hat{\Omega})F_2^+(\hat{\Omega}))^2 < \tilde{n}_3(f)\tilde{n}_3(f') > e^{-2\pi i(f-f')\hat{\Omega}\cdot\vec{x}_3}] \\
&\qquad \times\tilde{Q}(f)\tilde{Q}(f') \\
&= \frac{1}{2}\int_{-\infty}^{+\infty} df\, [(F_2^+(\hat{\Omega})F_3^\times(\hat{\Omega}) - F_2^\times(\hat{\Omega})F_3^+(\hat{\Omega}))^2 S_{n_1}(f) \\
&\qquad +(F_3^+(\hat{\Omega})F_1^\times(\hat{\Omega}) - F_3^\times(\hat{\Omega})F_1^+(\hat{\Omega}))^2 S_{n_2}(f) \\
&\qquad +(F_1^+(\hat{\Omega})F_2^\times(\hat{\Omega}) - F_1^\times(\hat{\Omega})F_2^+(\hat{\Omega}))^2 S_{n_3}(f)]|\tilde{Q}(f)|^2 \\
&= \frac{1}{2}\int_{-\infty}^{+\infty} df\, [\epsilon^{cab}\epsilon^{cde}F_a^+(\hat{\Omega})F_b^\times(\hat{\Omega})F_d^+(\hat{\Omega})F_e^\times(\hat{\Omega})S_{n_c}(f)]|\tilde{Q}(f)|^2
\end{aligned}
\tag{2.68}
$$

where we used $< \tilde{n}_a(f)\tilde{n}_b(f') >= \frac{1}{2}\delta_{ab}\delta(f+f')S_{n_a}(f)$. In order to maximize the signal-to-noise ratio, the optimal filtering function $\tilde{Q}(f)$ should be

$$
\tilde{Q}(f) = \frac{[\epsilon^{abc}F_a^+(\hat{\Omega})F_b^\times(\hat{\Omega})F_c^S(\hat{\Omega})]\tilde{\Phi}^*(f)}{\epsilon^{cab}\epsilon^{cde}F_a^+(\hat{\Omega})F_b^\times(\hat{\Omega})F_d^+(\hat{\Omega})F_e^\times(\hat{\Omega})S_{n_c}(f)} \tag{2.69}
$$

Then the signal-to-noise ratio is

$$
\left(\frac{S}{R}\right)^2 = \frac{\mathrm{E}(W^{\mathrm{S}})^2}{\mathrm{Var}(W^{\mathrm{S}})} = 4\int_0^{+\infty} df\, \frac{[\epsilon^{abc}F_a^+(\hat{\Omega})F_b^\times(\hat{\Omega})F_c^S(\hat{\Omega})]^2\ |\tilde{\Phi}(f)|^2}{\epsilon^{cab}\epsilon^{cde}F_a^+(\hat{\Omega})F_b^\times(\hat{\Omega})F_d^+(\hat{\Omega})F_e^\times(\hat{\Omega})S_{n_c}(f)} \tag{2.70}
$$

From the Fourier transform:

$$
\int_{-F}^{+F} \frac{1}{2\pi i}\frac{1}{f-i\epsilon}e^{-2\pi i f t}df = \frac{1}{2} - \frac{1}{\pi}\int_0^{2\pi F t}\frac{\sin x}{x}dx \simeq \theta(-t) \tag{2.71}
$$

This means for scalar gravitational wave memory, $\tilde{\Phi}(f) = \frac{\Phi_{\mathrm{I}}}{2\pi i}\frac{1}{f-i\epsilon}$ for $|f| < 1/\tau$, and the noise spectra of the three detectors are taken to be the same,

$$
\tilde{Q}(f) = -\frac{\mathcal{F}(\hat{\Omega})}{2\pi i}\frac{\Phi_{\mathrm{I}}}{f S_n(f)} \tag{2.72}
$$

$$
\left(\frac{S}{R}\right)^2 = \frac{\mathcal{F}(\hat{\Omega})}{\pi^2}\,\Phi_{\mathrm{I}}^2\int_0^{1/\tau} df\, \frac{1}{f^2 S_n(f)} \tag{2.73}
$$

where the correlated angular pattern function $\mathcal{F}(\hat{\Omega})$ is defined by

$$\mathcal{F}(\hat{\Omega}) = \frac{[\epsilon^{abc} F_a^+(\hat{\Omega}) F_b^\times(\hat{\Omega}) F_c^S(\hat{\Omega})]^2}{\epsilon^{cab}\epsilon^{cde} F_a^+(\hat{\Omega}) F_b^\times(\hat{\Omega}) F_d^+(\hat{\Omega}) F_e^\times(\hat{\Omega})} \tag{2.74}$$

Next we want to compute $\mathcal{F}(\hat{\Omega})$ for three ground based GW detectors: LIGO at Hanford, LIGO at Livingston and Virgo. First we need to specify the unit vectors pointing along the two arms of these detectors. In order to do this, we establish a coordinate system (θ, φ) where the north pole is defined at $\theta = 0°$, and φ denotes the longitude. The detector orientation angle α is the angle between the local east direction and the bisecting line of two arms of each detector measured counterclockwise. Where

$$\begin{cases} \hat{x}_1' = (\cos\varphi_1, \sin\varphi_1, 0) \\ \hat{y}_1' = (-\sin\varphi_1, \cos\varphi_1, 0) \\ \hat{z}_1' = (0, 0, 1) \end{cases} \qquad \begin{cases} \hat{x}_1 = \cos\theta_1 \hat{x}_1' - \sin\theta_1 \hat{z}_1' \\ \hat{y}_1 = \hat{y}_1' \\ \hat{z}_1 = \sin\theta_1 \hat{x}_1' + cos\theta_1 \hat{z}_1' \end{cases}$$

$$\begin{cases} \hat{u}_1 = \sin(\frac{\pi}{4} - \alpha_1)\hat{x}_1 + \cos(\frac{\pi}{4} - \alpha_1)\hat{y}_1 \\ \hat{v}_1 = -\cos(\frac{\pi}{4} - \alpha_1)\hat{x}_1 + \sin(\frac{\pi}{4} - \alpha_1)\hat{y}_1 \end{cases} \tag{2.75}$$

where

$$\begin{aligned} &\text{H}: \ \theta_1 = 43.5°, \ \varphi_1 = -119.4°, \ \alpha_1 = -45.0° \\ &\text{L}: \ \theta_2 = 59.4°, \ \varphi_2 = -90.8°, \ \alpha_2 = -243.0° \\ &\text{V}: \ \theta_3 = 46.4°, \ \varphi_3 = 10.5°, \quad \alpha_3 = 116.5° \\ &\text{K}: \ \theta_4 = 53.6°, \ \varphi_4 = 137.3°, \quad \alpha_4 = 74.9° \end{aligned}$$

Let $\hat{\Omega}$ denote the unit vector pointing towards the GW propagating direction. The coordinates of three orthogonal unit vectors $(\hat{m}, \hat{n}, \hat{\Omega})$ are

$$\begin{cases} \hat{m}' = (\cos\theta\cos\varphi, \cos\theta\sin\varphi, -\sin\theta) \\ \hat{n}' = (-\sin\varphi, \cos\varphi, 0) \\ \hat{\Omega}' = (\sin\theta\cos\varphi, \sin\theta\sin\varphi, \cos\theta) \end{cases} \qquad \begin{cases} \hat{m} = \cos\psi \ \hat{m}' + \sin\psi \ \hat{n}' \\ \hat{n} = -\sin\psi \ \hat{m}' + \cos\psi \ \hat{n}' \end{cases} \tag{2.76}$$

With all of these settings, we find the correlated angular pattern function $\mathcal{F}(\hat{\Omega})$ as a function of lattitude θ and longitude φ ($\mathcal{F}(\hat{\Omega})$ is independent of angle ψ).

The optimal direction for the source is located at (54.5°N, 142.5°E) and its opposite (54.5°S, 37.5°W). The optimal value of $\mathcal{F}(\hat{\Omega})$ at these directions is 0.485.

2.9 Appendix C: Detection strategy for scalar gravitational wave memory effect by correlating N detectors

Let's consider N ground-based GW detectors. Let a denote the a-th detector ($a = 1, ..., N$), then the Fourier transformed total output of detector a is a sum of its signal and noise:

$$\tilde{S}_a(f) = \tilde{s}_a(f) + \tilde{n}_a(f) \tag{2.77}$$

with expectations:

$$\mathrm{E}[\tilde{S}_a(f)] = \tilde{s}_a(f) = e^{2\pi i f \hat{\Omega}\cdot\vec{x}_a}[F_a^+(\hat{\Omega})\tilde{h}_+(f) + F_a^\times(\hat{\Omega})\tilde{h}_\times(f) + F_a^S(\hat{\Omega})\tilde{\Phi}(f)] \tag{2.78}$$

$$\mathrm{E}[\tilde{S}_a(f)\tilde{S}_b(f')] =< \tilde{n}_a(f)\tilde{n}_b(f') >= \frac{1}{2}\delta_{ab}\delta(f+f')S_{n_a}(f) \tag{2.79}$$

Let the filtered output of detector a be

$$w_a = \int_{-\infty}^{+\infty} df\ e^{-2\pi i f \hat{\Omega}\cdot\vec{x}_a}\tilde{S}_a(f)\tilde{Q}(f) \tag{2.80}$$

We can construct a linear combination of the 4 detectors

$$W = \sum_a \alpha_a w_a = \int_{-\infty}^{+\infty} df\ \left[\sum_a e^{-2\pi i f \hat{\Omega}\cdot\vec{x}_a}\alpha_a\tilde{S}_a(f)\right]\tilde{Q}(f) \tag{2.81}$$

Its expectation is

$$\mathrm{E}(W) = \int_{-\infty}^{+\infty}\left[\vec{\alpha}\cdot\vec{F}_+\tilde{h}_+(f) + \vec{\alpha}\cdot\vec{F}_\times\tilde{h}_\times(f) + \vec{\alpha}\cdot\vec{F}_S\tilde{\Phi}(f)\right]\tilde{Q}(f) \tag{2.82}$$

where $\vec{F}_A = (w_1, ..., w_N)$ and $\vec{\alpha} = (\alpha_1, ..., \alpha_N)$. We want it respond only to the scalar polarization, then we require that $\vec{\alpha}\cdot\vec{F}_+ = \vec{\alpha}\cdot\vec{F}_\times = 0$ and in this case

$$\mathrm{E}(W) = \int_{-\infty}^{+\infty} df\ \left(\sum_a \alpha_a F_a^S(\hat{\Omega})\right)\tilde{\Phi}(f)\tilde{Q}(f) \tag{2.83}$$

$$\mathrm{Var}(W) = \mathrm{E}(W^2) = \frac{1}{2}\int_{-\infty}^{+\infty} df\ \left(\sum_a \alpha_a^2 S_{n_a}(f)\right)|\tilde{Q}(f)|^2 \tag{2.84}$$

In order to maximize the SNR, the optimal filtering function should be

$$\tilde{Q}(f) = \frac{\left(\sum_a \alpha_a F_a^S(\hat{\Omega})\right)\tilde{\Phi}^*(f)}{\sum_a \alpha_a^2 S_{n_a}(f)} \tag{2.85}$$

In this case, the SNR is

$$\left(\frac{S}{R}\right)^2 = \frac{\mathrm{E}^2(W)}{\mathrm{Var}(W)} = 4\int_0^{+\infty} df\ \frac{\left(\sum_a \alpha_a F_a^S(\hat{\Omega})\right)^2|\tilde{\Phi}(f)|^2}{\sum_a \alpha_a^2 S_{n_a}(f)} \tag{2.86}$$

For scalar gravitational wave memory, $\tilde{\Phi}(f) = \frac{\Phi_{\rm I}}{2\pi i}\frac{1}{f-i\epsilon}$ and for convinience we take the noise spectra of the four detectors to be the same,

$$\tilde{Q}(f) = -\frac{\mathcal{F}(\hat{\Omega})}{2\pi i}\frac{\Phi_{\rm I}}{fS_n(f)} \tag{2.87}$$

$$\left(\frac{S}{R}\right)^2 = \frac{\mathcal{F}(\hat{\Omega})}{\pi^2}\Phi_{\rm I}^2\int_0^{1/\tau} df\ \frac{1}{f^2 S_n(f)} \tag{2.88}$$

where the correlated angular pattern function $\mathcal{F}(\hat{\Omega})$ is defined by

$$\mathcal{F}(\hat{\Omega}) = \frac{\left(\vec{\alpha}\cdot\vec{F}_S(\hat{\Omega})\right)^2}{\vec{\alpha}\cdot\vec{\alpha}} \tag{2.89}$$

We find that the mode of $\vec{\alpha}$ is irrelevant to the value of $\mathcal{F}$, hence we can simply set $|\vec{\alpha}| = 1$. Then our aim is to maximize

$$\mathcal{F} = \left(\vec{\alpha}\cdot\vec{F}_S\right)^2 \tag{2.90}$$

while requiring that

$$\begin{cases}\vec{\alpha}\cdot\vec{F}_+ = 0\\ \vec{\alpha}\cdot\vec{F}_\times = 0\end{cases} \tag{2.91}$$

The solution is

$$\begin{cases}\vec{\alpha} = \vec{F}_S'/|\vec{F}_S'|\\ \mathcal{F} = \vec{F}_S'\cdot\vec{F}_S'\end{cases} \tag{2.92}$$

where we defined

$$\begin{aligned}\vec{F}_S' = \vec{F}_S &- \frac{(\vec{F}_\times\cdot\vec{F}_\times)(\vec{F}_+\cdot\vec{F}_S) - (\vec{F}_+\cdot\vec{F}_\times)(\vec{F}_\times\cdot\vec{F}_S)}{(\vec{F}_+\cdot\vec{F}_+)(\vec{F}_\times\cdot\vec{F}_\times) - (\vec{F}_+\cdot\vec{F}_\times)^2}\vec{F}_+\\ &- \frac{(\vec{F}_+\cdot\vec{F}_+)(\vec{F}_\times\cdot\vec{F}_S) - (\vec{F}_+\cdot\vec{F}_\times)(\vec{F}_+\cdot\vec{F}_S)}{(\vec{F}_+\cdot\vec{F}_+)(\vec{F}_\times\cdot\vec{F}_\times) - (\vec{F}_+\cdot\vec{F}_\times)^2}\vec{F}_\times\ .\end{aligned} \tag{2.93}$$

In order to have a non-zero $\vec{F}_S'$, we should have at least 3 detectors. The maximized angular pattern function $\mathcal{F}(\hat{\Omega}) = \vec{F}_S'(\hat{\Omega})\cdot\vec{F}_S'(\hat{\Omega})$ as a function of lattitude θ and longitude φ ($\mathcal{F}(\hat{\Omega})$ is independent of angle ψ) by correlating detectors HLV and HLVK are shown in . For HLV, the optimal direction for the source is located at (54.5°N, 142.5°E) and its opposite (54.5°S, 37.5°W). The optimal value of $\mathcal{F}_3(\hat{\Omega})$ at these directions is 0.485. For HLVK, the optimal direction for the source is located at (33.2°N, 2.3°W) and its opposite (33.2°S, 177.7°E). The optimal value of $\mathcal{F}_4(\hat{\Omega})$ at these directions is 0.511. The averages of the correlated angular pattern function are $\int \mathcal{F}_3(\hat{\Omega})d\hat{\Omega}/4\pi = 0.0865$ and $\int \mathcal{F}_4(\hat{\Omega})d\hat{\Omega}/4\pi = 0.240$.

2.10 Appendix D: Gravitational Collapse in Oppenheimer-Snyder model

In the Damour-Esposito-Farese approximation, the collapse process can be described by the Oppenheimer-Snyder model. Let's consider a collapsing star with an initial mass M and radius R. The interior space-time is described by comoving coordinate (t, r, θ, φ):

$$ds^2 = -dt^2 + a^2(t)\left[\frac{dr^2}{1-kr^2} + r^2 d\theta^2 + r^2 \sin^2\theta d\varphi^2\right] \tag{2.94}$$

where $k \equiv 2GM/R^3$. Inside the star, the stress-energy tensor is

$$T^{\mu\nu} = \frac{M}{\frac{4}{3}\pi R^3}\begin{pmatrix} 1 & 0 & 0 & 0 \\ 0 & 0 & 0 & 0 \\ 0 & 0 & 0 & 0 \\ 0 & 0 & 0 & 0 \end{pmatrix} \tag{2.95}$$

Soving the Einstein field equation gives the Oppenheimer-Snyder solution:

$$\sqrt{k}t = \sqrt{(1-a(t))a(t)} + \frac{1}{4}\left[\pi + 2\arctan\left(\frac{1-2a(t)}{2\sqrt{(1-a(t))a(t)}}\right)\right] \tag{2.96}$$

Let t_s be the interior time when the star collapses into a singularity. At this time $a(t_s) = 0$, then $t_s = \frac{\pi}{2\sqrt{k}}$.

From Birkhoff's theorem, the exterior space-time can be described by Schwarzchild coordinate $(\bar{t}, \bar{r}, \bar{\theta}, \bar{\varphi})$:

$$ds^2 = -\left(1 - \frac{2GM}{\bar{r}}\right)d\bar{t}^2 + \frac{1}{\left(1-\frac{2GM}{\bar{r}}\right)}d\bar{r}^2 + \bar{r}^2 d\bar{\theta}^2 + \bar{r}^2 \sin^2\bar{\theta} d\bar{\varphi}^2 \tag{2.97}$$

By matching the exterior and interior space-time at the boundary, we find $\bar{\theta} = \theta$, $\bar{\varphi} = \varphi$. At the boundary, $\bar{r} = Ra(t)$. And

$$\frac{d\bar{t}}{dt} = \frac{\sqrt{1-\frac{2GM}{R}}}{1-\frac{2GM}{Ra(t)}}. \tag{2.98}$$

The slope is approximately $\frac{1}{\sqrt{1-2\mu}}$ with $\mu \equiv \frac{GM}{R}$. We use t_0 denotes the interior time when the boundary is inside the event horizon: $a(t_0)R = 2GM$, and

$$\sqrt{k}t_0 = \sqrt{(1-2\mu)2\mu} + \frac{1}{4}\left[\pi + 2\arctan\left(\frac{1-4\mu}{2\sqrt{(1-2\mu)2\mu}}\right)\right] \tag{2.99}$$

For $\mu = 0.20$, $t_0 = \frac{1.376}{\sqrt{k}}$, which is approximately equal to $t_s = \frac{\pi}{2\sqrt{k}}$. Then the collapsing time observed by an exterior observer is

$$\tau \simeq \frac{t_s}{\sqrt{1-2\mu}} = \frac{\pi}{2}\frac{GM}{\mu\sqrt{2\mu(1-2\mu)}} \tag{2.100}$$

For $M = 2M_\odot$, $\mu = 0.25$, the collapsing time $\tau \simeq 0.12$ms. This time is approximately equal to the numerical simulation in J. Novak's paper.

2.11 Appendix E: SNR and the detectable region in the parameter space

Now we can use eq.(40) to compute the SNR of a scalar GW memory effect. The noise spectral density $S_n(f)$ for advanced LIGO is taken from Table I of arXiv:0903.0338. We numerically compute the integral:

$$\int_0^{\frac{1}{0.12\times10^{-3}}} \frac{1}{f^2 S_n(f)}\, df = 2.3171 \times 10^{45} \tag{2.101}$$

If we take the correlated angular pattern function at its optimal value, then the SNR is

$$\frac{S}{R} = \frac{\sqrt{\mathcal{F}(\hat{\Omega})}}{\pi}\left[\int_0^{\frac{1}{0.15\times10^{-3}}} \frac{1}{f^2 S_n(f)}\, df\right]^{\frac{1}{2}} \Phi_{\rm I} = 1.067 \times 10^{22}\, \Phi_{\rm I} \tag{2.102}$$

In the paper, we have given

$$\Phi_{\rm I}(r) = -\frac{2\alpha_0^2 GM}{r|\beta_0|\mu} \times \begin{cases} 1 - \frac{\tanh\sqrt{3\mu|\beta_0|}}{\sqrt{3\mu|\beta_0|}} & (\beta_0 > 0) \\ \frac{\tan\sqrt{3\mu|\beta_0|}}{\sqrt{3\mu|\beta_0|}} - 1 & (\beta_0 < 0) \end{cases} \tag{2.103}$$

If we set the level of SNR to be 10, then

$$|\Phi_{\rm I}| = \frac{2\alpha_0^2 GM}{r|\beta_0|\mu} \times \begin{cases} 1 - \frac{\tanh\sqrt{3\mu|\beta_0|}}{\sqrt{3\mu|\beta_0|}} \\ \frac{\tan\sqrt{3\mu|\beta_0|}}{\sqrt{3\mu|\beta_0|}} - 1 \end{cases} = 9.372 \times 10^{-22} \tag{2.104}$$

For $M = 2M_\odot = 4 \times 10^{30}$ kg, $\mu = 0.25$, $r = 1$ Mpc $= 3.086 \times 10^{22}$ m, this equation gives $\lg \alpha_0$ as a function of β_0:

$$\lg \alpha_0 = \begin{cases} \frac{1}{2}\lg\left[\frac{1.22\times10^{-3}\beta_0}{1-\frac{\tanh\sqrt{0.75\beta_0}}{\sqrt{0.75\beta_0}}}\right] & (\beta_0 > 0) \\ \frac{1}{2}\lg\left[\frac{-1.22\times10^{-3}\beta_0}{\frac{\tan\sqrt{-0.75\beta_0}}{\sqrt{-0.75\beta_0}}-1}\right] & (\beta_0 < 0) \end{cases} \tag{2.105}$$

Fig[4] shows the constraints on α_0 and β_0 from solar system, pulsar timing as well as scalar GW memory.

Chapter 3

SCALAR STOCHASTIC GRAVITATIONAL-WAVE BACKGROUND IN BRANS-DICKE THEORY OF GRAVITY

We study the scalar stochastic gravitational-wave background (SGWB) from astrophysical sources, including compact binary mergers and stellar collapses, in the Brans-Dicke theory of gravity. By contrast to tensor waves, we found the scalar SGWB to predominantly arise from stellar collapses. These collapses not only have higher astrophysical rates, but also have larger energy emitted per event. This is because unlike tensor radiation, which mainly starts from quadrupole order, the scalar perturbation can be excited by changes in the monopole moment. In particular, in the case of stellar collapse into a neutron star or a black hole, the monopole radiation, at frequencies below 100 Hz, is dominated by the memory effect. At low frequencies, the scalar SGWB spectrum follows a power law of $\Omega_{\rm S} \propto f^{\alpha}$, with $\alpha = 1$. We predict that $\Omega_{\rm S}$ is inversely proportional to the square of $\omega_{\rm BD} + 2$, with $(\omega_{\rm BD} + 2)^2 \Omega_S(f = 25\,{\rm Hz}) = 2.8 \times 10^{-6}$. We also estimate the detectability of the scalar SGWB for current and third-generation detector networks, and the bound on $\omega_{\rm BD}$ that can be imposed from these observations.

3.1 Introduction

The first direct detection of gravitational waves (GWs) from the merger of binary black holes (BBHs) by the LIGO-Virgo collaboration [10] marks the beginning of gravitational-wave astronomy and opens up a new window to the Universe. Since then, more GW events, both from BBH mergers and from binary neutron star (BNS) mergers, are detected by the Advanced LIGO/Virgo network [12–15]. Besides these resolvable, individual GW sources we have discovered so far, a Stochastic Gravitational-Wave Background (SGWB), which arises from the population of unresolved GW events at larger distances, is anticipated to be detectable in the upcoming years [17, 20]. GW signals provide us with unprecedented opportunities to test general relativity (GR) and study modified theories of gravity [10, 11, 13, 16].

One significant prediction of general relativity is that gravitational waves only contain two tensor polarization modes (+ mode and × mode). On the other hand, additional polarization modes do exist in modified theories of gravity; if directly detected, they would become a strong evidence for extensions to Einstein's original

theory [73, 74]. For example, the Brans-Dicke (BD) theory [46], which minimally extends Einstein's gravity by incorporating a scalar field (Brans-Dicke field) coupled to the metric tensor, predicts the existence of a transverse scalar polarization mode (also referred to as the breathing, or the "$\circ$ mode"). Previously, several detection strategies for the non-tensorial SGWB have been proposed [51, 100, 113]. A recent study [21], based on the method in [51] and the data from LIGO's O1 observing run, has placed the first constraints on the contributions from non-tensorial polarizations to the SGWB.

All the works so far have assumed general, power-law models for the energy spectra of the non-tensorial SGWB — without considering its specific origins. However, in order to theoretically estimate the plausible magnitudes of the non-tensorial SGWB, and to experimentally make statistical inferences on parameters of modified gravity models from detector data, it is necessary to consider the astrophysical origins of the non-tensorial SGWB. Furthermore, obtaining astrophysicically motivated energy spectra may allow us to more efficiently search for the non-tensorial SGWB using a more optimal matched filtering technique [28] — than simply assuming a power-law spectrum.

In this paper, we focus on the SGWB in the transverse scalar mode of the Brans-Dicke (BD) theory: identifying its astrophysical origins, and obtaining its energy spectrum (as a function of the BD coupling constant). Candidates for sources of the SGWB include gravitational stellar collapses and compact binary mergers. As we will see, the existence of monopole scalar radiations makes stellar collapses by far the major contributor to this SGWB. This differs significantly from the tensorial SGWB in GR, which is dominated by BBH and BNS mergers.

This paper is organized as follows: In Sec. II, we will give an overview of the scalar GW in Brans-Dicke theory and its relation to scalar SGWB. In Secs. III and IV, we will calculate the contributions to the scalar SGWB from compact binary coalescences, including BBH and BNS mergers, as well as the contribution from gravitational stellar collapses. In Sec. V, we will explore how the scalar SGWB depends on variations in the underlying population models. In Sec. VI, we will discuss the detectability and possible constraints on the BD coupling constant $\omega_{\rm BD}$ from the current and future observations. Finally, in Sec. VII, we will draw conclusions and suggest prospective research directions.

3.2 Scalar GW in Brans-Dicke Theory and Relation to SGWB

In the Brans-Dicke (BD) theory, the Lagrangian density of the gravity sector in the original conformal frame is given by

$$\mathcal{L}_{\rm BD} = \sqrt{-g}\left[\phi R - \omega_{\rm BD}\,\frac{\partial^\mu\phi\partial_\mu\phi}{\phi}\right], \tag{3.1}$$

where the Ricci scalar R is associated with the spacetime metric tensor $g_{\mu\nu}$. The scalar field ϕ is related to the gravitational constant G via the relation

$$G\phi_0 = \frac{2\omega_{\rm BD}+4}{2\omega_{\rm BD}+3} \tag{3.2}$$

where ϕ_0 is the value of the scalar field at the null infinity. The matter sector Lagrangian density remains the same as in GR, which means the scalar field does not couple to the matter fields directly. When the model parameter $\omega_{\rm BD}$ approaches to infinity, Brans-Dicke theory recovers to GR. In this rest of this section, we shall discuss the polarization content of GWs in the BD theory, and describe the energy content of the scalar SGWB. Details can be found in Refs. [46, 100].

GWs in the BD Theory

To study GWs in Brans-Dicke theory, we perform a perturbation of the metric tensor and the scalar field around the Minkowski spacetime and the null infinity value, respectively:

$$g_{\mu\nu} = \eta_{\mu\nu} + h_{\mu\nu}, \qquad \phi = \phi_0 + \delta\phi, \tag{3.3}$$

where components of the metric tensor in Minkowski spacetime is chosen to be $\eta_{\mu\nu} = \mathrm{diag}(-1,1,1,1)$. The perturbative Lagrangian contains a quadratic cross term: $h_{\mu\nu}(\partial^\mu\partial^\nu - \eta^{\mu\nu}\Box)\delta\phi$. [Here we use $\Box$ as a shorthand for $\eta^{\alpha\beta}\partial_\alpha\partial_\beta$.] To eliminate this term we redefine the following physical degrees of freedom:

$$H_{\mu\nu} = h_{\mu\nu} + \eta_{\mu\nu}\frac{\delta\phi}{\phi_0}\,. \tag{3.4}$$

Under these treatments, the perturbative Lagrangian is expressed as:

$$\begin{aligned}
\mathcal{L}_{\rm BD} &= \mathcal{L}^{\rm kin}_{\rm BD} + \mathcal{L}^{\rm S}_{\rm BD} + \mathcal{L}^{\rm other}_{\rm BD}\,,\\
\mathcal{L}^{\rm kin}_{\rm BD} &= \frac{\phi_0}{2}H^{\mu\nu}V_{\mu\nu\rho\sigma}H^{\rho\sigma} + \frac{\omega_{\rm BD}+3/2}{\phi_0}\,\eta^{\mu\nu}\delta\phi\,\partial_\mu\partial_\nu\delta\phi\,,\\
\mathcal{L}^{\rm S}_{\rm BD} &= \frac{\omega_{\rm BD}+3/2}{\phi_0}\left(H^{\mu\nu} - \frac{1}{2}\eta^{\mu\nu}H\right)\partial_\mu\delta\phi\partial_\nu\delta\phi\,.
\end{aligned} \tag{3.5}$$

Here $\mathcal{L}^{\rm kin}_{\rm BD}$ represents the kinetic terms for the tensor field $H_{\mu\nu}$ and the scalar field $\delta\phi$, where the operator $V_{\mu\nu\rho\sigma}$ is defined as:

$$V_{\mu\nu\rho\sigma} = \frac{1}{2}\Big[(\eta_{\mu\rho}\eta_{\nu\sigma} - \eta_{\mu\nu}\eta_{\rho\sigma})\partial^2 + \eta_{\mu\nu}\partial_\rho\partial_\sigma + \eta_{\rho\sigma}\partial_\mu\partial_\nu - \eta_{\mu\rho}\partial_\nu\partial_\sigma - \eta_{\nu\sigma}\partial_\mu\partial_\rho\Big] .$$

The Lagrangian $\mathcal{L}^{\rm S}_{\rm BD}$ contains the leading interaction terms between the scalar and the tensor fields. Later we shall show that it relates to the scalar stress-energy tensor. The third term $\mathcal{L}^{\rm other}_{\rm BD}$ contains other higher order interaction terms. Notice that the Lagrangians in Eq. (3.5) is invariant under the infinitesimal diffeomorphism transformation $x^\mu \to x'^\mu = x^\mu + \xi^\mu(x)$:

$$\begin{cases} H_{\mu\nu} \to H'_{\mu\nu} = H_{\mu\nu} - \partial_\mu\xi_\nu - \partial_\nu\xi_\mu \\ \\ \delta\phi \to \delta\phi' = \delta\phi \ . \end{cases} \tag{3.6}$$

The vacuum field equation for $H_{\mu\nu}$ is obtained from $\delta\mathcal{L}^{\rm kin}_{\rm BD}/\delta H_{\mu\nu} = 0$, which gives $V^{\mu\nu\rho\sigma}H_{\rho\sigma} = 0$. If we choose the harmonic coordinate condition, this equation is reduced to

$$\begin{cases} \partial^2 H_{\mu\nu} = 0 \\ \partial^\mu H_{\mu\nu} - \frac{1}{2}\partial_\nu H = 0 \ . \end{cases} \tag{3.7}$$

Notice that the vacuum field equation Eq. (3.7) and the gauge transformation Eq. (3.6) have the same form as in GR, hence we can similarly gauge away redundant degrees of freedom which leave only two physical ones.

However, GW detectors respond directly to the change in the spacetime metric, i.e. $h_{\mu\nu}$, which depends both on $H_{\mu\nu}$ and $\delta\phi$. As a result, three physical degrees of freedom remain for $h_{\mu\nu}$ [100]. More specifically, within a spatial slice, let Σ_Ω be the 2-D plane perpendicular to the wave propagation direction $\hat{\Omega}$, and let $\hat{m}$, $\hat{n}$ be two the orthogonal unit vectors in Σ_Ω, then we can find a gauge in which the plain wave can be expanded as,

$$h_{ij}(x) = h_+(x)e^+_{ij} + h_\times(x)e^+_{ij} + h_{\rm S}(x)e^{\rm S}_{ij}. \tag{3.8}$$

Here, the amplitudes are related to H_{ij} and $\delta\phi$ via

$$h_+ = e^{ij}_+ H^{\rm TT}_{ij}/2, \quad h_\times = e^{ij}_\times H^{\rm TT}_{ij}/2, \quad h_{\rm S} = -\delta\phi/\phi_0, \tag{3.9}$$

here $H_{ij}^{\rm TT}$ is the transverse-traceless part of H_{ij} [139]. The polarization tensors are expressed as

$$e_{ij}^{+} = \hat{m}_i\hat{m}_j - \hat{n}_i\hat{n}_j, \qquad e_{ij}^{\times} = \hat{m}_i\hat{n}_j + \hat{n}_i\hat{m}_j,$$
$$e_{ij}^{S} = \hat{m}_i\hat{m}_j + \hat{n}_i\hat{n}_j. \tag{3.10}$$

Here $e^{+,\times}$ and $e^{\rm S}$ represent tensor and scalar polarizations of GW respectively because under an SO(2) rotation in Σ_Ω plane: $\hat{m}' + i\hat{n}' = \exp(i\theta)(\hat{m} + i\hat{n})$, they behave as $e^{+\prime} + ie^{\times\prime} = \exp(2i\theta)(e^{+} + ie^{\times})$ and $e^{S\prime} = e^{S}$.

The scalar SGWB

We expect the presence of the scalar GW would give rise to a stochastic background with scalar polarization, which is described by the dimensionless energy density spectrum:

$$\tilde{\Omega}_{\rm S}(f) = \frac{1}{\rho_c}\frac{d\rho_{\rm S}}{d\ln f}. \tag{3.11}$$

In this equation, $\rho_c = 3H_0^2/8\pi G$ is the critical density to close the Universe with H_0 representing the Hubble constant. The energy density of the scalar GW $\rho_{\rm S}$ relates to the scalar stress-energy tensor $T_{\rm S}^{\mu\nu}$ via $\rho_{\rm S} = T_{\rm S}^{00}$, with

$$T_{\rm S}^{\mu\nu} = \frac{1}{8\pi}\frac{\partial\mathcal{L}_{\rm BD}^{\rm S}}{\partial H_{\mu\nu}} = \frac{\omega_{\rm BD}+2}{8\pi G}\left(\partial^\mu h_{\rm S}\partial^\nu h_{\rm S} - \frac{\eta^{\mu\nu}}{2}\partial^\rho h_{\rm S}\partial_\rho h_{\rm S}\right). \tag{3.12}$$

Combining with the field equation $\partial^2 h_{\rm S} = 0$ and averaging over several wave length, we obtain [100]

$$\rho_{\rm S} = \frac{\omega_{\rm BD}+2}{8\pi G}\left\langle \dot{h}_{\rm S}^2(x)\right\rangle \tag{3.13}$$

Under the assumption that the stochastic background is stationary, isotropic and Gaussian, the ensemble average of the Fourier transformed amplitude $\tilde{h}_{\rm S}(f,\hat{\Omega})$ satisfies

$$\left\langle \tilde{h}_{\rm S}^*(f,\hat{\Omega})\tilde{h}_{\rm S}(f',\hat{\Omega}')\right\rangle = \frac{5}{8\pi}\delta(\hat{\Omega}-\hat{\Omega}')\delta(f-f')H_{\rm S}(f). \tag{3.14}$$

Here $\tilde{h}_{\rm S}(f,\hat{\Omega})$ relates to $h(t,\mathbf{x})$ via

$$h_S(t,\mathbf{x}) = \int \frac{d^3\mathbf{k}}{(2\pi)^3}e^{-i\omega(\mathbf{k})t+i\mathbf{k}\cdot\mathbf{x}}\tilde{h}_S + \text{c.c.} \tag{3.15}$$

with $\omega(\mathbf{k}) = |\mathbf{k}|/c$, and

$$\mathbf{k} = 2\pi f\hat{\Omega}/c \tag{3.16}$$

where $\hat{\Omega}$ is the unit vector along the direction of $\mathbf{k}$. The quantity $H_{\rm S}$ is defined as the spectral density for scalar GW. The factor of $5/8\pi$ follows the same convention in [21, 51].

Under this definition, $\tilde{H}_S$ is related to the scalar spectral density $\tilde{\Omega}^{\rm S}_{\rm GW}$ [Defined in Eq. (3.11)–(3.13)], via

$$\tilde{\Omega}_{\rm S}(f) = (\omega_{BD} + 2)\frac{20\pi^2}{3H_0^2} f^3 H_{\rm S}(f)\,. \tag{3.17}$$

As we shall see later in Sec. 3.5, the quantity H_S is directly related to the detectability of the scalar SGWB [see Eq. (5.1)]. In this way, even though $\tilde{\Omega}_S$ is directly proportional to the energy density of the scalar wave, detectability of the background, given the same $\tilde{\Omega}_S$, still depends on the coupling BD coupling constant $\omega_{\rm BD}$. This is related to the violation of the Isaacson formula in BD theory [28, 91]. Instead, following the same convention as Ref. [21], we define a new quantity

$$\Omega_{\rm S}(f) = \frac{\tilde{\Omega}_{\rm S}(f)}{\omega_{BD} + 2} = \frac{20\pi^2}{3H_0^2} f^3 H_{\rm S}(f), \tag{3.18}$$

In the following discussions, we will keep using this redefined energy density spectrum to describe the scalar SGWB.

3.3 Scalar and Tensor SGWB from Mergers of Compact Binary System

Tensor SGWB from Compact Binary Mergers in BD Theory

In GR, the SGWB has only tensor polarization and the major contribution within the bandwidth of ground based GW detectors is from the mergers of BBH, with $\Omega_{\rm T}(f = 25{\rm Hz}) \simeq 1.1 \times 10^{-9}$ [20]. Besides BBH, the mergers of BNS has a comparable contribution to the SGWB, with $\Omega_{\rm T}(f = 25{\rm Hz}) \simeq 0.7 \times 10^{-9}$ [17]. In BD, we expect the tensor SGWB takes approximately the same value as in GR, which is predicted from the relation [47, 118]:

$$P_{\rm T}^{\rm (BD)} = \frac{2\omega_{\rm BD} + 3}{2\omega_{\rm BD} + 4} P_{\rm T}^{\rm (GR)}, \tag{3.19}$$

where $P_{\rm T}^{\rm (BD)}$ and $P_{\rm T}^{\rm (GR)}$ denote the power emitted in GW with tensor polarization from a system of binary stars in BD and in GR respectively, at the same orbital frequency. For a large $\omega_{\rm BD}$, we expect the ratio between the two powers is approximately equal to one. As will be shown later in the next section, in BD most of gravitational radiation by binary stars is from tensor GW — with scalar radiation suppressed by $\omega_{\rm BD}$. Consequently, the coalescing trajectory of the compact binary system which is mainly a result from GW radiation, as well as the spectrum of tensor GW radiation, is nearly unchanged as in GR.

Scalar Radiation from a Compact Binary in BD Theory

As for the scalar part, the story is completely different: the contribution to the scalar SGWB from the mergers of BBH is exactly zero. This is a direct implication from Hawking's *no scalar-hair* theorem of black holes in BD theory of gravity [87]. The theorem states that for black holes in BD the exterior spacetine geometry is the same as in GR and the scalar field ϕ takes a constant value. Since $h_{\rm S} = 0$ everywhere, there is no scalar GW radiation from the merger of BBH.

On the other hand, the no scalar-hair theorem does not forbid scalar GWs emitted from mergers of BNS. Within the bandwidth of ground based GW detectors, the background is mainly from the inspiral stage, since BNS merger frequency is above 2 kHz [17]. The power of scalar GW emission from inspiraling binary systems has been studied in [47, 118]. Contrary to the tensor case, the scalar GW has monopole and dipole radiations in addition to quadrupole radiation. In the limit of vanishing eccentricity $e \to 0$ (this assumption should be valid since the orbital angular momentum should have been radiated away from GW emission for coalescing binary systems as they enter the band of ground-based detectors) the scalar energy spectrum for the monopole radiation ($j = 0$) is negligible (binary systems with circular orbit have no monopole moment), while the dipole ($j = 1$) and quadruple ($j = 2$) are given by

$$\begin{aligned}
\frac{dE_{\rm S}^{j=1}}{df} &= \frac{1}{\omega_{\rm BD}+2}\frac{5}{48}\left(\frac{\rm BE_1}{m_1}-\frac{\rm BE_2}{m_2}\right)\frac{m_1 m_2}{m_1+m_2}f^{-1} \\
\frac{dE_{\rm S}^{j=2}}{df}(f) &= \frac{1}{\omega_{\rm BD}+2}\frac{(\pi G)^{\frac{2}{3}}}{36}\frac{m_1 m_2}{(m_1+m_2)^{\frac{1}{3}}}f^{-\frac{1}{3}}\,.
\end{aligned} \tag{3.20}$$

Here f represents the frequency of GW, m_1 and m_2 the masses of the two neutron stars in the binary system. The energy spectrum is derived from the relation to the power: $dE_{\rm S}^j/df = P_{\rm S}^j/\dot{f}$, where we adopt the power of scalar GW emission $P_{\rm S}^j$ calculated by Brunetti et al. [47]. In the limit of $e \to 0$, the orbital frequency F and the GW frequency f are related by $f = jF$ for $j = 1, 2$. The rate of change of the orbital frequency due to GW emission is the same as in GR [110]:

$$\dot{F} = \frac{48\pi^{\frac{8}{3}}G^{\frac{5}{3}}}{5}\frac{m_1 m_2}{(m_1+m_2)^{\frac{1}{3}}}(2F)^{\frac{11}{3}} \tag{3.21}$$

In Eq. (3.20), BE represents the binding energy of neutron stars and we adopt the model by Lattimer and Prakash [97], which reads

$$\frac{\rm BE}{m} \simeq \frac{0.6\,\beta}{1-0.5\,\beta}, \tag{3.22}$$

where $\beta = Gm/R$ with R denoting the radius of the neutron star.

Scalar SGWB from Compact Binaries in BD Theory

The energy density spectrum of the produced SGWB can be obtained from the emission spectrum of a single BNS merger event via [20, 123]

$$\Omega_{\rm S}^{j}(f) = \frac{1}{\omega_{\rm BD}+2}\frac{f}{\rho_c}\int_0^{z_{\rm max}} dz\,\frac{R_m(z)\,\frac{dE_{\rm S}^{j}}{df}(f_z)}{(1+z)H(z)}\,, \tag{3.23}$$

where $f_z = (1+z)f$ is the frequency at emission. Note that the factor of $1/(\omega_{\rm BD}+2)$ is from the definition of Eq. (5.31). Here we adopt the ΛCMD cosmological model, with

$$H(z) = H_0[\Omega_M(1+z)^3 + \Omega_\Lambda]^{1/2}, \tag{3.24}$$

where the Hubble constant $H_0 = 70$km/s Mpc, $\Omega_M = 0.3$ and $\Omega_\Lambda = 0.7$. The redshift cutoff is chosen as $z_{\rm max} = 10$. In Eq. (3.23), $R_m(z)$ is the BNS merger rate per comoving volume at redshift z. We adopt the same merger rate as in [17], which is expressed as

$$R_m(z) = R_m(0)\frac{\int_{t_{\rm min}}^{t_{\rm max}} dt_d\; R_f[z_f(z,t_d)]p(t_d)}{\int_{t_{\rm min}}^{t_{\rm max}} dt_d\; R_f[z_f(0,t_d)]p(t_d)}\,. \tag{3.25}$$

Here, t_d denotes the time delay between formation and merger of BNS and $p(t_d)$ is its probability distribution function. We assume $p(t_d) \propto 1/t_d$ for $t_{\rm min} < t_d < t_{\rm max}$, with $t_{\rm min} = 20$ Mpc and $t_{\rm max}$ equal to the Hubble time H_0^{-1}. The BNS formation rate $R_f(z)$ is assumed to be proportional to the star formation rate (SFR): $R_f(z) \propto \dot{\rho}_*(z)$. As in [17, 20] we adopt the GRB-based SFR model given in [142], which is inferred from observed gamma-ray burst data at high redshift [93]. The local BNS merger rate is inferred from GW170817 [15] with $R_m(0) = 1540\ {\rm Gpc}^{-3}{\rm yr}^{-1}$, and $z_f(z,t_d)$ is the redshift at the binary formation time $t_f = t(z) - t_d$, with $t(z)$ the age of the Universe at merger.

In Eq. (3.23), the energy spectrum is given by Eq. (3.20) with the observed GW frequency f replaced by the frequency at emission f_z. The frequency cutoff is at the innermost stable circular orbit (ISCO) [153]: $f_{\rm max} = f_{\rm ISCO} \simeq 4400/(m_1+m_2)$ Hz, with the mass in the unit of $M_\odot$. As in [17], the neutron star masses m_1 and m_2 in the binary are assumed to follow a uniform distribution ranging from 1 to 2 $M_\odot$. We adopt the neutron star mass-radius relation from the baseline model of Steiner et al. [136]. Within our range of m, the radius is around $R \approx 12$ km.

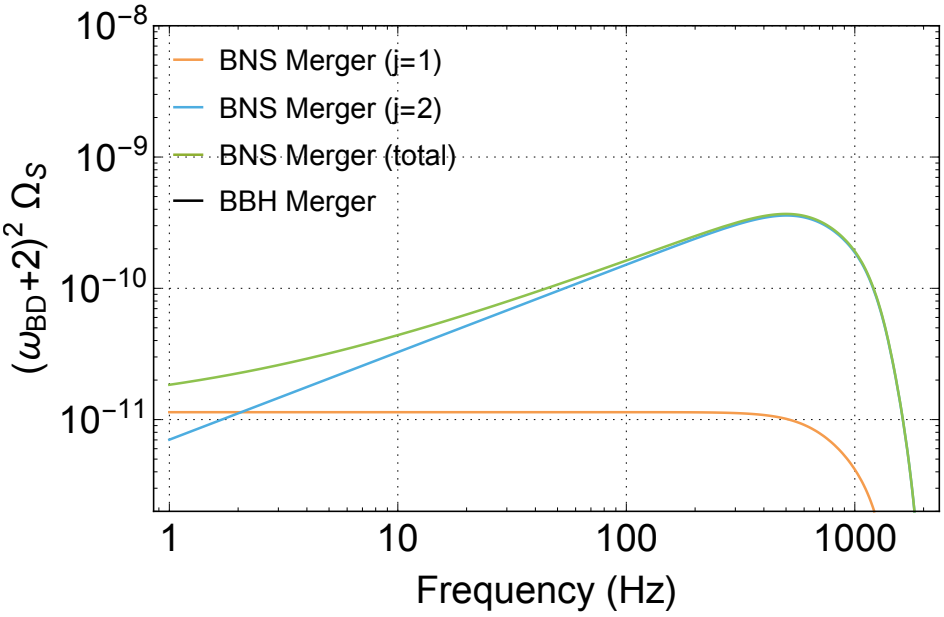

Figure 3.1: The scalar SGWB from compact binary systems. The yellow curve is the contribution from mergers of BNS with $j = 1$, at low frequencies it follows a power law of f^0. The blue curve is the contribution from mergers of BNS with $j = 2$, at low frequencies it follows a power law of $f^{2/3}$. The green curve is the total BNS scalar SGWB. The mergers of BBH has no contribution to the scalar SGWB, which is a direct consequence of Hawking's no scalar-hair theorem [87].

We show the resulting scalar SGWB in Fig 3.1. Note that the energy density spectrum Ω_S we have chosen to use scales with the BD parameter as $\Omega_S \propto (\omega_{BD} + 2)^{-2}$. For BNS mergers, we predict $(\omega_{BD}+2)^2\ \Omega_S^{j=1}(f = 25\text{Hz}) = 1.1\times10^{-11}$ with a power law of f^0 at low frequencies and $(\omega_{BD}+2)^2\ \Omega_S^{j=2}(f = 25\text{Hz}) = 6.0\times10^{-11}$ with a power law of $f^{2/3}$ at low frequencies. For $f > 10$Hz, the dipole ($j = 1$) contribution to the scalar SGWB is much less than the quadrupole ($j = 2$), which is a consequence from the small asymmetry between the two neutron stars in the binary system. Also, as discussed earlier BBH has no contribution to the scalar SGWB.

3.4 Scalar SGWB from Stellar Gravitational Core Collapse

It is well known that massive stars end their lives through gravitational core collapse. In GR, stellar core collapses only contribute a minor fraction to the total SGWB. For example, Crocker et al. [67] predict an SGWB from the black hole ringdown following the collapse with $\Omega_T(f = 25\text{Hz}) \simeq 2\times10^{-12}$, (Fig. 6 of [67], model 2 & 3). In [48] Buonanno et al. predict the background from the neutrino burst associated with the core collapse with $\Omega_T(f = 25\text{Hz}) \simeq 1\times10^{-13}$, (Fig. 1 of [48], the optimistic

model). The small contribution to the SGWB given the greater event rate of stellar collapses compared to binary mergers can be explained by the fact that in GR, the tensor GWs are emitted through secondary effects of stellar collapse: only the small asymmetry in the collapse gives rise to a non-zero quadrupole moment.

Scalar Emission from Gravitational Core Collapse

However, we expect a different picture in BD: the scalar GW emission starts from the monopole order, which indicates even the perfectly spherical collapses are able to emit scalar GW. Further, the progenitors of collapse are sources of the scalar field, with a monopole moment proportional to $m/(2\omega_{\rm BD}+4)$ [132]. As the progenitor collapses, this scalar monopole is radiated away. In this way, the scalar GW is dominated by the memory effect at low frequencies [71]: the scalar GW slumps from a nonzero initial value $h_{\rm S}^{\rm ini}$ to a zero final value if the collapse remnant is a black hole or a different nonzero final value if the remnant is a neutron star. The change in the amplitude of the scalar field is expressed as [71]:

$$\Delta h_{ij} = \begin{cases} -\dfrac{1}{\omega_{\rm BD}+2}\dfrac{G\,m}{r}\,e^{\rm S}_{ij} & \text{black hole remnant} \\ \\ -\dfrac{1}{\omega_{\rm BD}+2}\dfrac{G(m-m_{\rm NS})}{r}\,e^{\rm S}_{ij} & \text{neutron star remnant} \end{cases} . \tag{3.26}$$

Here, m and $m_{\rm NS}$ represent the mass of the progenitor and the mass of the remnant neutron star, respectively.

As discussed in [71], for ground-based GW detectors, most of the detection band is dominated over by the memory as the “zero-frequency limit". The resulting scalar energy spectrum from the memory effect is

$$\frac{dE_{\rm S}}{df} = \frac{G\,[m-m_{\rm NS}\Theta(M_{\rm BH}-m)]^2}{\omega_{\rm BD}+2}\Theta(m-M_C)\Theta(f_{\rm cut}-f), \tag{3.27}$$

where M_C is the minimum mass for the progenitor to end its life via core collapse and $M_{\rm BH}$ is the mass threshold above which the final product from collapse is a black hole instead of a neutron star. As suggested in [134], we choose $M_C = 8M_\odot$ and $M_{\rm BH} = 25M_\odot$. The NS mass is chosen as $M_{\rm NS} = 1.4M_\odot$. The cutoff frequency of the memory effect is $f_{\rm cut} \simeq 1/\tau_c$, where the collapsing time is approximated from the Oppenheimer-Snyder model [119]:

$$\tau_c \simeq Gm\frac{\pi}{\sqrt{8\beta^3(1-2\beta)}}, \tag{3.28}$$

where β is the same as in Eq. (3.22). Here we choose $\beta = 0.1$ for the progenitor as in [71, 132].

Scalar SGWB from Core Collapse

From the individual energy spectrum, the total scalar SGWB energy density spectrum can be obtained using knowledge of collapse rates throughout the age of the universe [67],

$$\Omega_{\rm S}(f) = \frac{1}{\omega_{\rm BD}+2}\frac{f}{\rho_c}\int_0^{z_{\rm max}} dz \int_{M_C}^{M_{\rm max}} dm\ \frac{\frac{dR_c}{dm}(z,m)\ \frac{dE_{\rm S}}{df}(f_z,m)}{(1+z)H(z)}\ . \tag{3.29}$$

In this equation, $M_{\rm max}$ is the upper limit of massive stars and here we choose $M_{\rm max} = 100M_\odot$ reference. The energy spectrum is from Eq. (3.27) and the other parameters are the same as in Eq. (3.23). The collapse rate density dR_c/dm (the number of collapses per unit proper time, per unit co-moving volume and per progenitor mass) is related to the Star Formation Rate (SFR) and initial mass function ξ via [77, 152]

$$\frac{dR_c}{dm}(z,m) = \frac{\dot\rho_*(z)\xi(m)}{\int_{M_{\rm min}}^{M_{\rm max}} d\mu\ \mu\ \xi(\mu)}. \tag{3.30}$$

Here we use the same SFR as in Section III, and choose the Salpeter IMF: $\xi(m) \propto m^{-2.35}$, with $M_{\rm min} = 0.1M_\odot$ and $M_{\rm max} = 100M_\odot$ [142]. The total merger $R_c(z)$ rate between M_C and $M_{\rm max}$ together with the BNS merger rate $R_m(z)$ are shown in Fig 5.1.

In Fig. 5.3, we show the resulting scalar SGWB from core collapse. Same as the BNS scalar SGWB, the predicted energy density spectrum scales with the BD parameter as $\Omega_{\rm S} \propto (\omega_{\rm BD}+2)^{-2}$. At the reference frequency, $(\omega_{\rm BD}+2)^2\ \Omega_{\rm S}(f = 25{\rm Hz}) = 2.8\times10^{-6}$. At frequencies below $\sim 40\,$Hz, Ω_S follows a power law of f^α, with $\alpha = 1$. Note that the core collapse scalar SGWB is around four orders of magnitude greater than BNS mergers. This difference can be accounted for by considering two factors. First, the collapse rate is much larger than the merger rate: at their peak values $R_c \simeq 10^6\ {\rm Gpc}^-3{\rm yr}^{-1}$ and $R_m \simeq 5\times10^3\ {\rm Gpc}^-3{\rm yr}^{-1}$. Second, the energy emitted from scalar GW radiation for a single collapse event is much larger than a merger event: notice that $E_{\rm S} \propto m^2$, for mergers $m \sim 1M_\odot$ and for collapses $m \sim 10M_\odot$.

In Table 3.1 we summarize the energy densities of SGWB with scalar polarization from varied sources, compared with the tensor SGWB.

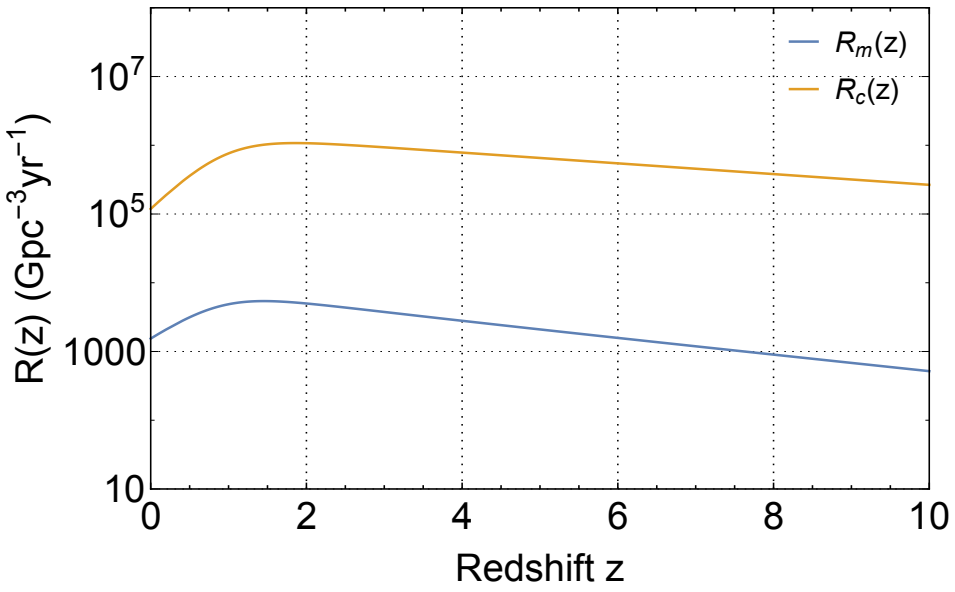

Figure 3.2: Comparison between the BNS merger rate $R_m(z)$ and the core collapse rate $R_c(z)$.

	$\Omega_T(f = 25\,\mathrm{Hz})$	$(\omega_{\mathrm{BD}} + 2)^2\Omega_S(f = 25\,\mathrm{Hz})$
BBH	1.1×10^{-9} [20]	0
BNS	0.7×10^{-9} [17]	7.1×10^{-11}
Collapse	2×10^{-12} [67]	2.8×10^{-6}

Table 3.1: Energy density of tensor and scalar SGWB at 25 Hz, from various origins.

Model dependence of the Core Collapse Scalar SGWB

In this section we want to explore the influence to the core collapse scalar SGWB from alternative models. From now on we refer the model described in Section IV as the *Baseline* model. More specifically, we consider four alternative models that follow.

(i) The *TimeDelay* model. In this model we take into account the time delay between the formation of a massive star and its core collapse. In this case, the collapse rate is modified as

$$\frac{dR_c}{dm}(z, m) = \frac{\int_{t_{\min}}^{t_{\max}} dt_d\ \dot{\rho}_*[z_f(z, t_d)]\xi(m)p(t_d)}{\int_{M_{\min}}^{M_{\max}} d\mu\ \mu\ \xi(\mu)}. \tag{3.31}$$

With the other parameters the same as in Eq. (3.30), we assume the distribution as $p(t_d) = \delta(t_d - T(m))$, with $T(m)$ the lifetime of a star with mass m. In addition, we use the relation $T(m) = T_\odot(m/M_\odot)^{-2.5}$ for main sequence stars, with $M_\odot$ representing the solar mass and $T_\odot = 10^4$ Myr.

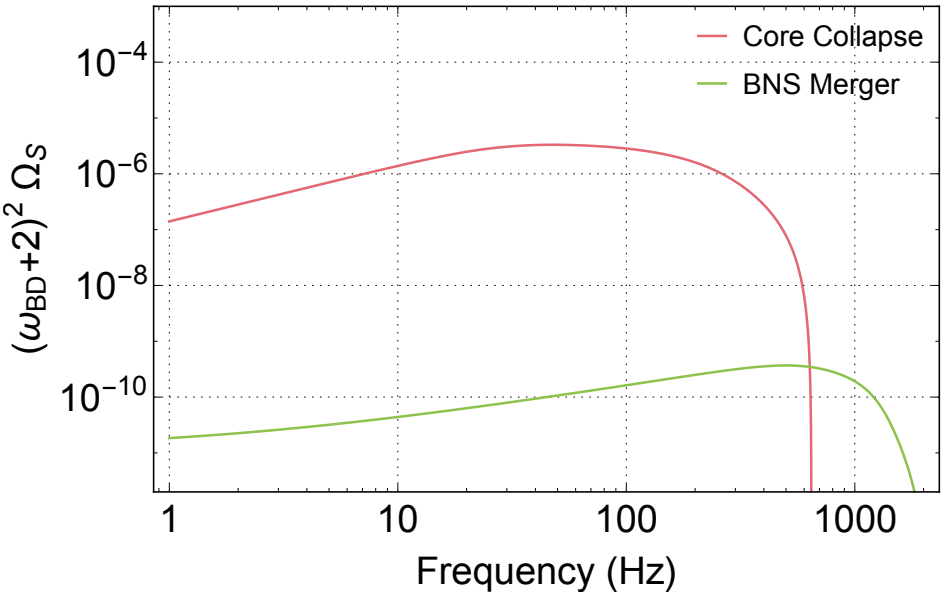

Figure 3.3: Red curve: The scalar SGWB from core collapse. The model parameters are given in Section IV. Green curve: The scalar SGWB from BNS merger, which is a sum of $j = 1$ and $j = 2$ radiation. The model parameters are given in Section III.

(ii) The *AltSFR* model. In the *baseline* model we adopt an SFR model which is based on the GRB rate. In the *AltSFR* model we consider an alternative SFR model [142], which based on the luminosity of star-forming galaxies [36]. This model is more conservative than the GRB-based SFR at high redshifts. We compare the two SFR models in Fig. 5.4.

(iii) The *BHonly* model. In this model we only consider the scalar SGWB from core collapses into BHs. In this case the scalar energy spectrum is given by

$$\frac{dE_S}{df} = \frac{G\,m^2}{\omega_{BD}+2}\Theta(m - M_{BH})\Theta(f_{cut} - f), \tag{3.32}$$

where the BH mass threshold M_{BH} and the cutoff frequency f_{cut} are the same as in the *Baseline* model.

(iv) The *HighMass* model. To reflect the recent observations of massive stars with $M \sim 200-300M_\odot$ [68], we replace the mass upper limit M_{max} to $200M_\odot$, with other parameters remaining the same.

We show the scalar SGWB from the alternative models in Fig. 3.5. We can see that *TimeDelay* and *AltSFR* have negligible influence on the background inside the detection band of ground-based detectors. The *BHonly* and *HighMass* alter the

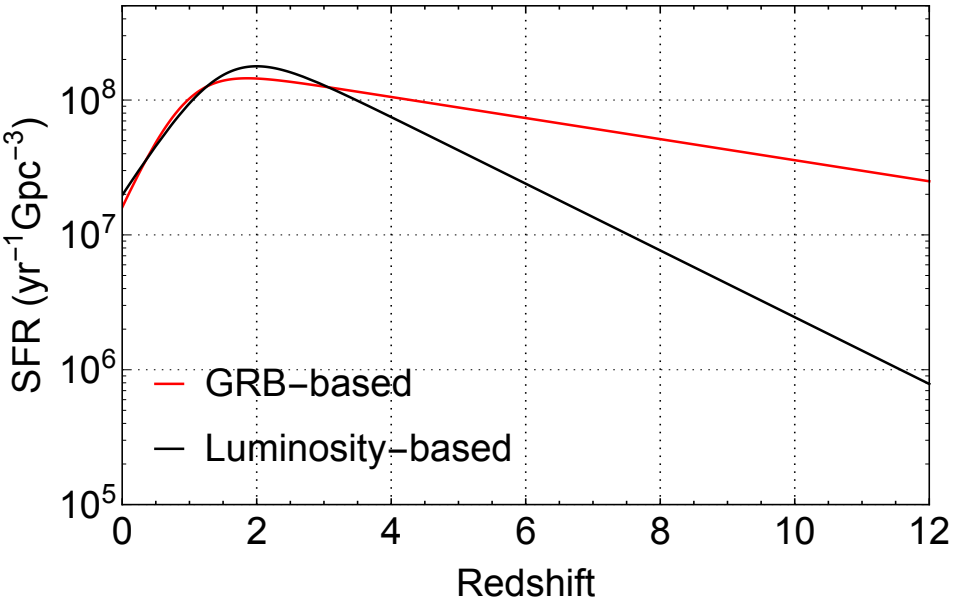

Figure 3.4: Comparison between the GRB-based SFR and the Luminosity-based SFR.

background in low and high frequencies respectively. At the reference frequency $f = 25$ Hz, *HighMass* predicts a value of Ω_S that is 1.1 times the *Baseline* value, while *BHonly* predicts 0.7 the baseline value. At this frequency, the impact from *TimeDelay* and *AltSFR* to the scalar SGWB spectra is less than 1%. At frequencies below ~ 10 Hz, the *HighMass* model predicts somewhat higher Ω_S, due to contributions from collapses of higher-mass objects. At frequency $f > 100$ Hz, the only non-negligible change to the spectrum is from the *BHonly* model. This is because the stars which collapse into NSs have lower mass compared to those collapse into BHs. The cut-off frequency in Eq. 3.32 is related to the collapsing time in Eq. 3.28 which is shorter for collapsing stars with lower mass. As a result, the high frequency part of the spectrum is depressed from the missing low mass progenitors.

3.5 Detectability

Since the dominant contribution to the scalar SGWB in BD theory is from the core collapses, in this section we will focus on the scalar background predicted by the baseline core collapse model as described in Section IV.

A resent analysis [21] based on Advanced LIGO's first observing run (O1) has put the first upper limit on the scalar SGWB, with $\Omega_S(f = 25\text{Hz}) < 1.1 \times 10^{-7}$. Compared with our prediction $(\omega_{BD} + 2)^2\ \Omega_S(f = 25\text{Hz}) = 2.8 \times 10^{-6}$, it is straightforward to obtain $\omega_{BD} > 3$. Much better upper limits are expected since the O1 data only

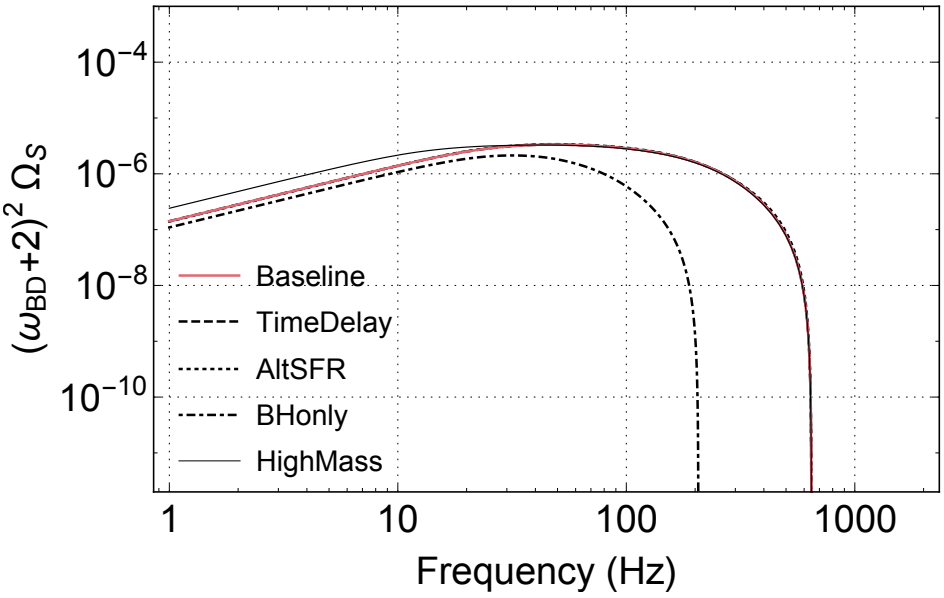

Figure 3.5: The scalar overlap reduction function γ_S for LIGO/Voyager and Einstein Telescope.

includes an observation time of four months and the detectors are running below the designed sensitivity.

Next we want to explore the detectability from Advanced LIGO at its designed sensitivity and the planed future ground based GW detectors. The optimal signal-to-noise ratio (SNR) for the scalar SGWB between a pair of detectors is given by [51, 113]

$$\mathrm{SNR} = \frac{3H_0^2}{10\pi^2}\sqrt{2T}\left(\int_0^\infty df\ \frac{\gamma_S(f)^2\Omega_S(f)^2}{f^6 P_1(f)P_2(f)}\right)^{1/2}, \tag{3.33}$$

where $P_{1,2}(f)$ are the detectors' noise spectral density and $\gamma_S(f)$ is the scalar overlap reduction function between the detectors [100]. Here we recall that it was the choice we had made in Eq. (5.31) for Ω_S that would lead to this expression for the SNR, which is similar to that for a tensor gravitational wave background.

Here we consider the design sensitivity of Advanced LIGO [27] and the planed sensitivities of LIGO Voyager [2] and Einstein Telescope (ET) [129]. The scalar overlap reduction function between the detectors at Hanford and Livingston is calculated in [51, 113], here we adopt the normalization convention as [51]. Voyager has the same overlap reduction function as LIGO. The co-located ET detectors have a constant $\gamma_S = -1/16$ for $f < 1000$Hz (see Appendix for more details). These overlap reduction functions are shown in Fig. 3.6. Note that our γ_S for LIGO is

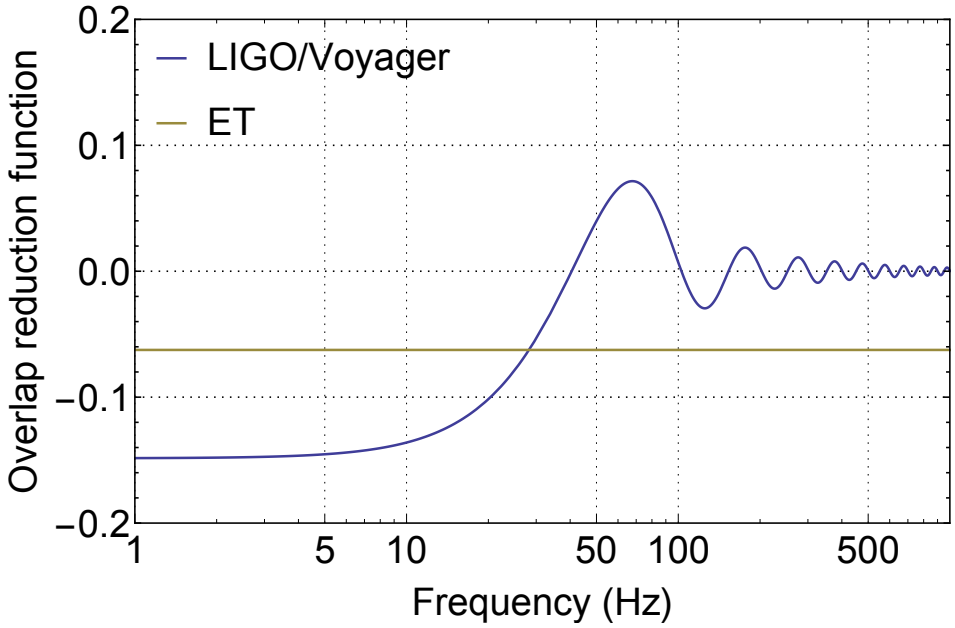

Figure 3.6: The scalar overlap reduction function γ_S for LIGO/Voyager and Einstein Telescope.

one half of [51], which is due to the fact that, as explained in Section II, only the breathing (traverse) and no longitudinal part of the scalar polarization exist in BD theory.

We show the maximal detectable $\omega_{\rm BD}$ for LIGO, Voyager and ET to reach an SNR threshold of 3 in Table 3.2 with observation times of 1 year and 5 years — and in Fig. 3.7 for a range of observation times. With 5-year integration, to reach SNR > 3 at ET, the BD parameter should be no less than 264. On the other hand, the current cosmological constraints on BD set $\omega_{\rm BD} > 692$ [33] and the solar system data from the Cassini mission put a stronger constraint that $\omega_{\rm BD} > 40000$ [42, 146].

T	LIGO	Voyager	ET
1 yr	10.8	54.1	175.8
5 yrs	17.1	81.8	263.8

Table 3.2: Maximal detectable BD parameter $\omega_{\rm BD}$ to reach an SNR threshold of 3 from the scalar SGWB with observation times of 1 year and 5 years.

3.6 Conclusions and Discussions

In this paper, we studied the scalar SGWB in BD theory, from astrophysical sources, in particular compact binary mergers and stellar collapses. Unlike the tensor SGWB

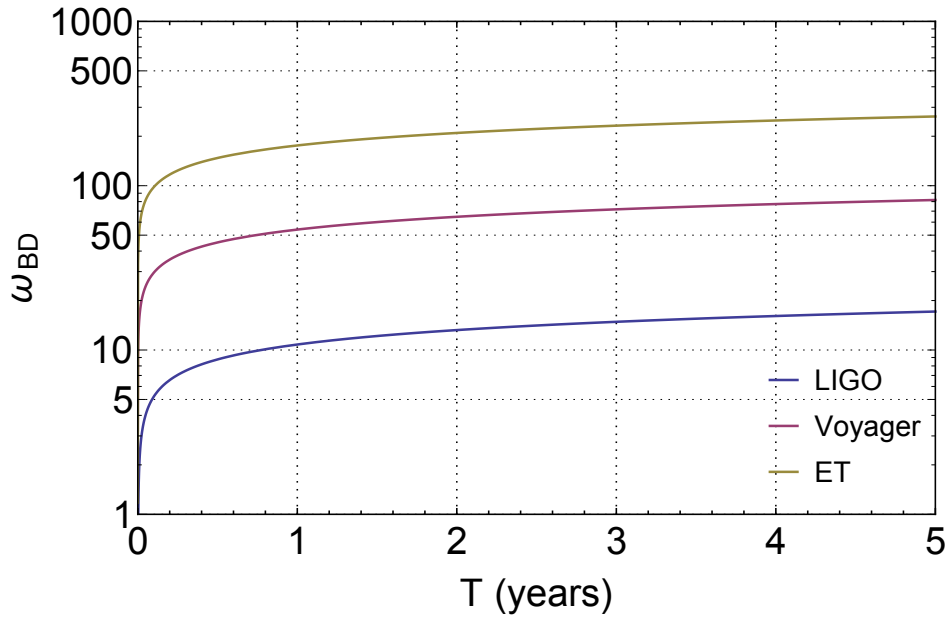

Figure 3.7: Maximal detectable BD parameter $\omega_{\rm BD}$ to reach an SNR threshold of 3 from the scalar SGWB as a function of observation of time.

in GR, we found that the scalar SGWB in the BD theory is dominated by stellar collapses, by roughly 4 orders of magnitude, over compact binary mergers. We have attributed this dominance to the higher rate of gravitational collapses than binary mergers, as well as the fact that scalar radiation does not require asymmetry.

Further more, scalar radiation from stellar collapses, in the LIGO band, is mainly dominated by the memory wave — as pointed out in an earlier paper [71]. Since the memory wave has a simple frequency dependence of $h(f) \sim 1/f$, this has lead to a $\Omega_S(f) \propto f$, which differs from the tenor SGWB, which as $\Omega_{\rm T} \propto f^{2/3}$.

For the dominant stellar-collapse scalar SGWB, we have studied a range of models, which had lead to consistent predictions, with the most significant uncertainty lying at low frequencies: up to within 30% at $f = 25$ Hz, mainly due to possible existence of heavier stars and the exclusion of the collapses whose remnant are NSs.

Upon obtaining the SGWB, we have estimated the detectability for current and future detector networks. It is estimated that 3rd-generation ground-based detectors can pose upper limit for $\omega_{\rm BD}$ around ~ 300.

The potential bound for $\omega_{\rm BD}$ from our calculation is low compare with solar-system bounds, and somewhat lower than cosmological bounds, this nevertheless provides an *independent* test. More importantly, having established that the scalar SGWB

mainly arise from stellar collapses, we can further investigate other models that lead to scalar radiations, e.g., scalar-tensor theories in which $\omega(\phi)$ depends on the value of ϕ instead of being a constant. As we had shown in Ref. [71], in such models the scalar memory, which dominates scalar radiation during collapse, can be significantly enhanced by such dependencies through *scalariation* [69], therefore might lead to much stronger SGWB enhanced by several orders of magnitude [85, 117]. In this case, we expect a considerable increase in the detectability from the current and the next generation of detectors. We leave these for further studies.

3.7 Acknowledgements

We thank Xi-Long Fan, Xiang-Cheng Ma and Atsushi Nishizawa for valuable discussions. We acknowledge support from the Brinson Foundation and the Simons Foundation. Our research has also been supported by the National Science Foundation, through grants PHY-1404569, PHY-1708212 and PHY-1708213.

3.8 Appendix A: Scalar Overlap Reduction Function For Einstein Telescope

In this appendix we calculate the scalar overlap reduction function $\gamma_S(f)$ for Einstein Telescope (ET). The configuration of ET is shown in Fig. 3.8. The coordinate system for the detectors are

$$\begin{cases} \hat{x} = (1, 0, 0) \\ \hat{y} = (0, 1, 0) \\ \hat{z} = (0, 0, 1) \end{cases} \tag{3.34}$$

In this coordinate system, the unit vectors for the ET detector arms are

$$\begin{aligned} &\hat{l}_{11} = \hat{x}, \qquad \hat{l}_{12} = \frac{1}{2}\hat{x} + \frac{\sqrt{3}}{2}\hat{y}, \\ &\hat{l}_{21} = -\frac{1}{2}\hat{x} + \frac{\sqrt{3}}{2}\hat{y}, \qquad \hat{l}_{22} = -\hat{l}_{11}, \\ &\hat{l}_{31} = -\hat{l}_{12}, \qquad \hat{l}_{32} = -\hat{l}_{21}, \end{aligned} \tag{3.35}$$

The detector tensors for ET are express by

$$D_a^{ij} = \frac{1}{2}(\hat{l}_{a1}^i \hat{l}_{a1}^j - \hat{l}_{a2}^i \hat{l}_{a2}^j), \tag{3.36}$$

where $a = 1, 2, 3$.

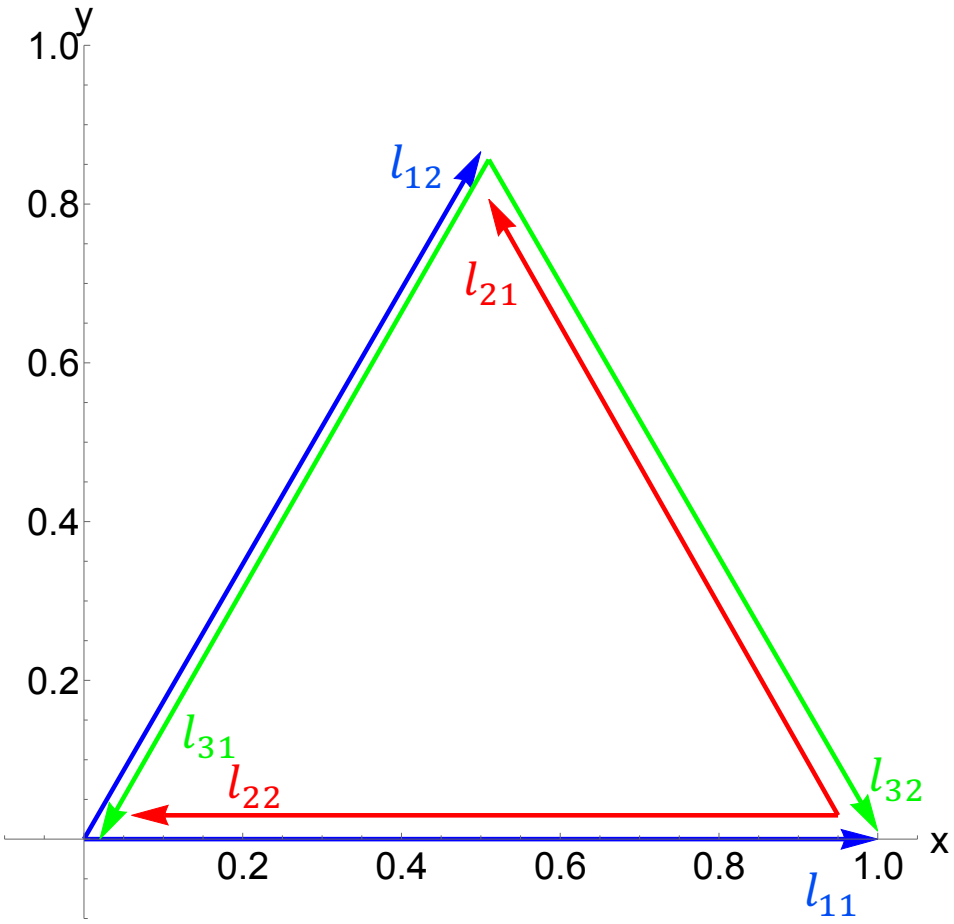

Figure 3.8: Configuration of Einstein Telescope.

Suppose the GW is propagating along the angle (θ, ϕ), the GW coordinate system can be constructed as

$$\begin{cases} \hat{m} = \cos\theta\cos\phi\ \hat{x} + \cos\theta\sin\phi\ \hat{y} - \sin\theta\ \hat{z} \\ \hat{n} = -\sin\phi\ \hat{x} + \cos\phi\ \hat{y} \\ \hat{\Omega} = \sin\theta\cos\phi\ \hat{x} + \sin\theta\sin\phi\ \hat{y} + \cos\theta\ \hat{z} \end{cases} \tag{3.37}$$

Then the angular pattern functions for scalar polarization are [28, 113]

$$F_a^{\mathrm{S}}(\hat{\Omega}) = \sum_{ij} D_a^{ij} e_{\mathrm{S}}^{ij}, \tag{3.38}$$

where the scalar polarization tensor e_{S}^{ij} are given in Eq. (3.10). It is straightforward

to find that

$$F_1^{\rm S}(\hat{\Omega}) = \frac{1}{8}\sin^2\theta(-3\cos 2\phi + \sqrt{3}\sin 2\phi)$$
$$F_2^{\rm S}(\hat{\Omega}) = \frac{1}{8}\sin^2\theta(3\cos 2\phi + \sqrt{3}\sin 2\phi)$$
$$F_3^{\rm S}(\hat{\Omega}) = -\frac{\sqrt{3}}{4}\sin^2\theta\sin 2\phi \tag{3.39}$$

The scalar overlap reduction function is defined as [51, 113]

$$\gamma_{ab}^{\rm S}(f) = \frac{5}{8\pi}\int d\hat{\Omega}\, e^{2\pi i f\hat{\Omega}\cdot\Delta x} F_a^{\rm S}(\hat{\Omega})F_b^{\rm S}(\hat{\Omega}). \tag{3.40}$$

Here we use the same normalization as [51]. For ET, the separation $|\Delta x|$ is equal to the arm length $d = 10$ km. Hence, for $f < 10^3$ Hz, the exponential function $e^{2\pi i f\hat{\Omega}\cdot\Delta x} \simeq 1$. In this case,

$$\gamma_{12}^{\rm S} = \frac{5}{8\pi}\int_0^{\pi} d\theta \int_0^{2\pi} d\phi \left[-\frac{3}{64}(1+2\cos 4\phi)\sin^5\theta\right] = -\frac{1}{16}. \tag{3.41}$$

Similarly, we can show $\gamma_{23}^{\rm S} = \gamma_{31}^{\rm S} = -1/16$ for $f < 10^3$ Hz.

Chapter 4

A GREEN'S FUNCTION APPROACH TO GRAVITATIONAL WAVE ECHOES

Gravitational wave astronomy provides an unprecedented opportunity to test the nature of black holes and search for exotic, compact alternatives. Recent studies have shown that exotic compact objects (ECOs) can ring down in a manner similar to black holes, but can also produce a sequence of distinct pulses resembling the initial ringdown. These "echoes" would provide definite evidence for the existence of ECOs. In this work we study the generation of these echoes in a generic, parametrized model for the ECO, using Green's functions. We show how to reprocess radiation in the near-horizon region of a Schwarzschild black hole into the asymptotic radiation from the corresponding source in an ECO spacetime. Our methods allow us to understand the connection between distinct echoes and ringing at the resonant frequencies of the compact object. We find that the quasinormal mode ringing in the black hole spacetime plays a central role in determining the shape of the first few echoes. We use this observation to develop a simple template for echo waveforms. This template preforms well over a variety of ECO parameters, and with improvements may prove useful in the analysis of gravitational waves.

4.1 Introduction

The existence of event horizons is one of the most astonishing predictions of General Relativity. Horizons generically [137] form during the gravitational collapse of classical matter and are expected to be common occurrences in our universe. Observations of black holes are undergoing a revolution, with the advent of gravitational wave astronomy [3–5, 7] and the promise of very-long-baseline radio observations of supermassive black holes by the Event Horizon Telescope [76, 92]. While black holes are consistent with all electromagnetic and gravitational wave observations to date [5–7, 148, 150], no experiment has been able probe spacetime near the event horizon [26, 53, 75]. Moreover, the event horizon is at the heart of the BH information paradox [141], and the role of black holes in a quantum theory of gravity is an open question.

These puzzles have inspired proposals for horizonless alternatives to black holes including gravastars [107], boson stars [130], wormholes [111], fuzzballs [105] and

others [34, 35, 90]. Many of these exotic compact objects (ECOs) can be ruled out on theoretical grounds. ECOs with angular momentum often suffer from a superradiant instability, although this instability can quenched by tuning the compactness and other parameters describing the ECO [89, 99]. Cardoso et al. [55] have conjectured that any ECO with an unstable photon orbit may suffer from nonlinear instabilities.

While the gravitational wave astronomy has the potential to probe black holes (BHs) like never before [148], distinguishing BHs from highly compact ECOs will be difficult. The problem is that astrophysical processes are usually insensitive to the spacetime geometry near the horizon, and highly compact ECOs behave very similarly to BHs [26]. Attempts to distinguish merging BHs from merging ECOs using inspiral waveforms are plagued by the strong equivalence principal, which means that the properties of extended self-gravitating bodies only appear in the equations of motion at high post-Newtonian order. Nonetheless, several promising studies [59, 102] predict tidal distortion and tidal heating effects will allow LISA [30] to distinguish merging black holes from highly compact, merging ECOs (see also e.g. [95, 122] for tests incorporating inspirals).

Spacetime near the event horizon has an especially interesting effect on the ringdown waveform of the merging objects. Standard tests of the nature of the final merged object call for the black hole's resonant frequencies [37, 114], known as quasinormal mode (QNM) frequencies, to be extracted from the ringdown portion of the waveform and compared to theoretical calculations [38, 41, 70, 120, 149]. Working in the test particle limit, Cardoso et al. [57] pointed out that in the case of highly compact wormholes, the ringdown of the final ECO is initially nearly identical to that of a BH despite the fact that QNM spectrum is radically changed [63, 115, 121]. A naive application of the QNM based tests would be fooled by a highly compact ECO.

However, Cardoso et al. [57] also realized that the later portion of the ringdown of highly compact ECOs contains a train of decaying echo pulses. The time delay between the echoes is related to the ECO compactness while the decay and shape of each pulse encodes the reflective properties of the ECO.

Further work established that this picture was robust across many different ECO models with many different test particle sources, but breaks down for less compact ECOs, which sometimes have ringdowns consistent with the resonant frequencies of the ECO [58, 126]. Price and Khanna conjectured that the echoes can be considered as a superposition of the resonant modes of the ECO [126]. Volkel and Kokkaotas

[143] then provided a method for inferring the exact details of the ECO model from the ECO modes. Namely, they demonstrated that the effective scattering potential experienced by the gravitational waves could be approximately reconstructed with a knowledge of ECO spectrum.

Recently, it has been proposed that LIGO has observed echoes in the binary black hole waveforms [23, 25]. While there has been much skepticism in the community [32], such tests will only become more definitive as LIGO accumulates binary merger observations.

Most of the past studies have been in the context of a particular ECO model, using specific orbits for the merging objects. The goal of this work is explicitly relate waveforms from black holes to waveforms from ECOs. We study evolution of test scalar fields as a proxy for gravitational perturbations, which allows us to replace a generic ECO with simple reflecting boundary conditions in a BH spacetime. We use this formalism to show that the ECO waveform can be understood either as a superposition of echo pulses or as a superposition of ECO modes and illustrate the types of behavior that can arise. We investigate which features of the BH waveforms shape the first few echoes, leading to a simple template for the ECO waveform.

In Sec. 4.2 we review the basic equations obeyed by the scalar field. We parameterize (completely) the influence of the ECO on scalar waves in the exterior vacuum region by a complex frequency-dependent reflectivity (a slight generalization of the models used in [89, 99, 112]). In Sec. 4.2 we relate the ECO and BH waveform by determining the relationship between the ECO and BH Green's function. We find that the ECO waveform can be constructed from the BH waveform and a reprocessed version of the waveform observed on the BH horizon. In Sec. 4.3 we show how the extra piece of the ECO waveform can be expressed as sum of echoes. In Sec. 4.4 we discuss the relationship between the ECO QNMs and the BH QNMs and study the ECO mode spectrum numerically for two particular ECO models. In Sec. 4.4 and Sec. 4.4, we show how the difference between the ECO waveform and the BH waveform can be expressed as a superposition of ECO modes. In Sec. 4.5 we determine general properties of the individual echoes and develop a simple template for the ECO waveform. We also study the energy in the ECO waveform, discovering a simple relationship to the energy in the black hole waveforms reaching infinity and passing through the horizon.

During the final stages of this work, we learned of the work of Nakano et al. [112], who discussed gravitational perturbations in the Kerr spacetime and arrived at a

similar expression for ECO waveforms by different means.

4.2 Waves near a compact object

Wave Equation and Boundary Conditions

We focus on static, spherically symmetric exotic compact objects. In this setting, an ECO consists of an exterior Schwarzschild spacetime patched to a spherically symmetric interior metric at an areal radius $r = r_0$.

We study a massless scalar field $\Phi(x^\mu)$ that obeys the sourced, curved spacetime wave equation,

$$\Box\Phi = -\rho\,. \tag{4.1}$$

If we define the scalar $\psi(x^\mu) = r\Phi$ and decompose this scalar into frequency and spherical harmonics [60],

$$\psi(x^\mu) = \int_{-\infty}^{\infty} \frac{d\omega}{2\pi} \sum_{\ell,m} \tilde{\psi}_{\ell m}(\omega, r) Y_{\ell m}(\theta, \phi) e^{-i\omega t}\,, \tag{4.2}$$

$$\rho(x^\mu) = \int_{-\infty}^{\infty} \frac{d\omega}{2\pi} \sum_{\ell,m} \tilde{\rho}_{\ell m}(\omega, r) Y_{\ell m}(\theta, \phi) e^{-i\omega t}\,, \tag{4.3}$$

then the wavefunctions $\tilde{\psi}_{\ell m}$ obey the following radial equation,

$$\frac{d^2\tilde{\psi}_{\ell m}}{dx^2} + \left(\omega^2 - fV\right)\tilde{\psi}_{\ell m} = \tilde{S}\,, \tag{4.4}$$

$$\tilde{S}(\omega, x) \equiv -r(x) f \rho_{\ell m}(\omega, x)\,. \tag{4.5}$$

Here x is the usual tortoise coordinate, defined through

$$\frac{dx}{dr} = \frac{1}{f(r)}\,, \tag{4.6}$$

while the metric component $f(r)$ and the potential $V(r)$ depend on the particular spacetime. In the exterior, Schwarzschild portion of the spacetime,

$$f = 1 - \frac{2M}{r}\,, \qquad\qquad V = \frac{\ell(\ell+1)}{r^2} + \frac{2M}{r^3}\,, \tag{4.7}$$

and we treat f and V as implicit functions of x through $r(x)$, with

$$x = r + 2M \ln\left(\frac{r - 2M}{M}\right)\,. \tag{4.8}$$

From here we suppress the harmonic indices (ℓ, m).

The scalar field $\tilde{\psi}$ obeys an outgoing wave boundary condition $\tilde{\psi} \sim e^{i\omega x}$ as $x \to \infty$. In addition, it obeys a boundary condition inside the ECO, such as regularity at $r = 0$. For wormholes, one would instead insist that the waves were outgoing at null infinity on the other side of the throat.

When the ECO is very compact, $r_0/(2M) - 1 \ll 1$, and all sources are restricted to reside in the Schwarzschild portion of the spacetime, we may replace the second boundary condition with a reflecting boundary condition at the ECO surface r_0. Namely, near the ECO the potential is small, $V \approx 0$, and $\tilde{\psi}$ is a linear combination of ingoing and outgoing waves $e^{\pm i\omega x}$. Therefore near the ECO surface $x_0 = x(r_0)$, we must have

$$\tilde{\psi} \propto e^{-i\omega(x-x_0)} + \tilde{\mathcal{R}}(\omega) e^{i\omega(x-x_0)} \,. \tag{4.9}$$

for some frequency dependent reflectivity $\tilde{\mathcal{R}}(\omega)$.

With this insight, we can study wave emission and propagation in the ECO spacetime using a Schwarzschild BH equipped with a reflecting boundary, as shown in Fig. 4.1. This perspective is useful since it allows us to reprocess the emission by test particles in a BH spacetime into the corresponding emission in the ECO spacetime, by taking the reflecting boundary into account. From here on we can focus on BH spacetimes, and compare wave propagation with the usual boundary conditions at the horizon to the case of a reflecting boundary.

Generating ECO waveforms from BH waveforms

We are interested in computing the scalar waves seen by distant observers in a BH spacetime with a reflecting boundary. For this we wish to construct the scalar radial Green's function $\tilde{g}_{\rm ref}(x, x')$, which obeys the scalar wave equation with a delta function source,

$$\frac{d^2\tilde{g}_{\rm ref}}{dx^2} + \left(\omega^2 - fV\right)\tilde{g}_{\rm ref} = \delta(x - x') \,, \tag{4.10}$$

and the reflecting boundary condition (4.9). With the Green's function, we can compute the field produced by sources $\tilde{S}$ through integration,

$$\tilde{\psi}(x) = \int_{-\infty}^{\infty} dx' \, \tilde{g}_{\rm ref}(x, x')\tilde{S}(x') \,. \tag{4.11}$$

We compute $\tilde{g}_{\rm ref}$ for sources outside the reflecting boundary, $x' > x_0$.

To compute $\tilde{g}_{\rm ref}$ we first recall how the scattering of waves works in the usual Schwarzschild spacetime [78]. Consider the two linearly independent, homogeneous

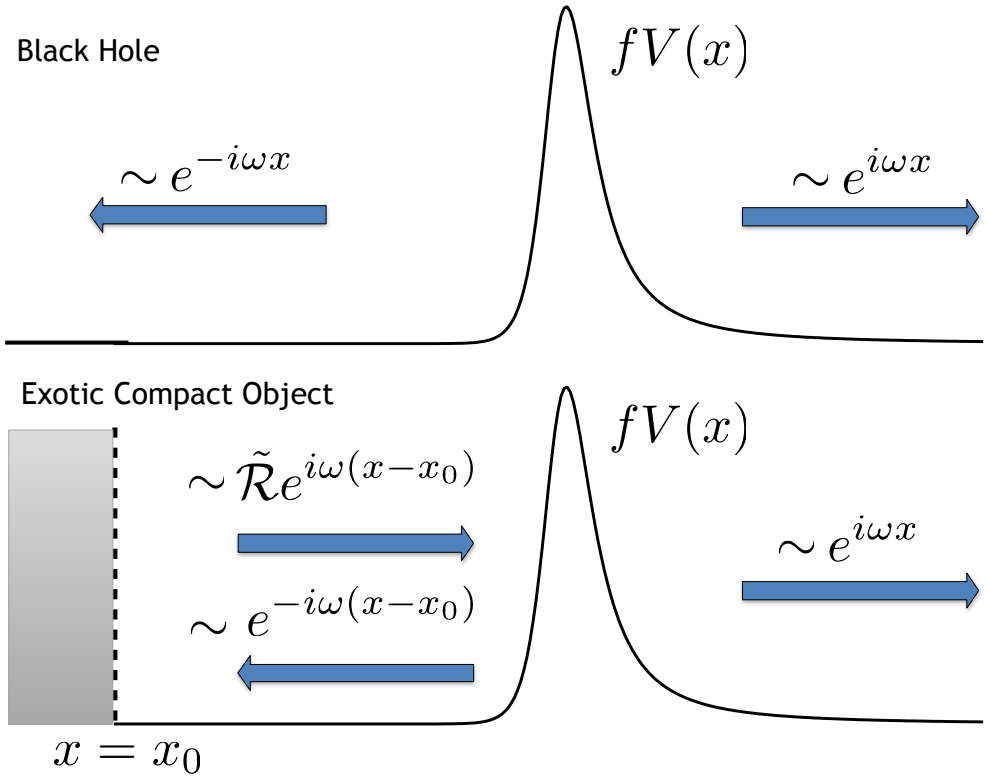

Figure 4.1: Top: The boundary conditions for waves propagating on a black hole spacetime. Bottom: The reflecting boundary conditions for the waves in the exterior of an ECO.

solutions $\tilde{\psi}_{\rm in}$,

$$\tilde{\psi}_{\rm in} \sim \begin{cases} A_{\rm out}(\omega)e^{i\omega x} + A_{\rm in}(\omega)e^{-i\omega x}, & x \to \infty, \\ e^{-i\omega x}, & x \to -\infty, \end{cases} \tag{4.12}$$

which is purely outgoing at the horizon, and ψ,

$$\psi \sim \begin{cases} e^{i\omega x}, & x \to \infty, \\ B_{\rm out}(\omega)e^{i\omega x} + B_{\rm in}(\omega)e^{-i\omega x}, & x \to -\infty, \end{cases} \tag{4.13}$$

which is purely outgoing at infinity.

The effective potential V provides a scattering barrier for waves in the BH spacetime. For waves incident from infinity, inspection of $\tilde{\psi}_{\rm in}$ shows that the reflection amplitude is $A_{\rm out}/A_{\rm in}$ and the transmission amplitude is $1/A_{\rm in}$. For our purpose, it is more convenient to consider the problem of reflection and transmission of waves incident on V from the left. By inspecting ψ we find that the reflection and transmission amplitudes for waves from the left are

$$\tilde{\mathcal{R}}_{\rm BH}(\omega) = \frac{B_{\rm in}}{B_{\rm out}}, \qquad \tilde{\mathcal{T}}_{\rm BH}(\omega) = \frac{1}{B_{\rm out}}. \tag{4.14}$$

The relationship between these and the usual reflection and transmission amplitudes can be derived by noting that $B_{\rm out} = A_{\rm in}$ and $B_{\rm in} = -A^*_{\rm out}$ [78] .

The Green's function for Schwarzschild, $g_{\rm BH}(x, x')$, also obeys Eq. (4.10), but with an ingoing boundary condition at the horizon and an outgoing boundary condition at infinity. In terms of the homogeneous solutions, it is

$$\tilde{g}_{\rm BH} = \frac{\tilde{\psi}_{\rm in}(x_<)\psi(x_>)}{W_{\rm BH}}\,, \tag{4.15}$$

where we have defined $x_> = \max(x, x')$, $x_< = \min(x, x')$, and the Wronskian $W_{\rm BH} = 2i\omega B_{\rm out}$ of $\tilde{\psi}_{\rm in}$ and ψ.

Since $\tilde{g}_{\rm BH}$ and $\tilde{g}_{\rm ref}$ both obey Eq. (4.10), we can construct $\tilde{g}_{\rm ref}$ by adding a homogenous solution of the scalar equation, times a free function of x', to $\tilde{g}_{\rm BH}$. The homogenous solution must have the correct boundary condition as $x \to \infty$, and so we use $\psi(x)$. Meanwhile, the free function in x' is fixed by ensuring that $\tilde{g}_{\rm ref}$ obeys the correct reflecting boundary condition,

$$\tilde{g}_{\rm ref}(x, x') \propto e^{-i\omega(x-x_0)} + \tilde{\mathcal{R}}(\omega)e^{i\omega(x-x_0)}\,. \tag{4.16}$$

This gives

$$\tilde{g}_{\rm ref}(x, x') = \tilde{g}_{\rm BH}(x, x') + \tilde{\mathcal{K}}\,\frac{\psi(x)\psi(x')}{W_{\rm BH}}\,, \tag{4.17}$$

$$\tilde{\mathcal{K}}(\omega) \equiv \frac{\tilde{\mathcal{T}}_{\rm BH}\tilde{\mathcal{R}}e^{-2i\omega x_0}}{1 - \tilde{\mathcal{R}}_{\rm BH}\tilde{\mathcal{R}}e^{-2i\omega x_0}}\,. \tag{4.18}$$

This is our first key result. It shows that wave propagation in the presence of the reflecting barrier is the same as in a BH spacetime, with an additional component controlled by the transfer function $\tilde{\mathcal{K}}$, which contains all the dependence on the reflectivity $\tilde{\mathcal{R}}$.

With the Green's function in hand, we can compute the waves seen by distant observers. Again it is useful to first consider a BH spacetime with the usual boundary conditions. We define the amplitudes of waves seen by distant observers $Z^{\infty}_{\rm BH}$ and of waves at the horizon $Z^{\rm H}_{\rm BH}$ through

$$\tilde{\psi}_{\rm BH}(x) \sim \begin{cases} Z^{\infty}_{\rm BH}(\omega)e^{i\omega x}\,, & x \to \infty\,, \\ Z^{\rm H}_{\rm BH}(\omega)e^{-i\omega x}\,, & x \to -\infty\,. \end{cases} \tag{4.19}$$

In terms of a given source $\tilde{S}$ with support outside x_0, Eqs. (4.11), (4.13) and (4.15) imply

$$Z^{\infty}_{\rm BH} = \int_{-\infty}^{\infty} dx' \frac{\tilde{\psi}_{\rm in}(x')\tilde{S}(x')}{W_{\rm BH}}, \tag{4.20}$$

$$Z^{\rm H}_{\rm BH} = \int_{-\infty}^{\infty} dx' \frac{\psi(x')\tilde{S}(x')}{W_{\rm BH}}. \tag{4.21}$$

With our definitions, $Z^{\infty}_{\rm BH}$ is simply related to the waveform measured by asymptotic observers in terms of the retarded time $u = t - x$,

$$\psi^{\infty}_{\rm BH}(u) = \int_{-\infty}^{+\infty} \frac{d\omega}{2\pi} Z^{\infty}_{\rm BH} e^{-i\omega u}. \tag{4.22}$$

Similarly, in terms of the advanced time $v = t + x$, the waveform at the BH horizon is the Fourier conjugate to $Z^{\rm H}_{\rm BH}$,

$$\psi^{\rm H}_{\rm BH}(v) = \int_{-\infty}^{+\infty} \frac{d\omega}{2\pi} Z^{\rm H}_{\rm BH} e^{-i\omega v}. \tag{4.23}$$

Having defined these amplitudes, in the presence of the reflecting boundary we can use $\tilde{g}_{\rm ref}$ from Eq. (4.17) in Eq. (4.11) to compute the asymptotic amplitude associated with scalar waves $\tilde{\psi}$,

$$\tilde{\psi} \sim Z^{\infty}_{\rm ref} e^{i\omega x}, \qquad\qquad x \to \infty. \tag{4.24}$$

We find that

$$Z^{\infty}_{\rm ref} = Z^{\infty}_{\rm BH} + \tilde{\mathcal{K}} Z^{\rm H}_{\rm BH}. \tag{4.25}$$

This is our second key result. It shows that the waveform seen by distant observers can be understood as the sum of the usual emission in a BH spacetime, along with an additional signal $\tilde{\mathcal{K}} Z^{\rm H}_{\rm BH}$. This additional emission arises from the reflection of the radiation which would normally enter the horizon, but is reprocessed by the transfer function $\tilde{\mathcal{K}}$. The power of Eq. (4.25) is that is allows us to compute the total asymptotic waveform in and ECO spacetime from the corresponding waveforms observed near infinity and the horizon in a BH spacetime, given a particular choice of $\tilde{\mathcal{R}}$ and x_0.

We gain further insight into the nature of the additional emission by expanding $\tilde{\mathcal{K}}$ as a geometric series,

$$\tilde{\mathcal{K}} = \tilde{\mathcal{T}}_{\rm BH} \tilde{\mathcal{R}} e^{-2i\omega x_0} \sum_{n=1}^{\infty} (\tilde{\mathcal{R}}_{\rm BH} \tilde{\mathcal{R}})^{(n-1)} e^{-2i(n-1)\omega x_0}. \tag{4.26}$$

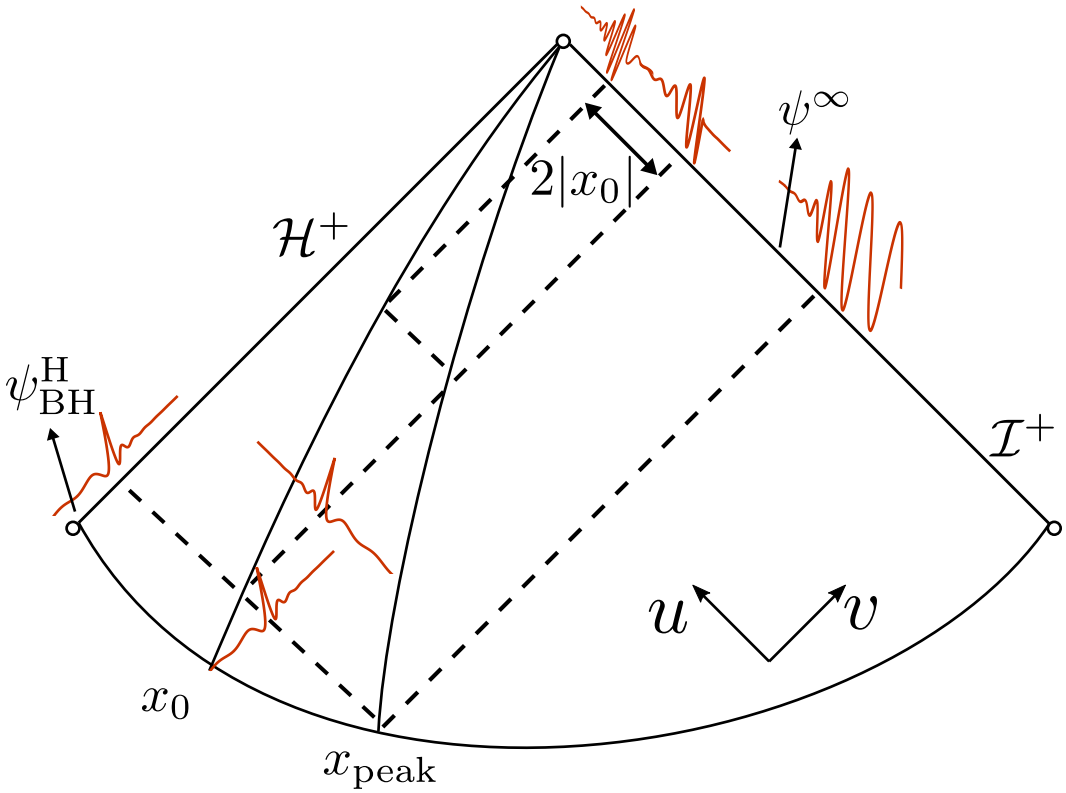

Figure 4.2: A conformal diagram illustrating the production of echoes. The waveform that impinges on the reflecting boundary at x_0 is approximately the same as the waveform that reaches the horizon in the BH spacetime, $\psi^{\mathrm{H}}_{\mathrm{BH}}(v)$. Repeated partial reflections between x_0 and the peak of the potential x_{peak} result in an asymptotic waveform $\psi^{\infty}(u)$ made up of a main burst followed by echoes. Each echo is a reprocessed version of the waveform on the horizon $\psi^{\mathrm{H}}_{\mathrm{BH}}(v)$.

This shows that the additional signal takes the form of a series of terms, each reprocessing the waves that impinge on the boundary with a different transfer function. As we show in Sec. 4.3, in many circumstances each term in this sequence results in a distinct pulse. Figure 4.2 illustrates the propagation of the echoes on a conformal diagram. The first term is the result of the primary reflection of $\psi^{\mathrm{H}}_{\mathrm{BH}}$ off of the boundary at x_0, which generates a factor of $\tilde{\mathcal{R}}$ along with a phase factor $2i\omega x_0$. The phase factor corresponds to a time delay between the first pulse and the main burst due the pulse's extra round trip journey between the boundary at x_0 and the peak of the scattering potential V at $x_{\mathrm{peak}} \approx 0$. When the pulse reaches the potential barrier, it is partially transmitted, contributing the final factor of $\tilde{\mathcal{T}}_{\mathrm{BH}}$.

The successive terms are "echoes" of this first reflection which bounce an integer number of times between the potential barrier, contributing a factor of $\tilde{\mathcal{R}}_{\mathrm{BH}}$, and

the reflecting boundary, contributing a factor of $\tilde{\mathcal{R}}$, before transmitting through the potential barrier with an additional propagation delay. Note that while the precise propagation delay of each pulse depends on the phases of $\tilde{\mathcal{T}}_{\rm BH}$, $\tilde{\mathcal{R}}_{\rm BH}$, and generically $\tilde{\mathcal{R}}$, the delay between echoes is constant starting with the second echo. With this picture in mind, we define the difference between the waveform and the corresponding BH waveform to be the echo amplitude

$$Z_{\rm echo} = \tilde{\mathcal{K}} Z^{\rm H}_{\rm BH} \,. \tag{4.27}$$

Meanwhile, we can also consider the entire transfer function $\tilde{\mathcal{K}}$ given in Eq. (4.18). This function possesses its own set of resonances, and there is a complementary perspective where the waves propagating towards the reflecting boundary excite the modes of a resonant cavity between the boundary and potential barrier. We discuss this perspective in Sec. 4.4.

4.3 Examples of Echoes

In this section we illustrate the reprocessing of the horizon waveform $\psi^{\rm H}_{\rm BH}$ using two simple examples: a spacetime with a frequency independent reflectivity $\tilde{\mathcal{R}}$ and a wormhole spacetime. We show that the additional waves appear as a sequence of echoes when the boundary is far from the peak of the potential barrier, but this behavior is lost for boundaries closer to the peak.

Individual echoes

The picture of successive echoes is made even more apparent by working in the time domain. The waveform seen by distant observers is determined through $Z^{\infty}_{\rm ref}$ by

$$\psi^{\infty}(u) = \int_{-\infty}^{\infty} \frac{d\omega}{2\pi} Z^{\infty}_{\rm ref} e^{-i\omega u} = \psi^{\infty}_{\rm BH}(u) + \psi_{\rm echo}(u) , \tag{4.28}$$

$$\psi_{\rm echo}(u) \equiv \int_{-\infty}^{\infty} \frac{d\omega}{2\pi} \tilde{\mathcal{K}} Z^{\rm H}_{\rm BH} e^{-i\omega u} , \tag{4.29}$$

where we have denoted the additional waveform due to the reflecting boundary $\psi_{\rm echo}$. For understanding the echoes, it is useful to further split $\psi_{\rm echo} = \sum_n \psi^{(n)}_{\rm echo}$ into contributions $\psi^{(n)}_{\rm echo}$ from each term in Eq. (4.26) for $\tilde{\mathcal{K}}$,

$$\psi^{(n)}_{\rm echo}(u) \equiv \int_{-\infty}^{+\infty} \frac{d\omega}{2\pi} \tilde{\mathcal{K}}^{(n)} Z^{\rm H}_{\rm BH} e^{-i\omega u} , \tag{4.30}$$

$$\tilde{\mathcal{K}}^{(n)}(\omega) \equiv (\tilde{\mathcal{T}}_{\rm BH}\tilde{\mathcal{R}})(\tilde{\mathcal{R}}_{\rm BH}\tilde{\mathcal{R}})^{(n-1)} e^{-2i\omega x_0 n} , \tag{4.31}$$

which are defined in terms of transfer functions $\tilde{\mathcal{K}}^{(n)}$ for each echo.

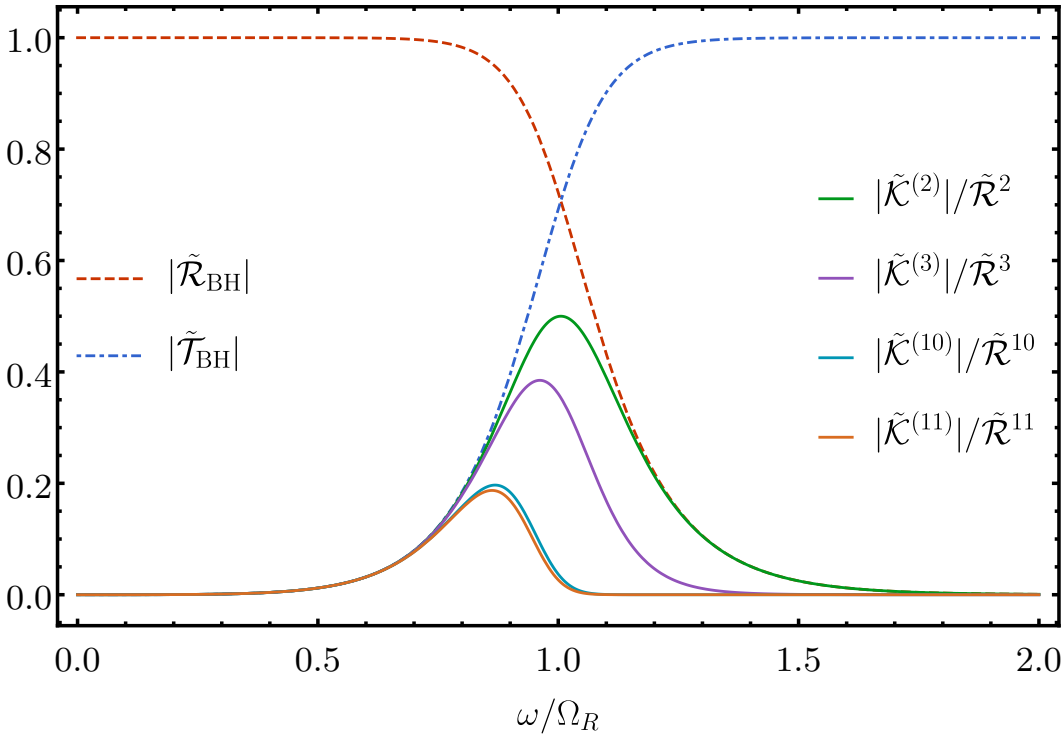

Figure 4.3: The frequency domain $\ell = 2$ black hole reflectivity $|\tilde{\mathcal{R}}_{\rm BH}|$ and transmissivity $|\tilde{\mathcal{T}}_{\rm BH}|$. We also plot the magnitude of the rescaled transfer functions $|\tilde{\mathcal{K}}^{(n)}|/\tilde{\mathcal{R}}^n$ for a boundary with constant reflectivity, for $n = 2, 3, 10$ and 11.

In the time domain, the reflection and transmission amplitudes are given by response functions

$$\mathcal{R}_{\rm BH}(t) = \int \frac{d\omega}{2\pi}\, \tilde{\mathcal{R}}_{\rm BH}(\omega) e^{-i\omega t}\,, \tag{4.32}$$

and similarly for $\mathcal{T}_{\rm BH}(t)$, $\mathcal{R}(t)$, and $\mathcal{K}(t)$.

To derive the expression for the echoes, recall that multiplication of two functions $\tilde{f}(\omega)$ and $\tilde{g}(\omega)$ in the frequency domain corresponds to convolution $(f * g)$ in the time domain, where

$$(f * g)(t) = \int_{-\infty}^{\infty} d\tau f(t-\tau) g(\tau)\,. \tag{4.33}$$

With this notation the first echo is

$$\begin{aligned} \psi^{(1)}_{\rm echo}(u) &= [\mathcal{K}^{(1)} * \psi^{\rm H}_{\rm BH}](u) \\ &= [(\mathcal{T}_{\rm BH} * \mathcal{R}) * \psi^{\rm H}_{\rm BH}](u + 2x_0), \end{aligned} \tag{4.34}$$

where $\mathcal{K}^{(n)}$ is the Fourier conjugate to $\tilde{\mathcal{K}}^{(n)}$, $\psi^{\rm H}_{\rm BH}$ is the Fourier conjugate to $Z^{\rm H}_{\rm BH}$, and recall that x_0 is negative for boundaries near the horizon. For the successive

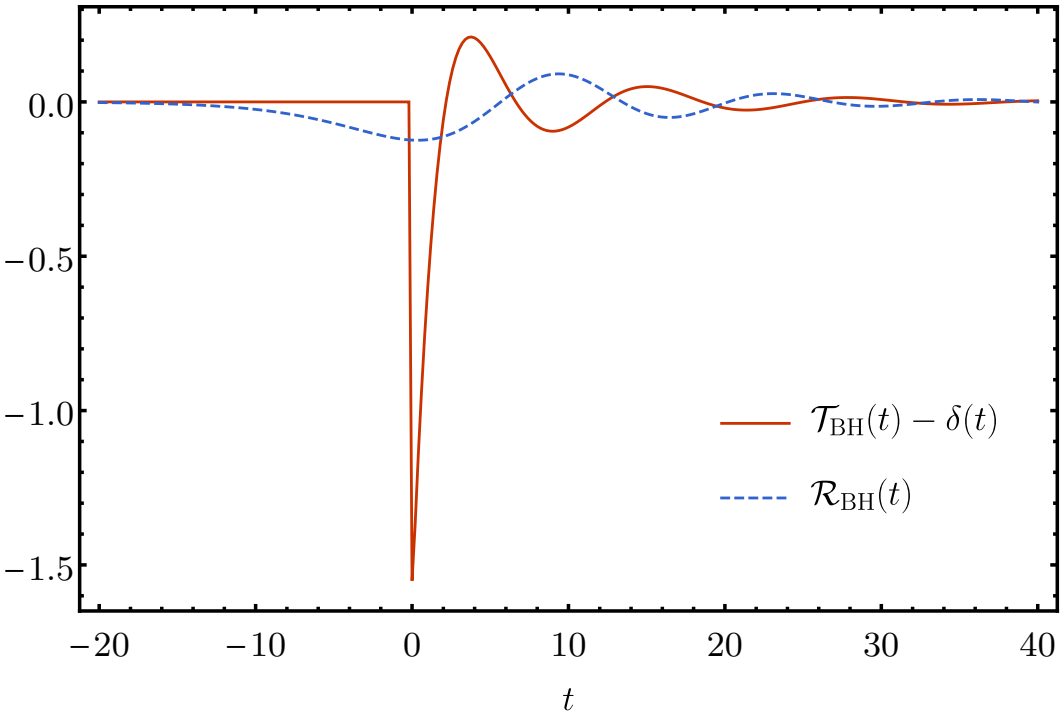

Figure 4.4: The $\ell = 2$ scalar reflectivity and transmissivity of the potential barrier, calculated numerically in the time domain.

echoes,

$$\begin{aligned}\psi^{(n)}_{\rm echo}(u) =& [\mathcal{K}^{(n)} * \psi^{\rm H}_{\rm BH}](u) \\ =& [(\mathcal{T}_{\rm BH} * \mathcal{R}) * (\mathcal{R}_{\rm BH} * \mathcal{R}) * \dots \\ & * (\mathcal{R}_{\rm BH} * \mathcal{R}) * \psi^{\rm H}_{\rm BH}](u + 2nx_0)\,. \end{aligned} \tag{4.35}$$

where there are $n-1$ convolutions of $(\mathcal{R}_{\rm BH} * \mathcal{R})$ with $\psi^{\rm H}_{\rm BH}$.

We calculate the BH response functions $\mathcal{R}_{\rm BH}$ and $\mathcal{T}_{\rm BH}$ both in the time and frequency domain using numerical methods described in Appendix 4.8. The blue and red dashed curves in Fig. 4.3 show $\tilde{\mathcal{R}}_{\rm BH}$ and $\tilde{\mathcal{T}}_{\rm BH}$ in the frequency domain for the $\ell = 2$ scalar wave equation[1]. As expected [52, 78, 144], at low frequencies compared to the size of the potential peak $(M\omega)^2 \ll V_p$, waves are completely reflected,

$$|\tilde{\mathcal{T}}_{\rm BH}(\omega)| \to 0, \qquad |\tilde{\mathcal{R}}_{\rm BH}(\omega)| \to 1, \tag{4.36}$$

[1] From their definitions, $\tilde{\mathcal{T}}_{\rm BH} = 1/B_{\rm out}$ and $\tilde{\mathcal{R}}_{\rm BH} = B_{\rm in}/B_{\rm out}$ possess resonances (poles) at the complex BH QNM frequencies [39]; however these resonances do not manifest themselves as clearly separated peaks on the real ω axis since the width of the QNM resonances is large compared to their spacing.

while at high frequencies $(M\omega)^2 \gg V_p$ waves are completely transmitted

$$\tilde{\mathcal{T}}_{\rm BH}(\omega) \to 1, \qquad\qquad |\tilde{\mathcal{R}}_{\rm BH}(\omega)| \to 0, \tag{4.37}$$

The transition between the two regimes occurs at approximately the real part of the $\ell = 2$ fundamental BH QNM frequency

$$M\Omega = M\Omega_R + iM\Omega_I \approx 0.48 - 0.10i\,, \tag{4.38}$$

since $V_p \approx (M\Omega_R)^2$.

Figure 4.4 shows $\mathcal{R}_{\rm BH}$ and $\mathcal{T}_{\rm BH}$ in the time domain. Both response functions ring down at the BH QNM frequency Ω. As is explained in the appendix, the high frequency behavior for $\tilde{\mathcal{T}}_{\rm BH}$ implies that in the time domain $\mathcal{T}_{\rm BH}(t)$ contains a $\delta(t)$ singularity at $t = 0$, which is subtracted off in the figure.

Using the echo response functions computed from $\tilde{\mathcal{T}}_{\rm BH}$ and $\tilde{\mathcal{R}}_{\rm BH}$, we now study the echo morphology from a variety of ECOs. When presenting numerical results, we use units so that the mass of the BH spacetime is unity, $M = 1$, and when we discuss a particle with scalar charge q we also set $q = 1$.

Frequency Independent Reflectivity

The simplest type of boundary condition in this model is a frequency independent reflectivity $\tilde{\mathcal{R}}$. In this case, the echoes have a straightforward dependence on the ECO parameters $\tilde{\mathcal{R}}$ and x_0. The reflectivity factors out of the response functions $\mathcal{K}^{(n)}$ and controls the size of each echo, without contributing any phase factors. Thus the majority of the time delay between echoes is due to the phase $2\omega x_0$, corresponding to a round trip journey from the potential peak near $x \approx 0$ and the boundary at x_0, with only a small contribution from the BH scattering coefficient $\tilde{\mathcal{R}}_{\rm BH}$.

The shape of each echo is described by the rescaled response functions

$$e^{2i\omega x_0 n}\tilde{\mathcal{K}}^{(n)}(\omega)/\tilde{\mathcal{R}}^n = \tilde{\mathcal{T}}_{\rm BH}(\omega)\tilde{\mathcal{R}}_{\rm BH}(\omega)^{(n-1)}\,, \tag{4.39}$$

which we show in Fig. 4.3. Recall that $|\tilde{\mathcal{T}}_{\rm BH}|$ is approximately zero low frequencies and approximately one at large frequencies, while the opposite is true for $|\tilde{\mathcal{R}}_{\rm BH}|$. This behavior produces a small window of frequencies where the second echo response function is nonzero. The third echo response comes from the multiplying the second echo response function by $\tilde{\mathcal{R}}_{\rm BH}$; this results in a smaller slightly shifted window of frequencies. This pattern repeats with each subsequent response function. However, as the window shifts to the left, $|\tilde{\mathcal{R}}_{\rm BH}| \to 1$ and so the change in absolute value of

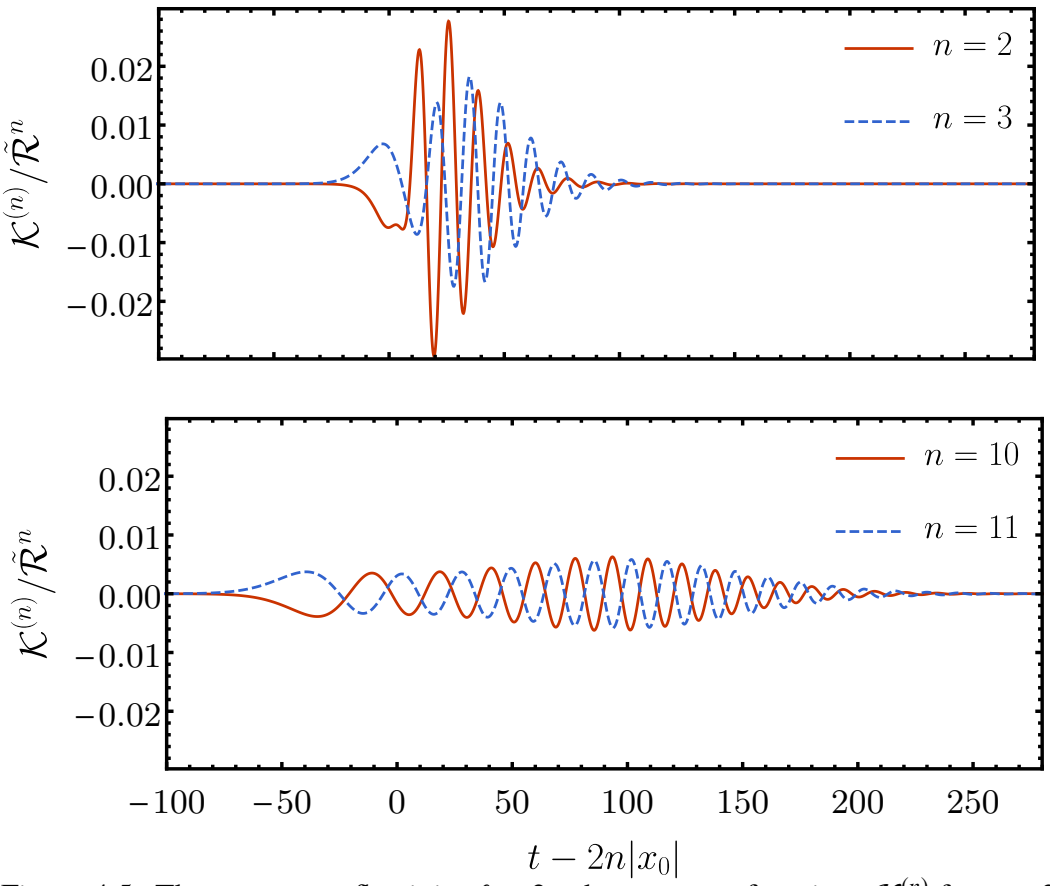

Figure 4.5: The constant reflectivity $\ell = 2$ echo response functions $\mathcal{K}^{(n)}$ for $n = 2$ and 3 (top) and $n = 10$ and 11 (bottom). We divide the response functions by $\tilde{\mathcal{R}}^n$ to rescale them and time shift each by $2n|x_0|$ so they overlap.

the transfer functions slows, so that there is very little difference between 10th and 11th echoes.

In the time domain, the rescaled response functions in Eq. (4.39) are time shifted to remove the delay between echoes due to the factor of $e^{2i\omega x_0 n}$. Figure 4.5 shows the rescaled and shifted time domain echo response functions, obtained by numerically performing the convolutions on $\mathcal{T}_{\rm BH}$ and $\mathcal{R}_{\rm BH}$. Each transfer function goes to zero at early times and is a decaying sinusoid at late times. The complex frequency of the sinusoid is nearly the fundamental QNM frequency Ω for the first few echoes, while for later echoes the decay time gets longer and the oscillation frequency gets slightly smaller.

Similar trends are seen in the echoes themselves. The waveforms at both infinity and on the horizon depend on our particular choice of sources and initial data. As an illustration throughout this paper, we consider the echoes produced by a test particle

with unit scalar charge following an orbit that we refer to as the ISCO plunge orbit. This orbit is a geodesic that spirals inward from the innermost stable circular orbit (ISCO), with the ISCO energy and angular momentum, and reaches the horizon at an advanced time $v_{\rm H}$. We select this orbit since it is a reasonable model for the ringdown portion of the scalar waveform for orbits that have been circularized prior to reaching the ISCO radius, by a mechanism such as radiation reaction [84]. We use a numerical Green's function to generate the waveform from this source, which we subsequently window at early times so it smoothly starts from zero. Details on the entire procedure are found in Appendix 4.9.

Since our method is to reprocess waveforms from BH spacetimes, our formalism cannot capture the emission in an actual ECO spacetime after the particle passes x_0. Namely, Eq. (4.17) for $\tilde{g}_{\rm ref}$ can only be used when the source is outside x_0, but we use Eq. (4.17) for all source locations. Using a particular ECO model, this additional radiation could be added directly to our waveforms, with only a small remaining inaccuracy due to the suppressed emission in our waveforms as the particle travels from x_0 to the horizon.

Figures 4.6 and 4.7 show the $(\ell, m) = (2, 2)$ horizon waveform and select echoes in the time domain from the ISCO plunge. At early times the horizon waveform frequency is $\omega = m\Omega_{\rm ISCO}$, where $\Omega_{\rm ISCO}$ is the ISCO orbital frequency, and at late times there is a ringdown at the fundamental BH QNM frequency. The echoes also display a highly suppressed oscillation at $\omega \approx m\Omega_{\rm ISCO}$ at early times and then asymptote to decaying sinusoids at late times. The complex frequency of the sinusoid displays the same qualitative behavior as the echo response functions; each echo decays less than the previous and has a slightly lower frequency, with consecutive early echoes differing more than consecutive late echoes. We explore these features in more detail in Sec. 4.5.

Wormhole

The echoes from specific ECO spacetimes can also be placed within the reflecting boundary formalism. Consider for example a wormhole produced by identifying two Schwarzschild spacetimes of mass M at an areal radius r_0. In Appendix 4.10, we show that an observer in one universe can describe the influence of the other universe on wave propagation by a reflecting boundary condition $\tilde{\psi} \propto \tilde{\mathcal{R}}(\omega)e^{i\omega(x-x_0)} + e^{-i\omega(x-x_0)}$ as $x \to x_0$, where

$$\tilde{\mathcal{R}}(\omega) = \tilde{\mathcal{R}}_{\rm BH}(\omega)e^{-2i\omega x_0}\,. \tag{4.40}$$

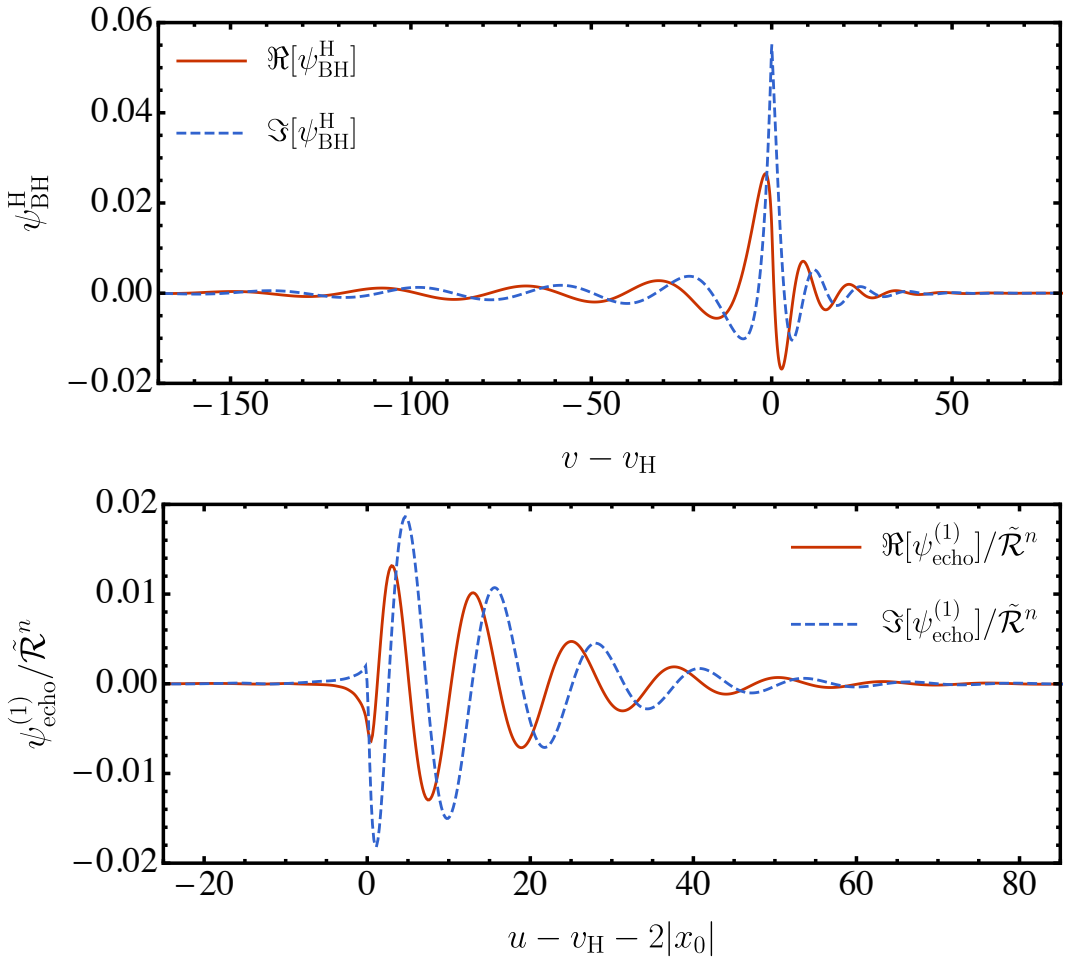

Figure 4.6: Top: The $(\ell, m) = (2, 2)$ waveform on the horizon $\psi^{\rm H}_{\rm BH}$, as produced by a test charge following the ISCO plunge orbit. Bottom: The corresponding first echo $\psi^{(1)}_{\rm echo}$, rescaled and shifted in time, for a frequency-independent reflectivity.

The free propagation phase $e^{-2i\omega x_0}$ appearing in the reflectivity accounts for the additional delay as the waves propagate to the potential peak in the other universe and back again.

Echoes in the wormhole spacetime are simply related to frequency independent $\tilde{\mathcal{R}} = 1$ echoes. Namely the nth echo in the wormhole spacetime is the $2n$th echo of the $\tilde{\mathcal{R}} = 1$ case, as can be seen from Eq. (4.31). Therefore, the wormhole echoes exhibit the same patterns as the frequency-independent echoes. A comparison of the first echoes and the fifth echoes produced by a test charge following the ISCO plunge orbit is shown in Fig. 4.8.

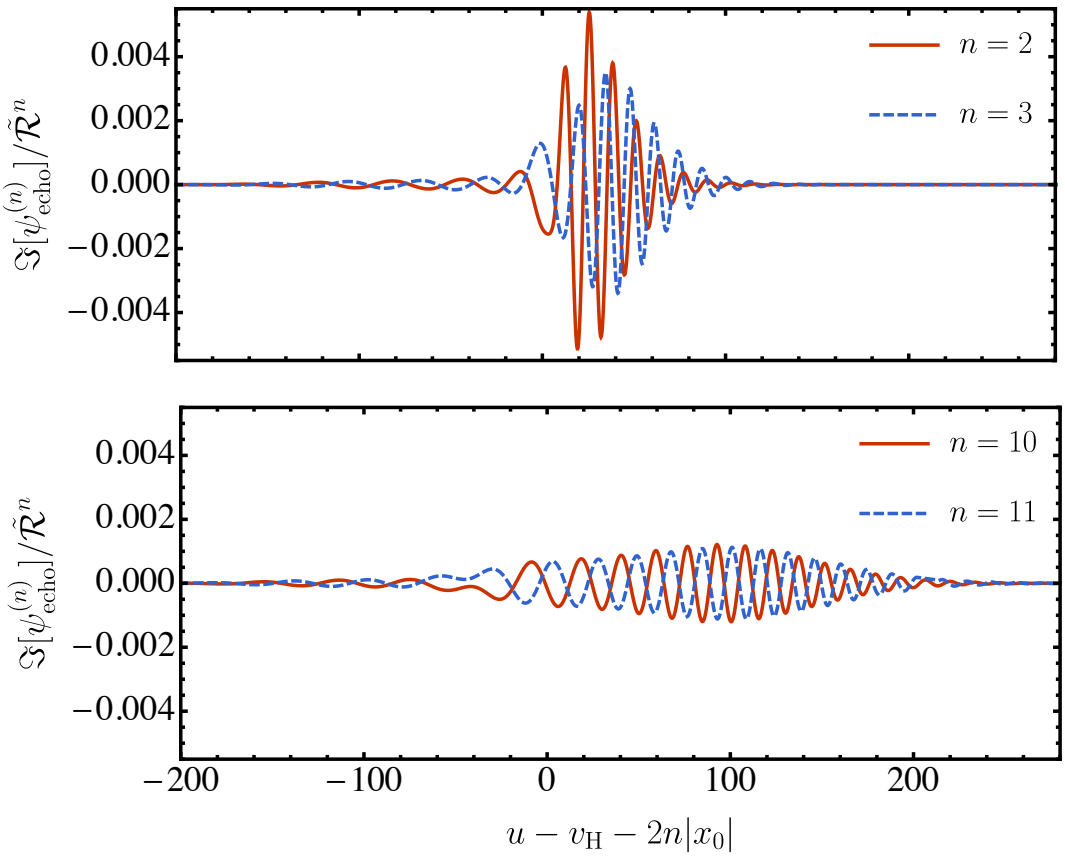

Figure 4.7: The $(\ell, m) = (2, 2)$ echoes for a frequency independent reflectivity $\tilde{\mathcal{R}}$. The source is a test charge following the ISCO plunge orbit. We show the imaginary part of each echo, rescaled by $\tilde{\mathcal{R}}^n$ and shifted in time to overlap. Top: The second and third echoes. Bottom: The tenth and eleventh echoes. At this stage, successive echoes change only slightly in duration and amplitude.

Echo interference

Having explored the individual echo pulses, we now examine the full echo waveform. When the spacing between echoes is large compared to the duration of each echo, the echoes do not interfere and the total waveform appears as a sum of echo pulses. Figure 4.9 shows the waveform $\psi^{\infty}(u)$ generated by the ISCO plunge orbit in the case $\tilde{\mathcal{R}} = 1$, truncating the echo sum at $n = 11$. We illustrate the $\ell = 2$ waveform for two locations x_0 of the boundary.

The top panel shows the total waveform for $x_0 = -50M$. The first part of the waveform is the BH waveform $\psi^{\infty}_{\rm BH}$, which initially oscillates at roughly a frequency of $m\Omega_{\rm ISCO}$ and transitions to ringing at the BH QNM frequencies. The transition occurs around a retarded time $u_{\rm LR}$, when the particle crosses the light ring. Roughly $|2x_0|$ later, there are three to four distinct echo pulses, each spaced by roughly $|2x_0|$.

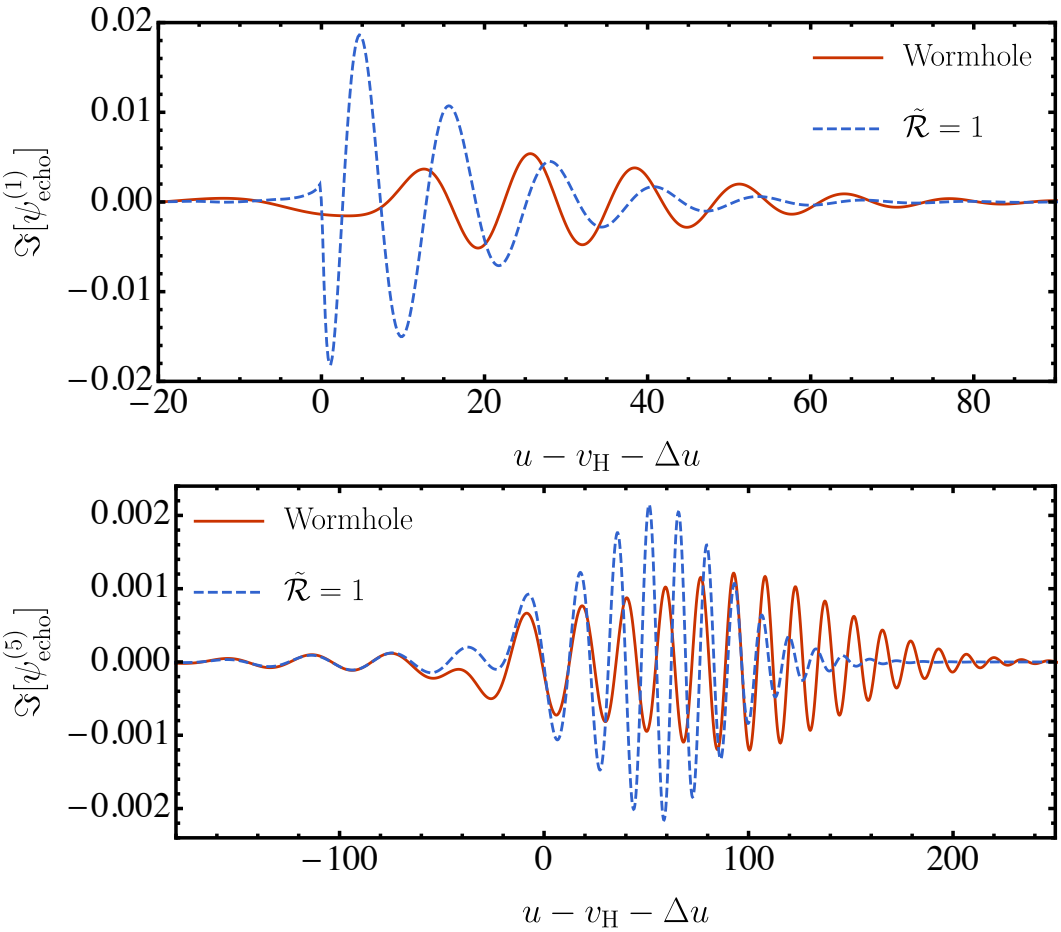

Figure 4.8: The imaginary part of the $(\ell, m) = (2, 2)$ time domain echoes excited by a test charge following the ISCO plunge orbit in a wormhole spacetime, as compared with the echoes of the $\tilde{\mathcal{R}} = 1$ reflecting boundary. We plot the first echo (top) and fifth echo (bottom). Each wormhole echo is shifted by $\Delta u = 4n|x_0|$, while each constant reflectivity echo is shifted by $\Delta u = 2n|x_0|$.

As we observed earlier, the later echoes decay more slowly and do not appear distinct because they have a long enough duration to interfere with each other. The bottom panel shows the case $x_0 = -20M$, where there are only two distinct pulses before the echoes begin to interfere.

We show additional examples in Fig. 4.10, using our ISCO plunge waveform. In this figure, the ECO surface is located at $x_0 = -50M$ and $\tilde{\mathcal{R}}$ ranges from 0.01 to 1. While only three to four distinct echoes are visible at large $\tilde{\mathcal{R}}$, for $\tilde{\mathcal{R}} = 0.1$ we can see many pulses in the rapidly decaying waveform.

The observation also holds for wormhole waveforms, which we show in Fig. 4.11. The doubled propagation time as compared to the $\tilde{\mathcal{R}} = 1$ case produces a longer

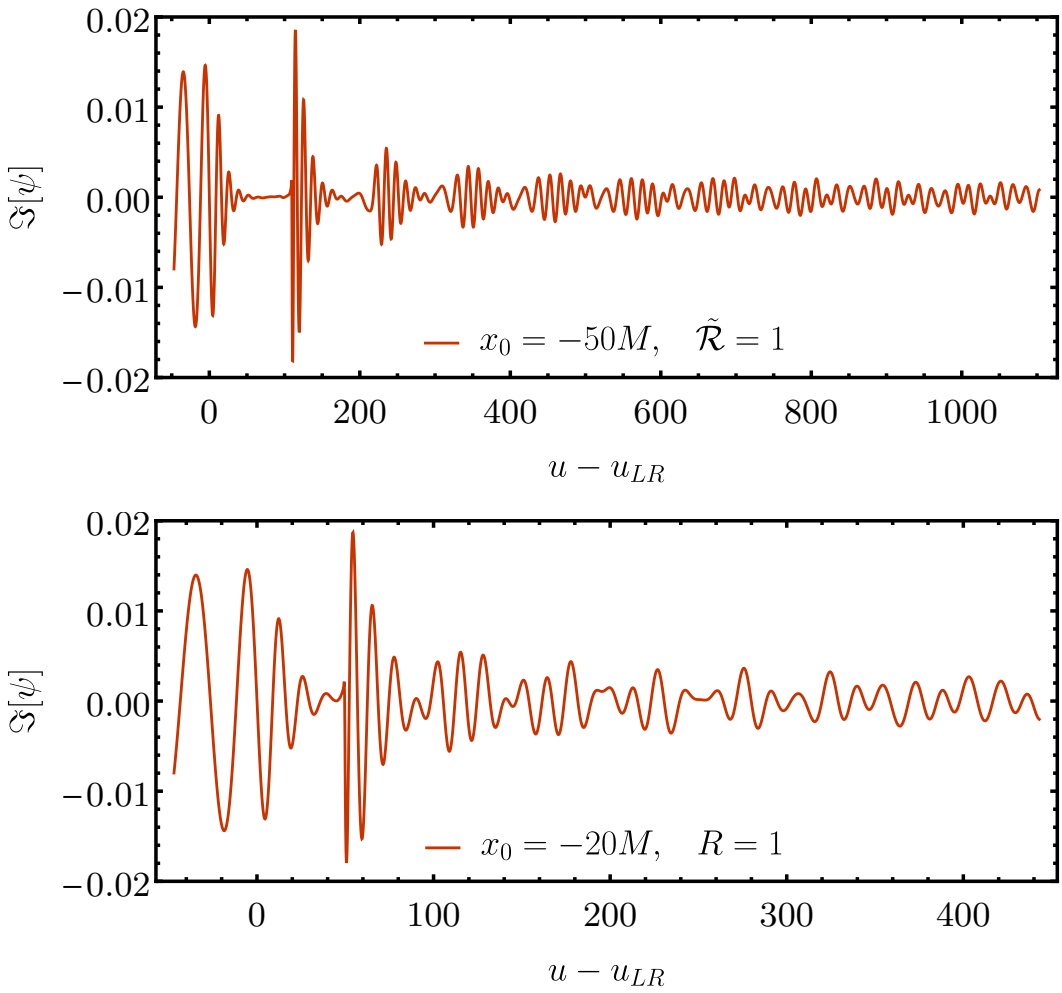

Figure 4.9: The imaginary part of the $(\ell, m) = (2, 2)$ total waveform ψ^{∞} excited by test charge following the ISCO plunge orbit. We show results for an ECO with $\tilde{\mathcal{R}} = 1$ and $x_0 = -50M$ (top), and an ECO with $\tilde{\mathcal{R}} = 1$ and $x_0 = -20M$ (bottom). We shift the time axis by the retarded time that the charge crosses the spherical photon orbit, $u_{\rm LR}$.

spacing between echoes. As such, the early wormhole echoes are more distinct than early $\tilde{\mathcal{R}} = 1$ echoes.

Meanwhile, when the spacing between the echoes is small compared to the echo duration, there can be no distinct pulses. Instead, the waveform resembles a single decaying sinusoid at a frequency different than the BH frequency. Figure 4.12 shows an occurrence of this for $\tilde{\mathcal{R}} = 1$, $x_0 = -3M$ and the ISCO plunge orbit. In this case, the total waveform, appearing as the red solid curve, initially agrees with the BH waveform $\psi^{\infty}_{\rm BH}$, appearing as the black dotted curve, but then transitions

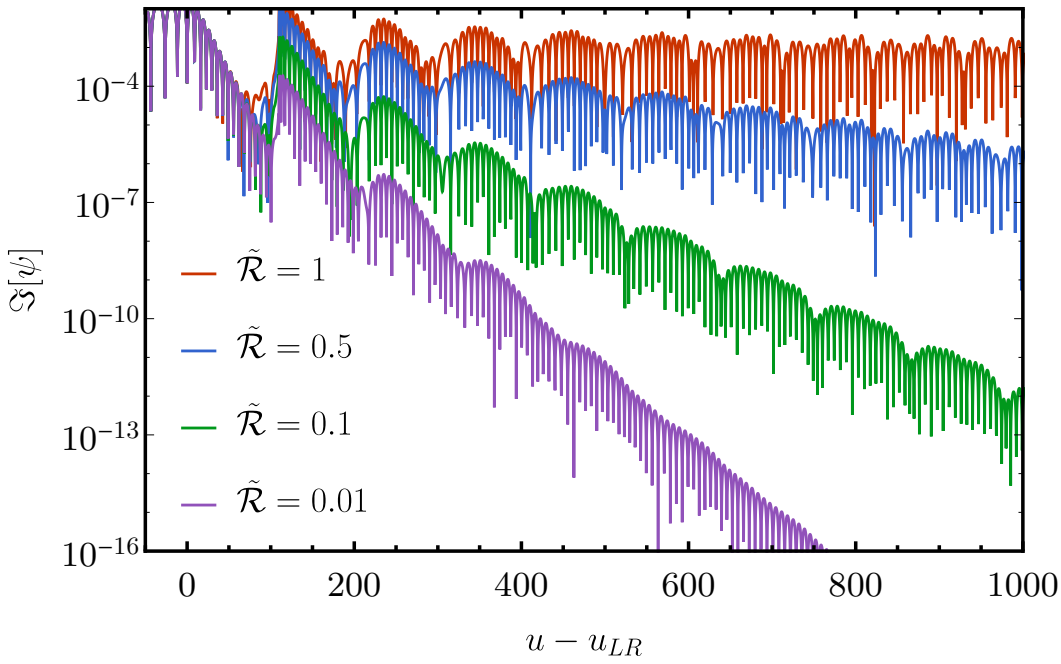

Figure 4.10: The imaginary part of the $(\ell, m) = (2, 2)$ total waveform ψ^{∞} excited by a test charge following the ISCO plunge orbit. We show results for ECOs with $x_0 = -50M$ and several different choices of a frequency independent $\tilde{\mathcal{R}}$.

to a decaying sinusoid. Note that this case pushes the limits of our approximation that the waves propagate freely near x_0; for $x_0 = -3M$, $r_0 \approx 2.08M$ and $V(r_0)$ is approximately 25% its peak value.

This decaying sinusoid is in fact the coherent superposition of the late echoes, a fact that we illustrate by plotting the last seven echoes appearing in the echo sum in purple. This coherent superposition occurs because the later echoes all have nearly the same frequency. Finally note that the missing echoes from the truncated sum are not negligible compared to the total waveform, a fact we illustrate by also plotting the last echo appearing in the sum in green. In Sec. 4.4 we study this example in the frequency domain, and we find that this is an example of the excitation of a single resonant mode of the ECO spacetime as described by our reflecting boundary condition.

4.4 Excitation of ECO Modes

The presence of the reflecting boundary condition drastically changes the spectrum of the spacetime. The result is a different set of resonant frequencies, those of the ECO spacetime. In this section we explore how our model treats these modes, and how they relate to the echoes discussed in Sec. 4.3.

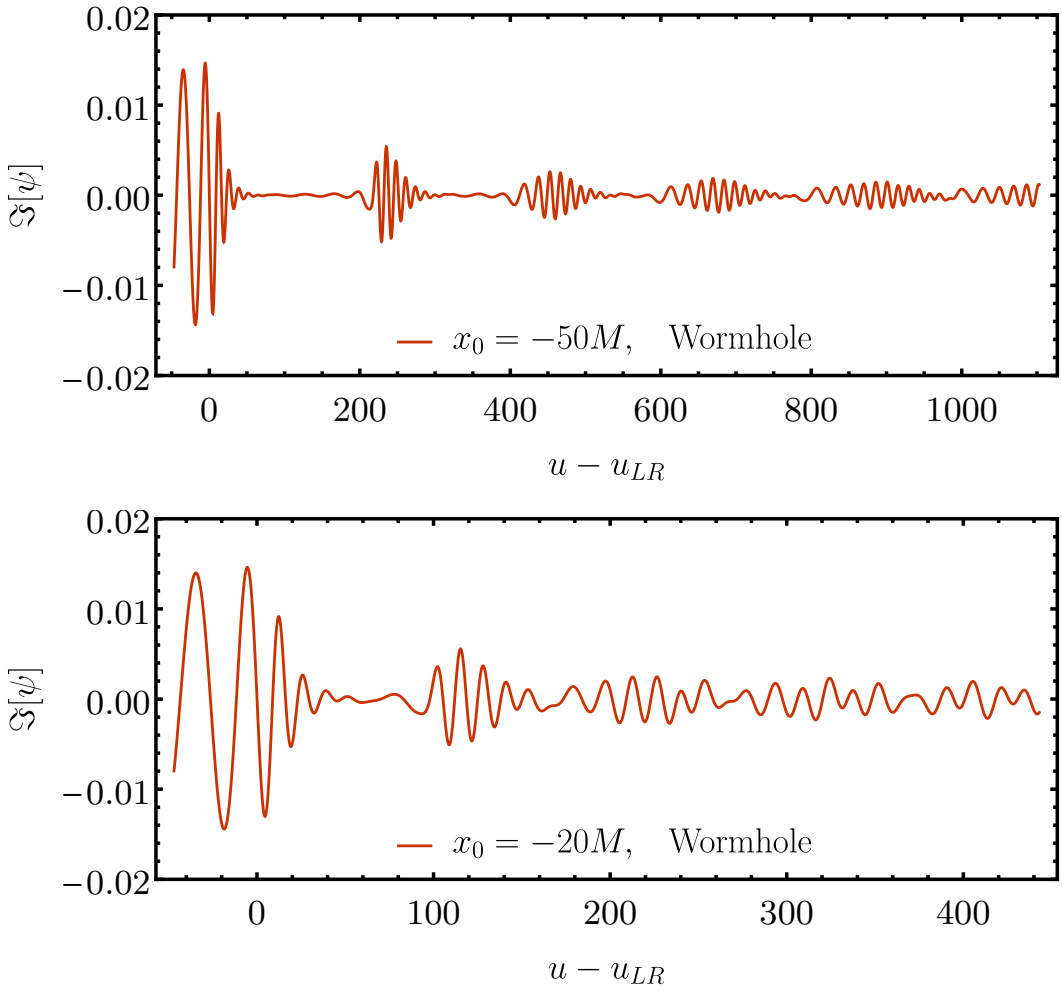

Figure 4.11: The imaginary part of the $(\ell, m) = (2, 2)$ total waveform ψ^{∞} excited by a test charge following the ISCO plunge orbit. We show results for a wormhole with $x_0 = -50M$ (top) and $x_0 = -20M$ (bottom).

New Modes

The QNM resonances are the complex poles of the Green's function. From Eq. (4.15), we see that for a BH, they occur when $W_{\rm BH} = 0$. The BH QNMs are not poles of the ECO Green's function. As is seen from Eq. (4.17), the first and second terms both have poles at the QNM frequencies, but these cancel in the full expression.

The modes of the ECO spacetime come from the poles of the response function $\tilde{\mathcal{K}}(\omega)$ appearing in the Green's function,

$$\tilde{\mathcal{K}} = \frac{\tilde{\mathcal{T}}_{\rm BH}\tilde{\mathcal{R}}e^{-2i\omega x_0}}{1 - \tilde{\mathcal{R}}_{\rm BH}\tilde{\mathcal{R}}e^{-2i\omega x_0}} \,.$$

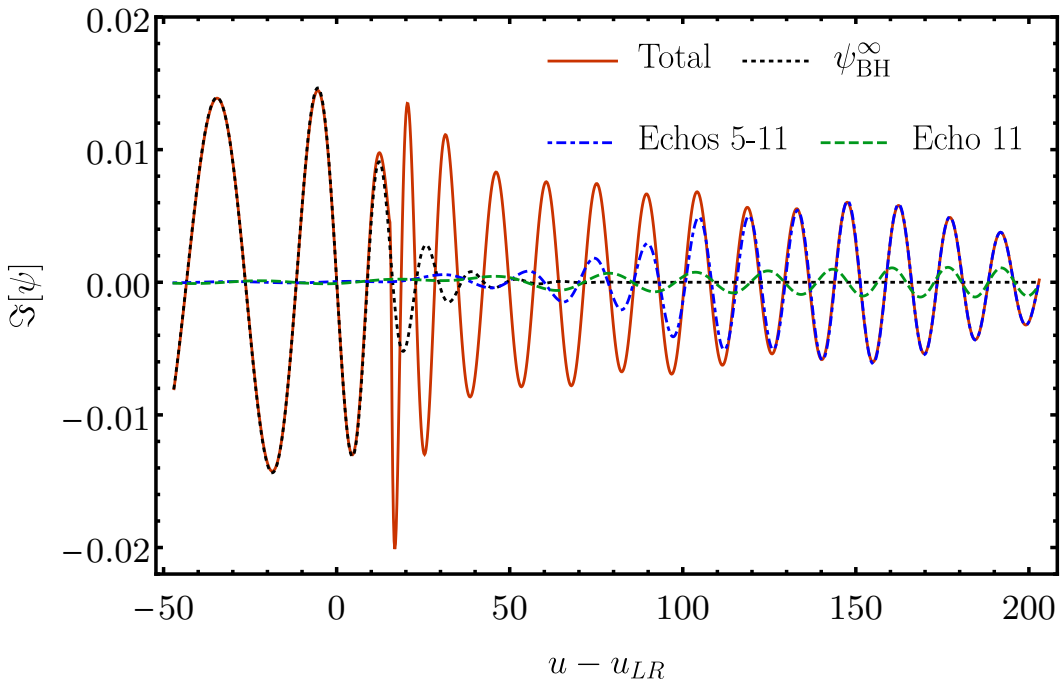

Figure 4.12: The imaginary part of the $(\ell, m) = (2, 2)$, time domain, total waveform excited by a test charge following the ISCO plunge orbit. We show results from an ECO with $\tilde{\mathcal{R}} = 1$ and $x_0 = -3M$. The total waveform is obtained by summing the black hole waveform $\psi^{\infty}_{\rm BH}$ and a finite number of echoes. Each curve contains a different numbers of echoes.

These modes obey both the reflecting boundary condition at x_0 as well as the outgoing wave condition at $\mathcal{I}^+$. Figure 4.13 shows the $|\tilde{\mathcal{K}}|$ for $\tilde{\mathcal{R}} = 1$, $\tilde{\mathcal{R}} = 0.5$, and for the wormhole spacetime, each for two values of x_0: $x_0 = -3M$ and $x_0 = -50M$. In the figure, each peak of $|\tilde{\mathcal{K}}|$ represents a resonance of the transfer function[2].

Observe that in all our cases there are no new modes at large frequencies $\omega \gg \Omega_R$. This behavior can be understood analytically. Recall that at large frequencies $\tilde{\mathcal{R}}_{\rm BH} \to 0$ and $\tilde{\mathcal{T}}_{\rm BH} \to 1$. This means that

$$\tilde{\mathcal{K}}(\omega) \to \tilde{\mathcal{R}}(\omega) e^{-2i\omega x_0}, \qquad \omega \to \infty, \tag{4.41}$$

and the additional resonances are exactly the poles of $\tilde{\mathcal{R}}$.

For $x_0 = -3M$, Fig. 4.13 clearly displays a single new mode at a frequency close to the fundamental QNM of a BH, for both $\tilde{\mathcal{R}} = 1$ and the wormhole. In the case

[2] A peak of the transfer function $\tilde{\mathcal{K}}$ on the real axis is a resonance in the sense that amplification occurs at this frequency. To show that a complex pole of the Green's function is responsible for this peak, one must examine $\tilde{\mathcal{K}}$ in the complex ω plane.

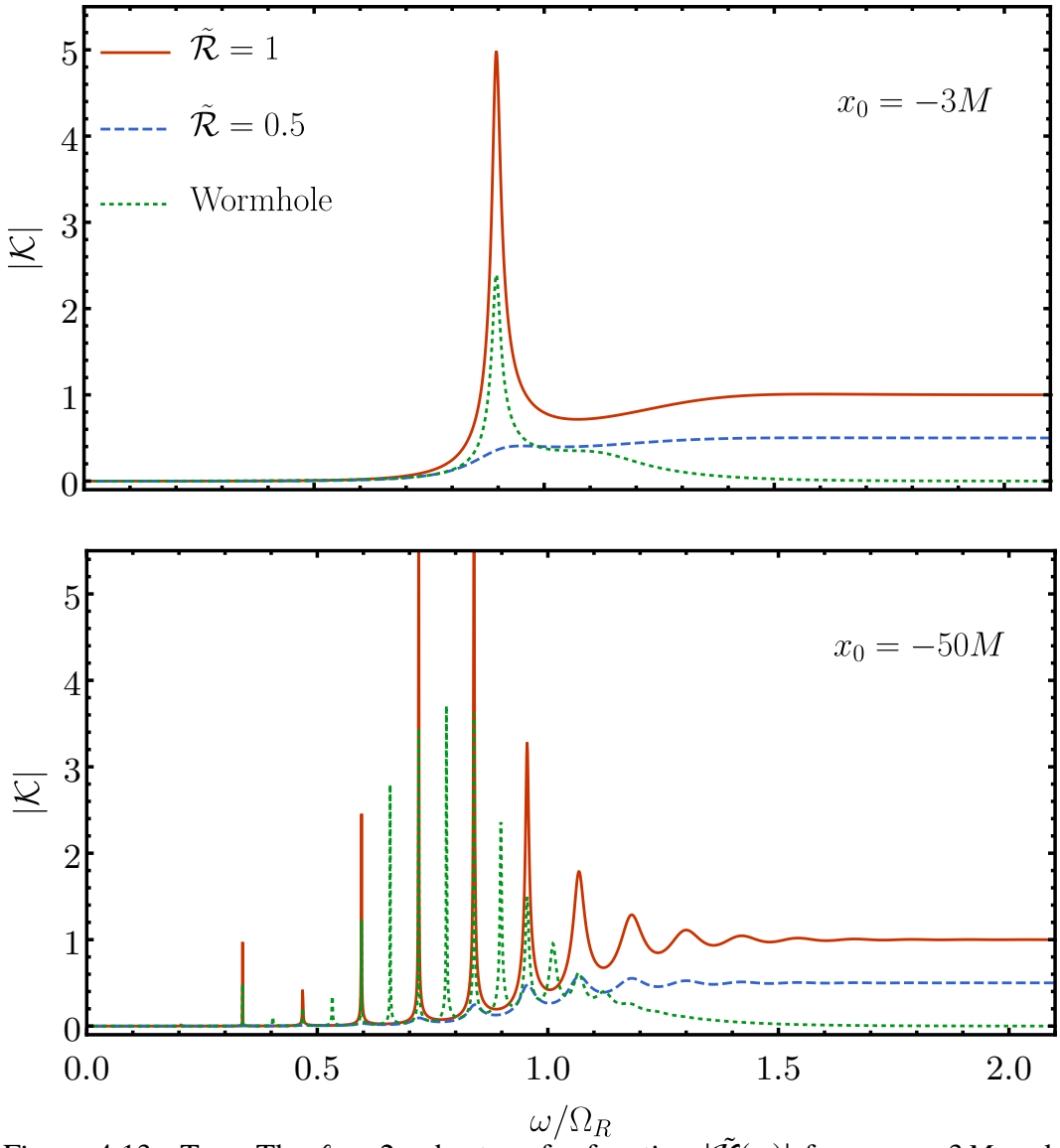

Figure 4.13: Top: The $\ell = 2$ echo transfer function $|\tilde{\mathcal{K}}(\omega)|$ for $x_0 = -3M$ and several choices of $\tilde{\mathcal{R}}$. Note that $|\tilde{\mathcal{K}}|$ is a symmetric function of ω. Bottom: The same plot for $x_0 = -50M$.

$\tilde{\mathcal{R}} = 0.5$, there is a small peak in $|\mathcal{K}|$ at about the same frequency, although it is less visible.

For $x_0 = -50M$ and constant $\tilde{\mathcal{R}}$, there is a set of new modes with a frequency spacing of $2\pi/(2|x_0|)$. For the wormhole, there is a set of new modes and with a spacing of $2\pi/(4|x_0|)$. This frequency spacing corresponds to approximately the light travel time T from the potential peak to the boundary and back. For an optical cavity, this

spacing is known as the free spectral range of the cavity,

$$\omega_{\rm FSR} = \frac{2\pi}{T} \,. \tag{4.42}$$

To understand the resonances, we can use techniques from similar problems involving optical cavities. The zeros of the denominator of Eq. (4.18) contribute a set of resonances ω_n given by

$$1 = \tilde{\mathcal{R}}_{\rm BH}(\omega_n)\tilde{\mathcal{R}}(\omega_n)e^{-2i\omega_n x_0} \,. \tag{4.43}$$

Consider first the case that $\tilde{\mathcal{R}}(\omega)$ is frequency independent. In this case, there are two frequency scales in the problem; the scale $\delta\omega_{\rm BH} \approx \tilde{\mathcal{R}}_{\rm BH}(\omega)/\partial_\omega\tilde{\mathcal{R}}_{\rm BH}(\omega)$ on which the reflectivity changes and the scale $\omega_{\rm FSR}$ on which the exponent of the exponential changes. When the frequency dependence of the $\tilde{\mathcal{R}}_{\rm BH}$ is weak, i.e. $\omega_{\rm FSR}/\delta\omega_{\rm BH} \ll 1$, then to leading order in $\omega_{\rm FSR}/\delta\omega_{\rm BH}$

$$\omega_n = n\omega_{\rm FSR} + i\frac{\omega_{\rm FSR}}{2\pi}\ln(\tilde{\mathcal{R}}\tilde{\mathcal{R}}_{\rm BH}) + O\left(\frac{\omega_{\rm FSR}}{\delta\omega_{\rm BH}}\right), \tag{4.44}$$

where $\tilde{\mathcal{R}}_{\rm BH}$ is evaluated at $n\omega_{\rm FSR}$. We see that the new modes are spaced by $\omega_{\rm FSR}$ in agreement with Fig. 4.13, and they decay provided $|\tilde{\mathcal{R}}| < 1$.

More generally, when $\tilde{\mathcal{R}}(\omega)$ has frequency dependence we can often separate it into factors with fast and slow frequency dependence,

$$\tilde{\mathcal{R}}(\omega)e^{-2i\omega x_0} = \hat{\mathcal{R}}(\omega)e^{i\omega T} \,, \tag{4.45}$$

where $\hat{\mathcal{R}}(\omega)$ varies appreciably over a characteristic range of frequencies $\delta\omega$ which is large compared to $2\pi/T$. Again, T is approximately the round trip travel time between the potential peak and the major features in the true potential characterizing the ECO. For the wormhole, $\delta\omega = \delta\omega_{\rm BH}$ and $T = -4x_0$ is the light travel time. Provided both $\omega_{\rm FSR}/\delta\omega_{\rm BH} \ll 1$ and $\omega_{\rm FSR}/\delta\omega \ll 1$, working to leading order, we again arrive at Eq. (4.44) where $\omega_{\rm FSR} = 2\pi/T$ and we must allow for $O(\omega_{\rm FSR}/\delta\omega)$ errors.

Notice also that the ECO resonances for $\tilde{\mathcal{R}} = 0.5$ are broader than the $\tilde{\mathcal{R}} = 1$ resonances, while the width of the wormhole resonances is similar to the $\tilde{\mathcal{R}} = 1$ resonances. This also follows from Eq. (4.44) since the width of the resonances is controlled by the decay rate of the new modes, which is proportional to $\omega_{\rm FSR}\ln(\tilde{\mathcal{R}}\tilde{\mathcal{R}}_{\rm BH})$. In the low frequency regime that the new modes appear at, $\tilde{\mathcal{R}} \approx 1$ for the wormhole and we expect the width to be similar to the $\tilde{\mathcal{R}} = 1$ case.

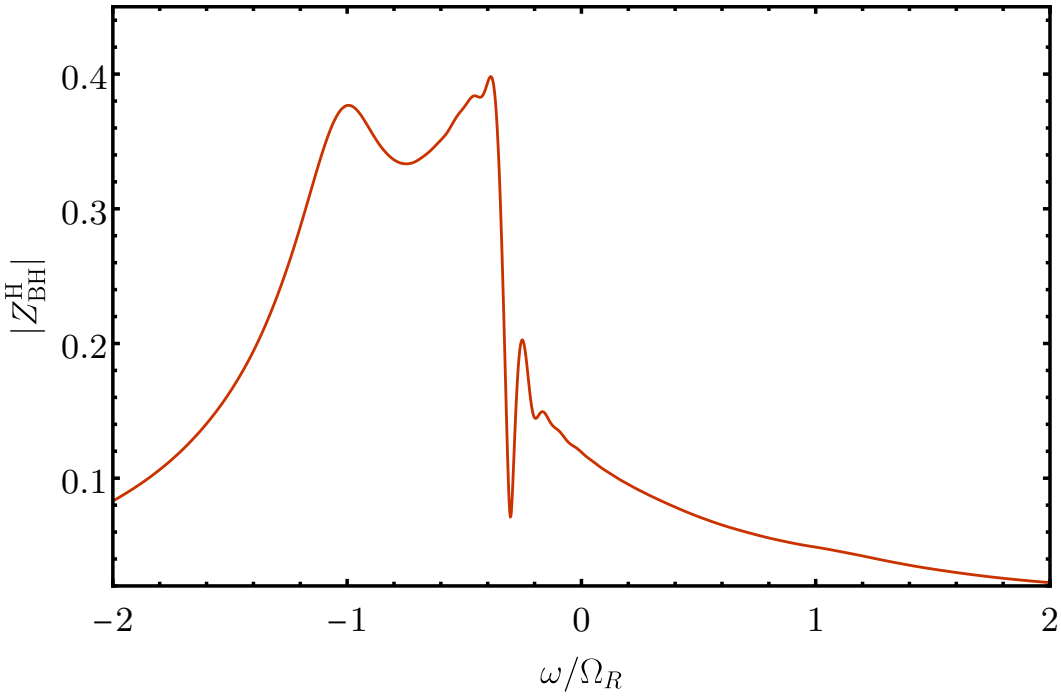

Figure 4.14: The modulus of the $(\ell, m) = (2, 2)$ horizon waveform generated by a test charge following the ISCO plunge orbit.

Single Mode Excitation

We return to Fig. 4.12, where for $\tilde{\mathcal{R}} = 1$ and $x_0 = -3M$ the echo waveform appears as a single decaying sinusoid which differs from the QNMs of the BH. This behavior can be interpreted as the excitation of a single resonant mode of $\tilde{\mathcal{K}}$ by the plunge. This is clearest in the frequency domain.

The excitation of the modes is encoded in the product $Z_{\mathrm{echo}} = \tilde{\mathcal{K}} Z^{\mathrm{H}}_{\mathrm{BH}}$. Figure 4.14 displays the horizon waveform $Z^{\mathrm{H}}_{\mathrm{BH}}$. For this orbit, most of the power is at negative frequencies and there are strong peaks near orbital frequency $\omega = -m\Omega_{\mathrm{ISCO}}$ and fundamental BH QNM frequency $\omega = -\Omega_R$. Furthermore, $Z^{\mathrm{H}}_{\mathrm{BH}}$ goes to zero at high frequencies.

The echo waveform Z_{echo} is shown in Fig. 4.15 for the case $\tilde{\mathcal{R}} = 1$, $x_0 = -3M$. Note that Z_{echo} inherits the resonance from $\tilde{\mathcal{K}}$. This resonant frequency is similar to the fundamental BH QNM, but has a much slower decay, as can be noted by the slenderness of the peak compared to the peak in the horizon amplitude at the same frequency.

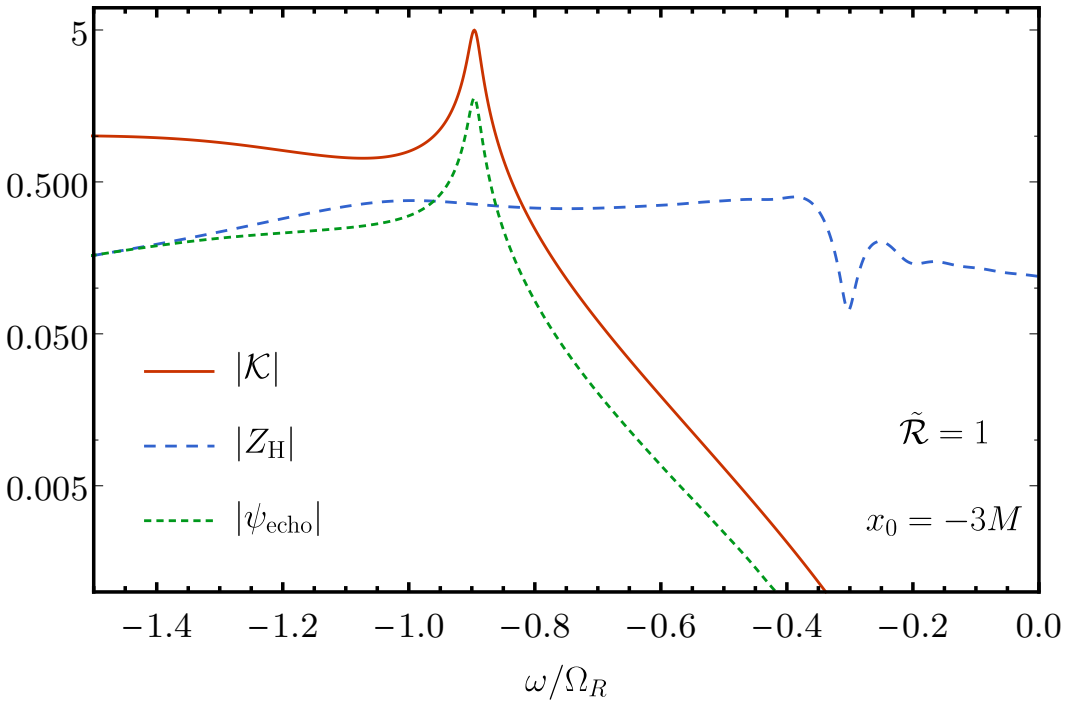

Figure 4.15: Single mode Excitation. The $(\ell, m) = (2, 2)$ response function $|\tilde{\mathcal{K}}|$, the horizon waveform $Z^{\rm H}_{\rm BH}$, and the echo sum $\tilde{\psi}_{\rm echo}$ for $\tilde{\mathcal{R}} = 1$ and $x_0 = -3M$. The waveforms are generated by a test charge following the ISCO plunge orbit

Echoes from Interference of Modes

Recall that for large values of x_0, the total waveform appears as a sum of distinct echo pulses. This scenario also can be understood in terms of the additional resonances of the ECO spacetime. Figure 4.16 shows the frequency domain echo amplitude $Z_{\rm echo}$ for three choices of $\tilde{\mathcal{R}}$, all with $x_0 = -50M$: $\tilde{\mathcal{R}} = 1$ appears in the top panel, $\tilde{\mathcal{R}} = 0.5$ appears in the middle panel, and the wormhole appears in the bottom panel. The horizon amplitude is substantial at all of the resonances of $\tilde{\mathcal{K}}$, which have spacing $\omega_{\rm FSR}$. The result is that all of the resonances appear in the $Z_{\rm echo}$ in all three cases.

In fact, this is what we expect a sum of echo pulses to look like in the frequency domain. Suppose that in the time domain a function $f(t)$ is a sum of delta function pulses spaced by $T = 2\pi/\Delta\omega$ beginning at time $t = 0$, with each pulse γ times smaller than than the previous,

$$f(t) = \sum_{n=0}^{\infty} \gamma^n \delta\left(t - nT\right) . \tag{4.46}$$

Then in the frequency domain $\tilde{f}(\omega)$ is an infinite sum of equally spaced, equally

excited resonances (see Appendix 4.11 for a derivation)

$$\tilde{f}(\omega) = \frac{i\Delta\omega}{2\pi} \sum_{n=-\infty}^{\infty} \frac{1}{\omega - \omega_n},$$
$$\omega_n = n\Delta\omega + i\frac{\Delta\omega}{2\pi} \ln\gamma\,. \tag{4.47}$$

Before the echoes begin to blend together, but after the initial BH waveform decays, the waveforms $\psi^{\infty}(u)$ shown in Figs. 4.9, 4.10 and 4.11 are loosely of the form of $f(u)$ if we view each pulse as a delta function and choose $T = 2|x_0|$ (or $T = 4|x_0|$ for the wormhole case). Therefore it is not surprising that $Z_{\rm echo}(\omega)$ resembles $\tilde{f}(\omega)$ at low frequencies, where it is more reasonable to approximate each pulse appearing in the plots by a delta function.

4.5 General Features of echoes

We turn now to some additional applications of our formalism for reprocessing black hole waveforms into waveforms from ECOs. After reviewing some general features of echoes in our model, we develop a simple template that broadly reproduces the echoes seen by distant observers. We also discuss the energy content of these echoes.

General Features of echoes

The horizon waveform $\psi^{\rm H}_{\rm BH}$ has some generic features which should hold for many sources. Much like the inspiral, merger, and ringdown signal emitted from a compact binary, there are three phases to $\psi^{\rm H}_{\rm BH}$. These phases are easily identifiable for the horizon waveform generated by the ISCO plunge, shown in the top panel of Fig. 4.6. At early times, when the small body is approximately on the ISCO orbit, the waveform frequency is approximately proportional to the ISCO orbital frequency, $\omega = m\Omega_{\rm ISCO}$. The waveform peaks around when the small body crosses the horizon at $v_{\rm H}$, and there is also a discontinuity in the derivative of $\psi^{\rm H}_{\rm BH}$ when the particle crosses the horizon (or x_0, in our large $|x_0|$ approximation). At late times, after the particle has crossed the horizon, the waveform is dominated by a decaying sinusoid at the fundamental BH QNM frequency. These features are also seen in the frequency domain waveform shown in Fig. 4.14 and discussed in Sec. 4.4.

The ringdown has a larger effect on the shape of the first few echoes than the earlier parts of $\psi^{\rm H}_{\rm BH}$, because the fundamental QNM frequency is transmitted more easily through the potential barrier. Meanwhile, the horizon waveform at early times, which is generally at lower frequencies associated with the inspiral orbital timescale, mostly reflects off of the inside of the potential barrier and contributes

less to the first echo. The later echoes, having already lost power at frequencies near $\omega = \Omega_R$ from each earlier scatter off of the potential barrier, depend more intricately on the details of the horizon waveform at early times.

We illustrate this in Fig. 4.17, which examines echoes from the ISCO plunge for constant reflectivity $\tilde{\mathcal{R}}$. Figure 4.17 shows the frequency domain horizon waveform $Z^{\rm H}_{\rm BH}$ as well as three echoes $Z^{(n)}_{\rm echo}$, where

$$Z^{(n)}_{\rm echo} = \tilde{\mathcal{K}}^{(n)} Z^{\rm H}_{\rm BH} \tag{4.48}$$

are the Fourier conjugates of the nth echoes $\psi^{(n)}_{\rm echo}(u)$. The first echo inherits the peak of $Z^{\rm H}_{\rm BH}$ near Ω_R, but the peak near $m\Omega_{\rm ISCO}$ is removed by $\tilde{\mathcal{T}}_{\rm BH}$. The third echo similarly retains a peak near $\omega = -\Omega_R$, although shifted to a slightly lower frequency compared to the first, and is significantly narrower. By the tenth eleventh echoes, the differences between successive echoes has become small, and the echoes retain a suppressed peak near (but to the right of) $\omega = -\Omega_R$. Overall, we see that because of the low frequency suppression in all the echoes, the ringdown portion of the horizon waveform is most important for determining the shape of the first several echoes.

Template for echoes

The observation that the ringdown of the horizon waveform $\psi^{\rm H}_{\rm BH}$ is the most important factor for determining the shape of the echoes leads to a simple idea for a template for the echoes. Construct a template $Z^{\rm H}_{\rm T}$ for the horizon waveform $Z^{\rm H}_{\rm BH}$ consisting of only a ringdown at the fundamental QNM frequency. Then construct a template $Z_{\rm T}$ for the echoes $Z_{\rm echo}$ and a template $Z^{(n)}_{\rm T}$ for each echo $Z^{(n)}_{\rm echo}$ using the transfer functions

$$Z_{\rm T} = \tilde{\mathcal{K}} Z^{\rm H}_{\rm T}, \qquad\qquad Z^{(n)}_{\rm T} = \tilde{\mathcal{K}}^{(n)} Z^{\rm H}_{\rm T}. \tag{4.49}$$

To model the ringdown of the horizon waveform, we take a superposition of decaying sinusoids that each are excited at a slightly different time. In the time domain our template for the horizon waveform is

$$\begin{aligned} \psi^{\rm H}_{\rm T}(t) &= (\psi_{\rm QNM} * h)(t) \\ h(t) &= \frac{\beta}{\sqrt{2\pi}} \exp\left(\frac{-(t-t_s)^2}{2/\beta^2}\right) \\ \psi_{\rm QNM}(t) &= \theta(t)\left(-i\alpha_+ e^{-i\Omega_+ t} - i\alpha_- e^{-i\Omega_- t}\right), \end{aligned} \tag{4.50}$$

where we use $\psi^{\rm H}_{\rm T}$ to indicate the Fourier conjugate of $Z^{\rm H}_{\rm T}$. We weight each decaying sinusoid by the Gaussian $h(t)$. The template is parametrized by two complex

amplitudes $\alpha_\pm$ for the sinusoids at the positive and negative QNM frequencies, $\Omega_\pm = \pm\Omega_R + i\Omega_I$, a central start time t_s, and a frequency width β. In the frequency domain, the template for the horizon waveform takes the even simpler form

$$Z_{\rm T}^{\rm H}(\omega;\vec{p}) = e^{i\omega t_s} e^{-\omega^2/(2\beta^2)} \left(\frac{\alpha_+}{\omega-\Omega_+} + \frac{\alpha_-}{\omega-\Omega_-}\right), \tag{4.51}$$

where $\vec{p} = (\alpha_+, \alpha_-, t_s, \beta)$ are the template parameters.

To evaluate the template we investigate its ability to match both individual echoes and complete waveforms produced from a test charge following the ISCO plunge orbit, in the case of a constant $\tilde{\mathcal{R}}$. To quantify the match, we define the overlap of two waveforms as

$$\rho^2(Z_1, Z_2) = \frac{|<Z_1|Z_2>|^2}{<Z_1|Z_1><Z_2|Z_2>}, \tag{4.52}$$

in terms of the inner product

$$<a|b> = \int_{-\infty}^{\infty} \frac{d\omega}{2\pi} \tilde{a}^*(\omega)\tilde{b}(\omega)\,. \tag{4.53}$$

The overlap satisfies $0 \leq \rho \leq 1$, with $\rho \approx 1$ indicating a good match.

For our first test of the model, we consider the overlap for the individual echoes, $\rho(Z_{\rm T}^{(n)}, Z_{\rm echo}^{(n)}; \vec{p})$. Note that the overlap for the individual echoes is independent of x_0 and $\tilde{\mathcal{R}}$. We set the template parameters $\vec{p} = \vec{p}_1$ by analytically maximizing the overlap over $\alpha_\pm$ [154] at fixed nonlinear model parameters t_s and β; we then numerically search for optimal parameters t_s and β. We compute the overlap for successive echoes using the same fixed $\vec{p}_1$.

In Fig. 4.18, we plot $\rho(Z_{\rm T}^{(n)}, Z_{\rm echo}^{(n)}; \vec{p}_1)$ versus n for the first twenty echoes. We see that the overlap is approximately between 0.96 and 0.97 and asymptotes to a constant as the echo number n grows. We show a direct comparison of the template and the first echo in Fig. 4.19 to give an example of the type of match produced by an overlap in this range[3]. Importantly, this analysis shows that the first echo can be used to generate values of the template parameters that produce reasonably good overlaps for later echoes.

[3] Note that our procedure does not completely fix the parameters $\alpha_\pm$ since the normalized overlap is invariant under shifts $Z_{\rm T}^{(n)} \to aZ_{\rm T}^{(n)}$ for any complex constant a. To completely fix the parameters for Figs. 4.19 and 4.20, we also impose the constraints $<Z_{\rm T}^{(n)}|Z_{\rm T}^{(n)}> = <Z_{\rm echo}^{(n)}|Z_{\rm echo}^{(n)}>$ and $\mathrm{ph}(<Z_{\rm T}^{(n)}|Z_{\rm echo}^{(n)}>) = 0$. This is equivalent to minimizing the least squares differences between the waveforms while holding $<Z_{\rm T}^{(n)}|Z_{\rm T}^{(n)}>$ constant.

It is insightful to compare these overlaps to the corresponding overlap $\rho(Z_{\rm T}^{\rm H}, Z_{\rm BH}^{\rm H}; \vec{p}_1)$ between the horizon waveform and its template at the same parameters $\vec{p}_1$. This overlap is $\rho = 0.72$, and it is smaller than the overlap for the individual echoes. A direct comparison of the horizon waveform and its template, shown in Fig. 4.20, reveals that the template misses key features of the horizon waveform at low frequencies $|\omega| < \Omega_R$. We explain the enhanced performance of the template for the echoes compared to the horizon waveform as being due to the echo transfer functions $\tilde{\mathcal{K}}^{(n)}$, which filter out the low frequencies where the template performs poorly.

To investigate how the template models the full echo amplitude $Z_{\rm echo}$, we investigate the overlap $\rho(Z_{\rm T}, Z_{\rm echo}; \vec{p})$. Note that this overlap does depend on x_0 and $\tilde{\mathcal{R}}$. We fix x_0 and $\tilde{\mathcal{R}}$ and maximize over the template parameters $\vec{p}$. The results are shown in Fig. 4.21 for $x_0 = -3M, -20M$, and $-50M$ at several values of $\tilde{\mathcal{R}}$ ranging from 0.01 to 1.

We see that the overlap is generally greater than 0.96 for $\tilde{\mathcal{R}} < 0.99$. For $\tilde{\mathcal{R}} \geq 0.99$, the overlap for the larger values of x_0 drops significantly. The dramatic reduction in the overlap occurs because the amount of power (as determined by the power density $dP/d\omega = |Z_{\rm echo}|^2$) in the echo waveform at low frequencies significantly increases as $\tilde{\mathcal{R}} \to 1$ when x_0 is large. This power is contained in the narrow resonances appearing in Fig. 4.16. This degrades the overlap because the template is only designed to perform well for frequencies near the BH QNM frequency Ω_R. For example when $x_0 = -50M$ and $\tilde{\mathcal{R}} = 0.999$, less than 8% of the power is at frequencies $|\omega| < 0.6\Omega_R$, while when $\tilde{\mathcal{R}} = 1$, the number jumps to 35%.

Energy in the echoes

Our formalism also allows us to relate the energy in the ECO waveform to the energy in the BH waveforms on the horizon $\mathcal{H}^+$ and at asymptotic infinity $\mathcal{I}^+$. For very compact ECOs, we derive a simple relationship between the energy in the black hole waveform and the energy in the ECO waveform.

The stress energy tensor for the scalar field is $T_{\mu\nu} = \nabla_\mu\phi\nabla_\nu\phi - (1/2)g_{\mu\nu}\nabla^\rho\phi\nabla_\rho\phi$ and energy flow is governed by the energy flux vector $-T_{\mu\nu}(\partial/\partial t)^\nu$. Given a wave $\psi(v)$ that impinges on the horizon or a wave $\psi(u)$ that is incident on $\mathcal{I}^+$, the energy

$\mathcal{E}[\psi]$ is the functional

$$\mathcal{E}[\psi] = \sum_{\ell m} E_{\ell m}[\psi], \tag{4.54}$$

$$E_{\ell m}[\psi] = \int_{-\infty}^{\infty} d\tau |\dot{\psi}_{\ell m}(\tau)|^2 = \int_{-\infty}^{\infty} \frac{d\omega}{2\pi} \omega^2 |Z_{\ell m}(\omega)|^2, \tag{4.55}$$

where we have temporarily restored the harmonic indices. The last equality is an application of Parseval's theorem, and we have denoted Z_{lm} as the Fourier conjugate of ψ_{lm}.

The energy of the ECO waveform E^{∞} can be expressed in terms of the energy in the black hole waveform $E^{\infty}_{\rm BH} = E[\psi^{\infty}_{\rm BH}]$, the energy in the echoes $E_{\rm echo} = E[\psi_{\rm echo}]$, and correlations between the echoes and the black hole waveform

$$\begin{aligned} E[\psi^{\infty}_{\rm BH}] &= E[\psi^{\infty}_{\rm BH} + \psi_{\rm echo}] \\ &= E^{\infty}_{\rm BH} + E_{\rm echo} + 2\Re\left[\int_{-\infty}^{\infty} d\tau\, \dot{\psi}^{\infty}_{\rm BH}(\tau)\dot{\psi}_{\rm echo}(\tau)^*\right]. \end{aligned} \tag{4.56}$$

In the limit that x_0 is much larger than the duration of each echo, the different echoes do not overlap, allowing us to neglect the correlations, so that

$$E^{\infty} \approx E^{\infty}_{\rm BH} + E_{\rm echo}. \tag{4.57}$$

An identical argument allows us to write the echo energy as an approximate sum of the energy in each echo.

$$\begin{aligned} E_{\rm echo} &\approx \sum_{n=1}^{\infty} E[\psi^{(n)}_{\rm echo}] = \sum_{n=1}^{\infty} \int \frac{d\omega}{2\pi} \omega^2 |Z^{(n)}_{\rm echo}|^2 \\ &= \int \frac{d\omega}{2\pi} |\tilde{\mathcal{R}}\tilde{\mathcal{T}}_{\rm BH}|^2 \sum_{m=0}^{\infty} |\tilde{\mathcal{R}}\tilde{\mathcal{R}}_{\rm BH}|^{2m} \omega^2 |Z^{\rm H}_{\rm BH}|^2 \\ &= \int \frac{d\omega}{2\pi} \frac{|\tilde{\mathcal{R}}\tilde{\mathcal{T}}_{\rm BH}|^2}{1 - |\tilde{\mathcal{R}}\tilde{\mathcal{R}}_{\rm BH}|^2} \omega^2 |Z^{\rm H}_{\rm BH}|^2, \end{aligned} \tag{4.58}$$

where we have used Eqs. (4.31) and (4.48).

When $\tilde{\mathcal{R}} = 1$, since $|\tilde{\mathcal{T}}_{\rm BH}|^2 = 1 - |\tilde{\mathcal{R}}_{\rm BH}|^2$, the echo energy $E_{\rm echo}$ is precisely the energy $E^{\rm H}_{\rm BH} = E[\psi^{\rm H}_{\rm BH}]$ that would have gone down the horizon in the BH spacetime. When $|\tilde{\mathcal{R}}| < 1$, there will be less energy in the echoes than the horizon waveform, falling to 0 as $\tilde{\mathcal{R}} \to 0$. Finally, Eq. (4.58) predicts that for very compact ECOs, the relationship between the energy in the ECO waveform and BH waveforms on $\mathcal{H}^+$ and $\mathcal{I}^+$ is independent of x_0.

Figure 4.22 shows $E_{\rm echo}/E^{\rm H}_{\rm BH}$ for $(\ell, m) = (2, 2)$ waveforms from the ISCO plunge orbit for a variety of $\tilde{\mathcal{R}}$ and x_0. As expected, smaller values of $\tilde{\mathcal{R}}$ produce echoes containing less energy and the ratio becomes independent of x_0 as $x_0 \to \infty$. For perfectly reflecting, extremely compact ECOs with $x_0 > 20M$, more than 97% of the energy in the horizon waveform is radiated in the echoes.

4.6 Conclusions

In this work, we derive a relationship between the Green's functions for a massless scalar field in a BH spacetime and in the exterior region of ECOs. This is accomplished by replacing the compact object with a reflecting boundary near the horizon of the BH. The exterior of any ECO can be modeled with a particular choice of boundary location and frequency dependent reflectivity.

We use the relationship between Green's functions to show that the ECO waveform seen by asymptotic observers is the same as that seen in the BH spacetime, plus additional emission from reflection off the boundary. This additional emission can be computed by reprocessing the horizon waveform in the BH spacetime using a simple transfer function. We find that the difference between the BH and ECO waveforms at infinity can be understood either as a superposition of echo pulses or a superposition of modes associated with poles in the ECO Green's function. Furthermore, we show how both the individual echoes and the new mode frequencies encode the information describing the ECO model; namely the boundary reflectivity and location.

Our formalism also explains how the BH QNMs imprint themselves in ECO waveforms: The ECO waveform has a main burst that rings down at the black hole QNM frequencies. In addition, the frequency content of the individual echo pulses is largely determined by the frequency content in the horizon waveform $\psi^{\rm H}_{\rm BH}$ near the BH QNM frequencies. Despite the imprint of these frequencies on the ECO waveform, our formalism also shows that the BH QNM frequencies are not poles in the ECO Green's function. Rather, the piece of the Green's function responsible for producing the main burst and the piece responsible for the echoes both have poles at the BH QNM frequencies, which cancel in the full expression.

We demonstrate how our formalism can be used to reprocess a black hole waveform into an ECO waveform by studying the echoes produced by a test charge spiralling in from the ISCO. We use our numerical results and analytic observations to design a simple template for the echoes that accurately reproduces our waveforms, with

normalized overlaps $\rho > 0.95$ for most values of boundary location and reflectivity (taken here to be frequency independent).

To determine the significance of our proposed template, future work will be required to extend the formalism to gravitational perturbations of Kerr. In addition to the added algebraic complexity, one will have to overcome the absence of Birkhoff's theorem in Kerr, as well as the lack of a simple scheme for parameterizing reflecting boundary conditions for gravitational perturbations [126] (see [112] for one possible prescription). Ideally, future work will also extend the formalism beyond test particle sources, so that comparable mass binaries can be treated. Nevertheless, our results indicate that a relatively simple template, combined with a prescription for reprocessing waveforms generated in black hole spacetimes, can be used to investigate the existence of ECOs and their echoes using gravitational wave observations.

4.7 acknowledgments

We thank Vitor Cardoso, Baoyi Chen, Chad Galley, Davide Gerosa, Yiqiu Ma, David Nichols, Samaya Nissanke, Paolo Pani, Leo Stein, Saul Teukolsky, and Huan Yang for valuable discussions. We are grateful to Ofek Birnholtz, Vitor Cardoso, Gaurav Khanna, Hiroyuki Nakano, and Paolo Pani for providing feedback on a draft of this manuscript. The figures were made using the MaTeX package [1]. This research was supported at Caltech by NSF grant PHY-1404569, the Walter Burke Institute for Theoretical Physics, and the David and Barbara Groce startup fund.

4.8 Appendix A: Calculation of the reflection and transmission coefficients

In this appendix we describe our calculation of the reflection and transmission coefficients $\mathcal{R}_{\rm BH}$ and $\mathcal{T}_{\rm BH}$, in both the time and frequency domains.

Time Domain

The scattering coefficients $\tilde{\mathcal{R}}_{\rm BH}$ and $\tilde{\mathcal{T}}_{\rm BH}$ are defined from the frequency domain solution $\tilde{\psi}_{\rm up}$ to Eq. (4.4). An equivalent time-domain definition is found in terms of a solution ψ to the characteristic initial value problem

$$\frac{\partial^2\psi}{\partial u\partial v} + \frac{fV}{4}\psi = 0 \tag{4.59}$$

with characteristic initial data posed on the past horizon $\mathcal{H}^-$ and past null infinity $\mathcal{I}^-$ consisting of a delta function pulse

$$\psi(u)|_{\mathcal{H}^-} = \delta(u), \qquad \psi(v)|_{\mathcal{I}^-} = 0 \tag{4.60}$$

as shown in Fig. 4.23. Then $\mathcal{T}_{\rm BH}(u)$ is the field $\psi(u)|_{\mathcal{I}^+}$ evaluated at future null infinity and $\mathcal{R}_{\rm BH}(v)$ is the field $\psi(v)|_{\mathcal{H}^+}$ evaluated on the future horizon. This is seen as follows.

When $V = 0$, the general solution to Eq. (4.59) is a superposition of an outward traveling wave and an inward traveling wave,

$$\psi(v, u) = h(u) + k(v), \tag{4.61}$$

where h and k are free functions. The potential can be neglected, $V \approx 0$, in the near horizon region, roughly bounded by the left blue dashed line in Fig. 4.23, and also in the far field region, roughly bounded by the right blued dashed line. We match the general solution Eq. (4.61) to the boundary data in these regions to obtain

$$\psi(v, u) = \begin{cases} \delta(u) + \psi(v)|_{\mathcal{H}^+}, & x \to -\infty, \\ \psi(u)|_{\mathcal{I}^+}, & x \to \infty\,. \end{cases} \tag{4.62}$$

Notice the field on the horizon is not determined by the initial conditions in the near horizon matching region. Likewise the field at future null infinity is not determined by the initial conditions in the far-field matching region. Calculating these fields requires all of the initial data.

Rewriting the solution in (t, x) coordinates and taking the Fourier transform with respect to t yields

$$\tilde{\psi}(\omega, x) = \begin{cases} e^{i\omega x} + \tilde{\psi}(\omega)|_{\mathcal{H}^+} e^{-i\omega x}, & x \to -\infty \\ \tilde{\psi}(\omega)|_{\mathcal{I}^+} e^{i\omega x}, & x \to \infty. \end{cases} \tag{4.63}$$

Comparing this with frequency domain definition Eq. (4.14) of $\mathcal{R}_{\rm BH}$ and $\mathcal{T}_{\rm BH}$, we identify

$$\tilde{\psi}(\omega)|_{\mathcal{H}^+} = \tilde{\mathcal{R}}_{\rm BH}(\omega), \tag{4.64}$$

$$\tilde{\psi}(\omega)|_{\mathcal{I}^+} = \tilde{\mathcal{T}}_{\rm BH}(\omega), \tag{4.65}$$

establishing the equivalence of the two definitions.

For our numerical calculations, it is important to realize that $\mathcal{T}_{\rm BH}(u)$ only has support for $u \geq 0$ and $\mathcal{T}_{\rm BH}(0) = \delta(0)$. The first fact follows from $\psi(v, u) = 0$ for $u < 0$, since for these times ψ lies in the domain of dependence of the portion of initial data which is equal to zero. The second conclusion follows from the high frequency behavior $\tilde{\mathcal{T}}_{\rm BH} \to 1$ as $\omega/\Omega_R \to \pm\infty$ [52]. This implies that $\tilde{\mathcal{T}}_{\rm BH} = 1 + f(\omega)$, where

$f \to 0$ as $\omega \to \pm\infty$. Taking the Fourier transform of both sides gives the delta function at $u = 0$.

We use our characteristic code for homogeneous solutions to wave equations detailed in Sec. 4.9 to solve this characteristic initial value problem. Namely, we pose the initial data on the future part of a null cone described by $v = v_0$ and $u = 0$ and choose $-v_0$ large enough that the delta function pulse $\delta(u)$ is deep in the near horizon region. We use a discrete approximation for the delta function in the initial data

$$\delta(u) = \begin{cases} \dfrac{1}{2(2h)}, & u = 0 \\ 0, & \text{otherwise} \end{cases} . \tag{4.66}$$

where our numerical grid is spaced by $2h$. We extract $\mathcal{R}_{\rm BH}$ off of the ray $u = u_E$ in our computational domain that is closest to $\mathcal{H}^+$. Similarly we extract $\mathcal{T}_{\rm BH}$ off of the ray $v = v_E$ in our computational domain that is closest to $\mathcal{I}^+$.

We performed convergence checks on our choice of stepsize h, initial data ray location v_0 and the location of the extraction rays v_E and u_E. We used $h = 0.025M$. We verified that the same numerical approximation of the $\delta(u)$ that we used in our initial data appears in $\mathcal{T}_{\rm BH}$. For calculations in the paper that rely on $\mathcal{T}_{\rm BH}$, we insert the δ function analytically and only use the smooth part of $\mathcal{T}_{\rm BH}$ from our code. To obtain the smooth part of $\mathcal{T}_{\rm BH}(u)$ near zero we extrapolated this data backwards in time a single time step.

Frequency Domain

For computations that required accurate frequency domain representations of $\tilde{\mathcal{R}}_{\rm BH}$ and $\tilde{\mathcal{T}}_{\rm BH}$, we also computed $\tilde{\mathcal{R}}_{\rm BH}$ and $\tilde{\mathcal{T}}_{\rm BH}$ directly in the frequency domain. This also provided an independent check of our time domain methods.

At a fixed frequency, the homogeneous wave equation (4.4) together with one of the two boundary conditions in Eq. (4.13) forms a boundary value problem for $\tilde{\psi}_{\rm up}(\omega, x)$. The coefficients $B_{\rm out}$ and $B_{\rm in}$ necessary to compute $\tilde{\mathcal{R}}_{\rm BH}$ and $\tilde{\mathcal{T}}_{\rm BH}$ are determined from the solution and its derivative near the opposite boundary by comparing to the remaining boundary condition.

We numerically integrated outward from the horizon, using an analytic third-order expansion of $\tilde{\psi}$ to match the boundary condition there. We extracted the field at a large radius $r = 1000M$, matching to an asymptotic expansion of $\tilde{\psi}$ including terms up to third order in $1/r$.

4.9 Appendix B: Point Particle Waveforms

In this appendix we provide Green's functions solutions for the scalar field $\psi_{\rm BH}$ in the BH spacetime, specialized to point particle sources for observers at future null infinity $\mathcal{I}^+$ and the future horizon $\mathcal{H}^+$.

Green's Function solution

The boundary conditions for $\psi_{\rm BH}$ in Eq. (4.19) select the retarded solution to the Klein-Gordon equation

$$\begin{aligned}\psi_{\rm BH}(x,t) &= \int_{-\infty}^{\infty} dt' \int_{-\infty}^{\infty} dx' S(x,t) g_{\rm BH}(x,x',t-t'),\\ S(x,t) &= -rf(r)\rho_{\ell m}(x,t),\end{aligned} \tag{4.67}$$

constructed from the retarded (biscalar) Green's function $g_{\rm BH}(x,x',\tau)$ and the spherical harmonic components of the scalar charge density[4]. The retarded Green's function obeys $g_{\rm BH}(x,x',t-t') = 0$ when $t-t' < |x-x'|$ and the differential equation

$$\frac{\partial^2 g_{\rm BH}}{\partial x^2} - \frac{\partial^2 g_{\rm BH}}{\partial t^2} - f(r)V(r)g_{\rm BH} = \delta(t-t')\delta(x-x'). \tag{4.68}$$

We are interested in the waveforms on either the BH horizon or at asymptotic infinity. This leads us to consider the asymptotic Green's functions

$$g_{\rm BH} \sim \begin{cases} g_{\rm H}(x', v-v'), & \text{as } x \to -\infty,\ v \text{ fixed},\\ g_{\infty}(x', u-u'), & \text{as } x \to \infty,\ u \text{ fixed}, \end{cases} \tag{4.69}$$

which describe the response on the horizon and at infinity, respectively.

We also need the appropriate source functions, specialized to ingoing coordinates (v,x) and outgoing coordinates (u,x). The scalar charge density of a point particle of scalar charge q, following the trajectory $x_p^\mu(\tau)$ is

$$\rho(x^\mu) = q\int d\tau \frac{\delta^{(4)}(x^\mu - x_p^\mu(\tau))}{\sqrt{-g}}, \tag{4.70}$$

Resolving into spherical harmonics $\rho = \sum_{\ell m}\rho_{\ell m}Y_{\ell m}$, re-parameterizing by advanced time, and writing the result in ingoing coordinates leads to

$$\begin{aligned} S(x,v) &= \hat{S}_{\rm in}(v)\delta(x-x_p),\\ \hat{S}_{\rm in}(v) &= \frac{-qY^*_{\ell m}(\theta_p,\phi_p)}{r_p(dv_p/d\tau)}, \end{aligned} \tag{4.71}$$

[4]Note that S, $\psi_{\rm BH}$, $g_{\rm BH}$ and all variants of them which appear in this appendix have (ℓ,m) indices which we suppress for brevity.

where the trajectory is evaluated at v. Similarly, if we re-parameterize by the retarded time, and write the result in outgoing coordinates, the source is

$$\begin{aligned} S(x,u) &= \hat{S}_{\rm out}(u)\delta(x-x_p), \\ \hat{S}_{\rm out}(u) &= \frac{-qY^*_{\ell m}(\theta_p,\phi_p)}{r_p(du_p/d\tau)}, \end{aligned} \tag{4.72}$$

where the trajectory is evaluated at the retarded time u.

With these definitions, the horizon waveform is

$$\begin{aligned} \psi^{\rm H}_{\rm BH}(v) &= \int_{-\infty}^{\infty} dx' \int_{-\infty}^{\infty} dv' S(x',v') g_{\rm H}(x', v-v') \\ &= \int_{-\infty}^{\infty} dv' \hat{S}_{\rm in}(v') g_{\rm H}(x_p(v'), v-v'). \end{aligned} \tag{4.73}$$

For a particle that crosses the horizon at an advance time $v = v_{\rm H}$, this becomes, using the causal property of the retarded Green's function,

$$\psi^{\rm H}_{\rm BH}(v) = \begin{cases} \displaystyle\int_{-\infty}^{v} dv' \hat{S}_{\rm in}(v') g_{\rm H}(x_p(v'), v-v'), & v < v_{\rm H}\,, \\ \displaystyle\int_{-\infty}^{v_{\rm H}} dv' \hat{S}_{\rm in}(v') g_{\rm H}(x_p(v'), v-v'), & v \geq v_{\rm H}\,. \end{cases} \tag{4.74}$$

Meanwhile, the asymptotic waveform is given by

$$\begin{aligned} \psi^{\infty}_{\rm BH}(u) &= \int_{-\infty}^{\infty} dx' \int_{-\infty}^{\infty} du' S(x',u') g_{\infty}(x', u-u') \\ &= \int_{-\infty}^{u} du' \hat{S}_{\rm out}(u') g_{\infty}(x_p(u'), u-u'). \end{aligned} \tag{4.75}$$

where we have again used causality to truncate the upper limit of the integration to u.

In this paper, we extensively study the radiation produced by a test charge on the ISCO plunge orbit. Such a particle asymptotes to the ISCO radius $r = 6M$ as $t \to -\infty$ and has a specific energy $E_{\rm ISCO} = 2\sqrt{2}/3$ and a specific angular momentum of $L_{\rm ISCO} = \sqrt{12}M$. To calculate the waveforms $\psi^{\infty}_{\rm BH}$ and $\psi^{\rm H}_{\rm BH}$ we rely on Eqs. (4.74) and (4.75) with analytic expressions for the trajectory found in [84], and a Green's function that we compute numerically using a characteristic code detailed in Sec. 4.9.

Characteristic Initial Value Problem for the Green's function

We obtain the retarded Green's function $g_{\rm BH}$ for the scalar field in the BH spacetime as the solution of a characteristic initial value problem. In null coordinates (v, u),

Eq. (4.68) for $g_{\rm BH}(v, v', u, u')$ takes the form

$$\frac{\partial^2 g_{\rm BH}}{\partial v \partial u} + \frac{fV}{4} g_{\rm BH} = -\frac{1}{2}\delta(\Delta u)\delta(\Delta v) \tag{4.76}$$

where $\Delta u = u - u'$, $\Delta v = v - v'$. Causality motivates us to look for a distributional solution

$$g_{\rm BH}(v, v', u, u') = \hat{g}(v, v', u, u')\theta(\Delta u)\theta(\Delta v), \tag{4.77}$$

where $\hat{g}$ is a smooth function defined in the future light cone of the source point (v', u'). Substitution of the ansatz (4.77) in (4.76) yields

$$\begin{aligned} &\delta(\Delta u)\delta(\Delta v)\hat{g} + \theta(\Delta u)\delta(\Delta v)\frac{\partial \hat{g}}{\partial u} + \theta(\Delta v)\delta(\Delta u)\frac{\partial \hat{g}}{\partial v} \\ &+ \theta(\Delta u)\theta(\Delta v)\left(\frac{\partial^2 \hat{g}}{\partial v \partial u} + \frac{fV}{4}\hat{g}\right) = -\frac{1}{2}\delta(\Delta u)\delta(\Delta v) \end{aligned} \tag{4.78}$$

We now equate terms of equal singularity strength. The first term on the LHS balances the RHS if we demand $[\hat{g}] \equiv g(v', v', u', u') = -1/2$. The second term, which is only nonzero along $v = v'$, vanishes if we demand $\partial_u \hat{g}|_{v=v'} = 0$, which can be integrated to yield $\hat{g}|_{v=v'} = -1/2$. Likewise, setting the third term to zero yields $\hat{g}|_{u=u'} = -1/2$. Finally, the fourth term vanishes if $\hat{g}$ satisfies the homogeneous wave equation equation

$$\frac{\partial^2 \hat{g}}{\partial v \partial u} + \frac{fV}{4}\hat{g} = 0 \tag{4.79}$$

in the forward light cone of source point.

Equation (4.79), together with the initial data $\hat{g} = -1/2$ posed on the future part of the null cone formed by the rays $u = u'$ and $v = v'$, is a characteristic initial value problem for $g_{\rm BH}$. We solve this numerically using a characteristic code described in Sec. 4.9.

Characteristic Code

We numerically compute $\hat{g}_{\rm BH}$ using a finite-difference characteristic code based on the method of Price and Lousto [98]. For this, we fix a source point (v', u') and solve the homogeneous wave equation (4.79) obeyed by $\hat{g}(v, u)$. We discretize the field point coordinates (v, u) onto a rectangular grid with nodes spaced by $2h$.

A standard computational cell centered on the point $C = (v, u)$ is shown in Fig. 4.24. Referring to the figure, given the data ψ_S, ψ_W, and ψ_E on the bottom three corners of

a computational cell, the value on top corner ψ_N can be obtained with the stepping algorithm

$$\psi_N = -\psi_S + (1 + 2W_C h^2)(\psi_E + \psi_W) \tag{4.80}$$

$$W_C = -\frac{fV}{4}\bigg|_C . \tag{4.81}$$

This algorithm can be derived by integrating the homogeneous wave equation (4.79) over a computational cell with $O(h^4)$ accuracy. Our code inputs initial data on the future part of the light cone formed by the rays $v = v'$ and $u = u'$ and is second order convergent. We generate values for ψ on the remaining nodes of the grid using the stepping algorithm (4.80).

To obtain $g_\infty(x', \Delta u)$, we further fix Δu and use our characteristic code to obtain $g_{\rm BH}$ as a function of field point radius r. Using the fact that the field has an expansion in powers of $1/r$, we then extrapolate the field to future null infinity using Richardson extrapolation.

To extract $g_{\rm H}(x', \Delta v)$, we use our characteristic code to obtain $g_{\rm BH}$ evaluated on the ray u = constant that is closest to the horizon in our computational domain. For early advanced time Δv, this ray is buried deep in the near horizon region, and we approximate $g_{\rm H}(x', \Delta v)$ as $g_{\rm BH}$ evaluated on this ray. We check that this scheme converges as we move the extraction ray u = constant towards $\mathcal{H}^+$.

We perform these calculations for radii between $r' - 2M = 1.7 \times 10^{-5}$ and $r' = r_{\rm ISCO} = 6M$ with $\Delta x' = 1$. We then interpolate between these values to obtain $g_{\rm H}(x', \Delta v)$ and $g_\infty(x', \Delta u)$ that we use in the calculations presented in this paper.

Windowing and Frequency Domain Waveforms

Waveforms from physically relevant orbits are finite in duration. The waveforms produced by the exact ISCO plunge orbit are not; at late times, the waveforms ringdown to zero, but at arbitrarily early times they have an oscillation at $\omega = m\Omega_{\rm ISCO}$ due to the test charge orbiting on the ISCO.

Hence, for all calculations in this paper we consider the echoes produced by a windowed horizon waveform. More precisely we apply a one-sided version of the

Planck-Taper [108] window function to the exact ISCO plunge horizon waveforms:

$$\sigma_T(t, t_1, n) = \begin{cases} 0, & t \leq t_1 \\ \dfrac{1}{1+e^z}, & t_1 < t < t_2 \\ 1, & t \geq t_2 \end{cases}, \tag{4.82}$$

where t_1 is free parameter indicating when the window starts, $t_2 = t_1 + 2a\pi/\Omega_{\rm ISCO}$ with a a free parameter, and z is a function that goes from ∞ at t_1 to $-\infty$ at t_2,

$$z = \frac{t_2 - t_1}{t - t_1} + \frac{t_2 - t_1}{t - t_2}. \tag{4.83}$$

We choose parameters that leave 3 oscillations at early times near $\omega \approx m\Omega_{\rm ISCO}$ and smoothly turn on over the course of two oscillations.

We obtain the horizon waveform $Z^{\rm H}_{\rm BH}$ in the frequency domain by numerically performing the inverse Fourier transform of the time domain waveform $\psi^{\rm H}_{\rm BH}$.

4.10 Appendix C: Wormhole Reflectivity

In this appendix, we compute $\tilde{\mathcal{R}}(\omega)$ for a wormhole [57] describing two Schwarzschild spacetimes of mass M identified with a thin shell of exotic stress-energy at an areal radius r_0 corresponding to a tortoise coordinate location of x_0. Note that the value of $\tilde{\mathcal{R}}$ depends on our phase convention, and we use that of Eq. (4.9), which is invariant under shifts of the origin of the tortoise coordinate x.

To begin, define a new tortoise coordinate y covering the entire wormhole spacetime,

$$\frac{dr}{dy} = \begin{cases} \left(1 - \dfrac{2M}{r}\right), & y > 0 \\ -\left(1 - \dfrac{2M}{r}\right), & y < 0, \end{cases} \tag{4.84}$$

with a different origin $y(r_0) = 0$ than is used for the coordinate x. Scalar waves propagating in the wormhole spacetime are described by the scalar wave equation on the domain $-\infty < y < \infty$, with a non-differentiable, but continuous potential $V(y)$ at $y = r_0$. The reflectivity $\tilde{\mathcal{R}}$ is determined by matching the solution obeying the outgoing boundary condition in the left half of the universe to a solution in the right half.

We accomplish this using the homogeneous solution $\tilde{\psi}_{\rm up}$, although with a different phase normalization than in Eq. (4.13) due to the shift in the origin y,

$$\tilde{\psi}_{\rm up}(y) \sim e^{i\omega y}, \qquad\qquad y \to \infty \tag{4.85}$$

For compact wormholes $r_0 \to 2M$ the potential $V \approx 0$ near the location $x = 0$ and we have

$$\tilde{\psi}_{\rm up}(y) \sim C_{\rm out}(\omega)e^{i\omega y} + C_{\rm in}(\omega)e^{-i\omega y}\,, \qquad\qquad y \to 0 \tag{4.86}$$

From these we define $\tilde{\mathcal{R}}_{\rm W} = C_{\rm in}/C_{\rm out}$ to denote the reflection coefficient using the phase convention (4.85).

In the left half of the universe, $\tilde{\psi}_{\rm up}(-y)$ is the solution describing waves that are completely outgoing at null infinity. Near the matching radius $y = 0$, we have by definition

$$\tilde{\psi}_{\rm up}(-y) \propto e^{-i\omega y} + \tilde{\mathcal{R}}_{\rm W}e^{i\omega y}. \tag{4.87}$$

This matches to the form of desired boundary condition for waves in the right half, $\psi \propto e^{-i\omega y} + \tilde{\mathcal{R}}e^{i\omega y}$, if we choose $\tilde{\mathcal{R}} = \tilde{\mathcal{R}}_{\rm W}$.

Finally, we express this result in terms of the BH scattering coefficients, which use the phase convention of Eq. (4.13). The scattering coefficients defined by Eq. (4.85) are related to those of Eq. (4.13) through a simple shift of the origin of y. This means that

$$\tilde{\mathcal{R}}_{\rm W} = e^{-2i\omega x_0}\tilde{\mathcal{R}}_{\rm BH} \tag{4.88}$$

We see then that the wormhole can be treated using a reflecting boundary at x_0 with

$$\tilde{\mathcal{R}}(\omega) = \tilde{\mathcal{R}}_{\rm BH}(\omega)e^{-2i\omega x_0}\,. \tag{4.89}$$

We use this simple result to explore the echoes in wormhole spacetimes.

4.11 Appendix D: Fourier Transform of Decaying Sequence of Pulses

In this appendix, we derive the Fourier transform of the $f(t)$ given in Eq. (4.46)

$$f(t) = \sum_{n=0}^{\infty} \gamma^n \delta\left(t - nT\right)\,, \tag{4.90}$$

which involves some nontrivial manipulations to arrive at the form in Eq. (4.47). Namely, directly evaluating the Fourier transform with the delta functions gives

$$\tilde{f}(\omega) = \int_{-\infty}^{\infty} dt\, f(t)e^{i\omega t} = \sum_{n=0}^{\infty} \gamma^n e^{i\omega nT} \tag{4.91}$$

The derivation of the two different forms is related to the fact that one can write the Fourier transform $\tilde{c}(\omega)$ of a Dirac comb with period $T = 2\pi/\Delta\omega$

$$c(t) = \sum_{n=-\infty}^{\infty} \delta(t - nT) \tag{4.92}$$

in two different ways. On one hand, directly integrating over the δ functions gives

$$\tilde{c}(\omega) = \sum_{n=-\infty}^{\infty} e^{i\omega nT}. \tag{4.93}$$

On the other hand, the Dirac comb is a periodic function with a period T and can be expanded as a Fourier series

$$\begin{aligned} c(t) &= \sum_{n=-\infty}^{\infty} c_n e^{-i\Delta\omega nt}, \\ c_n &= \frac{1}{T}\int_{-T/2}^{T/2} dt e^{i\Delta\omega nt} c(t) = \frac{1}{T}\,. \end{aligned} \tag{4.94}$$

Comparing this to the expression for the inverse Fourier transform $c(t) = 1/(2\pi)\int d\omega e^{-i\omega t}\tilde{c}(\omega)$ leads to the alternate form of $\tilde{c}(\omega)$

$$\tilde{c}(\omega) = \Delta\omega \sum_{n=-\infty}^{\infty} \delta(\omega - n\Delta\omega) \tag{4.95}$$

We use this result to derive Eq. (4.47) for $\tilde{f}$.

First note that f has a simple relationship to the Dirac comb

$$\begin{aligned} f(t) &= \sum_{n=0}^{\infty} \gamma^n \delta(t - nT) \\ &= e^{(t/T)\ln\gamma} \sum_{n=0}^{\infty} \delta(t - nT) = b(t)c(t), \end{aligned} \tag{4.96}$$

$$b(t) \equiv \theta(t) e^{(t/T)\ln\gamma}, \tag{4.97}$$

where $\theta(t)$ is the unit step function. Then the convolution property of the Fourier transform implies that

$$\tilde{f}(\omega) = \int_{-\infty}^{\infty} \frac{d\omega'}{2\pi} \tilde{b}(\omega - \omega')\tilde{c}(\omega'). \tag{4.98}$$

The Fourier transform $\tilde{b}(\omega)$ is

$$\tilde{b}(\omega) = \int_0^{\infty} dt\, e^{i\omega t + (t/T)\ln\gamma} = -\frac{1}{i\omega + \ln\gamma/T}\,, \tag{4.99}$$

where we have used the fact that $\ln\gamma < 0$ for $0 < \gamma \leq 1$. Substituting Eq. (4.95) and Eq. (4.99) into Eq. (4.98) and integrating over the Dirac comb then yields Eq. (4.47).

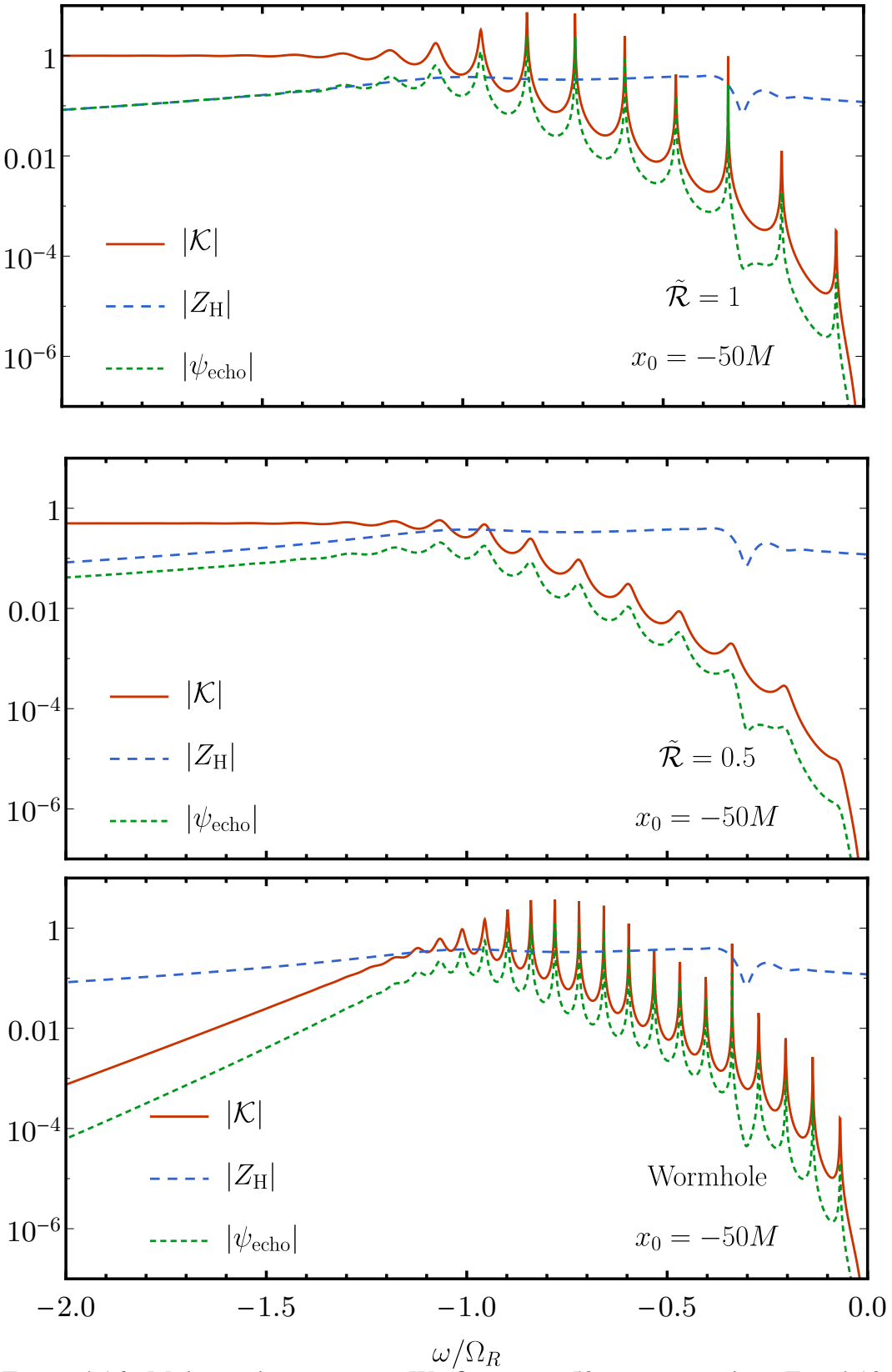

Figure 4.16: Multi-mode excitation. We fix $x_0 = -50M$, a case where Fig. 4.10 shows that the time domain waveform contains echoes for a range of $\tilde{\mathcal{R}}$. We show the $(\ell, m) = (2, 2)$ response function $|\tilde{\mathcal{K}}|$, the horizon waveform $Z^{\rm H}_{\rm BH}$, and the echo sum $\tilde{\psi}_{\rm echo}$. The waveforms ares generated by a test charge following the ISCO plunge orbit. The top panel corresponds to $\tilde{\mathcal{R}} = 1$, the middle panel to $\tilde{\mathcal{R}} = 0.5$, and the lower panel is the wormhole waveform.

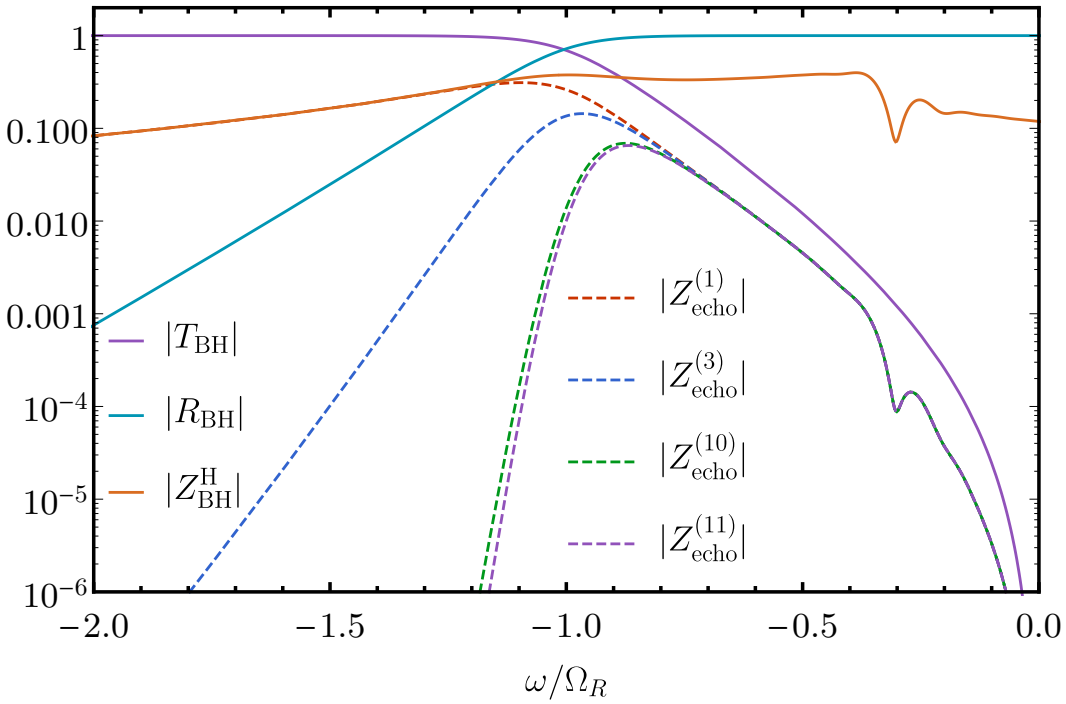

Figure 4.17: The modulus of the $(\ell, m) = (2, 2)$ horizon waveform $Z^{\rm H}_{\rm BH}$ and select $\tilde{\mathcal{R}} = 1$ echoes $Z^{(n)}_{\rm echo}$ generated by a test charge following the ISCO plunge orbit. Also shown are $\tilde{\mathcal{R}}_{\rm BH}$ ad $\tilde{\mathcal{T}}_{\rm BH}$.

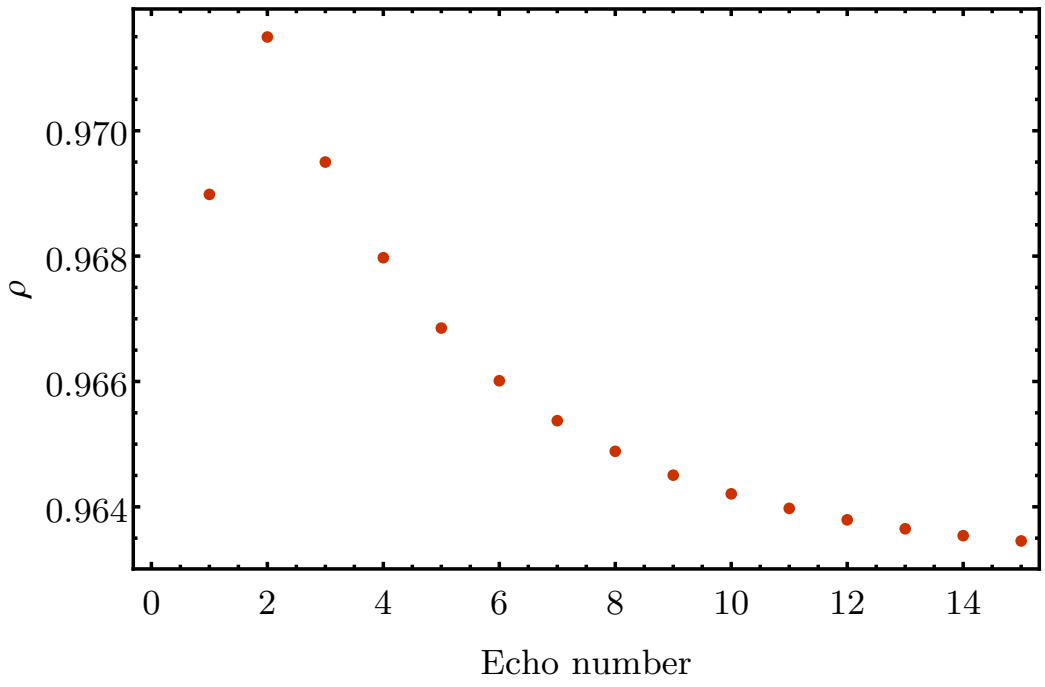

Figure 4.18: The overlap $\rho(Z_{\rm T}^{(n)}, Z_{\rm echo}^{(n)}; \vec{p}_1)$ for the nth individual echo plotted versus echo number n. The parameters $\vec{p}_1$ are determined by maximizing the overlap for the first $n = 1$ echo. We show results for $(\ell, m) = (2, 2)$ and use a test charge following the ISCO plunge trajectory as a source for the $Z_{\rm echo}^{(n)}$.

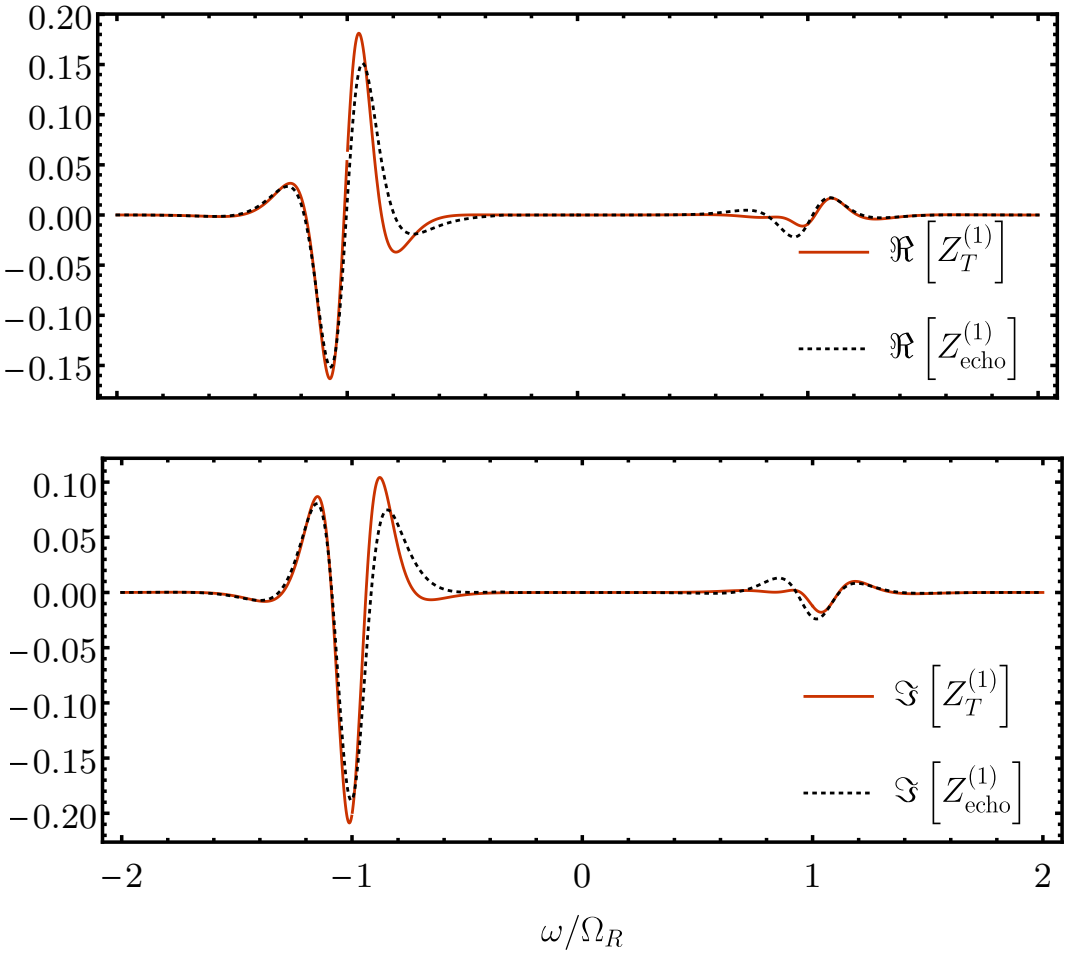

Figure 4.19: A comparison of the $(\ell, m) = (2, 2)$ real (top) and imaginary (bottom) parts of the $n = 1$ echo template $Z_{\mathrm{T}}^{(1)}$ and the first echo. The echo is generated by a test charge following the ISCO plunge orbit and the parameters for the template are determined by maximizing the overlap ρ given by Eq. (4.52) between the template and the echo. The value of the overlap is $\rho = 0.969$.

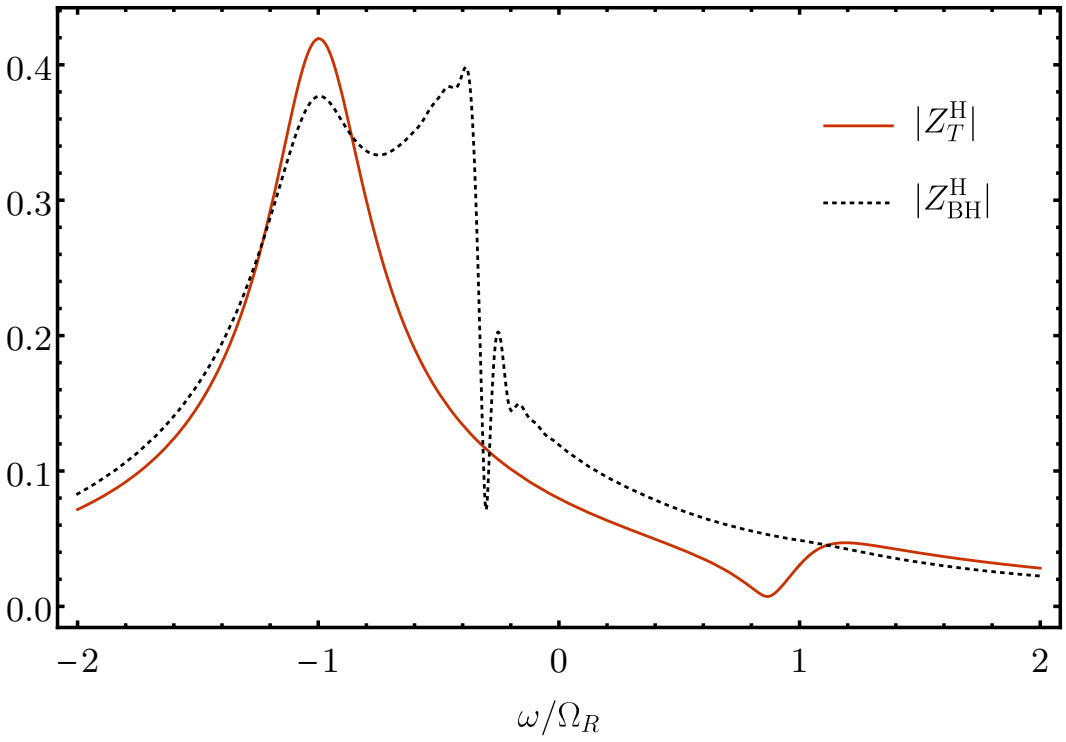

Figure 4.20: A comparison of the modulus of the $(\ell, m) = (2, 2)$ of the horizon waveform template $Z^{\rm H}_{\rm T}$ and numerically computed horizon waveform. The waveform is generated by a test charge following the ISCO plunge orbit and the parameters for the template are determined by maximizing the overlap ρ between the first echo template and the numerically calculated first echo. The value of the overlap is $\rho = 0.72$.

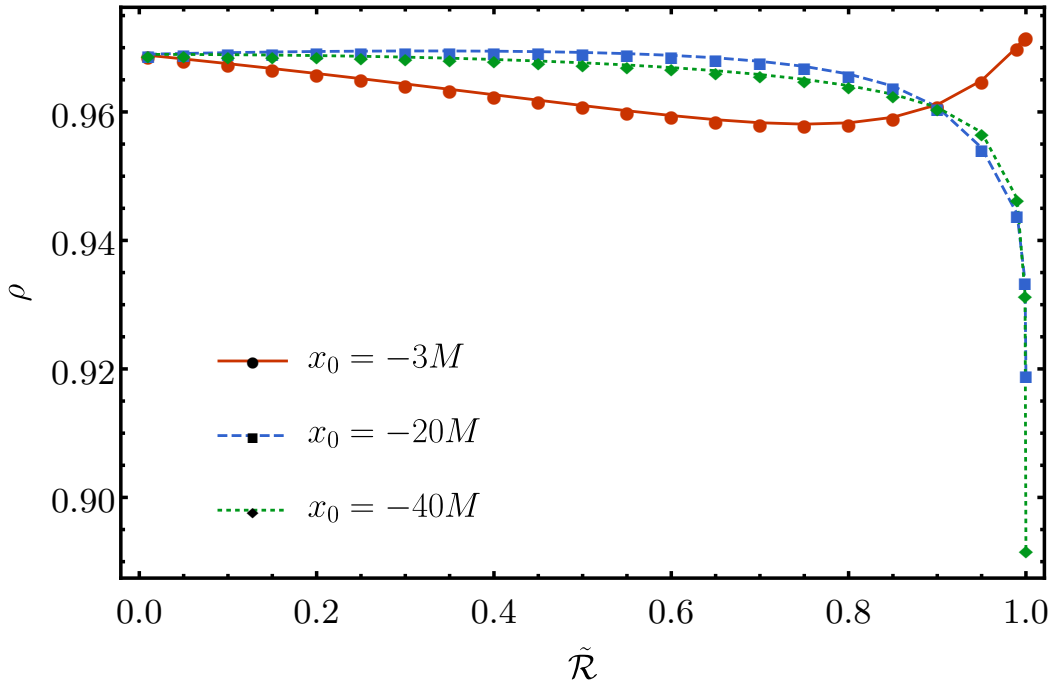

Figure 4.21: The overlap ρ for the $(\ell, m) = (2, 2)$ echo sum Z_{echo} for select values of x_0 and and $\tilde{\mathcal{R}}$. The waveform is generated by a test charge following the ISCO plunge orbit. The template parameters $\vec{p}$ are fixed in each case by maximizing the overlap for the corresponding parameters.

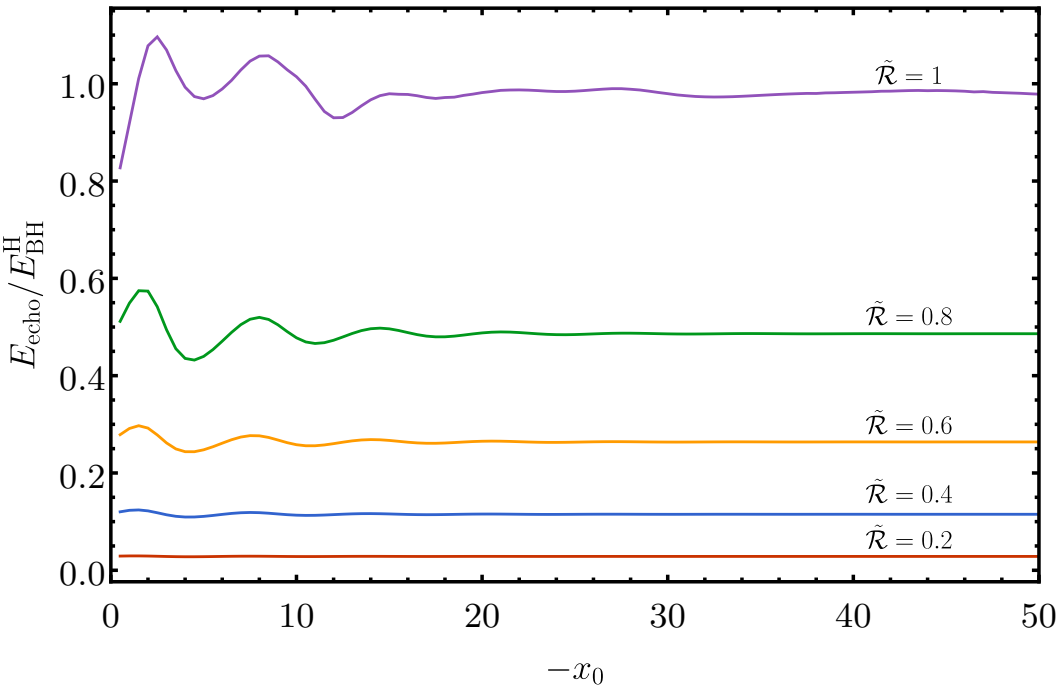

Figure 4.22: The energy $E_{\rm echo}$ in the $(\ell, m) = (2, 2)$ component of the echo waveform compared to energy $E^{\rm H}_{\rm BH}$ in the horizon waveform for different values of $\tilde{\mathcal{R}}$ and x_0. The waveforms come from a test charge following an ISCO plunge orbit.

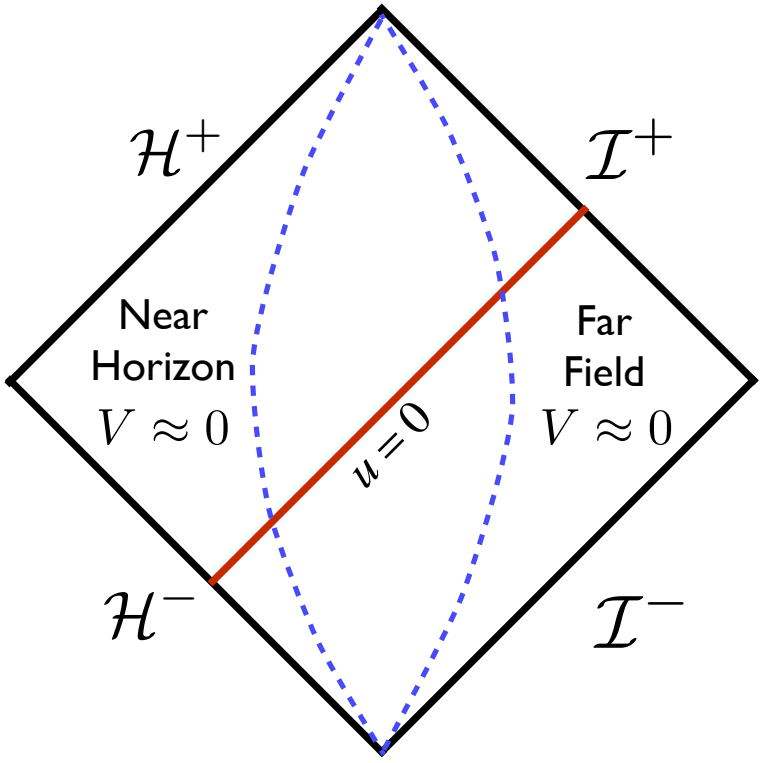

Figure 4.23: A Penrose diagram illustrating the relevant surfaces of the characteristic initial value definition of $\mathcal{T}_{\rm BH}$ and $\mathcal{R}_{\rm BH}$. Initial data, consisting of a delta function pulse at $u = 0$ (red line), is posed on $\mathcal{H}^-$ and $\mathcal{I}^-$. The transfer function $\mathcal{T}_{\rm BH}$ is extracted off of $\mathcal{I}^+$ and $\mathcal{R}_{\rm BH}$ is extracted off of $\mathcal{H}^+$. The blue dashed lines approximately bound the near-horizon and far-field regions where $V \approx 0$.

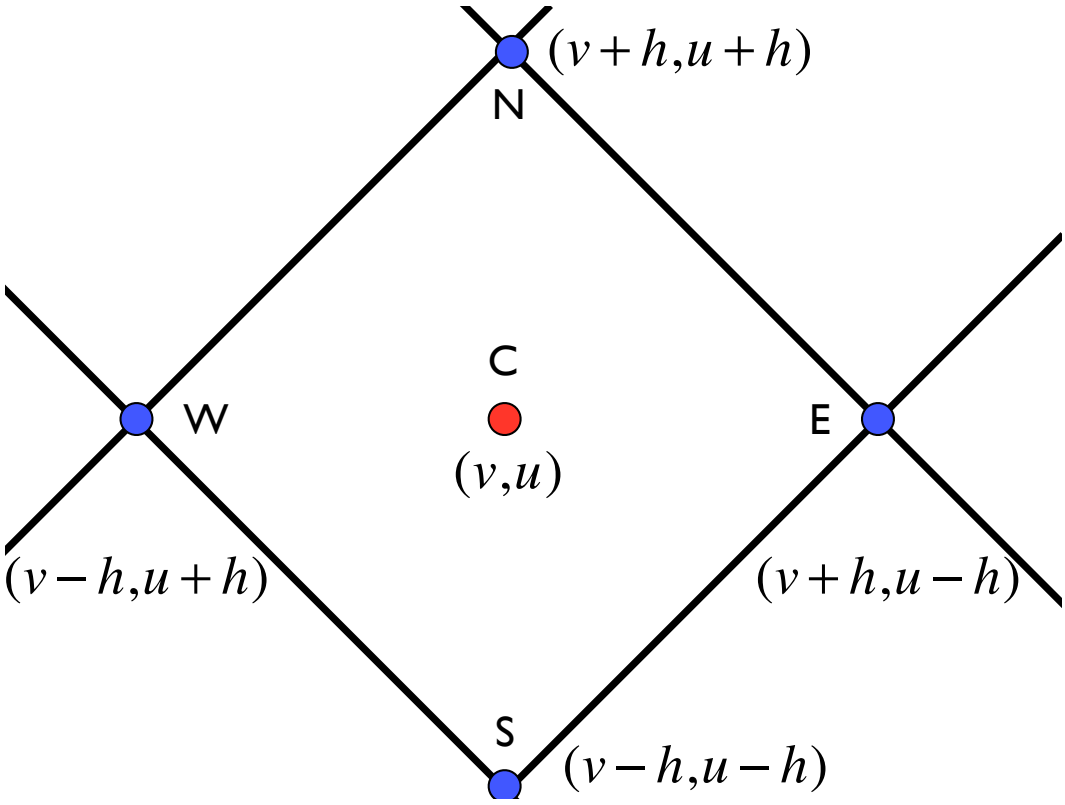

Figure 4.24: A generic computational cell in our characteristic evolution scheme.

Chapter 5

SEARCHING FOR NEAR-HORIZON QUANTUM STRUCTURES IN THE BINARY BLACK-HOLE STOCHASTIC GRAVITATIONAL-WAVE BACKGROUND

Quantum gravity corrections have been speculated to lead to modifications to space-time geometry near black hole horizons. Such structures may reflect gravitational waves, causing *echoes* that follow the main gravitational waves from binary black hole coalescence. By studying two phenomenological models of the near-horizon structures under Schwarzschild approximation, we show that such echoes, if exist, will give rise to a stochastic gravitational-wave background, which is very substantial if the near-horizon structure has a near unity reflectivity for gravitational waves, readily detectable by Advanced LIGO. In case the reflectivity is much less than unity, the background will mainly be arising from the first echo, with a level proportional to the power reflectivity of the near-horizon structure, but robust against uncertainties in the location and the shape of the structure — as long as it is localized and close to the horizon. Sensitivity of third-generation detectors allows the detection of a background that corresponds to power reflectivity $\sim 3\times10^{-3}$, if uncertainties in the binary black-hole merger rate can be removed. We note that the echoes do alter the $f^{2/3}$ power law of the background spectra at low frequencies, which is rather robust against uncertainties.

5.1 Introduction

Black holes (BH) are monumental predictions of general relativity (GR) [79]. It is often believed that, inside a BH, a singularity exists, around which classical GR will break down and must be replaced by a full quantum theory of gravity (QTG). The Planck scale of $l_{\rm P} \sim 1.6\times10^{-35}$ m is often cited as the scale at which full-blown QTG is required. However, interesting effects already arise as one applies quantum mechanics to fluctuations around the BH horizon, the boundary of the region from which one can escape toward infinity, even though space-time curvature does not blow up here. Hawking showed that BHs evaporate, leading to the so-called Black-Hole Information Paradox. During attempts to resolve this Paradox — as well as in other contexts — it was proposed that space-time geometry near the horizon may differ from the Kerr geometry, by having additional, quantum structures [83].

Candidate proposals include firewall [29], fuzzball [104] and gravastar [106].

Detection of gravitational waves (GW) generated by binary black-hole (BBH) collisions marked the dawn of GW astronomy [8], and brings an experimental tool to study the nature of BH horizon. Cardoso et al. proposed that geometric structures very close to the horizon can be probed by GW echoes that follow BBH waves, arising from the reflection from these structures, and the subsequent rebounds between these structures and the BH potential barrier [54, 56]. Whether the observed individual GW events have already provided positive experimental evidence towards the echoes is still under debate [22, 24, 31]. Furthermore, the particular echo model employed by [22, 24] was considered rather naive and needed refinement [103, 125]. For example, Mark *et al.*, using scalar field generated by a point particle falling into a Schwarzschild BH, illustrated that, the echoes can have a variety of time-domain features, which depend on the location, and (in general frequency-dependent) reflectivity of the near-horizon structure [101]. Echo structure during the entire inspiral-merger-ringdown wave was also analyzed in the Dyson series formalism in Ref. [66].

In this letter, we propose to search for near-horizon structures via the stochastic GW background (SGWB) from BBH mergers. Because the echo contribution to the background depends only on their energy spectra, it is much less sensitive to details of echo generation, making the method more robust against uncertainties in the near-horizon structures. We estimate the magnitude and rough feature of this SGWB, and illustrate its dependence on the near-horizon structure, following an Effective One-Body (EOB) approach: the two-body dynamics and waveform is approximated by the plunge of a point particle toward a Schwarzschild BH, following a trajectory that smoothly transitions from inspiral to plunge [49**?**].

5.2 GW amplitudes and power emitted

GWs emitted from a test particle plunging into a Schwarzschild BH can be described by the Sasaki-Nakamura (SN) equation [128]:

$$\left(\partial_{r_*}^2 + \omega^2 - V_l(r)\right) X_{lm}(\omega, r_*) = S_{lm}(\omega, r), \tag{5.1}$$

where r_* is the tortoise coordinate with

$$dr/dr_* = 1 - 2M/r \tag{5.2}$$

with effective potential given by

$$V_l(r) = \left(1 - \frac{2M}{r}\right)\left(\frac{l(l+1)}{r^2} - \frac{6M}{r^3}\right). \tag{5.3}$$

with M the mass of the BH. The source term is given by

$$S_{lm}(\omega, r) = W_{lm}(\omega, r) r^{-5} e^{-i\omega r_*}, \tag{5.4}$$

where W_{lm} is a functional of the trajectory of the test particle and its explicit expression can be found in Eqs. (19)—(21) of [128]. The wave function X_{lm} is related to GW in the $r \to +\infty$ limit via

$$h_+ + i h_\times = 8 r^{-1} \sum_{lm} {}_{-2}Y_{lm} X_{lm}(t), \tag{5.5}$$

where ${}_sY_{lm}$ are spin-s weighted spherical harmonics and

$$X_{lm}(t) = \int_{-\infty}^{+\infty} d\omega \; e^{-i\omega t} X_{lm}(\omega). \tag{5.6}$$

The GW energy spectrum is given by

$$dE/d\omega = \sum_{lm} 16\pi\omega^2 |X_{lm}(\omega, r_* \to \infty)|^2. \tag{5.7}$$

For BHs, imposing in-going boundary condition near the horizon and out-going condition near null infinity, solution to Eq. (5.1) is expressed as

$$X^{(0)}_{lm}(\omega, r_* \to \infty) = e^{i\omega r_*} Z^{(0)}_{lm}(\omega), \tag{5.8}$$

with $Z^{(0)}_{lm}$ defined as

$$Z^{(0)}_{lm}(\omega) = \int_{-\infty}^{+\infty} dr'_* \left[S_{lm}(\omega, r'_*) X^{(0)}_{\rm in}(\omega, r'_*) \right] / W^{(0)}(\omega), \tag{5.9}$$

and

$$W^{(0)} = X^{(0)}_{\rm in} \partial_{r_*} X^{(0)}_{\rm out} - X^{(0)}_{\rm out} \partial_{r_*} X^{(0)}_{\rm in} \tag{5.10}$$

is the Wronskian between the two homogenous solutions:

$$X^{(0)}_{\rm in} \sim e^{-i\omega r_*} \quad \text{for } r_* \to -\infty, \tag{5.11}$$

$$X^{(0)}_{\rm out} \sim e^{+i\omega r_*} \quad \text{for } r_* \to +\infty, \tag{5.12}$$

respectively.

5.3 Echoes from near-horizon structure

Let us now modify the Schwarzschild geometry near the horizon by creating a *Planck-scale potential barrier* V_p:

$$V_l \to V_l + V_p, \tag{5.13}$$

with V_p centered at

$$r^p = 2M + \epsilon, \tag{5.14}$$

with $\epsilon \ll M$; In tortoise coordinate, $\epsilon = l_p$ corresponds to $r_*^p \approx -182M$. As discussed by [101] the effect of V_p is the same as replacing the horizon ($r_* \to -\infty$) boundary condition for Eq. (5.1) by

$$X_{\rm in}^{\rm (R)} \sim e^{-i\omega r_*} + \mathcal{R} e^{i\omega r_*} \qquad \text{for} \quad r_* \to r_*^p, \tag{5.15}$$

while keeping the $r_* \to +\infty$ boundary condition unchanged. Here, $\mathcal{R}(\omega)$ can be viewed as a complex reflectivity of the potential barrier. Here we will obtain $\mathcal{R}(\omega)$ from V_p, while the problem of obtaining V_p once $\mathcal{R}(\omega)$ is measured is the so-called inverse scattering problem. The location of reflection is implicitly contained in its frequency dependence; for example, a Dirichlet boundary condition corresponds to

$$\mathcal{R}_D(\omega) = -e^{-2i\omega r_*^p}. \tag{5.16}$$

In general, if $\mathcal{R}(\omega) = \rho(\omega) e^{i\psi(\omega)}$ with $\rho(\omega)$ a slowly varying complex amplitude and ψ a fast-varying phase, then the effective location of reflection for a wavepacket with central frequency ω_0 is around $[\partial\psi/\partial\omega]_{\omega=\omega_0}/2$.

Defining

$$X_{lm}^{\rm (R)} = Z_{lm}^{\rm (R)} e^{i\omega r_*}, \tag{5.17}$$

where $Z_{lm}^{\rm (R)}$ can be written as a sum the main wave (for BH) and a series of echoes [101]:

$$Z_{lm}^{\rm (R)} = Z_{lm}^{(0)} + \mathcal{R} Z_{lm}^{(1)} \sum_{n=0}^{+\infty} (\mathcal{R}\mathcal{R}_{\rm BH})^n, \tag{5.18}$$

with $\mathcal{R}_{\rm BH}$ the complex reflectivity of the Regge-Wheeler potential V_l [see Eq. (2.14) of [101]] and

$$Z_{lm}^{(1)}(\omega) = \int_{-\infty}^{+\infty} dr_*' \frac{S_{lm}(\omega, r_*') \bar{X}_{\rm in}^{(0)}(\omega, r_*')}{W^{(0)}(\omega)} + \mathcal{R}_{\rm BH} Z_{lm}^{(0)}, \tag{5.19}$$

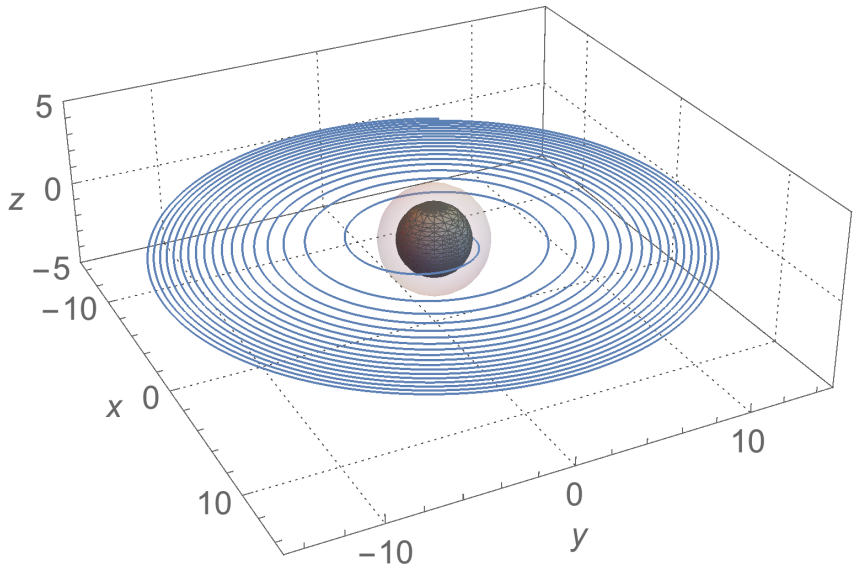

Figure 5.1: Trajectory of the EOB effective particle moving in a coalescing quasi-circular orbit. The symmetric mass ratio $\nu = 0.25$. The inner black sphere with radius $2M$ represents the horizon of a Schwarzschild BH. The outer translucent sphere with radius $3M$ represents the photon sphere.

with $\bar{X}^{(0)}_{\rm in}$ the complex conjugate of $X^{(0)}_{\rm in}$.

Note that each echo delayed from the previous one by $\sim 2|r^p_*|$ in the time domain. For small $\mathcal{R}$, we write

$$Z^{(\rm R)}_{lm} \approx Z^{(0)}_{lm} + \mathcal{R} Z^{(1)}_{lm} \tag{5.20}$$

and

$$\left(\frac{dE}{d\omega}\right)_R \approx 16\pi\omega^2 \sum_{lm} \left[\left|Z^{(0)}_{lm}\right|^2 + \left|\mathcal{R} Z^{(1)}_{lm}\right|^2 + 2{\rm Re}(\mathcal{R} Z^{(1)}_{lm} \bar{Z}^{(0)}_{lm}) \right]. \tag{5.21}$$

This is the sum of energies from *main wave*, the *first echo*, and the *beat* between the main wave and the first echo. While the beat is linear in $\mathcal{R}$, it is highly oscillatory in ω, since the main wave and the echo are well separated in the time domain.

5.4 Models of Reflectivity and Energy Spectra of Echoes

Without prior knowledge about details of near-horizon structures, we only assume it is short-ranged and localized at r^p_*. The simplest would be to introduce a δ-potential

$$V_p = \mathcal{A}\, \delta[(r_* - r^p_*)/M], \tag{5.22}$$

with parameter $\mathcal{A}$ defined as the *area under the Planck potential*:

$$\mathcal{A} = M \int_{-\infty}^{+\infty} V_p \, dr_*. \tag{5.23}$$

Note that $\mathcal{A}$ is a dimensionless quantity. As a comparison, the area under the Regge-Wheeler potential is [62]

$$M\int_{-\infty}^{+\infty} V_l\, dr_* = (l-1)(l+2)/2 + 1/4. \tag{5.24}$$

Such a model corresponds to a reflectivity

$$\mathcal{R}(\omega) = e^{-2i\omega r_*^p}\frac{\mathcal{A}}{2iM\omega - \mathcal{A}}\,. \tag{5.25}$$

This is more physical than the Dirichlet case, by reducing $|\mathcal{R}|$ at larger ω. Since $|\mathcal{R}(0)| = 1$ and $\mathcal{R}(+\infty) = 0$ are general properties of all physical potentials, we expect Eq. (5.25) to describe a large class of near-horizon quantum structures.

To further explore the shape of V_p, we also study the Pöschl-Teller potential [124]

$$V_p = \frac{\alpha^2\lambda(1-\lambda)}{M^2\cosh^2[\alpha(r_* - r_*^p)/M]}. \tag{5.26}$$

Dimensionless parameters α and λ are related to the area under V_p via

$$\mathcal{A} = 2\alpha\lambda(1-\lambda)\,. \tag{5.27}$$

The corresponding reflectivity is [61]

$$\mathcal{R}(\omega) = e^{-2i\omega r_*^p}\frac{\Gamma(i\frac{M\omega}{\alpha})\Gamma(\lambda - i\frac{M\omega}{\alpha})\Gamma(1-\lambda - i\frac{M\omega}{\alpha})}{\Gamma(-i\frac{M\omega}{\alpha})\Gamma(1-\lambda)\Gamma(\lambda)}\,, \tag{5.28}$$

where $\Gamma(\cdot)$ is the Gamma function. In the following, we will keep $\mathcal{A}$ fixed and vary α and λ to explore shapes of V_p.

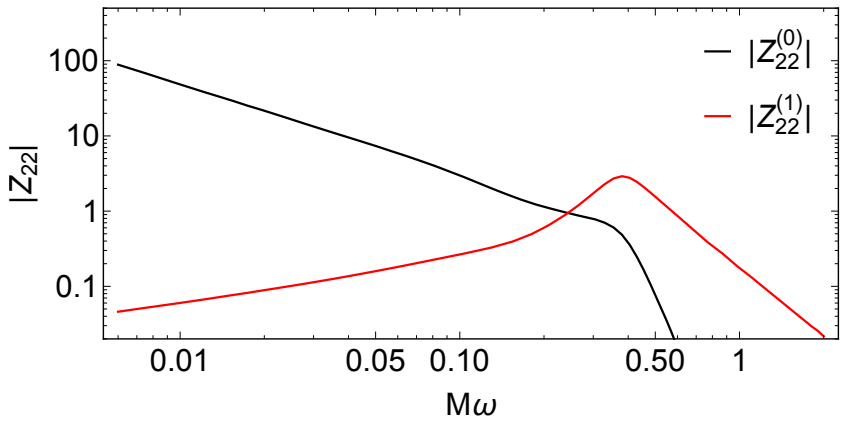

Figure 5.2: The main wave $Z_{22}^{(0)}$ and the wave $Z_{22}^{(1)}$ that generates echoes via Eq. (5.18).

To estimate of the echoes' energy spectrum, we adopt the EOB approach [49**?**]: for BHs with m_1 and m_2, we consider a point particle with reduced mass $\mu = m_1 m_2/(m_1+m_2)^2$ falling down a Schwarzschild BH with total mass $M = m_1 + m_2$; the symmetric mass ratio is defined as $\nu = \mu/M$. For motion in the equatorial plane, we have a Hamiltonian for (r, p_r, ϕ, p_ϕ), with radiation reaction incorporated as a generalized force $\mathcal{F}_\phi$ [Eqs. (3.41)–(3.44) of [49]]. Upon obtaining the trajectory (see Fig. 5.1 for $\nu = 0.25$), we obtain source term S_{lm}, and compute $Z^{(0)}_{lm}$ and $Z^{(1)}_{lm}$ using Eqs. (5.9) and (5.19), which will then lead to the GW energy spectrum.

We will focus on the $(l, m) = (2, 2)$ mode, which carries most of the GW energy.

As seen in Fig. 5.2, the main wave $|Z^{(0)}_{22}|$ recovers the $f^{-7/6}$ power law at low frequencies, as predicted by post-Newtonian approximation, also qualitatively mimics a BBH waveform at intermediate (merger) to high frequencies (ringdown). Note that the ringdown makes the the $|Z^{(0)}_{22}|$ curve turn up slightly near the leading $(2, 2)$ Quasi-Normal Mode (QNM) frequency of the Schwarzschild BH before sharply decreasing, similar to Fig. 3 of Ref. [27]. The wave $|Z^{(1)}_{22}|$ peaks roughly at the QNM frequency.

Horizon structures with $\mathcal{A}$ of order unity lead to significant modifications in GW energy spectrum $dE/d\omega$. In the upper panel of Fig. 5.3, we choose the reflectivity (5.25) with $\epsilon = l_p$ and $\mathcal{A} = 0.25$, 0.5, 0.75 and 1. At low frequencies, near-horizon structures add peaks separated by

$$\Delta\omega \sim 0.017 M^{-1} \sim \pi/r^p_* \tag{5.29}$$

to the post-Newtonian $dE/df \propto f^{-1/3}$. These resonant peaks are related to the poles of $1/(1 - \mathcal{R}\mathcal{R}_{\rm BH})$ in the series sum of Eq. (5.18). Near the QNM frequency, there is substantial additional radiation, which is due to the large value of $|Z^{(1)}_{22}|$. In the left panel, we choose several different values of ϵ which lead to different peak separation at low frequencies. In the right panel, we consider reflectivity (5.28) and find that the shape of the Planck potential, as characterized by α, has negligible influence to $dE/d\omega$ as long as the area keeps fixed.

5.5 Stochastic Gravitational-Wave Background (SGWB)

The SGWB is usually expressed as

$$\Omega(f) = {\rho_c}^{-1} d\rho_{\rm GW}/d\ln f, \tag{5.30}$$

where ρ_c represents the critical density to close the universe and ρ_{GW} the GW energy density; it is related the dE/df of a single GW source via [153]

$$\Omega(f) = \frac{f}{\rho_c} \int_0^{z_{\max}} dz \, \frac{R_m(z)[dE/df]_{f_z}}{(1+z)H(z)}, \tag{5.31}$$

where $f_z = f(1+z)$ is the frequency at emission. Here we adopt the ΛCDM cosmological model with

$$H(z) = H_0[\Omega_M(1+z)^3 + \Omega_\Lambda]^{1/2}, \tag{5.32}$$

where the Hubble constant $H_0 = 70$km/s Mpc, $\Omega_M = 0.3$ and $\Omega_\Lambda = 0.7$. $R_m(z)$ is the BBH merger rate per comoving volume at redshift z. We use the *fiducial model* described in [18], where $R_m(z)$ is proportional to the star formation rate with metallicity $Z < Z_\odot/2$ and delayed by the time between BBH formation and merger. As in the Fiducial model, the parameters of BBH follow GW150914: $M = 65M_\odot$, $\nu = 0.25$ with a local merger rate $R_m(0) = 16\text{Gpc}^{-3}\ \text{yr}^{-1}$.

For $\mathcal{A} \sim 1$, we get substantial additional SGWB from the echoes (left panel of Fig. 5.4) in a way that is insensitive to the location and shape of the near-horizon structure, as characterized by ϵ and α (right panel). This robustness indicates the area under the Planck potential is the most relevant observable of the near-horizon structures in SGWB. For smaller $\mathcal{A}$, we plot the *additional* SGWB, defined as $\Delta\Omega \equiv \Omega_{\mathcal{A}>0} - \Omega_{\mathcal{A}=0}$ in Fig. 5.5. Here $\Delta\Omega$ is approximately $\propto \mathcal{A}^2$, for $\mathcal{A} > 0.03$ and $\epsilon/M < \sqrt{l_P M}$: beating between the main wave and the echoes Eq. (5.21) is unimportant, and the additional SGWB mainly arise from energy contained in the first echo.

5.6 Detectability

The optimal signal-to-noise ratio (SNR) for a SGWB between a pair of detectors is given by $\sqrt{\langle\Omega|\Omega\rangle}$ [50], with

$$\langle\Omega_A|\Omega_B\rangle \equiv 2T\left(\frac{3H_0^2}{10\pi^2}\right)^2 \int_0^{+\infty} df \, \frac{\Omega_A(f)\gamma^2(f)\Omega_B(f)}{f^6 P_1(f)P_2(f)}, \tag{5.33}$$

where $\gamma(f)$ is the normalized overlap reduction function between the detectors, and $P_{1,2}(f)$ are the detectors' noise spectral densities. We consider advanced LIGO at design sensitivity [27], LIGO Voyager [2] and Einstein Telescope (ET) [129] at planned sensitivities. Advanced LIGO and LIGO Voyager have the same γ and we take the constant $\gamma = -3/8$ for co-located ET detectors [113]. The 1-year SNRs are

$\mathcal{A}$	LIGO	Voyager	ET
0	1.42	27.5	196
0.25	1.60	30.8	270
0.5	2.15	40.9	513
1	3.99	75.2	1215
2	8.76	164.7	2561

Table 5.1: One-year SNR of three generations of GW detectors for SGWB $\Omega_{\mathcal{A}}$, varying $\mathcal{A}$. The reflectivity corresponds to Eq. (5.25) with $\epsilon = l_p$. Other parameters are the same as in the fiducial model.

listed in Table 5.1 for values of $\mathcal{A}$ at order unity, in which case the echoes contribute significantly to the SNRs.

For lower values of $\mathcal{A}$, we apply the model-selection method of Ref. [50] to distinguish the SGWB with and without echo contributions. The log-likelihood ratio (LR) between two models is given by

$$\ln \Lambda = \frac{1}{4}\langle \Delta\Omega | \Delta\Omega \rangle \tag{5.34}$$

and two models considered discernible when $\ln \Lambda > c > 1$. Here we choose $c = 12$, which corresponds to a false alarm rate of 10^{-6} [145]. Minimum distinguishable $\mathcal{A}$ to reach this LR threshold is shown in Tab. 5.2; with 5-year integration, Voyager can detect $\mathcal{A} \approx 0.21$, while ET can detect $\mathcal{A} \approx 0.042$.

T	LIGO	Voyager	ET
1 yr	1.87	0.32	0.062
5 yrs	1.07	0.21	0.042

Table 5.2: The minimal distinguishable $\mathcal{A}$ to reach a log-likelihood ratio $\ln \Lambda > 12$ for current and future GW detector with different integration times. The reflectivity corresponds to Eq. (5.25) with $\epsilon = l_p$. Other parameters are the same as in the fiducial model.

5.7 Conclusions and Discussions

As we have seen in this paper, the $\Delta\Omega$ due to the echoes is largely independent from uncertainties in r_*^p. For strong near-horizon structures, with $\mathcal{A}$ the order of unity, SGWB from the echoes will be clearly visible. For weak near-horizon structures, $\Delta\Omega$ is mainly given by the first echo, and is simply proportional to the power reflectivity $|\mathcal{R}|^2$. The level detectable by ET corresponds to $\mathcal{A} \sim 0.042$, which corresponds to $|\mathcal{R}|^2 \approx 3 \times 10^{-3}$ near the peak of the echo energy spectrum. Further details of the

background not only depends on details in the Planck potential barrier V_p, we will also need to generalize the analysis to a Kerr BH.

Uncertainties also exist in the SGWB of the main, insprial-merger-ringdown wave, e.g., arising from different star formation rates, different metallicity thresholds to form BHs, details in the evolution of binary stars and the distributions in the time delay between BBH formation and merger — all of these lead to uncertainties in the local BBH merger rate and the local distribution of mass M and symmetric mass ratio ν [18]. It is believed these uncertainties will be well quantified and narrowed down by future BBH detections. For example, the range of BBH local merger rate has been narrowed down to $12-213$ Gpc^{-3} yr^{-1} using GW170104 [19]. On the other hand, as demonstrated by Zhu *et al.*, these uncertainties only scale the background spectra linearly at low frequencies and hence keep the power law $\Omega(f) \propto f^{2/3}$ for $f < 100$ Hz unchanged [153]. Our result shows the appearance of the near-horizon structures changes the slfaope of $\Omega(f)$, making it devaite from the $f^{2/3}$ power law even at low frequencies. This may be used to alleviate the influence from uncertainties.

In addition to BBH, binary neutron star (BNS) mergers also contribute to the background with a comparable magnitude [9]. Within the bandwidth of ground-based GW detectors, this background arises solely from inspiral, which gives an $f^{2/3}$ power law and is not influenced by the presence of the near-horizon structure. As a result, the echo SGWB $\Delta\Omega$ remains unchanged and our analysis on detectability still holds.

Echoes may also be detectable from individual events. Our calculations indicate for an event similar to GW150914, to reach an echo SNR of 10 the value of $\mathcal{A}$ should be at least 0.24 (LIGO), 0.050 (Voyager) and 0.011 (ET), respectively. However, in the matched filtering search of individual signal, the exact waveform is required, which in our model depends not only on $\mathcal{A}$, but also on ϵ and α, but may depend further on other unknown details of the Planck-scale potential — making it less robust. An analysis combined both background and individual signals will be presented in a separate publication.

5.8 Acknowledgements

This work is supported by NSF Grants PHY-1708212 and PHY-1404569 and PHY-1708213. and the Brinson Foundation. We thank Yiqiu Ma, Zachary Mark, Aaron Zimmerman for discussions, in particular ZM and AZ for sharing insights on the

echoes. We are grateful to Eric Thrane and Xing-Jiang Zhu for providing feedback on the manuscript.

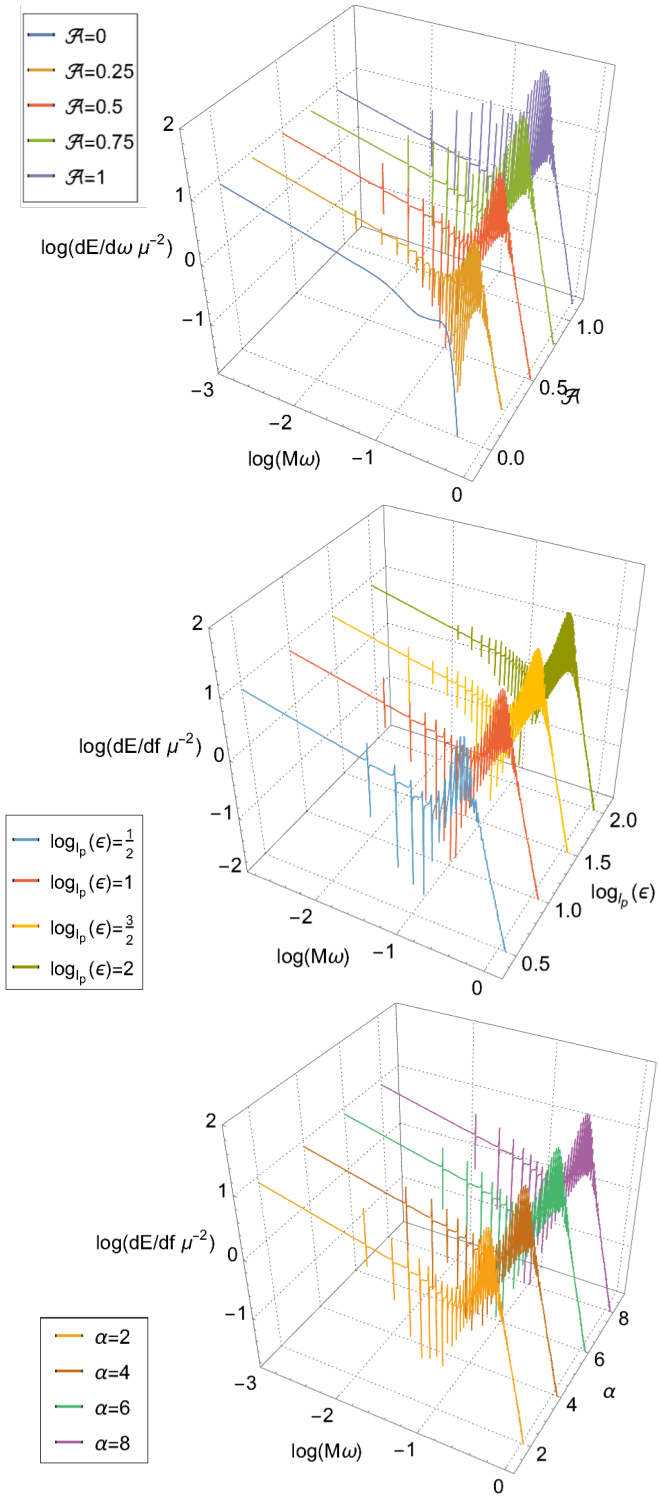

Figure 5.3: The energy spectra of GW emission from $\nu = 0.25$ coalescing BBH. Upper Panel: energy spectra for different values of $\mathcal{A}$, for $\epsilon = l_p$, with $\mathcal{R}$ given by Eq. (5.25). Middle Panel: energy spectra for different values of ϵ, for $\mathcal{A} = 0.5$ with $\mathcal{R}$ given by Eq. (5.25) . Lower Panel: energy spectra for different values of α, for $\epsilon = l_p$, with $\mathcal{R}$ given by Eq. (5.28), fixing $\mathcal{A} = 2\alpha\lambda(1-\lambda) = 0.5$.

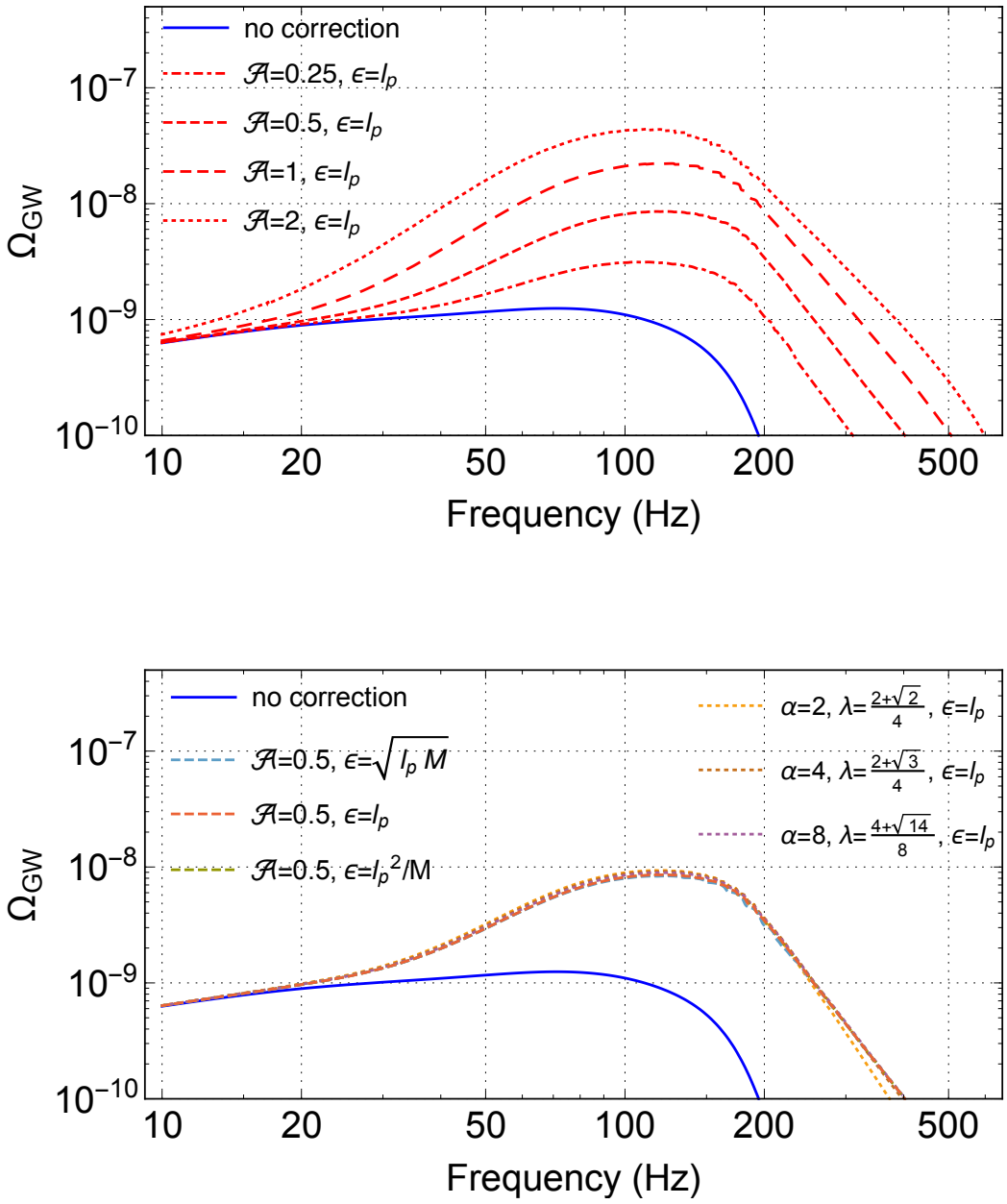

Figure 5.4: The influence to the fiducial [18] BBH SGWB with varied areas, locations and shapes of the near-horizon potential. Upper Panel: The spectral energy density $\Omega_{\rm GW}(f)$ for different values of $\mathcal{A}$; reflectivity given by Eq. (5.25) with $\epsilon = l_p$. Lower Panel: $\Omega_{\rm GW}(f)$ for different values of ϵ (dashed) and α (dotted); reflectivity given by Eq. (5.25) with $\mathcal{A} = 0.5$ (dashed) as well as Eq. (5.28) with $2\alpha\lambda(1-\lambda) = 0.5$, $\epsilon = l_p$ (dotted) respectively.

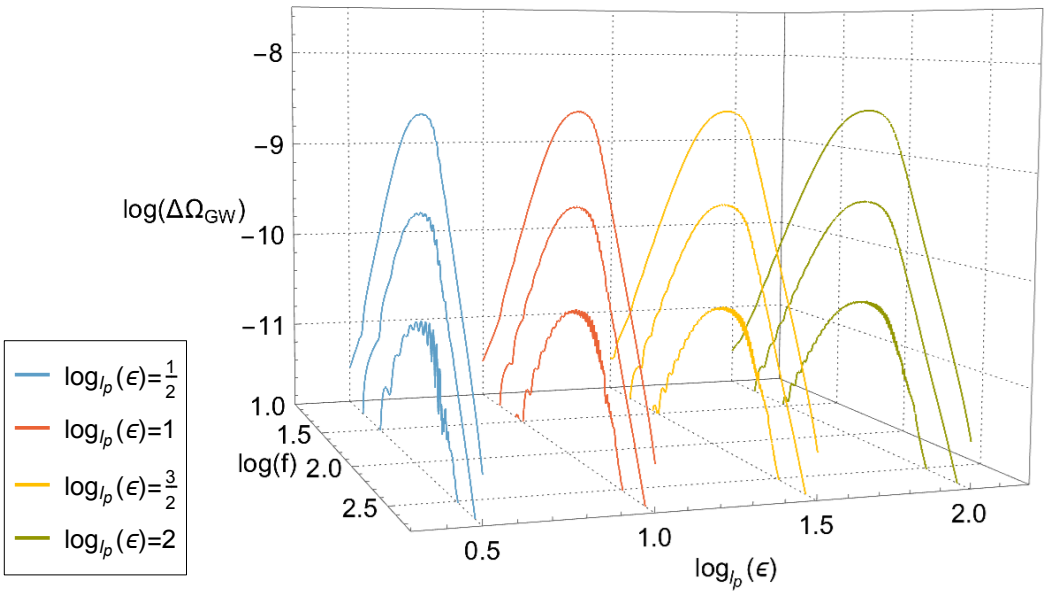

Figure 5.5: $\Delta\Omega_{\rm GW}$ as functions of f, for $\mathcal{A} = 0.3$, 0.1 and 0.03, and $\epsilon/M = (l_{\rm P}/M)^{1/2,1,3/2,2}$, reflectivity (5.25). Here $\Delta\Omega \propto \mathcal{A}^2$, except for the oscillations shown for small values of $\mathcal{A}$ and larger values of ϵ, when the beat term of Eq. (5.21) is not completely smoothed out. Other parameters are the same as in the fiducial model.

Appendix A

GRAVITATIONAL-WAVES IN GENERAL RELATIVITY

In this appendix we provide a pedagogical treatment to the gravitational-wave in general relativity based on perturbative field theory, with an application to the binary system.

A.1 Linearized Einstein field equation

First expand the metric $g_{\mu\nu}$ in Minkowski space-time:

$$g_{\mu\nu} = \eta_{\mu\nu} + h_{\mu\nu} \tag{A.1}$$

$$g^{\mu\nu} = \eta^{\mu\nu} - h^{\mu\nu} + O(h^2) \tag{A.2}$$

Then the affine connection,

$$\Gamma^{\lambda}_{\mu\nu} = \Gamma^{(1)\lambda}_{\mu\nu} + \Gamma^{(2)\lambda}_{\mu\nu} + O(h^3) \tag{A.3}$$

$$\Gamma^{(1)\lambda}_{\mu\nu} = \frac{1}{2}(h^{\lambda}_{\mu,\nu} + h^{\lambda}_{\nu,\mu} - h_{\mu\nu,}{}^{\lambda}) \tag{A.4}$$

$$\Gamma^{(2)\lambda}_{\mu\nu} = -\frac{1}{2}h^{\lambda\rho}(h_{\rho\mu,\nu} + h_{\rho\nu,\mu} - h_{\mu\nu,\rho}) \tag{A.5}$$

and the Ricci tensor,

$$R_{\mu\nu} = R^{(1)}_{\mu\nu} + R^{(2)}_{\mu\nu} + O(h^3) \tag{A.6}$$

$$R^{(1)}_{\mu\nu} = -\frac{1}{2}(h_{\mu\nu,}{}^{\lambda}{}_{\lambda} + h^{\lambda}_{\lambda,\mu\nu} - h^{\lambda}_{\mu,\lambda\nu} - h^{\lambda}_{\nu,\lambda\mu}) \tag{A.7}$$

$$\begin{aligned} R^{(2)}_{\mu\nu} =& \frac{1}{2}h^{\lambda\rho}(h_{\mu\nu,\lambda\rho} + h_{\lambda\rho,\mu\nu} - h_{\lambda\mu,\rho\nu} - h_{\lambda\nu,\rho\mu}) \\ &+ \frac{1}{4}(h^{\lambda}_{\lambda,}{}^{\rho} - 2h^{\lambda\rho}{}_{,\lambda})(h_{\rho\mu,\nu} + h_{\rho\nu,\mu} - h_{\mu\nu,\rho}) \\ &+ \frac{1}{4}(h^{\rho}_{\lambda,\mu} + h^{\rho}_{\mu,\lambda} - h_{\lambda\mu,}{}^{\rho})(h^{\lambda}_{\rho,\nu} + h_{\rho\nu,}{}^{\lambda} - h^{\lambda}_{\nu,\rho}) \end{aligned} \tag{A.8}$$

Then the Einstein field equation

$$\begin{aligned} &R_{\mu\nu} - \frac{1}{2}g_{\mu\nu}g^{\rho\sigma}R_{\rho\sigma} = 8\pi G T_{\mu\nu} \quad \Rightarrow \\ &R^{(1)}_{\mu\nu} - \frac{1}{2}\eta_{\mu\nu}\eta^{\rho\sigma}R^{(1)}_{\rho\sigma} = 8\pi G(T_{\mu\nu} + t_{\mu\nu}) \end{aligned} \tag{A.9}$$

Eq.(A.9) is the so-called linearized Einstein field equation, where $t_{\mu\nu}$ is the stress-energy tensor for gravitational field itself,

$$\begin{aligned} t_{\mu\nu} \equiv & \frac{1}{8\pi G}[R^{(1)}_{\mu\nu} - \frac{1}{2}\eta_{\mu\nu}\eta^{\rho\sigma}R^{(1)}_{\rho\sigma} - R_{\mu\nu} + \frac{1}{2}g_{\mu\nu}g^{\rho\sigma}R_{\rho\sigma}] \\ = & \frac{1}{8\pi G}[-R^{(2)}_{\mu\nu} + \frac{1}{2}\eta_{\mu\nu}\eta^{\rho\sigma}R^{(2)}_{\rho\sigma} - \frac{1}{2}\eta_{\mu\nu}h^{\rho\sigma}R^{(1)}_{\rho\sigma} + \frac{1}{2}h_{\mu\nu}\eta^{\rho\sigma}R^{(1)}_{\rho\sigma}] + O(h^3), \end{aligned} \tag{A.10}$$

It is straightforward to prove $R^{(1)}_{\mu\nu}$ satisfies the linearized Bianchi identity:

$$\partial_\mu(R^{(1)\mu\nu} - \frac{1}{2}\eta^{\mu\nu}\eta^{\rho\sigma}R^{(1)}_{\rho\sigma}) = 0 \tag{A.11}$$

hence the total (matter+gravity) stress energy tensor is locally conserved:

$$\partial_\mu(T^{\mu\nu} + t^{\mu\nu}) = 0 \tag{A.12}$$

For infinitesimal coordinate transformation

$$x'^\mu = x^\mu + \xi^\mu(x) \tag{A.13}$$

The transformation of $h_{\mu\nu}$ is obtained from

$$\begin{aligned} g'_{\mu\nu} = \frac{\partial x^\rho}{\partial x'^\mu}\frac{\partial x^\sigma}{\partial x'^\nu}g_{\rho\sigma} \quad \Rightarrow \\ h'_{\mu\nu} = h_{\mu\nu} - \partial_\mu\xi_\nu - \partial_\nu\xi_\mu \end{aligned} \tag{A.14}$$

We only keep the linear terms of ξ, and hence all other fields are unchanged under the gauge transformation. Eq.(A.14) keeps the left hand side of eq.(A.9) invariant, hence is often called the gauge transformation of $h_{\mu\nu}$.

Although some exact solutions can be found (the Bondi solution), the non-linear nature of gravity theory makes eq.(A.9) extremely hard to solve. However, general solution can be obtained if we take the weak field approximation, where the contribution from the stress-energy tensor of gravity is omitted. In this case eq.(A.9) is truly linear:

$$\begin{aligned} R^{(1)}_{\mu\nu} - \frac{1}{2}\eta_{\mu\nu}\eta^{\rho\sigma}R^{(1)}_{\rho\sigma} = & 8\pi G T_{\mu\nu} \quad \Rightarrow \\ \partial^2 h_{\mu\nu} + \partial_\mu\partial_\nu h^\lambda{}_\lambda - \partial_\lambda\partial_\mu h^\lambda{}_\nu - \partial_\lambda\partial_\nu h^\lambda{}_\mu = & -16\pi G(T_{\mu\nu} - \frac{1}{2}\eta_{\mu\nu}T^\lambda{}_\lambda) \end{aligned} \tag{A.15}$$

Our next mission is to solve eq.(A.15).

A.2 Plane gravitational wave and the gauge condition

First expand $h_{\mu\nu}$ as the composition of plane wave:

$$h_{\mu\nu}(x) = \int \frac{d^3k}{(2\pi)^3}[\tilde{h}_{\mu\nu}(\boldsymbol{k})e^{ik\cdot x} + \tilde{h}^*_{\mu\nu}(\boldsymbol{k})e^{-ik\cdot x}] \tag{A.16}$$

In vacuum, eq.(A.15) is equivalent to

$$\begin{aligned} k^2\tilde{h}_{\mu\nu} + k_\mu k_\nu \tilde{h}^\lambda_{\ \lambda} - k_\lambda k_\mu \tilde{h}^\lambda_{\ \nu} - k_\lambda k_\nu \tilde{h}^\lambda_{\ \mu} = 0 \quad \Rightarrow \\ k^2\tilde{h}_{\mu\nu} = k_\mu(k_\lambda \tilde{h}^\lambda_{\ \nu} - \frac{1}{2}k_\nu \tilde{h}^\lambda_{\ \lambda}) + k_\nu(k_\lambda \tilde{h}^\lambda_{\ \mu} - \frac{1}{2}k_\mu \tilde{h}^\lambda_{\ \lambda}) \end{aligned} \tag{A.17}$$

In order to describe the free propagating gravitational wave, the on-shell condition $k^2 = 0$ should be satisfied, hence $h_{\mu\nu}$ should satisfy Lorenz gauge condition:

$$k_\lambda \tilde{h}^\lambda_{\ \mu} - \frac{1}{2}k_\mu \tilde{h}^\lambda_{\ \lambda} = 0 \tag{A.18}$$

Then eq.(A.15) becomes

$$\begin{cases} \partial^2 h_{\mu\nu} = -16\pi G(T_{\mu\nu} - \frac{1}{2}\eta_{\mu\nu}T^\lambda_{\ \lambda}) \\ \partial_\lambda h^\lambda_{\ \mu} - \frac{1}{2}\partial_\mu h^\lambda_{\ \lambda} = 0 \end{cases} \tag{A.19}$$

It is more convinient to solve if we introduce $\bar{h}_{\mu\nu} \equiv h_{\mu\nu} - \frac{1}{2}\eta_{\mu\nu}h^\lambda_{\ \lambda}$,

$$\begin{cases} \partial^2 \bar{h}_{\mu\nu} = -16\pi G T_{\mu\nu} \\ \partial_\lambda \bar{h}^\lambda_{\ \mu} = 0 \end{cases} \tag{A.20}$$

The gauge transformation eq.(A.14) for $\bar{h}_{\mu\nu}$ is

$$\bar{h}'_{\mu\nu} = \bar{h}_{\mu\nu} - \partial_\mu \xi_\nu - \partial_\nu \xi_\mu + \eta_{\mu\nu}\partial^\lambda \xi_\lambda \tag{A.21}$$

For the Lorenz condition to be holden after coordinate transformation, ξ_μ should satisfy $\partial^2 \xi_\mu = 0$, which means ξ_μ can also be expanded as

$$\xi_\mu(x) = \int \frac{d^3k}{(2\pi)^3}[\tilde{\xi}_\mu(\boldsymbol{k})e^{ik\cdot x} + \tilde{\xi}^*_\mu(\boldsymbol{k})e^{-ik\cdot x}] \tag{A.22}$$

Before solving eq.(A.20) we want to study the degree of freedom (DOM) of $\bar{h}_{\mu\nu}$. Symmetric tensor $\tilde{\bar{h}}_{\mu\nu}$ has 10 DOM:

$$\tilde{\bar{h}}_{\mu\nu} = \begin{pmatrix} \tilde{\bar{h}}_{00} & \tilde{\bar{h}}_{01} & \tilde{\bar{h}}_{02} & \tilde{\bar{h}}_{03} \\ \tilde{\bar{h}}_{01} & \tilde{\bar{h}}_{11} & \tilde{\bar{h}}_{12} & \tilde{\bar{h}}_{13} \\ \tilde{\bar{h}}_{02} & \tilde{\bar{h}}_{12} & \tilde{\bar{h}}_{22} & \tilde{\bar{h}}_{23} \\ \tilde{\bar{h}}_{03} & \tilde{\bar{h}}_{13} & \tilde{\bar{h}}_{23} & \tilde{\bar{h}}_{33} \end{pmatrix} \tag{A.23}$$

Take the GW propagating direction $\boldsymbol{n}$ as the 3rd axis, estabalish a spatial orthonormal coordinate system:

$$\begin{cases} u^\mu = (0,1,0,0) \\ v^\nu = (0,0,1,0) \\ n^\nu = (0,0,0,1) \end{cases} \tag{A.24}$$

In this coordinate system, the 4-momentum of GW becomes $k^\mu = k(1,0,0,1)$. The Lorenz condition $k^\mu \bar{\tilde{h}}_{\mu\nu} = 0$ in this coordinate system is

$$\bar{\tilde{h}}_{00} + \bar{\tilde{h}}_{30} = 0, \quad \bar{\tilde{h}}_{01} + \bar{\tilde{h}}_{31} = 0, \quad \bar{\tilde{h}}_{02} + \bar{\tilde{h}}_{32} = 0, \quad \bar{\tilde{h}}_{03} + \bar{\tilde{h}}_{33} = 0 \tag{A.25}$$

After adding the Lorenz condition, only $10 - 4 = 6$ DOM are left.

$$\bar{\tilde{h}}_{\mu\nu} = \begin{pmatrix} \bar{\tilde{h}}_{33} & -\bar{\tilde{h}}_{13} & -\bar{\tilde{h}}_{23} & -\bar{\tilde{h}}_{33} \\ -\bar{\tilde{h}}_{13} & \bar{\tilde{h}}_{11} & \bar{\tilde{h}}_{12} & \bar{\tilde{h}}_{13} \\ -\bar{\tilde{h}}_{23} & \bar{\tilde{h}}_{12} & \bar{\tilde{h}}_{22} & \bar{\tilde{h}}_{23} \\ -\bar{\tilde{h}}_{33} & \bar{\tilde{h}}_{13} & \bar{\tilde{h}}_{23} & \bar{\tilde{h}}_{33} \end{pmatrix} \tag{A.26}$$

When a specific coordinate is choosen, it is not possible to make a global Lorentz transformation without changing the basis vectors. However, we are still free to make a coordinate-dependent translation eq.(A.13), i.e. the gauge transformation for $\bar{h}_{\mu\nu}$. Recalling eq.(A.21) and (A.22), which give $\bar{\tilde{h}}'_{\mu\nu} = \bar{\tilde{h}}_{\mu\nu} - ik_\mu\tilde{\xi}_\nu - ik_\nu\tilde{\xi}_\mu + i\eta_{\mu\nu}k^\lambda\tilde{\xi}_\lambda$, in our coordinate system,

$$\begin{aligned} &\bar{\tilde{h}}'_{11} = \bar{\tilde{h}}_{11} + ik(\tilde{\xi}_0 + \tilde{\xi}_3), \quad \bar{\tilde{h}}'_{13} = \bar{\tilde{h}}_{13} - ik\tilde{\xi}_1, \quad \bar{\tilde{h}}'_{12} = \bar{\tilde{h}}_{12} \\ &\bar{\tilde{h}}'_{22} = \bar{\tilde{h}}_{22} + ik(\tilde{\xi}_0 + \tilde{\xi}_3), \quad \bar{\tilde{h}}'_{23} = \bar{\tilde{h}}_{23} - ik\tilde{\xi}_2, \quad \bar{\tilde{h}}'_{33} = \bar{\tilde{h}}_{33} + ik(\tilde{\xi}_0 - \tilde{\xi}_3) \end{aligned} \tag{A.27}$$

We can choose the following gauge transformation:

$$\begin{aligned} &\tilde{\xi}_0 = \frac{i}{4k}(\bar{\tilde{h}}_{11} + \bar{\tilde{h}}_{22} + 2\bar{\tilde{h}}_{33}), \quad \tilde{\xi}_1 = -\frac{i}{k}\bar{\tilde{h}}_{13}, \quad \tilde{\xi}_2 = -\frac{i}{k}\bar{\tilde{h}}_{23}, \\ &\tilde{\xi}_3 = \frac{i}{4k}(\bar{\tilde{h}}_{11} + \bar{\tilde{h}}_{22} - 2\bar{\tilde{h}}_{33}) \end{aligned} \tag{A.28}$$

Then only $6 - 4 = 2$ DOM remain, this choice of coordinates is often called the transverse tracless (TT) gauge and in the $(\boldsymbol{u}, \boldsymbol{v}, \boldsymbol{n})$ system,

$$\bar{\tilde{h}}^{\mathrm{TT}} = \tilde{h}^{\mathrm{TT}} = \begin{pmatrix} 0 & 0 & 0 & 0 \\ 0 & \tilde{h}_+ & \tilde{h}_\times & 0 \\ 0 & \tilde{h}_\times & \tilde{h}_+ & 0 \\ 0 & 0 & 0 & 0 \end{pmatrix} \tag{A.29}$$

Where $\tilde{h}_+ = \frac{1}{2}(\tilde{\tilde{h}}_{11} - \tilde{\tilde{h}}_{22})$, $\tilde{h}_\times = \tilde{\tilde{h}}_{12}$. They are gauge invariant.

We can rewrite this result in a coordinate system independent (i.e. Lorentz invariant) way:

$$\begin{cases} h_+ = \frac{1}{2}(u^i u^j - v^i v^j)\bar{h}_{ij} \\ h\times = u^i v^j \bar{h}_{ij} \end{cases} \tag{A.30}$$

Where $\boldsymbol{u}$ and $\boldsymbol{v}$ are unit vectors orthogonal to the GW propagating direction $\boldsymbol{n}$. We can compute $\bar{h}_{ij}$ in any coordinate system (as long as the Lorenz condition is maintained) and utilize eq.(A.30) to convert it into the h_+ and $h_\times$ in the observer's coordinate system.

A.3 Gravitational wave solution I. Quadrupole radiation

The general solution to eq.(A.20) is the retarded potential solution.

$$\begin{aligned} \partial^2 \bar{h}^{\mu\nu}(t, \boldsymbol{x}) = -16\pi G\, T^{\mu\nu}(t, \boldsymbol{x}) \quad \Rightarrow \\ \bar{h}^{\mu\nu}(t, \boldsymbol{x}) = 4G \int d^3y\, \frac{T^{\mu\nu}(t - |\boldsymbol{x} - \boldsymbol{y}|, \boldsymbol{y})}{|\boldsymbol{x} - \boldsymbol{y}|} \end{aligned} \tag{A.31}$$

For far field approximation: $|\boldsymbol{y}| \ll |\boldsymbol{x}| \equiv r$,

$$\bar{h}^{\mu\nu}(t, \boldsymbol{x}) \approx \frac{4G}{r} \int d^3y\, T^{\mu\nu}(t - r, \boldsymbol{y}) \tag{A.32}$$

From eq.(A.30), we only need $\bar{h}^{ij}$ to compute the two physcial DOM, then eq.(A.32) can be further simplified from the conservation of stress-energy tensor.

$$\begin{aligned} &\bar{h}^{ij}(t, \boldsymbol{x}) = \frac{4G}{r} \int d^3y\, T^{ij} \\ =&\frac{4G}{r} \int d^3y [\partial_k (y^i T^{ki}) - y^i \partial_k T^{kj}] = \frac{4G}{r} \int d^3y\, y^i \partial_t T^{0j} \\ =&\frac{2G}{r} \partial_t \int d^3y (y^i T^{0j} + y^j T^{0i}) = \frac{2G}{r} \partial_t \int d^3y [\partial_k (y^i y^j T^{0k}) - y^i y^j \partial_k T^{0k}] \\ =&\frac{2G}{r} \partial_t^2 \int d^3y\, y^i y^j T^{00}(t - r, \boldsymbol{y}) = \frac{2G}{r} \ddot{I}(t - r) \end{aligned} \tag{A.33}$$

Where the quadrupole tensor is defined as

$$I^{ij}(t) = \int d^3x\, x^i x^j T^{00}(t, \boldsymbol{x}) \tag{A.34}$$

Eq.33 is often called the quadrupole formula for gravitational radiation.

Note that in gravitationally bound system such as binary stars, (i) $\bar{h}^{ij} = \frac{4G}{r}\int d^3y\, T^{ij}$ and (ii) $\bar{h}^{ij} = \frac{2G}{r}\partial_t^2 \int d^3y\, y^i y^j T^{00}$ can give different results. This is because in these systems the stress-energy of gravitional field cannot be omitted, hence $T_{\mu\nu} + t_{\mu\nu}$ is conserved instead of $T_{\mu\nu}$ alone. In this case, we should have $\bar{h}^{ij} = \frac{4G}{r}\int d^3y\, (T^{ij} + t^{ij})$ and $\bar{h}^{ij} = \frac{2G}{r}\partial_t^2 \int d^3y\, y^i y^j (T^{00} + t^{00})$. But $t^{00} \ll T^{00}$, $t^{ij} \sim T^{ij}$, which means (ii) is a much better approximation than (i) in computing the GW in these systems.

A.4 Gravitational wave solution II. Moving particles radiation

The stress-energy tensor for a system consisting of several moving particles is

$$T^{\mu\nu}(t, \boldsymbol{x}) = \sum_n p_n^\mu(t) v_n^\nu(t) \delta^3(\boldsymbol{x} - \boldsymbol{x}_n(t)) \tag{A.35}$$

Where $p_n^\mu \equiv m_n dx_n^\mu/d\tau$, $v_n^\mu \equiv dx_n^\mu/dt$. Let's compute $\bar{h}^{ij}$ directly from the retarded potential eq.(A.31) without taking the far field approximation,

$$\begin{aligned}
&\bar{h}^{ij}(t, \boldsymbol{x}) = 4G \int d^3y\, \frac{T^{ij}(t - |\boldsymbol{x} - \boldsymbol{y}|, \boldsymbol{y})}{|\boldsymbol{x} - \boldsymbol{y}|} \\
=&4G \sum_n \int d^3y\, \frac{p_n^i(t - |\boldsymbol{x} - \boldsymbol{y}|)\, v_n^j(t - |\boldsymbol{x} - \boldsymbol{y}|)}{|\boldsymbol{x} - \boldsymbol{y}|}\, \delta^3(\boldsymbol{y} - \boldsymbol{x}_n(t - |\boldsymbol{x} - \boldsymbol{y}|)) \\
=&4G \sum_n \int d^3y\, \frac{p_n^i(t - |\boldsymbol{x} - \boldsymbol{y}|)\, v_n^j(t - |\boldsymbol{x} - \boldsymbol{y}|)}{|\boldsymbol{x} - \boldsymbol{y}|}\, \frac{\delta^3(\boldsymbol{y} - \boldsymbol{x}_n(t'))}{1 - \frac{\boldsymbol{x}-\boldsymbol{y}}{|\boldsymbol{x}-\boldsymbol{y}|} \cdot \boldsymbol{v}_n(t - |\boldsymbol{x} - \boldsymbol{y}|)} \\
=&4G \sum_n \frac{m_n}{\sqrt{1 - \boldsymbol{v}_n^2(t')}} \frac{v_n^i(t') v_n^j(t')}{r_s(t') - \boldsymbol{r}_s(t') \cdot \boldsymbol{v}_n(t')}
\end{aligned} \tag{A.36}$$

This result is called the Lienard-Wiechert potential. Here, $t' = t - |\boldsymbol{x} - \boldsymbol{x}_n(t')|$ is the GW emitted time and $\boldsymbol{x}_n(t') = \boldsymbol{x}_n(t - |\boldsymbol{x} - \boldsymbol{x}_n(t')|)$ is the position of the n-th particle when GW is emittet. $x_n(t')$ is the solution for $\boldsymbol{y}$ to the equation inside the δ function: $\boldsymbol{y} - \boldsymbol{x}_n(t - |\boldsymbol{x} - \boldsymbol{y}|) = 0$. $\boldsymbol{r}_s(t') \equiv \boldsymbol{x} - \boldsymbol{x}_n(t')$ is the position vector pointing from the GW emitted particle to the observer.

If all the particles move in a small region nere the origin, then $r_s(t') \approx r,\ t' \approx t - r$. In this case,

$$\bar{h}^{ij}(t, \boldsymbol{x}) = \frac{4G}{r} \sum_n \frac{m_n}{\sqrt{1 - \boldsymbol{v}_n^2(t - r)}} \frac{v_n^i(t - r) v_n^j(t - r)}{1 - \boldsymbol{n} \cdot \boldsymbol{v}_n(t - r)} \tag{A.37}$$

This differs to the naive result which we put eq.(A.35) directly into $\bar{h}^{ij} = \frac{4G}{r}\int d^3y\, T^{ij}$ by a factor of $1/(1 - \boldsymbol{n} \cdot \boldsymbol{v}_n)$, which can be omitted in the low-speed approximation.

A.5 Stress-energy tensor for gravitational wave

First expand $h_{\mu\nu}(x)$ as eq.(A.16), then the value of $h_{\mu\nu}(x)h_{\rho\sigma}(x)$ is

$$h_{\mu\nu}(x)h_{\rho\sigma}(x) = \int \frac{d^3k}{(2\pi)^3}\frac{d^3k'}{(2\pi)^3}[\tilde{h}_{\mu\nu}(\boldsymbol{k})\tilde{h}_{\rho\sigma}(\boldsymbol{k'})e^{i(k+k')\cdot x} + \tilde{h}_{\mu\nu}(\boldsymbol{k})\tilde{h}^*_{\rho\sigma}(\boldsymbol{k'})e^{i(k-k')\cdot x} + \tilde{h}^*_{\mu\nu}(\boldsymbol{k})\tilde{h}^*_{\rho\sigma}(\boldsymbol{k'})e^{-i(k+k')\cdot x} + \tilde{h}^*_{\mu\nu}(\boldsymbol{k})\tilde{h}_{\rho\sigma}(\boldsymbol{k'})e^{-i(k-k')\cdot x}] \tag{A.38}$$

Integrate in a region V much larger than the GW wavelength,

$$\int_V d^3x\ e^{i\boldsymbol{k}\cdot\boldsymbol{x}} \approx (2\pi)^3\ \delta^3(\boldsymbol{k}) \tag{A.39}$$

Hence we have

$$\begin{aligned}\int_V d^3x\ e^{i(k+k')\cdot x} &= \int d^3x\ e^{i(\boldsymbol{k}+\boldsymbol{k'})\cdot x}\ e^{-i(|\boldsymbol{k}|+|\boldsymbol{k'}|)t} = (2\pi)^3\delta^3(\boldsymbol{k}+\boldsymbol{k'})e^{-2i|\boldsymbol{k}|t}\\ \int_V d^3x\ e^{i(k-k')\cdot x} &= \int d^3x\ e^{i(\boldsymbol{k}-\boldsymbol{k'})\cdot x}\ e^{-i(|\boldsymbol{k}|-|\boldsymbol{k'}|)t} = (2\pi)^3\delta^3(\boldsymbol{k}-\boldsymbol{k'})\end{aligned} \tag{A.40}$$

Then,

$$\int_V d^3x\ h_{\mu\nu}(x)h_{\rho\sigma}(x) = \int \frac{d^3k}{(2\pi)^3}[\tilde{h}_{\mu\nu}(\boldsymbol{k})\tilde{h}^*_{\rho\sigma}(\boldsymbol{k}) + \tilde{h}^*_{\mu\nu}(\boldsymbol{k})\tilde{h}_{\rho\sigma}(\boldsymbol{k}) + \tilde{h}_{\mu\nu}(\boldsymbol{k})\tilde{h}_{\rho\sigma}(\boldsymbol{k})e^{-2i|\boldsymbol{k}|t} + \tilde{h}^*_{\mu\nu}(\boldsymbol{k})\tilde{h}^*_{\rho\sigma}(\boldsymbol{k})e^{+2i|\boldsymbol{k}|t}] \tag{A.41}$$

After averaging over several periods, terms associated with $e^{\pm i|\boldsymbol{k}|t}$ vanish, only left

$$\int_V d^3x\ h_{\mu\nu}(x)h_{\rho\sigma}(x) = \int \frac{d^3k}{(2\pi)^3}\ \tilde{h}^*_{\mu\nu}(\boldsymbol{k})h_{\rho\sigma}(\boldsymbol{k}) + \text{c.c.} \tag{A.42}$$

In the same way,

$$\int_V d^3x\ h_{\mu\nu,\lambda}(x)h_{\rho\sigma,\kappa}(x) = \int \frac{d^3k}{(2\pi)^3}\ k_\lambda k_\kappa \tilde{h}^*_{\mu\nu}(\boldsymbol{k})h_{\rho\sigma}(\boldsymbol{k}) + \text{c.c.} \tag{A.43}$$

$$\int_V d^3x\ h_{\mu\nu}(x)h_{\rho\sigma,\lambda\kappa}(x) = -\int \frac{d^3k}{(2\pi)^3}\ k_\lambda k_\kappa \tilde{h}^*_{\mu\nu}(\boldsymbol{k})h_{\rho\sigma}(\boldsymbol{k}) + \text{c.c.} \tag{A.44}$$

Put them into eq.(A.8),

$$\begin{aligned}\int_V d^3x\ R^{(2)}_{\mu\nu} = \int \frac{d^3k}{(2\pi)^3}[&-\frac{1}{2}\tilde{h}^{*\lambda\rho}(k_\lambda k_\rho \tilde{h}_{\mu\nu} + k_\mu k_\nu \tilde{h}_{\lambda\rho} - k_\lambda k_\mu \tilde{h}_{\rho\nu} - k_\lambda k_\nu \tilde{h}_{\rho\mu})\\ &+ \frac{1}{4}(k^\rho \tilde{h}^{*\lambda}{}_{\lambda} - 2k_\lambda \tilde{h}^{*\lambda\rho})(k_\mu \tilde{h}_{\rho\nu} + k_\nu \tilde{h}_{\rho\mu} - k_\rho \tilde{h}_{\mu\nu})\\ &+ \frac{1}{4}(k_\mu \tilde{h}^{*\lambda\rho} + k^\lambda \tilde{h}^{*\rho}{}_{\mu} - k^\rho \tilde{h}^{*\lambda}{}_{\mu})(k_\nu \tilde{h}_{\lambda\rho} + k_\lambda \tilde{h}_{\rho\nu} - k_\rho \tilde{h}_{\lambda\nu})] + \text{c.c.}\end{aligned} \tag{A.45}$$

Applying the Lorenz condition: $k^\mu \tilde{h}_{\mu\nu} = \frac{1}{2} k_\nu \tilde{h}^\mu{}_\mu$ and the on-shell condition: $k^2 = 0$, we obtain

$$\begin{aligned}
&\int_V d^3x\ R^{(2)}_{\mu\nu} \\
&= \int \frac{d^3k}{(2\pi)^3}[-\frac{1}{2}(k_\mu k_\nu \tilde{h}^{*\lambda\rho}\tilde{h}_{\lambda\rho} - \frac{1}{2}k_\mu k_\nu \tilde{h}^{*\rho}{}_\rho \tilde{h}^\lambda_\lambda) + \frac{1}{4}(k_\mu k_\nu \tilde{h}^{*\lambda\rho}\tilde{h}_{\lambda\rho} - \frac{1}{2}k_\mu k_\nu \tilde{h}^{*\rho}{}_\rho \tilde{h}^\lambda_\lambda)] + \text{c.c.} \\
&= \int \frac{d^3k}{(2\pi)^3}[-\frac{k_\mu k_\nu}{2}(\tilde{h}^{*\lambda\rho}\tilde{h}_{\lambda\rho} - \frac{1}{2}|\tilde{h}^\lambda_\lambda|^2)] = \int \frac{d^3k}{(2\pi)^3}[-\frac{k_\mu k_\nu}{2}(\tilde{\bar{h}}^{*\lambda\rho}\tilde{\bar{h}}_{\lambda\rho} - \frac{1}{2}|\tilde{\bar{h}}^\lambda_\lambda|^2)]
\end{aligned} \tag{A.46}$$

Notice that $\eta^{\rho\sigma} R^{(2)}_{\rho\sigma} = 0$. On the other hand, from the linear Einstein field equation in vacuum we have $R^{(1)}_{\mu\nu} = 0$, then from eq.(A.10)

$$\int_V d^3x\ t_{\mu\nu} = \int \frac{d^3k}{(2\pi)^3}\frac{k_\mu k_\nu}{16\pi G}(\tilde{\bar{h}}^{*\lambda\rho}\tilde{\bar{h}}_{\lambda\rho} - \frac{1}{2}|\tilde{\bar{h}}^\lambda_\lambda|^2) \tag{A.47}$$

Insert eq.(A.26), we get

$$\int_V d^3x\ t_{\mu\nu} = \int \frac{d^3k}{(2\pi)^3}\frac{k_\mu k_\nu}{16\pi G}(|\frac{1}{2}(\tilde{\bar{h}}_{11} - \tilde{\bar{h}}_{22})|^2 + |\tilde{\bar{h}}_{12}|^2) \tag{A.48}$$

From eq.(A.27), $(\tilde{\bar{h}}_{11} - \tilde{\bar{h}}_{22})/2$ and $\tilde{\bar{h}}_{12}$ are gauge invariant and hence $t_{\mu\nu}$ is also gauge invariant, and

$$\int_V d^3x\ t_{\mu\nu} = \int \frac{d^3k}{(2\pi)^3}\frac{k_\mu k_\nu}{8\pi G}(|\tilde{\bar{h}}_+|^2 + |\tilde{\bar{h}}_\times|^2) \tag{A.49}$$

On the other hand,

$$\begin{aligned}
&\int_V d^3x\ \partial_\mu h_+(x)\partial_\nu h_+(x) = \int \frac{d^3k}{(2\pi)^3}\ 2k_\mu k_\nu |\tilde{\bar{h}}_+|^2 \quad \Rightarrow \\
&\int_V d^3x\ t_{\mu\nu} = \int_V d^3x\ \frac{1}{16\pi G}[\partial_\mu h_+(x)\partial_\nu h_+(x) + \partial_\mu h_\times(x)\partial_\nu h_\times(x)]
\end{aligned} \tag{A.50}$$

Remember that V is a region greater than several wavelengths. This means that in the sense of averaging over several wavelengths and periods, the stress-energy tensor for GW is equal to

$$t_{\mu\nu}(x) = \frac{1}{16\pi G}[\partial_\mu h_+(x)\partial_\nu h_+(x) + \partial_\mu h_\times(x)\partial_\nu h_\times(x)] \tag{A.51}$$

Or equivalently, from eq.(A.47),

$$t_{\mu\nu}(x) = \frac{1}{32\pi G}[\partial_\mu h^{\lambda\rho}(x)\partial_\nu h_{\lambda\rho}(x) - \frac{1}{2}\partial_\mu h^\lambda{}_\lambda(x)\partial_\nu h^\rho{}_\rho(x)] \tag{A.52}$$

A.6 Power from gravitational wave emitting

The power of the GW emitting is related to the energy flux density t^{0i} via

$$P = \oint_{S_2} t^{0i}\, d\Sigma^i = \int t^{0i} n^i r^2 d\Omega \tag{A.53}$$

Combining eq.(A.30) and eq.(A.33) we find

$$\partial_t h_+ = \frac{2G}{r}\frac{u_j u_k - v_j v_k}{2}\ddot{I}_{jk}\,, \qquad \partial_i h_+ = -\frac{2G}{r}\frac{u_j u_k - v_j v_k}{2}\ddot{I}_{jk} n_i + O(\frac{1}{r^2}) \tag{A.54}$$

$$\partial_t h_\times = \frac{2G}{r} u_j v_k \ddot{I}_{jk}\,, \qquad \partial_i h_+ = -\frac{2G}{r} u_j v_k \ddot{I}_{jk} n_i + O(\frac{1}{r^2}) \tag{A.55}$$

Insert into eq.(A.51),

$$\begin{aligned}
t^{0i} &= -\frac{1}{16\pi G}[\partial_t h_+ \partial_i h_+ + \partial_t h_\times \partial_i h_\times] \\
&= \frac{G}{4\pi r^2}[\frac{1}{4}(u_j u_k u_l u_m + v_j v_k v_l v_m - u_j u_k v_l v_m - v_j v_k u_l u_m) + \frac{1}{2}(u_j u_k v_l v_m + v_j v_k u_l u_m)] \\
&\quad \times \ddot{I}_{jk}\ddot{I}_{lm}\, n^i + O(\frac{1}{r^3}) \\
&= \frac{G}{8\pi r^2}[(u_j u_l + v_j v_l)(u_k u_m + v_k v_m) - \frac{1}{2}(u_j u_k + v_j v_k)(u_l u_m + v_l v_m)]\ddot{I}_{jk}\ddot{I}_{lm}\, n^i + O(\frac{1}{r^3}) \\
&= \frac{G}{8\pi r^2}[(\delta_{jl} - n_j n_l)(\delta_{km} - n_k n_m) - \frac{1}{2}(\delta_{jk} - n_j n_k)(\delta_{lm} - n_l n_m)]\ddot{I}_{jk}\ddot{I}_{lm}\, n^i + O(\frac{1}{r^3}) \\
&= \frac{G}{8\pi r^2}[(\delta_{jl}\delta_{km} - \frac{1}{2}\delta_{jk}\delta_{lm}) + (\frac{1}{2}\delta_{jk} n_l n_m + \frac{1}{2}\delta_{lm} n_j n_k - \delta_{jl} n_k n_m - \delta_{km} n_j n_l) \\
&\quad + \frac{1}{2} n_j n_k n_l n_m] \times \ddot{I}_{jk}\ddot{I}_{lm}\, n^i + O(\frac{1}{r^3})
\end{aligned} \tag{A.56}$$

Where in the fourth line we used the completeness relation: $u_j u_k + v_j v_k + n_j n_k = \delta_{jk}$. Since the configuration of unit vector $\boldsymbol{n}$ is isotropic (like a hedgehog), it satisfies the following integration identities:

$$\begin{aligned}
&\int d\Omega \;= 4\pi, \quad \int n_j n_k d\Omega \;= \frac{4\pi}{3}\delta_{jk}, \\
&\int n_j n_k n_l n_m d\Omega \;= \frac{4\pi}{15}(\delta_{jk}\delta_{lm} + \delta_{jl}\delta_{km} + \delta_{jm}\delta_{kl})
\end{aligned} \tag{A.57}$$

Then the power is,

$$\begin{aligned}
P = \int t^{0i} n^i r^2 d\Omega \;&= \frac{G}{8\pi}[\frac{8\pi}{5}\delta_{jl}\delta_{km} - \frac{8\pi}{15}\delta_{jk}\delta_{lm}]\ddot{I}_{jk}\ddot{I}_{lm} \\
&= \frac{G}{5}(\ddot{I}_{ij}\ddot{I}_{ij} - \frac{1}{3}\ddot{I}_{ii}\ddot{I}_{jj})
\end{aligned} \tag{A.58}$$

Eq.(A.58) is the expression of the power from GW emission.

A.7 Application to Binary Systems

Suppose two stars with masses m_1 and m_2 are inspiraling along circular orbit (this is a good approximation at the late inspiral stage since the orbital angular momentum should have been radiated away from GW emission). Let r_1 and r_2 be the radiuses from the star 1 and star 2 to the mass center respectively, $R = r_1 + r_2$ the distance between the two stars, $M = m_1 + m_2$ the total mass of the system, and Ω the orbit angular velocity. In the Newtonian limit, the movement of the binary system is governed by

$$\frac{Gm_1m_2}{R^2} = m_1r_1\Omega^2 = m_2r_2\Omega^2 ,$$

which gives

$$\begin{aligned} &r_1 = m_2R/M , \qquad r_2 = m_1R/M , \\ &R^3\Omega^2 = GM . \end{aligned} \tag{A.59}$$

We are free to choose a coordinate system so that the binary stars are moving in the $x - y$ plane. In this case, their world-lines are

$$\begin{aligned} \boldsymbol{x}_1(t) &= (m_2R/M\cos\Omega t\ ,\ m_2R/M\sin\Omega t\ ,\ 0) \\ \boldsymbol{x}_2(t) &= (-m_1R/M\cos\Omega t\ ,\ -m_1R/M\sin\Omega t\ ,\ 0) \end{aligned}$$

From eq.(A.35), the 00 component of the stress-energy tensor of this system is

$$\begin{aligned} T^{00}(t,\boldsymbol{x}) &= \sum_n m_n\delta^3\left(\boldsymbol{x} - \boldsymbol{x}_n(t)\right) \\ &= m_1\delta(x - m_2R/M\cos\Omega t)\ \delta(y - m_2R/M\sin\Omega t)\ \delta(z) \\ &+ m_2\delta(x + m_1R/M\cos\Omega t)\ \delta(y + m_1R/M\sin\Omega t)\ \delta(z) . \end{aligned} \tag{A.60}$$

From eq.(A.34), the quadrupole momentum I^{ij} is

$$I^{ij}(t) = \int d^3x\ x^ix^jT^{00}(t,\boldsymbol{x}) = \frac{m_1m_2}{2M}R^2\begin{pmatrix} 1+\cos 2\Omega t & \sin 2\Omega t & 0 \\ \sin 2\Omega t & 1-\cos 2\Omega t & 0 \\ 0 & 0 & 0 \end{pmatrix} . \tag{A.61}$$

Then from eq.(33), the GW $\bar{h}^{ij}$ emitted from this system is

$$\bar{h}^{ij}(t,\boldsymbol{x}) = \frac{2G}{r}\ddot{I}(t-r) = \frac{4Gm_1m_2}{Mr}\Omega^2R^2\begin{pmatrix} -\cos 2\Omega(t-r) & -\sin 2\Omega(t-r) & 0 \\ -\sin 2\Omega(t-r) & \cos 2\Omega(t-r) & 0 \\ 0 & 0 & 0 \end{pmatrix} .$$

Here r is the distance from the source to the observer. In our coordinate system where the binary star is located at the origin, the GW propagating direction $\boldsymbol{n}$ is the unit vector pointing from the origin to the observer at $\boldsymbol{r}$, with the other two unit vectors $\boldsymbol{u}$ and $\boldsymbol{v}$ orthogonal to $\boldsymbol{n}$ to be chosen as

$$\begin{cases} \boldsymbol{u} = (\cos\theta\cos\varphi,\ \cos\theta\sin\varphi,\ -\sin\theta) \\ \boldsymbol{v} = (-\sin\varphi,\ \cos\varphi,\ 0), \\ \boldsymbol{n} = (\sin\theta\cos\varphi,\ \sin\theta\sin\varphi,\ \cos\theta) \end{cases} \tag{A.62}$$

Then h_+ and $h_\times$ can be computed from eq.(A.30), and the results are

$$\begin{cases} h_+(t,\boldsymbol{x}) = -\frac{4G}{r}\frac{m_1m_2}{M}\ \Omega^2R^2\ \frac{1+\cos^2\theta}{2}\cos\left[2\Omega(t-r)-2\varphi\right] \\ h_\times(t,\boldsymbol{x}) = -\frac{4G}{r}\frac{m_1m_2}{M}\ \Omega^2R^2\cos\theta\sin\left[2\Omega(t-r)-2\varphi\right] \end{cases}. \tag{A.63}$$

This result suggests the relation between the orbital angular frequency Ω and the GW angular frequency ω:

$$\omega = 2\Omega \quad \Rightarrow \quad f = \omega/2\pi = \Omega/\pi \tag{A.64}$$

Notice that h_+ and $h_\times$ are not rotation invariant. If we make an $SO(2)$ rotation in the $\boldsymbol{u}-\boldsymbol{v}$ plane, there will be a mixture of these two.

Next we want to compute the power of GW emission from this binary system. In sert eq.(A.61) into eq.(A.51):

$$\begin{aligned} \ddot{I}_{ij} &= 4\frac{m_1m_2}{M}R^2\Omega^3\begin{pmatrix} \sin 2\Omega t & -\cos 2\Omega t & 0 \\ -\cos 2\Omega t & -\sin 2\Omega t & 0 \\ 0 & 0 & 0 \end{pmatrix} \quad \Rightarrow \\ P &= -\frac{dE}{dt} = \frac{G}{5}(\dddot{I}_{ij}\ddot{I}_{ij} - \frac{1}{3}\dddot{I}_{ii}\ddot{I}_{jj}) = \frac{32}{5}G\left(\frac{m_1m_2}{M}\right)^2\Omega^6R^4 \\ &= \frac{32}{5}G^4M(m_1m_2)^2R^{-5} = \frac{32}{5}G^{\frac{7}{3}}\left(\frac{m_1m_2}{M}\right)^2\Omega^{\frac{10}{3}} \end{aligned} \tag{A.65}$$

Another way to compute the power is to start from the stress-energy tensor. Insert eq.(A.63) into eq.(A.51),

$$\begin{cases} \partial_t h_+ = \frac{8G}{r}\frac{m_1m_2}{M}\ \Omega^3R^2\ \frac{1+\cos^2\theta}{2}\sin\left[2\Omega(t-r)-2\varphi\right], \quad \partial_i h_+ = -n^i\partial_t h_+ + O(\frac{1}{r^2}) \\ \partial_t h_\times = -\frac{8G}{r}\frac{m_1m_2}{M}\ \Omega^3R^2\cos\theta\cos\left[2\Omega(t-r)-2\varphi\right], \quad \partial_i h_\times = -n^i\partial_t h_\times + O(\frac{1}{r^2}) \end{cases}$$

which leads to

$$
\begin{aligned}
t^{0i} =& -\frac{1}{16\pi G}[\partial_t h_+ \partial_i h_+ + \partial_t h_\times \partial_i h_\times] \\
=& \frac{4G}{\pi r^2}\left(\frac{m_1 m_2}{M}\right)^2 \Omega^6 R^4 \\
& \times \left\{(\frac{1+\cos^2\theta}{2})^2 \sin^2[2\Omega(t-r)-2\varphi] + \cos^2\theta\cos^2[2\Omega(t-r)-2\varphi]\right\} n^i \\
=& \frac{2G}{\pi r^2}\left(\frac{m_1 m_2}{M}\right)^2 \Omega^6 R^4 \left[(\frac{1+\cos^2\theta}{2})^2 + \cos^2\theta\right] n^i \ . \qquad \text{(A.66)}
\end{aligned}
$$

Here the third equal sign is from the fact that eq.(A.51) holds in the sense of averaging over time. Then the power is

$$
\begin{aligned}
P =& \int t^{01} n^i r^2 d\Omega = \frac{2G}{\pi}\left(\frac{m_1 m_2}{M}\right)^2 \Omega^6 R^4 \int [(\frac{1+\cos^2\theta}{2})^2 + \cos^2\theta]\, d\Omega \\
=& \frac{32}{5} G \left(\frac{m_1 m_2}{M}\right)^2 \Omega^6 R^4 \qquad \text{(A.67)}
\end{aligned}
$$

It gives the same result as eq.(A.65).

Next we want to compute the orbit change due to the GW emission. Start from the total energy of the binary system

$$
\begin{aligned}
E = T + V =& \frac{1}{2} m_1 \left(\frac{m_2}{M} R\Omega\right)^2 + \frac{1}{2} m_2 \left(\frac{m_1}{M} R\Omega\right)^2 - \frac{G m_1 m_2}{R} \\
=& -\frac{1}{2}\frac{G m_1 m_2}{R} = -\frac{1}{2}(\pi G)^{\frac{2}{3}} \frac{m_1 m_2}{M^{\frac{1}{3}}} f^{\frac{2}{3}} \ . \qquad \text{(A.68)}
\end{aligned}
$$

Taking derivative of this equation gives the energy spectrum and power of GW emission:

$$
\frac{dE_{\rm GW}}{df} = -\frac{dE}{df} = \frac{1}{3}(\pi G)^{\frac{2}{3}} \mathcal{M}^{\frac{5}{3}} f^{-\frac{1}{3}} \ . \qquad \text{(A.69)}
$$

$$
\frac{dE}{dt} = \frac{1}{2}\frac{G m_1 m_2}{R^2}\frac{dR}{dt} = -\frac{1}{3}(\pi G)^{\frac{2}{3}} \frac{m_1 m_2}{M^{\frac{1}{3}}} f^{-\frac{1}{3}} \dot{f} \ . \qquad \text{(A.70)}
$$

Here the chirp mass $\mathcal{M}$ is defined as

$$
\mathcal{M} = (m_1 m_2)^{\frac{3}{5}} M^{-\frac{1}{5}} \ . \qquad \text{(A.71)}
$$

Combining eq.(A.65) and eq.(A.70) gives the relating between the changing rate of the GW frequency and the chirp mass as well as the changing rate of orbital distance:

$$
\mathcal{M} = \frac{1}{G}\left[\frac{5}{96}\pi^{-\frac{8}{3}} f^{-\frac{11}{3}} \dot{f}\right]^{\frac{3}{5}} \ . \qquad \text{(A.72)}
$$

$$
\frac{dR}{dt} = -\frac{64}{5} G^3 M m_1 m_2 R^{-3} \ . \qquad \text{(A.73)}
$$

From eq.(A.72), we can solve for the GW frequency as a function of time:

$$f(t)^{-\frac{8}{3}} = -\frac{256}{5}\pi^{\frac{8}{3}}\left(G\mathcal{M}\right)^{\frac{5}{3}}\left(t - t_0\right) . \tag{A.74}$$

From eq.(A.73), we can solve for the orbital equations of the inspiraling binary system:

$$R(t) = \left[R_0^4 - \frac{256}{5}G^3 M m_1 m_2\, t\right]^{\frac{1}{4}} , \tag{A.75}$$

$$t(R) = \frac{5}{256}\frac{R_0^4 - R^4}{G^3 M m_1 m_2} , \tag{A.76}$$

$$\Omega(t) = \frac{d\phi(t)}{dt} = (GM)^{\frac{1}{2}}\left[R_0^4 - \frac{256}{5}G^3 M m_1 m_2\, t\right]^{-\frac{3}{8}} , \tag{A.77}$$

$$\phi(t) = \frac{R_0^{\frac{5}{2}} - R(t)^{\frac{5}{2}}}{32 G^{\frac{5}{2}} M^{\frac{1}{2}} m_1 m_2} . \tag{A.78}$$

As our first example, let's consider the binary neutron star PSR B1913+16, with mass $m_1 = m_2 = 1.44 M_\odot$ and orbit period $T_0 = 7.75$h. From eq.(A.59), the orbital separation is $R_0 = 9.81 \times 10^8$m. From eq.(A.73), currently the radius decreases per year: $\Delta R_0 = -0.15$m, or $\Delta R_0/R_0 \sim 10^{-10}$. From eq.(A.75), two neutron stars will collide with each other in $t = 1.6 \times 10^9$yr. Notice that this predicted lifetime is longer than the actual PSR B1913+16, which has a non-circular orbit with eccentricity $e = 0.617$. The power of GW emission from highly elliptic orbit is greater due to the larger quadrupole momentum of the system.

Our next example is the binary black hole in GW150914. The strain data from the LIGO Livingston and LIGO Hanford detectors provide valuable information such as the peak value and the frequencies over time, from which we can infer the properties of the source.

The GW frequency–time data is provided in Ref.[131], which is listed in Tab. A.1. Eq.(A.74) suggests a linear relation between $f^{-8/3}$ and t and the coefficient only depends on the chirp mass. A least square-fit of the data in Tab. A.1 gives $y = x \cdot \beta + \beta_0$, with $y = f^{-8/3}$, $x = t$, $\beta = -6.52 \times 10^{-4}$, $\beta_0 = 2.75 \times 10^{-4}$ and an R square of 0.94. From eq.(A.74), the coefficient translates into a chirp mass of $37 M_\odot$. Notice that this estimation is slightly greater than the actual chirp mass $\mathcal{M} = 30 M_\odot$ for two reasons: (i) uncertainty is large in the observed data, (ii) the post-Newtonian corrections are neglected. By assuming the two black holes have equal mass, we have $m_1 = m_2 \simeq 35 M_\odot$.

time (s)	GW frequency (Hz)
0.3491	42
0.3598	47
0.3698	50
0.3812	43
0.3904	55
0.3975	71
0.4042	74
0.4100	86
0.4141	120
0.4176	141
0.4201	195
0.4223	242

Table A.1: The GW frequencies over time from the strain of GW150914.

Another information contained in the observation is the peak amplitude of the strain, which marks the end of the inspiral stage. This happens at $t_{\max} \simeq 0.42$ s, with $h_{\max} \simeq 1 \times 10^{-21}$ and $f_{\max} \simeq 150$ Hz. From eq.(A.59), this frequency corresponds to an orbit separation $R_{\max} = 350$ km. Comparing the orbital separation with the Schwarzschild radius $r_s \simeq 100$ km for $m = 35M_\odot$ strongly suggests that the merger is from two black holes.

The GW energy emitted during the inspiral stage can be estimated from eq,(A.68):

$$E_{\rm GW} = E_i - E_f = 0 - \left(-\frac{1}{2}\frac{Gm_1m_2}{R_{\max}}\right) \simeq 2.6M_\odot \ . \tag{A.79}$$

This provides a lower boundary for the total emitted energy, which should also include the merger, ringdown (and probably the echo) stages.

Eq.(A.63) suggests a relation between the amplitude of strain h and the distance of the source r:

$$r = \frac{2}{5}\frac{4G^2}{c^4}\frac{m_1m_2}{R\ h} \ , \tag{A.80}$$

where the factor $2/5$ comes from the angular pattern function of the detector. Insert the values of $h_{\max}$ and $R_{\max}$, we obtain $r \simeq 400$ Mpc. This estimation is very close to the actual observed distance.

BIBLIOGRAPHY

[1] https://github.com/szhorvat/MaTeX.

[2] The lsc-virgo white paper on instrument science. *LIGO Document T1400316*, 2015.

[3] B. P. Abbott et al. Observation of Gravitational Waves from a Binary Black Hole Merger. *Phys. Rev. Lett.*, 116(6):061102, 2016. doi: 10.1103/PhysRevLett.116.061102.

[4] B. P. Abbott et al. GW151226: Observation of Gravitational Waves from a 22-Solar-Mass Binary Black Hole Coalescence. *Phys. Rev. Lett.*, 116(24): 241103, 2016. doi: 10.1103/PhysRevLett.116.241103.

[5] B. P. Abbott et al. Binary Black Hole Mergers in the first Advanced LIGO Observing Run. *Phys. Rev.*, X6(4):041015, 2016. doi: 10.1103/PhysRevX.6.041015.

[6] B. P. Abbott et al. Tests of general relativity with GW150914. *Phys. Rev. Lett.*, 116(22):221101, 2016. doi: 10.1103/PhysRevLett.116.221101.

[7] B. P. Abbott et al. GW170104: Observation of a 50-Solar-Mass Binary Black Hole Coalescence at Redshift 0.2. *Phys. Rev. Lett.*, 118:221101, Jun 2017. doi: 10.1103/PhysRevLett.118.221101. URL https://link.aps.org/doi/10.1103/PhysRevLett.118.221101.

[8] Benjamin P Abbott, Richard Abbott, TD Abbott, MR Abernathy, Fausto Acernese, Kendall Ackley, Carl Adams, Thomas Adams, Paolo Addesso, RX Adhikari, et al. Observation of gravitational waves from a binary black hole merger. *Physical review letters*, 116(6):061102, 2016.

[9] Benjamin P Abbott, R Abbott, TD Abbott, F Acernese, K Ackley, C Adams, T Adams, P Addesso, RX Adhikari, VB Adya, et al. Gw170817: Implications for the stochastic gravitational-wave background from compact binary coalescences. *Physical review letters*, 120(9):091101, 2018.

[10] Benjamin P Abbott et al. Observation of gravitational waves from a binary black hole merger. *Physical review letters*, 116(6):061102, 2016.

[11] Benjamin P Abbott et al. Tests of general relativity with gw150914. *Physical Review Letters*, 116(22):221101, 2016.

[12] Benjamin P Abbott et al. Gw151226: observation of gravitational waves from a 22-solar-mass binary black hole coalescence. *Phys Rev Lett*, 116: 241103, 2016.

[13] Benjamin P Abbott et al. Gw170104: observation of a 50-solar-mass binary black hole coalescence at redshift 0.2. *Physical Review Letters*, 118(22): 221101, 2017.

[14] Benjamin P Abbott et al. Gw170814: A three-detector observation of gravitational waves from a binary black hole coalescence. *Physical review letters*, 119(14):141101, 2017.

[15] Benjamin P Abbott et al. Gw170817: observation of gravitational waves from a binary neutron star inspiral. *Physical Review Letters*, 119(16):161101, 2017.

[16] Benjamin P Abbott et al. Gravitational waves and gamma-rays from a binary neutron star merger: Gw170817 and grb 170817a. *The Astrophysical Journal Letters*, 848(2):L13, 2017.

[17] Benjamin P Abbott et al. Gw170817: Implications for the stochastic gravitational-wave background from compact binary coalescences. *Physical review letters*, 120(9):091101, 2018.

[18] BP Abbott, Richard Abbott, TD Abbott, MR Abernathy, Fausto Acernese, Kendall Ackley, Carl Adams, Thomas Adams, Paolo Addesso, RX Adhikari, et al. Gw150914: Implications for the stochastic gravitational-wave background from binary black holes. *Physical review letters*, 116(13):131102, 2016.

[19] BP Abbott, R Abbott, TD Abbott, F Acernese, K Ackley, C Adams, T Adams, P Addesso, RX Adhikari, et al. Gw170104: Observation of a 50-solar-mass binary black hole coalescence at redshift 0.2. *Physical Review Letters*, 118 (22):221101, 2017.

[20] BP Abbott et al. Gw150914: Implications for the stochastic gravitational-wave background from binary black holes. *Physical review letters*, 116(13): 131102, 2016.

[21] BP Abbott et al. A search for tensor, vector, and scalar polarizations in the stochastic gravitational-wave background. *arXiv preprint arXiv:1802.10194*, 2018.

[22] Jahed Abedi, Hannah Dykaar, and Niayesh Afshordi. Echoes from the abyss: Evidence for planck-scale structure at black hole horizons. *arXiv preprint arXiv:1612.00266*, 2016.

[23] Jahed Abedi, Hannah Dykaar, and Niayesh Afshordi. Echoes from the Abyss: Evidence for Planck-scale structure at black hole horizons. 2016.

[24] Jahed Abedi, Hannah Dykaar, and Niayesh Afshordi. Echoes from the abyss: The holiday edition! *arXiv preprint arXiv:1701.03485*, 2017.

[25] Jahed Abedi, Hannah Dykaar, and Niayesh Afshordi. Echoes from the Abyss: The Holiday Edition! 2017.

[26] Marek A. Abramowicz, Wlodek Kluzniak, and Jean-Pierre Lasota. No observational proof of the black hole event-horizon. *Astron. Astrophys.*, 396: L31–L34, 2002. doi: 10.1051/0004-6361:20021645.

[27] Parameswaran Ajith, Stanislav Babak, Yanbei Chen, Martin Hewitson, Badri Krishnan, AM Sintes, John T Whelan, B Brügmann, P Diener, Nils Dorband, et al. Template bank for gravitational waveforms from coalescing binary black holes: Nonspinning binaries. *Physical Review D*, 77(10):104017, 2008.

[28] Bruce Allen and Joseph D Romano. Detecting a stochastic background of gravitational radiation: Signal processing strategies and sensitivities. *Physical Review D*, 59(10):102001, 1999.

[29] Ahmed Almheiri, Donald Marolf, Joseph Polchinski, and James Sully. Black holes: complementarity or firewalls? *Journal of High Energy Physics*, 2013 (2):62, 2013.

[30] Pau Amaro-Seoane, Sofiane Aoudia, Stanislav Babak, Pierre Binetruy, Emanuele Berti, et al. eLISA/NGO: Astrophysics and cosmology in the gravitational-wave millihertz regime. *GW Notes*, 6:4–110, 2013.

[31] Gregory Ashton, Ofek Birnholtz, Miriam Cabero, Collin Capano, Thomas Dent, Badri Krishnan, Grant David Meadors, Alex B Nielsen, Alex Nitz, and Julian Westerweck. Comments on:" echoes from the abyss: Evidence for planck-scale structure at black hole horizons". *arXiv preprint arXiv:1612.05625*, 2016.

[32] Gregory Ashton, Ofek Birnholtz, Miriam Cabero, Collin Capano, Thomas Dent, Badri Krishnan, Grant David Meadors, Alex B. Nielsen, Alex Nitz, and Julian Westerweck. Comments on: "Echoes from the abyss: Evidence for Planck-scale structure at black hole horizons". 2016.

[33] A Avilez and C Skordis. Cosmological constraints on brans-dicke theory. *Physical review letters*, 113(1):011101, 2014.

[34] C. Barcelo, L. J. Garay, and G. Jannes. Quantum Non-Gravity and Stellar Collapse. *Found. Phys.*, 41:1532–1541, 2011. doi: 10.1007/s10701-011-9577-9.

[35] Carlo Barcelo, Raul Carballo-Rubio, Luis J. Garay, and Gil Jannes. The lifetime problem of evaporating black holes: mutiny or resignation. *Class. Quant. Grav.*, 32(3):035012, 2015. doi: 10.1088/0264-9381/32/3/035012.

[36] Peter S Behroozi, Risa H Wechsler, and Charlie Conroy. The average star formation histories of galaxies in dark matter halos from z= 0-8. *The Astrophysical Journal*, 770(1):57, 2013.

[37] E. Berti, V. Cardoso, and A. O. Starinets. TOPICAL REVIEW: Quasinormal modes of black holes and black branes. *Classical and Quantum Gravity*, 26 (16):163001, August 2009. doi: 10.1088/0264-9381/26/16/163001.

[38] Emanuele Berti, Vitor Cardoso, and Clifford M. Will. On gravitational-wave spectroscopy of massive black holes with the space interferometer LISA. *Phys. Rev.*, D73:064030, 2006. doi: 10.1103/PhysRevD.73.064030.

[39] Emanuele Berti, Vitor Cardoso, and Andrei O. Starinets. Quasinormal modes of black holes and black branes. *Class. Quant. Grav.*, 26:163001, 2009. doi: 10.1088/0264-9381/26/16/163001.

[40] Emanuele Berti, Vitor Cardoso, Tanja Hinderer, Madalena Lemos, Frans Pretorius, Ulrich Sperhake, and Nicolás Yunes. Semianalytical estimates of scattering thresholds and gravitational radiation in ultrarelativistic black hole encounters. *Physical Review D*, 81(10):104048, 2010.

[41] Emanuele Berti, Alberto Sesana, Enrico Barausse, Vitor Cardoso, and Krzysztof Belczynski. Spectroscopy of Kerr black holes with Earth- and space-based interferometers. *Phys. Rev. Lett.*, 117(10):101102, 2016. doi: 10.1103/PhysRevLett.117.101102.

[42] Bruno Bertotti, Luciano Iess, and Paolo Tortora. A test of general relativity using radio links with the cassini spacecraft. *Nature*, 425(6956):374, 2003.

[43] RJ Bontz and RH Price. The spectrum of radiation at low frequencies. *The Astrophysical Journal*, 228:560–575, 1979.

[44] VB Braginskii and LP Grishchuk. Kinematic resonance and memory effect in free-mass gravitational antennas. *Soviet Physics-JETP*, 62(3):427–430, 1985.

[45] Vladimir B Braginsky and Kip S Thorne. Gravitational-wave bursts with memory and experimental prospects. *Nature*, 327(6118):123, 1987.

[46] Carl Brans and Robert H Dicke. Mach's principle and a relativistic theory of gravitation. *Physical review*, 124(3):925, 1961.

[47] Maura Brunetti, E Coccia, V Fafone, and F Fucito. Gravitational wave radiation from compact binary systems in the jordan-brans-dicke theory. *Physical Review D*, 59(4):044027, 1999.

[48] Alessandra Buonanno and Thibault Damour. Effective one-body approach to general relativistic two-body dynamics. *Physical Review D*, 59(8):084006, 1999.

[49] Alessandra Buonanno and Thibault Damour. Transition from inspiral to plunge in binary black hole coalescences. *Physical Review D*, 62(6):064015, 2000.

[50] Thomas Callister, Letizia Sammut, Shi Qiu, Ilya Mandel, and Eric Thrane. Limits of astrophysics with gravitational-wave backgrounds. *Physical Review X*, 6(3):031018, 2016.

[51] Thomas Callister, A Sylvia Biscoveanu, Nelson Christensen, Maximiliano Isi, Andrew Matas, Olivier Minazzoli, Tania Regimbau, Mairi Sakellariadou, Jay Tasson, and Eric Thrane. Polarization-based tests of gravity with the stochastic gravitational-wave background. *Physical Review X*, 7(4):041058, 2017.

[52] Rachel Capon. *Radiation Reaction Near Black Holes*. PhD thesis, University of Wales, 1998.

[53] Vitor Cardoso and Paolo Pani. The observational evidence for black holes. unpublished, 2017.

[54] Vitor Cardoso and Paolo Pani. Tests for the existence of black holes through gravitational wave echoes. *Nature Astronomy*, 1(9):586, 2017.

[55] Vitor Cardoso, Luis C. B. Crispino, Caio F. B. Macedo, Hirotada Okawa, and Paolo Pani. Light rings as observational evidence for event horizons: long-lived modes, ergoregions and nonlinear instabilities of ultracompact objects. *Phys. Rev.*, D90(4):044069, 2014. doi: 10.1103/PhysRevD.90.044069.

[56] Vitor Cardoso, Edgardo Franzin, and Paolo Pani. Is the gravitational-wave ringdown a probe of the event horizon? *Physical review letters*, 116(17): 171101, 2016.

[57] Vitor Cardoso, Edgardo Franzin, and Paolo Pani. Is the gravitational-wave ringdown a probe of the event horizon? *Phys. Rev. Lett.*, 116(17): 171101, 2016. doi: 10.1103/PhysRevLett.117.089902,10.1103/PhysRevLett.116.171101. [Erratum: Phys. Rev. Lett.117,no.8,089902(2016)].

[58] Vitor Cardoso, Seth Hopper, Caio F. B. Macedo, Carlos Palenzuela, and Paolo Pani. Gravitational-wave signatures of exotic compact objects and of quantum corrections at the horizon scale. *Phys. Rev.*, D94(8):084031, 2016. doi: 10.1103/PhysRevD.94.084031.

[59] Vitor Cardoso, Edgardo Franzin, Andrea Maselli, Paolo Pani, and Guilherme Raposo. Testing strong-field gravity with tidal Love numbers. *Phys. Rev.*, D95(8):084014, 2017. doi: 10.1103/PhysRevD.95.084014.

[60] Marc Casals and Brien C. Nolan. Geometric properties of a 2D spacetime arising in 4D black hole physics. *Phys. Rev.*, D92(10):104030, 2015. doi: 10.1103/PhysRevD.92.104030.

[61] D Cevik, Manuel Gadella, Ş Kuru, and Javier Negro. Resonances and antibound states for the pöschl–teller potential: Ladder operators and susy partners. *Physics Letters A*, 380(18-19):1600–1609, 2016.

[62] Subrahmanyan Chandrasekhar and Steven Detweiler. The quasi-normal modes of the schwarzschild black hole. *Proceedings of the Royal Society of London. Series A, Mathematical and Physical Sciences*, pages 441–452, 1975.

[63] E. S. C. Ching, P. T. Leung, W. M. Suen, and K. Young. Wave propagation in gravitational systems: Completeness of quasinormal modes. *Phys. Rev.*, D54:3778–3791, 1996. doi: 10.1103/PhysRevD.54.3778.

[64] Demetrios Christodoulou. Nonlinear nature of gravitation and gravitational-wave experiments. *Physical review letters*, 67(12):1486, 1991.

[65] Timothy Clifton, Pedro G Ferreira, Antonio Padilla, and Constantinos Skordis. Modified gravity and cosmology. *Physics reports*, 513(1-3):1–189, 2012.

[66] Miguel R Correia and Vitor Cardoso. Characterization of echoes: a dyson-series representation of individual pulses. *Physical Review D*, 97(8):084030, 2018.

[67] K Crocker, V Mandic, T Regimbau, K Belczynski, W Gladysz, K Olive, T Prestegard, and E Vangioni. Model of the stochastic gravitational-wave background due to core collapse to black holes. *Physical Review D*, 92(6): 063005, 2015.

[68] PA Crowther, O Schurr, R Mirschi, N Yusof, RJ Parker, SP Goodwin, and HA Kassim. The emergence of super canonical stars in r136-type starburst clusters. *MNRAS*, 408:731, 2010.

[69] Thibault Damour and Gilles Esposito-Farese. Nonperturbative strong-field effects in tensor-scalar theories of gravitation. *Physical Review Letters*, 70 (15):2220, 1993.

[70] O. Dreyer, B. Kelly, B. Krishnan, L. S. Finn, D. Garrison, and R. Lopez-Aleman. Black-hole spectroscopy: testing general relativity through gravitational-wave observations. *Classical and Quantum Gravity*, 21:787–803, February 2004. doi: 10.1088/0264-9381/21/4/003.

[71] S. M. Du and Y. Chen. *in preparation*, 2018.

[72] Douglas M Eardley, David L Lee, and Alan P Lightman. Gravitational-wave observations as a tool for testing relativistic gravity. *Physical Review D*, 8 (10):3308, 1973.

[73] Douglas M Eardley, David L Lee, and Alan P Lightman. Gravitational-wave observations as a tool for testing relativistic gravity. *Physical Review D*, 8 (10):3308, 1973.

[74] Douglas M Eardley, David L Lee, Alan P Lightman, Robert V. Wagoner, and Clifford M. Will. Gravitational-wave observations as a tool for testing relativistic gravity. *Physical Review Letters*, 30(18):884, 1973.

[75] Andreas Eckart, Andreas Huttemann, Claus Kiefer, Silke Britzen, Michal Zajaek, Claus Lammerzahl, Manfred Stockler, Monica Valencia-S, Vladimir Karas, and Macarena Garcia-Marin. The Milky Way?s Supermassive Black Hole: How Good a Case Is It? *Found. Phys.*, 47(5):553–624, 2017. doi: 10.1007/s10701-017-0079-2.

[76] Heino Falcke, Fulvio Melia, and Eric Agol. Viewing the shadow of the black hole at the galactic center. *Astrophys. J.*, 528:L13, 2000. doi: 10.1086/312423.

[77] Valeria Ferrari, Sabino Matarrese, and Raffaella Schneider. Gravitational wave background from a cosmological population of core-collapse supernovae. *Monthly Notices of the Royal Astronomical Society*, 303(2):247–257, 1999.

[78] V. P. Frolov and I. D. Novikov, editors. *Black hole physics: Basic concepts and new developments*. 1998.

[79] Valeri Frolov and Igor Novikov. *Black hole physics: basic concepts and new developments*, volume 96. Springer Science & Business Media, 2012.

[80] Chris L Fryer and Kimberly CB New. Gravitational waves from gravitational collapse. *Living Reviews in Relativity*, 14(1):1, 2011.

[81] Yasunori Fujii and Kei-ichi Maeda. *The scalar-tensor theory of gravitation*. Cambridge University Press, 2003.

[82] Davide Gerosa, Ulrich Sperhake, and Christian D Ott. Numerical simulations of stellar collapse in scalar-tensor theories of gravity. *Classical and Quantum Gravity*, 33(13):135002, 2016.

[83] Steven B Giddings. Gravitational wave tests of quantum modifications to black hole structure?with post-gw150914 update. *Classical and Quantum Gravity*, 33(23):235010, 2016.

[84] Shahar Hadar and Barak Kol. Post-ISCO Ringdown Amplitudes in Extreme Mass Ratio Inspiral. *Phys. Rev.*, D84:044019, 2011. doi: 10.1103/PhysRevD.84.044019.

[85] Tomohiro Harada. Neutron stars in scalar-tensor theories of gravity and catastrophe theory. *Physical Review D*, 57(8):4802, 1998.

[86] Tomohiro Harada, Takeshi Chiba, Ken-ichi Nakao, and Takashi Nakamura. Scalar gravitational wave from oppenheimer-snyder collapse in scalar-tensor theories of gravity. *Physical Review D*, 55(4):2024, 1997.

[87] SW Hawking. Black holes in the brans-dicke. *Communications in Mathematical Physics*, 25(2):167–171, 1972.

[88] Kazuhiro Hayama and Atsushi Nishizawa. Model-independent test of gravity with a network of ground-based gravitational-wave detectors. *Physical Review D*, 87(6):062003, 2013.

[89] Shahar Hod. Onset of superradiant instabilities in rotating spacetimes of exotic compact objects. 2017.

[90] Bob Holdom and Jing Ren. Not quite a black hole. *Phys. Rev.*, D95(8): 084034, 2017. doi: 10.1103/PhysRevD.95.084034.

[91] Richard A Isaacson. Gravitational radiation in the limit of high frequency. i. the linear approximation and geometrical optics. *Physical Review*, 166(5): 1263, 1968.

[92] Michael D. Johnson et al. Resolved Magnetic-Field Structure and Variability Near the Event Horizon of Sagittarius A*. *Science*, 350(6265):1242–1245, 2015. doi: 10.1126/science.aac7087.

[93] Matthew D Kistler, Hasan Yuksel, and Andrew M Hopkins. The cosmic star formation rate from the faintest galaxies in the unobservable universe. *arXiv preprint arXiv:1305.1630*, 2013.

[94] SJ Kovacs Jr and KS Thorne. The generation of gravitational waves. iv-bremsstrahlung. *The Astrophysical Journal*, 224:62–85, 1978.

[95] N. V. Krishnendu, K. G. Arun, and Chandra Kant Mishra. Testing the binary black hole nature of a compact binary coalescence. 2017.

[96] Ryan N Lang. Compact binary systems in scalar-tensor gravity. ii. tensor gravitational waves to second post-newtonian order. *Physical Review D*, 89 (8):084014, 2014.

[97] JM Lattimer and M Prakash. Neutron star structure and the equation of state. *The Astrophysical Journal*, 550(1):426, 2001.

[98] Carlos O. Lousto and Richard H. Price. Understanding initial data for black hole collisions. *Phys. Rev.*, D56:6439–6457, 1997. doi: 10.1103/PhysRevD.56.6439.

[99] Elisa Maggio, Paolo Pani, and Valeria Ferrari. Exotic Compact Objects and How to Quench their Ergoregion Instability. 2017.

[100] Michele Maggiore and Alberto Nicolis. Detection strategies for scalar gravitational waves with interferometers and resonant spheres. *Physical Review D*, 62(2):024004, 2000.

[101] Zachary Mark, Aaron Zimmerman, Song Ming Du, and Yanbei Chen. A recipe for echoes from exotic compact objects. *Physical Review D*, 96(8): 084002, 2017.

[102] Andrea Maselli, Paolo Pani, Vitor Cardoso, Tiziano Abdelsalhin, Leonardo Gualtieri, and Valeria Ferrari. Probing Planckian corrections at the horizon scale with LISA binaries. 2017.

[103] Andrea Maselli, Sebastian H Völkel, and Kostas D Kokkotas. Parameter estimation of gravitational wave echoes from exotic compact objects. *Physical Review D*, 96(6):064045, 2017.

[104] Samir D Mathur. The fuzzball proposal for black holes: An elementary review. *Fortschritte der Physik*, 53(7-8):793–827, 2005.

[105] Samir D. Mathur. The Fuzzball proposal for black holes: An Elementary review. *Fortsch. Phys.*, 53:793–827, 2005. doi: 10.1002/prop.200410203.

[106] Pawel O Mazur and Emil Mottola. Gravitational condensate stars: An alternative to black holes. *arXiv preprint gr-qc/0109035*, 2001.

[107] Pawel O. Mazur and Emil Mottola. Gravitational condensate stars: An alternative to black holes. 2001.

[108] D. J. A. McKechan, C. Robinson, and B. S. Sathyaprakash. A tapering window for time-domain templates and simulated signals in the detection of gravitational waves from coalescing compact binaries. *Class. Quant. Grav.*, 27:084020, 2010. doi: 10.1088/0264-9381/27/8/084020.

[109] CW Misner, KS Thorne, and JA Wheeler. Gravitation, chap. 35, 1973.

[110] C.W. Misner, K.S. Thorne, and J.A. Wheeler. *Gravitation*. Freeman, San Francisco, 1973.

[111] M. S. Morris, K. S. Thorne, and U. Yurtsever. Wormholes, Time Machines, and the Weak Energy Condition. *Phys. Rev. Lett.*, 61:1446–1449, 1988. doi: 10.1103/PhysRevLett.61.1446.

[112] Hiroyuki Nakano, Norichika Sago, Hideyuki Tagoshi, and Takahiro Tanaka. Black hole ringdown echoes and howls. 2017.

[113] Atsushi Nishizawa, Atsushi Taruya, Kazuhiro Hayama, Seiji Kawamura, and Masa-aki Sakagami. Probing nontensorial polarizations of stochastic gravitational-wave backgrounds with ground-based laser interferometers. *Physical Review D*, 79(8):082002, 2009.

[114] Hans-Peter Nollert. Quasinormal modes: the characteristic 'sound' of black holes and neutron stars. *Classical and Quantum Gravity*, 16(12):R159, 1999. URL `http://stacks.iop.org/0264-9381/16/i=12/a=201`.

[115] Hans-Peter Nollert and Richard H. Price. Quantifying excitations of quasinormal mode systems. *J. Math. Phys.*, 40:980–1010, 1999. doi: 10.1063/1.532698.

[116] Jerome Novak. Spherical neutron star collapse toward a black hole in a tensor-scalar theory of gravity. *Physical Review D*, 57(8):4789, 1998.

[117] Jérôme Novak. Neutron star transition to a strong-scalar-field state in tensor-scalar gravity. *Physical Review D*, 58(6):064019, 1998.

[118] RF O'Connell and A Salmona. Radiation of gravitational waves in brans-dicke general-relativity theory. *Physical Review*, 160(5):1108, 1967.

[119] J Robert Oppenheimer and Hartland Snyder. On continued gravitational contraction. *Physical Review*, 56(5):455, 1939.

[120] Paolo Pani. Advanced Methods in Black-Hole Perturbation Theory. *Int. J. Mod. Phys.*, A28:1340018, 2013. doi: 10.1142/S0217751X13400186.

[121] Paolo Pani, Emanuele Berti, Vitor Cardoso, Yanbei Chen, and Richard Norte. Gravitational wave signatures of the absence of an event horizon. I. Nonradial oscillations of a thin-shell gravastar. *Phys. Rev.*, D80:124047, 2009. doi: 10.1103/PhysRevD.80.124047.

[122] Paolo Pani, Emanuele Berti, Vitor Cardoso, Yanbei Chen, and Richard Norte. Gravitational-wave signatures of the absence of an event horizon. II. Extreme mass ratio inspirals in the spacetime of a thin-shell gravastar. *Phys. Rev.*, D81:084011, 2010. doi: 10.1103/PhysRevD.81.084011.

[123] ES Phinney. A practical theorem on gravitational wave backgrounds. *arXiv preprint astro-ph/0108028*, 2001.

[124] G Pöschl and E Teller. Bemerkungen zur quantenmechanik des anharmonischen oszillators. *Zeitschrift für Physik*, 83(3-4):143–151, 1933.

[125] Richard Price and Gaurav Khanna. Gravitational wave sources: reflections and echoes. *arXiv preprint arXiv:1702.04833*, 2017.

[126] Richard H. Price and Gaurav Khanna. Gravitational wave sources: reflections and echoes. 2017.

[127] Laura Sampson, Nicolas Yunes, Neil Cornish, Marcelo Ponce, Enrico Barausse, Antoine Klein, Carlos Palenzuela, and Luis Lehner. Projected constraints on scalarization with gravitational waves from neutron star binaries. *Physical Review D*, 90(12):124091, 2014.

[128] M Sasaki and T Nakamura. The regge-wheeler equation with sources for both even and odd parity perturbations of the schwarzschild geometry. *Physics Letters A*, 87(3):85–88, 1981.

[129] Bangalore Suryanarayana Sathyaprakash and Bernard F Schutz. Physics, astrophysics and cosmology with gravitational waves. *Living Reviews in Relativity*, 12(1):2, 2009.

[130] F. E. Schunck and E. W. Mielke. General relativistic boson stars. *Class. Quant. Grav.*, 20:R301–R356, 2003. doi: 10.1088/0264-9381/20/20/201.

[131] LIGO Scientific, VIRGO Collaborations, BP Abbott, R Abbott, TD Abbott, MR Abernathy, F Acernese, K Ackley, C Adams, T Adams, P Addesso, et al. The basic physics of the binary black hole merger gw150914. *Annalen der Physik*, 529(1-2):1600209, 2017.

[132] Masaru Shibata, Kenichi Nakao, and Takashi Nakamura. Scalar-type gravitational wave emission from gravitational collapse in brans-dicke theory: Detectability by a laser interferometer. *Physical Review D*, 50(12):7304, 1994.

[133] Larry Smarr. Gravitational radiation from distant encounters and from head-on collisions of black holes: The zero-frequency limit. *Physical Review D*, 15(8):2069, 1977.

[134] Stephen J Smartt. Progenitors of core-collapse supernovae. *Annual Review of Astronomy and Astrophysics*, 47:63–106, 2009.

[135] Thomas P Sotiriou and Valerio Faraoni. Black holes in scalar-tensor gravity. *Physical review letters*, 108(8):081103, 2012.

[136] Andrew W Steiner, James M Lattimer, and Edward F Brown. The neutron star mass-radius relation and the equation of state of dense matter. *The Astrophysical Journal Letters*, 765(1):L5, 2013.

[137] K. S. Thorne. NONSPHERICAL GRAVITATIONAL COLLAPSE: A SHORT REVIEW. 1972.

[138] Kip S Thorne. Gravitational-wave bursts with memory: The christodoulou effect. *Physical Review D*, 45(2):520, 1992.

[139] KS Thorne. *Three hundred years of gravitation*. Cambridge University Press, 1989.

[140] KS Thorne, S Hawking, and W Israel. 300 years of gravitation, 1987.

[141] William G. Unruh and Robert M. Wald. Information Loss. 2017.

[142] Elisabeth Vangioni, Keith A Olive, Tanner Prestegard, Joseph Silk, Patrick Petitjean, and Vuk Mandic. The impact of star formation and gamma-ray burst rates at high redshift on cosmic chemical evolution and reionization. *Monthly Notices of the Royal Astronomical Society*, 447(3):2575–2587, 2015.

[143] Sebastian H. Volkel and Kostas D. Kokkotas. Ultra Compact Stars: Reconstructing the Perturbation Potential. 2017.

[144] J.A. Wheeler and J.R. Klauder. *Magic Without Magic: John Archibald Wheeler: A Collection of Essays in Honor of His Sixtieth Birthday*. W. H. Freeman, 1972. ISBN 9780716703372. URL `https://books.google.com/books?id=TQduOwAACAAJ`.

[145] Samuel S Wilks. The large-sample distribution of the likelihood ratio for testing composite hypotheses. *The Annals of Mathematical Statistics*, 9(1): 60–62, 1938.

[146] Clifford M Will. The confrontation between general relativity and experiment. *Living reviews in relativity*, 9(1):3, 2006.

[147] Alan G Wiseman and Clifford M Will. Christodoulou's nonlinear gravitational-wave memory: Evaluation in the quadrupole approximation. *Physical Review D*, 44(10):R2945, 1991.

[148] Kent Yagi and Leo C. Stein. Black Hole Based Tests of General Relativity. *Class. Quant. Grav.*, 33(5):054001, 2016. doi: 10.1088/0264-9381/33/5/054001.

[149] Huan Yang, Kent Yagi, Jonathan Blackman, Luis Lehner, Vasileios Paschalidis, Frans Pretorius, and Nicolas Yunes. Black hole spectroscopy with coherent mode stacking. *Phys. Rev. Lett.*, 118(16):161101, 2017. doi: 10.1103/PhysRevLett.118.161101.

[150] Nicolas Yunes, Kent Yagi, and Frans Pretorius. Theoretical Physics Implications of the Binary Black-Hole Mergers GW150914 and GW151226. *Phys. Rev.*, D94(8):084002, 2016. doi: 10.1103/PhysRevD.94.084002.

[151] Ya B Zel'Dovich and AG Polnarev. Radiation of gravitational waves by a cluster of superdense stars. *Soviet Astronomy*, 18:17, 1974.

[152] Xing-Jiang Zhu, Eric Howell, and David Blair. Observational upper limits on the gravitational wave production of core collapse supernovae. *Monthly Notices of the Royal Astronomical Society: Letters*, 409(1):L132–L136, 2010.

[153] Xing-Jiang Zhu, Eric J Howell, David G Blair, and Zong-Hong Zhu. On the gravitational wave background from compact binary coalescences in the band of ground-based interferometers. *Monthly Notices of the Royal Astronomical Society*, 431(1):882–899, 2013.

[154] Aaron Zimmerman and Yanbei Chen. New Generic Ringdown Frequencies at the Birth of a Kerr Black Hole. *Phys. Rev.*, D84:084012, 2011. doi: 10.1103/PhysRevD.84.084012.